

FLEXURAL BEHAVIOR OF COLD-FORMED AND HOT-ROLLED STEEL
SHEET PILING SUBJECTED TO SIMULATED SOIL PRESSURE

Pawin Ritthiruth

Thesis submitted to the faculty of the Virginia Polytechnic Institute and State

University in partial fulfillment of the requirements for the degree of

MASTER OF SCIENCE

In

CIVIL ENGINEERING

Matthew H. Hebdon, Chair
Matthew R. Eatherton
Rodrigo Sarlo

December 20, 2020

Blacksburg, Virginia

Keywords: sheet piling, flexural capacity, uniform pressure test, transverse stresses

FLEXURAL BEHAVIOR OF COLD-FORMED AND HOT-ROLLED STEEL SHEET PILING SUBJECTED TO SIMULATED SOIL PRESSURE

Pawin Ritthiruth

ABSTRACT

Hot-rolled sheet piling has long-been believed to have a better flexural performance than cold-formed sheet piling based on a test conducted by Hartman Engineering twenty years ago. However, cold-formed steel can have similar strength to the hot-rolled steel. This experimental program studied the flexural behavior of hot-rolled and cold-formed steel sheet pilings. This program quantified the influence of transverse stresses from soil pressure on the longitudinal flexural strength. Four cross-sections with two pairs of equivalent sectional modulus were investigated. Sheet-piling specimens were subjected to simulated soil pressure from an air bladder loaded transversely to their longitudinal axis. The span lengths were varied, while the loading area remains unchanged to examine the effect of different transverse stresses. Lateral bracings were provided at discrete locations to establish a sheet piling wall behavior and allow the development of transverse stresses. Load-pressure, load-deflection, load-strain, and moment-deflection responses were plotted to demonstrate the behavior of each specimen. The moment-deflection curves were then normalized to the corresponding yield stress from tensile coupon tests to make a meaningful comparison. The results indicate that transverse stresses influence the flexural capacity of the sheet pilings. The longer span length has less amount of transverse strains, resulting in a higher moment capacity. The hot-rolled sheet pilings have better flexural performance also because of less transverse strains.

FLEXURAL BEHAVIOR OF COLD-FORMED AND HOT-ROLLED STEEL SHEET PILING SUBJECTED TO SIMULATED SOIL PRESSURE

Pawin Ritthiruth

GENERAL AUDIENCE ABSTRACT

Sheet piling wall is an essential structure used during the excavation process. Sheet piling can be hot-rolled and cold-formed. Hot-rolled sheet piling has long-been believed to have a better bending performance based on a test conducted by Hartman Engineering twenty years ago. However, cold-formed steel can have similar strength to hot-rolled steel. This experimental program studied the bending behavior of hot-rolled and cold-formed steel sheet pilings. This program quantified the influence of lateral loading from soil pressure on the moment capacity of the sheet piling. Four cross-sections with two pairs of equivalent bending properties were investigated. Sheet-piling specimens were set up as beam members and subjected to simulated soil pressure from an air bladder. The span lengths of the specimens were varied, while the loading area remains unchanged to examine the effect of different amounts of load. Lateral bracings were provided at discrete locations to establish a sheet piling wall behavior and allow local deflection of the cross-section. Load-pressure, load-deflection, load-strain, and moment-deflection responses were plotted to demonstrate the behavior of each specimen. The moment-deflection curves were then normalized to the corresponding material property of each specimen to make a meaningful comparison between different specimens. The results indicate that lateral loading of the soil pressure influences the bending capacity of the sheet pilings. The longer span length has less amount of transverse strains, resulting in a higher bending capacity. The hot-rolled sheet pilings have better bending performance also because of less transverse strains.

Table of Contents

ABSTRACT.....	ii
GENERAL AUDIENCE ABSTRACT.....	iii
List of Figures.....	vi
List of Tables.....	xi
CHAPTER 1: Introduction.....	1
1.1 Background.....	1
1.2 Objective and Scope.....	3
CHAPTER 2: Literature Review.....	4
2.1 General Concepts of Structural Steel Sheet Pilings.....	5
2.2 Development of Hat-Type Sheet Pile 900 (Harata et al, 2008).....	7
2.4 Investigation of the Effect of Transverse Loads on the Behavior of Z-shape Steel Sheet Piling (Hartman R.J. and Neal J.A., 1997).....	17
2.5 Flexural Behavior, Web Crippling, and Interaction of Transverse Stress and Bending Moment in Cold-formed Steel and Hot-rolled Steel Sheet piling (NBM Technologies, Inc.).....	22
2.6 Experiments on Flexural Behavior of Cold-formed and Hot-rolled Steel Sheet Pilings.....	35
Phase I: Four-point Bending Tests (NBM Technologies, Inc., 2017).....	35
CHAPTER 3: Experimental Testing Methods.....	48
3.1 Specimen Design.....	53
3.1 Test Setup.....	55
3.3 Specimen Instrumentation.....	63
3.4 Flexural Testing Procedure.....	66
3.5 Material Testing.....	67
3.6 Data Evaluation and Documentation.....	68
CHAPTER 4: Results.....	70
4.1 Recorded Data.....	70
4.2 Test Results.....	72
CHAPTER 5: Discussion.....	88
5.1 General Behavior.....	88
5.2 Moment-deflection Responses.....	95
5.3 Existence of Transverse Stresses and Their Effects on Flexural Behavior.....	100
5.4 Normalized Moment vs. Deflection Responses.....	101
5.5 Effect of Span Length to Moment Capacity.....	108

5.6 Comparison between Hot-rolled and Cold-formed Sheet Piling	111
CHAPTER 6: Conclusions	116
6.1 Conclusions.....	116
6.2 Future Improvement and Research	121
REFERENCES	123
APPENDIX A.....	125
Wiring Diagram and Programing of Test Sensors	125
APPENDIX B	137
Calculation of Sectional Modulus and Plastic Modulus	137
APPENDIX C	140
Test Results of All Specimens	140
C.1 Load-Pressure Responses	140
C.2 Load-Deflection Responses.....	143
C.3 Strain Gauge data	161
C.4 Tensile Coupon Results.....	163
APPENDIX D.....	165
Frictional Resistance of Clamps	165
APPENDIX E	167
Sensor Models and Specifications	167
E.1 Enerpac Hydraulic Ram.....	167
E.2 String Potentiometers	168
E.3 Strain Gauges.....	170
E.3 Pressure Transducer.....	171

List of Figures

Figure 1: Sheet Piling Wall (DesignBuildings, 2017)	1
Figure 2: Steel Sheet Piling Specimens	5
Figure 3: Types of Sheet Piling Cross-sections (Eurocode, 1993)	6
Figure 4: Comparison of Hat-type and U-type Sheet Piles (Harata et al, 2008).....	7
Figure 5: Sheet Pile Driving Methods (Harata et al, 2008).....	8
Figure 6: Field Test Data For Vibro-hammer Method (Harata et al, 2008).....	9
Figure 7: Field Test Data for Hydraulic Jacking Method (Harata et al., 2008)	10
Figure 8: Bending Test Results (Harata et al., 2008).....	11
Figure 9: PZ27 and CZ114 Cross-sections (Hartman R.J. and Neal J.A., 1992).....	12
Figure 10: Flexure Test Setup (Hartman R.J. and Neal J.A., 1992)	13
Figure 11: Strain Data of CZ114 (Hartman R.J. and Neal J.A., 1992)	15
Figure 12: Strain Data of PZ27 (Hartman R.J. and Neal J.A., 1992).....	15
Figure 13: Finite Segment Model for Sheet Piling Cross-Section (Hartman R.J. and Neal J.A., 1997)	18
Figure 14: Finite Segment Model and Data for AZ13 section (Hartman R.J. and Neal J.A., 1997)	19
Figure 15: Design Interaction Curve For AZ13 Sections (Hartman R.J. and Neal J.A., 1997)	20
Figure 16: Sectional Drawing of Sheet Piles (NBM Technologies, Inc., 2016).....	22
Figure 17: Finite Element Models of Sheet Piling Specimens (NBM Technologies, Inc., 2016)	24
Figure 18: Stress Distribution at 0.02 Radians of Bending (NBM Technologies, Inc., 2016)	25
Figure 19: Comparison of Moment-rotation Responses (NBM Technologies, Inc., 2016).....	25
Figure 20: Model for Web Crippling Limit State (NBM Technologies, Inc., 2016)	27
Figure 21: Web Crippling Stress Distributions near Peak Load (NBM Technologies, Inc., 2016).....	28
Figure 22: Web Crippling Load-displacement Responses (NBM Technologies, Inc., 2016).....	28
Figure 23: Interaction Curves for Hot-rolled PZ27 and Cold-formed CZ114RD Profiles (Hartman R.J. and Neal J.A., 1997)	30
Figure 24: Example of Von Mises Stress from Hydrostatic Pressure near Peak Load for Different Span Lengths (NBM Technologies, Inc., 2016)	31
Figure 25: Pressure-moment Interaction Curve for PZC-18 (NBM Technologies, Inc., 2016).....	32
Figure 26: Residual Stresses and Effective Plastic Strains for Cold-formed Sheet Piling Profiles (NBM Technologies, Inc., 2016).....	33
Figure 27: Deformed Shape due to Residual Stresses for XZ-95 Profile (NBM Technologies, Inc., 2016)	33

Figure 28: Effect of Residual Stresses on Cold-formed XZ-95 and JZ-120 (NBM Technologies, Inc., 2016)	34
Figure 29: Four-point Bending Test Setup (NBM Technologies, Inc., 2017)	36
Figure 30: Test Setup for Phase I Project (NBM Technologies, Inc., 2017)	38
Figure 31: Lateral Support Assembly (NBM Technologies, Inc., 2017).....	39
Figure 32: String Potentiometer Layout (NBM, 2017).....	40
Figure 33: Strain Gage Location (NBM, 2017)	41
Figure 34: Load-Deformation Response (NBM, 2017)	42
Figure 35: Moment vs Deflection at Midspan (NBM Technologies, Inc., 2017)	43
Figure 36: Moment at Midspan VS End Rotation Response (NBM Technologies, Inc., 2017).....	44
Figure 37: Comparison of Normalized Moment VS Scaled Deflection at Midspan in Cold-formed and Hot-rolled Cross-sections (NBM, 2017).....	45
Figure 38: Comparison of Normalized Moment VS Scaled end rotation at Midspan in Cold-formed and Hot-rolled Cross-sections (NBM, 2017).....	45
Figure 39: Normalized Longitudinal Strain vs Normalized Bending Moment at Midspan (NBM, 2017)	46
Figure 40: Normalized Transverse Strain vs Normalized Bending Moment at Midspan (NBM, 2017) ...	47
Figure 41: Three Different Types of Strains on a Sheet Piling.....	51
Figure 42: Different Span Length Configuration.....	52
Figure 43: Test Setup Views.....	57
Figure 44: Actual Boundary Condition of Sheet Piling	58
Figure 45: 12-inch Heavy Duty Clamps	59
Figure 46: 3D Views of Lateral Supports	59
Figure 47: Hilman Roller Parts	60
Figure 48: Spreader Frame Components	61
Figure 49: Air Bladder Cross-section	62
Figure 50: Air Bladder Assembly	62
Figure 51: Instrumentation Locations	65
Figure 52: Manual Load and Pressure vs Midspan Deflection Plot for PZC18-35	67
Figure 53: Tensile Coupon Cut.....	68
Figure 54: Tensile Coupon Drawing per ASTM E6.....	68
Figure 55: Deformed JZ120-16 Specimen during Test.....	71
Figure 56: Deformed JZ120-35 Specimen During Test.....	72
Figure 57: Manually Ram Load VS Air Bladder Pressure Plot for PZC26-35.....	73
Figure 58: Comparison of Load-pressure Plots For PZC26-35 and JZ120-16 Test Groups.....	75

Figure 59: Load-Deformation Plots for JZ120-16-3.....	78
Figure 60: Deformed JZ120-16-3 Specimen after Test	79
Figure 61: Load VS Local Stresses for JZ120-16-3 Specimen.....	81
Figure 62: Load VS Midspan Deflection for All Specimens in a Test Group	84
Figure 63: Tensile Coupon Test Setup.....	86
Figure 64: Example of Stress-strain Relationship for Tensile Coupon Test.....	86
Figure 65: Air bladder Behavior under High Load.....	90
Figure 66: Interlock Buckling of XZ95-35	92
Figure 67: Strain Gauge Data for XZ95-35-3.....	93
Figure 68: Calculation Aid for Structural Analysis of Test Setup (AISC, 2017)	95
Figure 69: Moment-Deflection Responses for All Specimens in a Test Group.....	99
Figure 70: Normalized Moment-Deflection Responses of All Specimens	104
Figure 71: Comparison on Capacities of JZ120-16 Tests from NBM (2016) and VT (2020).....	107
Figure 72: Comparison on Transverse Strains of JZ120-16 from NBM (2016) and VT (2020)	107
Figure 73: Comparison on Transverse Stresses of JZ120-16 and JZ120-35.....	109
Figure 74: Comparison on Normalized Moment vs. Deflection Curves for Different Span Lengths	110
Figure 75: Comparison on Normalized Moment vs. Deflection Curves for Hot-rolled and Cold-formed Sheet Piling	112
Figure 76: Comparison on Transverse Strain Data of Hot-rolled and Cold-formed Cross-sections	115
Figure 77: Design Aid Example for JZ120 Profile	121
Figure 78: DAQ Configuration.....	125
Figure 79: DAQ Scan Interval	125
Figure 80: DAQ Voltage Block	126
Figure 81: DAQ Voltage Block 1 (Air Bladder Pressure)	126
Figure 82: DAQ Voltage Block 2 (Hydraulic Ram Load).....	127
Figure 83: DAQ Voltage Block 3 (String Potentiometers).....	127
Figure 84: DAQ Filtered Voltage Slot 8 (String Potentiometers).....	128
Figure 85: DAQ Filtered Voltage Slot 9 (String Potentiometers).....	128
Figure 86: DAQ Filtered Voltage Slot 10 Block 1 (String Potentiometers)	129
Figure 87: DAQ Filtered Voltage Slot 10 Block 2 (Strain Gauges)	129
Figure 88: DAQ Filtered Voltage Slot 11 (Strain Gauges).....	130
Figure 89: DAQ Filtered Voltage Slot 12 (Strain Gauges).....	130
Figure 90: DAQ Wiring Diagram for Slot 1 to 7.....	131
Figure 91: Daq Wiring Diagram for Slot 8.....	132

Figure 92: DAQ Wiring Diagram for Slot 9	133
Figure 93: DAQ Wiring Diagram for Slot 10	134
Figure 94: DAQ Wiring Diagram for Slot 11	135
Figure 95: DAQ Wiring Diagram for Slot 12	136
Figure 96: MASSPROP for JZ120.....	137
Figure 97: MASSPROP for PZC26	138
Figure 98: MASSPROP for XZ95	138
Figure 99: MASSPROP for PZC18	139
Figure 100: Load-pressure Relationship for All Specimens In a Test Group	142
Figure 101: Load-Deflection Data For JZ120-16-1	143
Figure 102: Load-deflection Data for JZ120-16-2.....	144
Figure 103: Load-deflection Data for JZ120-16-3.....	145
Figure 104: Load-deflection Data for XZ95-25-1	146
Figure 105: Load-deflection for XZ95-25-2.....	147
Figure 106: Load-deflection Data for XZ95-25-3	148
Figure 107: Load-deflection Data for JZ120-35-1.....	149
Figure 108: Load-deflection Data for JZ120-35-2.....	150
Figure 109: Load-Deflection Data for JZ120-35-3.....	151
Figure 110: Load-deflection Data for XZ95-35-1	152
Figure 111: Load-Deflection Data for Xz95-35-2	153
Figure 112: Load-deflection Data for XZ95-35-3	154
Figure 113: Load-Deflection Data for PZC26-35-1.....	155
Figure 114: Load-Deflection Data for PZC26-35-2.....	156
Figure 115: Load-Deflection Data for PZC26-35-3.....	157
Figure 116: Load-deflection Data for PZC18-35-1	158
Figure 117: Load-deflection Data for PZC18-35-2	159
Figure 118: Load-deflection Data for PZC18-35-3	160
Figure 119: Strain Gauge Data.....	163
Figure 120: Tensile Coupon Results.....	164
Figure 121: 12-inch Heavy-duty Clamp Catalog (McMaster, 2020).....	165
Figure 122: Enerpac Ram Property (Enerpac, 2020).....	167
Figure 123: Enerpac Ram Dimensions (Enerpac, 2020).....	168
Figure 124: String Potentiometer Specification (Celesco, 2005).....	168
Figure 125: String Potentiometer Drawing (Celesco, 2005).....	169

Figure 126: String Potentiometer Circuit (Celesco, 2005).....	169
Figure 127: Strain Gauge Package.....	170
Figure 128: Strain Gauge Data Sheet (Tokyo Measuring Instruments Lab., 2017).....	170
Figure 129: Pressure Transducer (Omega Engineering, 2019).....	171
Figure 130: Pressure Transducer Specification (Omega Engineering, 2019).....	171
Figure 131: Pressure Transducer Wiring Diagram (Omega Engineering, 2019).....	172

List of Tables

Table 1: Test Results (Hartman R.J. and Neal J.A., 1992)	14
Table 2: Sheet Pile Sectional Properties (NBM Technologies, Inc., 2016)	23
Table 3: Web Yielding and Crippling Capacities per AISC 360-10 (NBM Technologies, Inc., 2016)	26
Table 4: Computed Span Length to Isolate Web Crippling Limit State (NBM Technologies, Inc., 2016)	26
Table 5: Comparison of the Capacity per AISC 360-10 and from the Study (NBM Technologies, Inc., 2016)	29
Table 6: Test Matrix (NBM Technologies, Inc., 2017)	36
Table 7: Specimen Web Crippling Capacity (NBM Technologies, Inc., 2017)	37
Table 8: Specimen Shear Capacity (NBM Technologies, Inc., 2017)	37
Table 9: Specimen Connecting Bolt Design (NBM Technologies, Inc., 2017).....	38
Table 10: Tensile Coupon Result (NBM Technologies, Inc., 2017)	42
Table 11: Test Matrix.....	55
Table 12: Target Load and Pressure Given from Finite Element Analysis By NBM.....	66
Table 13: Tensile Coupon Results	87
Table 14: Ratio of Maximum moment to Yield and Plastic Moments	105
Table 15: Plastic Modulus Calculation	139

CHAPTER 1: Introduction

1.1 Background

Sheet piling is one of the necessary components commonly used in the construction process. It is capable of supporting soil or water mass during excavation and construction of a structural foundation. Several sheet piles are driven into the ground and connected to form a retaining wall such that they behave similarly to a flexural cantilever member (See **Figure 1**). Understanding the failure modes of sheet piles and the effect of uniform soil pressure is vital for the design of a sheet-piling wall. This research investigated behavior, failure modes, flexural capacity, and the relationship between longitudinal and transverse stresses of sheet piling specimens. The experiment included several specimens with differences in cross-sections and span lengths. Two main types of specimens, including hot-rolled and cold-formed sheet piling, were tested. The data obtained from the test can be used to examine the effect of the transverse soil pressure on the flexural capacity of a sheet pile, the effect of span lengths, and the comparison between hot-rolled and cold-formed sheet-piles.



FIGURE 1: SHEET PILING WALL (DESIGNBUILDINGS, 2017)

Sheet piles behave unlike other steel sections. They are made of thin steel plates formed or rolled into a unique shape to have better sectional properties. The members are connected and loaded simultaneously like a wall restraining soil pressure. The sheet piles are subjected to uniform flexural loading in both

longitudinal and transverse directions. The lateral deformation of a sheet piling member is prevented because it is laterally braced at the interlocks by other sheet piles in the retaining wall system. This lateral bracing condition makes the sheet pile develop transverse stresses.

This research was motivated to evaluate and discuss the perceived structural capacity differences in the steel sheet piling industry between cold-formed and hot-rolled cross-sections. Hartman and Neal conducted a project with different hot-rolled and cold-formed piling configurations (Hartman R.J. and Neal J.A., 1992 and 1997). They created design curves in which the moment capacity of both hot-rolled and cold-formed sections decrease from the full capacity to zero at some higher points of the applied hydrostatic pressure (See an example in **Figure 15**). The decrease in capacity was due to the existence of transverse stresses. They also concluded that the hot-rolled sheet pilings' capacity was better than the cold-formed sheet piles even though both cross-sections had similar sectional modulus. The result has been believed and used for more than 20 years. However, today, cold-formed steel can have similar strength with the hot-rolled steel. Samuel Roll Form Group company, and NBM technologies company, conducted a finite element analysis and four-point bending tests (NBM Technologies, Inc., 2016 and 2017). The results showed that Hartman's conclusion was inaccurate since only a few tests were conducted in 1992, and the difference in transverse stress and longitudinal stress ratios were not considered. The analysis suggested consistent flexural responses for hot-rolled and cold-formed sheet pilings with similar sectional modulus. Therefore, the uniform bending experiment will be performed to confirm the results from the finite element analysis.

1.2 Objective and Scope

This experimental program compares the relationship between transverse stress and flexural capacity of hot-rolled and cold-formed sheet piling specimens. The transverse stress causes a sheet piling section to buckle locally before reaching the specified yield strength of the cross-section, preventing it from reaching the specified capacity (NBM Technologies, Inc., 2016). Four different cross-sections include cold-formed (JZ-120 and XZ-95) and hot-rolled (PZC-18 and PZC-26) profiles were evaluated. The same type of the cross-section, for example JZ120 and XZ95, has the same shape of the middle interlock. The sheet piles were loaded uniformly under pressure through an air bladder at the mid-span, which generated simultaneous longitudinal and transverse loading. The objectives were to investigate the flexural behavior of sheet piling under with an existence of transverse loading, effects of span length, and performance between hot-rolled and cold-formed sheet-pilings. The main research questions the research team planned to study included:

- How do the transverse bending stresses associated with the local bending of the flanges or webs due to the applied pressure perpendicular to their surfaces, and the axial stresses due to loading against the restrained conditions affect and interact with the longitudinal stresses associated with the major axis moment and how do the effect and the interaction influence the maximum moment of the cross-section?
- How and why the different amount of uniform loading in both vertical and lateral directions to the cross-section that is required to obtain a similar moment for the different span lengths affect the maximum moment of the cross-section?
- How and why the hot-rolled and cold-formed sheet pilings are or are not equivalent in terms of their flexural behavior and what could be the factors?

CHAPTER 2: Literature Review

The major types of literature to be reviewed in this study are related to steel sheet piling tests. These include the development of steel sheet pilings, flexural behavior, effects of longitudinal and transverse strains, failure modes, different material properties of hot-rolled and cold-formed sheet piling processes, and hydrostatic test on sheet piles. Sheet piling standards and specifications are also reviewed.

This project builds on research conducted at Lehigh University (NBM Technologies, Inc., 2017). The major difference between this research and previous research is the loading method; a four-point bending test was used for Phase I, and a uniform pressure test was used for Phase II in the current research. To control the failure mechanism, the layout of the test was designed based on the finite element study (NBM Technologies, Inc., 2016).

Other former tests were conducted by Hartman R.J. and Neal J.A. They tested a hot-rolled and a cold-formed cross-section with similar sectional modulus (Hartman R.J. and Neal J.A., 1992). They used a water bladder to apply a hydrostatic pressure on the sheet piles to study their flexural behavior. Five years later, they created design aids for many sheet-piling profiles (Hartman R.J. and Neal J.A. 1997). These experimental programs were the inspirations of all the tests outlined above.

The data reviewed were used to design test setup for Phase II program, controlling the failure mode of the sheet piling specimens, preventing issues that may occur during the test according to the previous studies, selecting analytical methods, and presenting the result from the study.

2.1 General Concepts of Structural Steel Sheet Pilings

Sheet piling is a structural member used for establishing continuous systems or walls to retain water and/or soil pressure. Sheet piling cross-sections are produced either from hot-rolled or cold-formed steel plates (JD Field, 2015). Sheet piles are installed using a mechanical pile driver in sequences along the excavation perimeter. Members are connected using longitudinal interlocks at both sides of the cross-section to form a continuous wall. They can be used as temporary structures during an excavation process or permanent retaining structures as shown in **Figure 1**. An example of sheet piling cross-sections (JZ-120 and XZ-95) is shown in **Figure 2**.

There are many advantages of sheet piling members, making them very popular to use as a retaining wall elements. They are convenient to be lifted and transported. Also, they can be reused and recycled, similar to other steel structures. Pile length and design are adjustable to the site condition. The sheet pile cost itself and the maintenance cost are relatively less expensive than other types of retaining walls. However, it is difficult to drive a sheet pile into rocky soil, and there is some disturbance to the vicinity during pile driving process. Also, the costs of removing sheet piles used as temporary systems need to be considered (Designingbuildings, 2018).



FIGURE 2: STEEL SHEET PILING SPECIMENS

Steel sheet piles were first introduced in the 19th century. During that time, wood and cast iron were still common materials for structural applications. However, these materials lack ductility; therefore, a sheet pile was manufactured using medium steel and became more popular. The development of sheet pile required the following main characteristics (F.R. Mackley, 2010): economy, sufficient strength to retain soil or water pressure without an excessive amount of bracing, stiffness to prevent buckling under the driving hammer, water-tightness, and economical cross-sections. One of the most famous developers is Try Larsen, a German chief engineer. He invented the first steel sheet pile with a U-section, which has straight webs and riveted interlocks. His design concept had been used for the following sheet piling developments until a new rivet-less interlock was debuted. However, the U-shape cross-section is still commonly used in structural applications (JD Field, 2015). The most common cross-sectional types of steel sheet pile are shown in **Figure 3**.

Type of cross-section	Single pile	Double pile
Z - profiles		
U - profiles		
Straight web profiles		
<small>Note: Reference should be made to EN 10248 for details of the interlocks.</small>		

FIGURE 3: TYPES OF SHEET PILING CROSS-SECTIONS (EUROCODE, 1993)

The next generation of sheet piles, which is Z-section or hat-section, was created with improvements in cross-section details to enhance the structural properties, such as higher local buckling strength. A continuous web connecting to the flanges was also introduced. These sectional changes resulted in a greater strength-to-weight ratio and efficient installing process (JD Field, 2015).

2.2 Development of Hat-Type Sheet Pile 900 (Harata et al, 2008)

Introduction

Steel sheet piles were first reported to be used for an earth retaining wall in Japan in 1903. Then, in 1923 large amounts of steel sheet piles were imported to the country for post-disaster construction and damage repair of the Great Kanto Earthquake of 1923 (Harata et al, 2008). After that, Japan started to produce more sheet piles domestically, and finally, the amounts of sheet piles produced each year reached 600,000 ton for recent years. In the beginning, U-type sheet piles were the most popular type of cross-sections. U-type cross-section has only one top flange and two webs. Nippon steel had improved its technology related to rolling and pile driving. In 2005, the Hat-type Sheet Pile 900 was manufactured and sold (Harata et al., 2008). **Figure 4** compares the difference in sheet piling walls from U-type and Hat-type sheet piles. The major difference between the two types are the shape of the interlocks and how the members are connected to form a sheet piling wall.

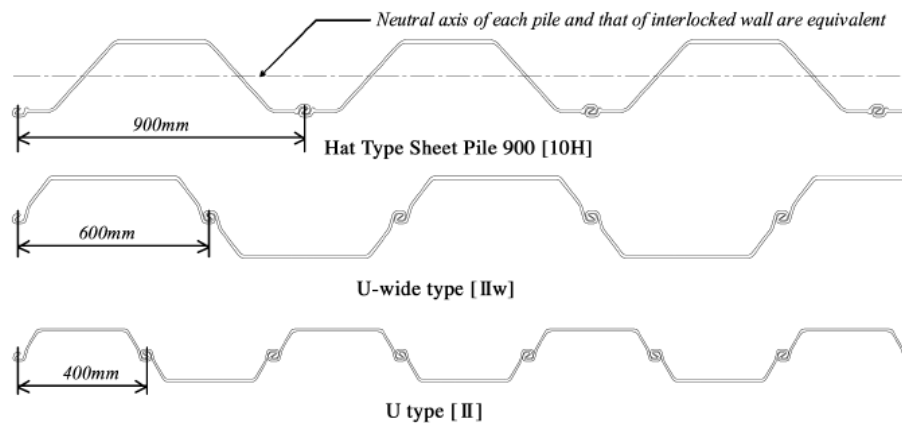


FIGURE 4: COMPARISON OF HAT-TYPE AND U-TYPE SHEET PILES (HARATA ET AL, 2008)

Shape and Features of Hat-Type Sheet Pile 900

A hat-type sheet piling cross-section is relatively thin, with a large sectional area. This makes it more efficient for pile-driving work because this section is more rigid than a U-type sheet pile. Pile deformation is restrained while the pile is being driven. A hat-type sheet pile has better joint efficiency since the neutral

axis of a wall system is approximately in the middle of the cross-section, not the joint's location, unlike the U-type sheet piling wall. This leads to higher structural reliability (Harata et al., 2008). Furthermore, the hat-type sheet pile reduces the number of sheet piles per unit wall area, which helps shorten the construction period and decrease the amount of steel used, as shown in **Figure 4**.

Pile-driving Methods

In general, there are two main methods to drive a sheet pile into the ground: vibratory driving method (or Vibro-hammer method) and hydraulic jacking method (See **Figure 5**). In the first method, the top of a sheet pile is attached to a Vibro-hammer, which vibrates and pushes the sheet pile into the ground. The second method uses the resistance to withdrawal of a sheet pile, which has already driven into the ground to push new sheet piles statically into the ground. This method is useful for low-vibration and low-noise requirements (Harata et al., 2008).



Figure6a: Vibratory Driving Method



Figure6b: Hydraulic jacking Method

FIGURE 5: SHEET PILE DRIVING METHODS (HARATA ET AL, 2008)

Driving Performance with Vibro-hammer Method

A driving test was conducted in Futtcu City, Chiba, Japan to compare Hat-type Sheet Pile 900 and U-wide-type Sheet Pile performance. The specimens had the same length of 12 meters. **Figure 6** shows the soil profile at the site, driving time, and power of vibrator for driving these two sheet piling profiles. The performance in terms of time and power used for driven these two types of sheet piles are very similar. However, the hat-type profile has better sectional properties. Therefore, the Hat-type Sheet Pile 900 has good driving performance with the Vibro-hammer method (Harata et al., 2008).

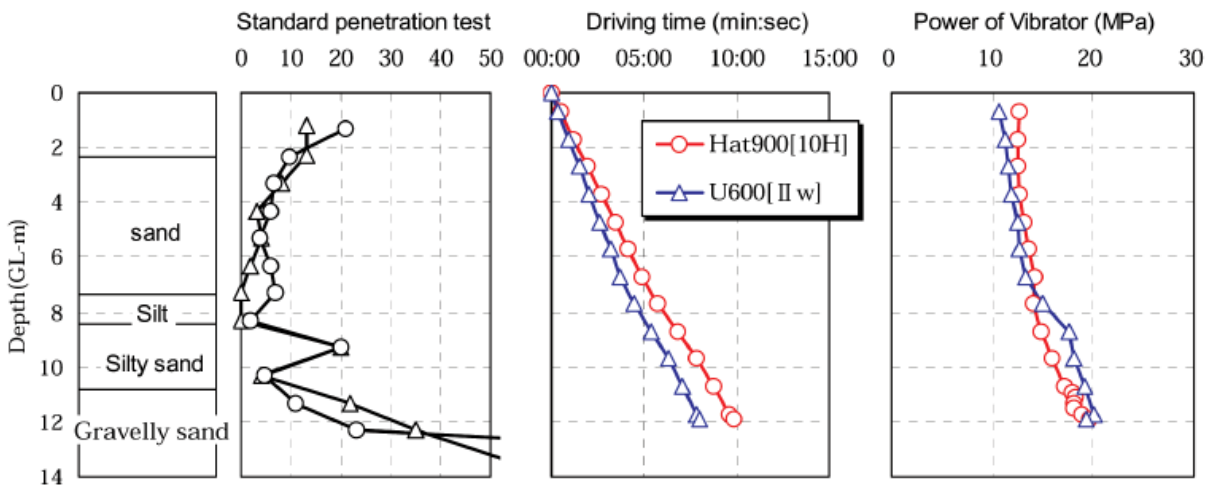


FIGURE 6: FIELD TEST DATA FOR VIBRO-HAMMER METHOD (HARATA ET AL, 2008)

Driving Performance with Hydraulic Jacking Method

Another test was conducted in Kochi City using 15-meter sheet piles. The same two-sheet piling profiles were investigated. In the test, the specimens were driven in straight and curved alignments of the wall, and the test data, including the soil profile at the site, driving time, and load of piling, is shown in **Figure 7**. The results from this test show that the hat type cross-section required higher driving time and load for driving. However, because of its larger sectional area, it may be said that the Hat-type Sheet Pile 900 has good driving performance (Harata et al., 2008).

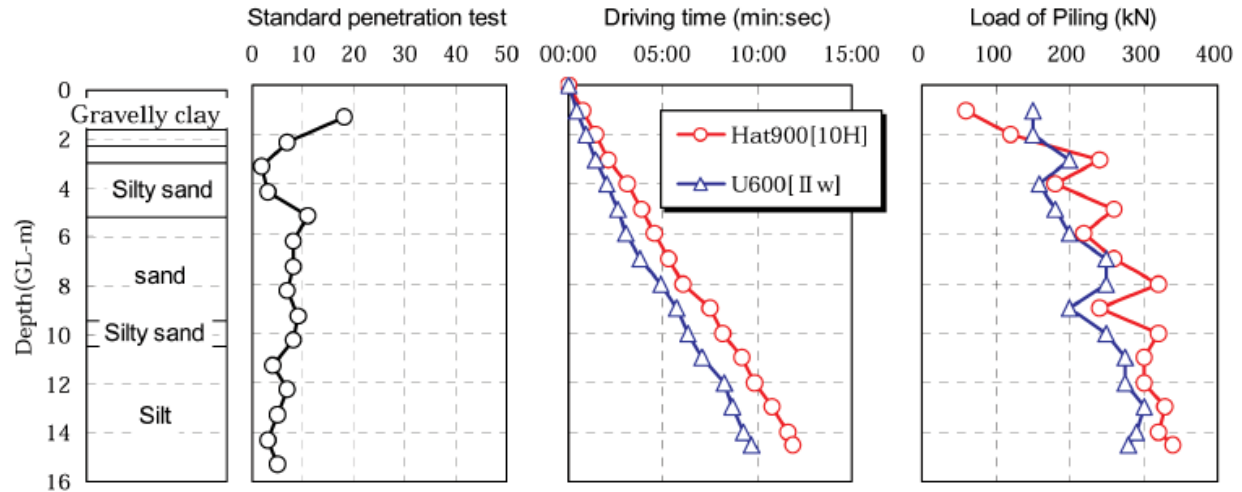


FIGURE 7: FIELD TEST DATA FOR HYDRAULIC JACKING METHOD (HARATA ET AL., 2008)

Four Point Bending Test

A single pile and two piles jointed side by side were subjected to a bending test to investigate the flexural resistance of the Hat-type Sheet Pile 900 (Harata et al., 2008). The test configuration and results are illustrated in **Figure 9**. The Y-axis represents the applied load converted in terms of sheet pile width per meter to compare both types of specimens. The horizontal dash lines are the calculated load for the first yield and the full plastic load based on sectional properties. Up to the yield point, the load-displacement curves are almost the same as a theoretical estimation. However, the single pile specimen cannot reach fully plastic because of local buckling, unlike the jointed piles. The jointed piles also show an equivalent relationship to the single pile in the bending test. This concludes that the Hat-type Sheet Pile 900 has joint efficiency, as mentioned previously in this study (Harata et al., 2008).

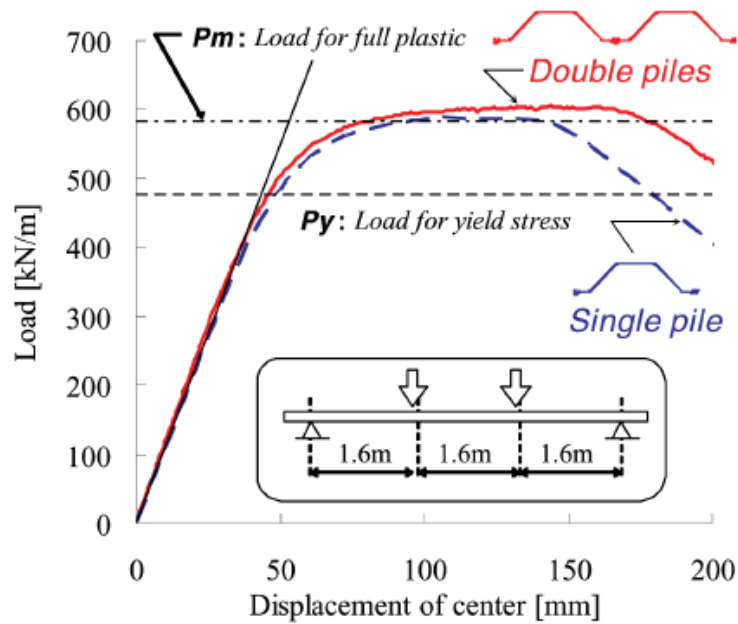


FIGURE 8: BENDING TEST RESULTS (HARATA ET AL., 2008)

Tensile Test of Joints

A joint of Hat-type Sheet Pile 900 was tested to ensure the tensile strength of the joint (Harata et al., 2008). 100-mm long test specimens were subjected to tensile loading until the steel ruptured or the joint separated. The average maximum load exceeded 62.6 kN, which the joint separated before the steel had ruptured for all the specimens. However, the tensile test for U-wide-type sheet piling joints in the past showed the maximum load of 50 kN. Therefore, the Hat-type Sheet Pile 900 has good joint strength comparable to the U-wide-type sheet pile (Harata et al., 2008).

Conclusion

A hat-type sheet pile, such as the Hat-type Sheet Pile 900, is a structural steel product that applies sheet pile manufacturing technology and engineering applications. It has been proven that the sectional properties and performances are comparable to the former U-type sheet piles in terms of driving performances, flexural strength, and joint efficiency. Therefore, hat-type sheet piles can be used and applied to all the same sheet piling applications, which the conventional U-type can do with comparable or better performance in some aspects (Harata et al., 2008).

2.3 Summary Excerpted from Report of Investigation and Test Program Related to Behavior of Steel Sheet Piling Subjected to Hydrostatic Test Loading (Hartman R.J. and Neal J.A., 1992)

Introduction

The testing program was conducted by the collaboration of Hartman Engineering and the State University of New York at Buffalo in 1992 to determine whether the current cold-rolled steel sheet piling is structurally equivalent to traditional hot-rolled sheet piling. Sheet piling cross-sections with equivalent structural properties were tested. **Figure 9** shows the drawings and sectional modulus of PZ27 and CZ144 sheet piles tested. The cold-form sections CZ114 has specified section modulus of 31.6 inches cubed per foot of the wall, and the hot-rolled sections PZ27 has a value of 30.2. Although both cross-sections have almost the same section modulus; width, depth, and width-to-thickness ratios are all different. Flexural behavior under hydrostatic pressure was investigated (Hartman R.J. and Neal J.A., 1992).

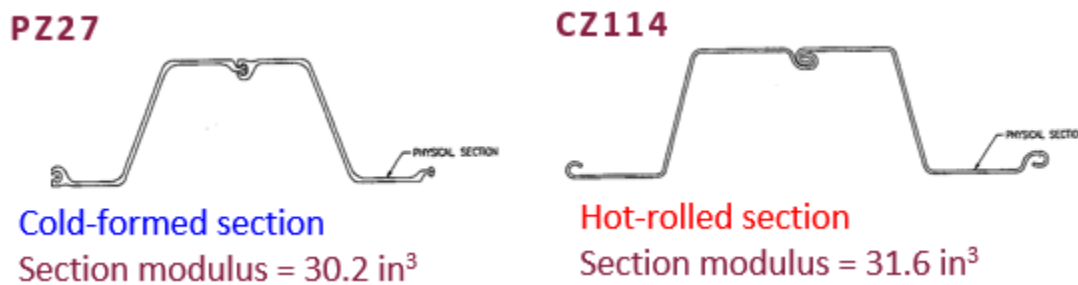


FIGURE 9: PZ27 AND CZ114 CROSS-SECTIONS (HARTMAN R.J. AND NEAL J.A., 1992)

Test Setup and Test Procedure

The specimens were 40-feet long, restrained by steel wales at the midspan and both ends, and loaded by water pressure. Each test assembly consisted of two test piles, six enclosure piles, an interlock closure system, a bladder, and a restraint frame. The piling test was set up in two layers with four piles in each layer to create a wall system. The two test specimens were in the middle of the upper layer (Hartman R.J. and Neal J.A., 1992). **Figure 11** shows the test setup components.

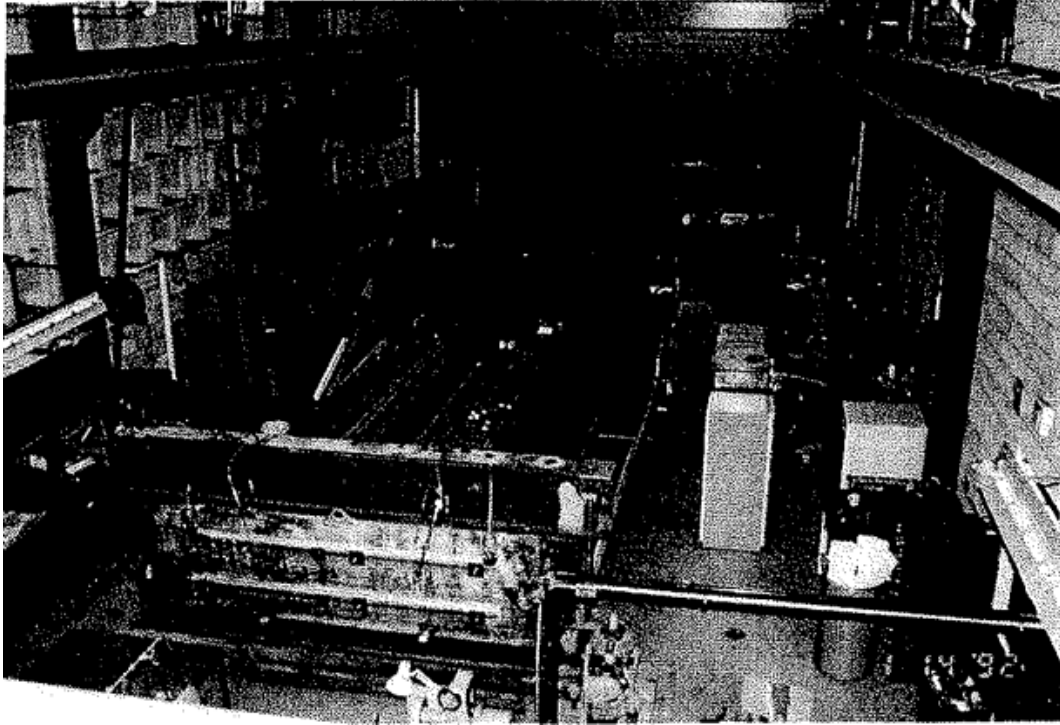


FIGURE 10: FLEXURE TEST SETUP (HARTMAN R.J. AND NEAL J.A., 1992)

Water pressure was applied to the bladder slower than one psi per minute to establish the static loading until failure of the test sheet piles. The water valve was turned off at the time pressure, and strain data were recorded. Strain gauges were attached to one of the two test specimens on the upper flanges, webs, and lower flanges. After each test, tensile coupons were cut from the specimen to determine the actual material properties (Hartman R.J. and Neal J.A., 1992).

Test Results and Discussion

In this project, there were three successful tests in total. The first successful test of a CZ114 specimen was conducted in May 1991. Before that, there were two unsuccessful tests due to the failure of the bladder that was not strong enough to resist the pressure (Hartman R.J. and Neal J.A., 1992). Afterwards, a test for PZ27 and a confirmation test for CZ114 were done.

The results showed that the specimen's accelerated deformation occurred when the applied water pressure reached 17.6 psi for CZ114 and 26.8 to 28 psi for the PZ27 section. The confirmation test gave the result

of 17.1 psi. The failure mechanism observed was web crippling for both hot-rolled and cold-formed specimens, and the top flanges then deformed inelastically (Hartman R.J. and Neal J.A., 1992). The summary of the result is shown in **Table 1**.

TABLE 1: TEST RESULTS (HARTMAN R.J. AND NEAL J.A., 1992)

Section	Yield Stress (ksi)	Calculated Yield		Test Failure Pressure (psi)	Failure Ratio
		Bending Moment (k-in/ft)	Applied Pressure (psi)		
CZ114 5/30/91	51.9	1641	21.2	17.6	0.83
PZ27	48.2	1456	18.8	26.8	1.42
CZ114 1/16/92	50.7	1603	20.7	17.1	0.83

The data plotted in **Figure 11** and **Figure 12** indicate that there were significant transverse stresses (perpendicular to the longitudinal axis of the sheet piles), which in some cases are larger than the longitudinal bending stresses. This point reinforces that analyses of sheet piles using combined stress methods would be more accurate than the standard beam theories used to predict the flexure behavior. A deviation from linearity in the curves indicates redistribution of stress and variation in the state of stresses within the sheet piles. The plots for PZ27 show that the flanges yield, but the specimen can redistribute the force to maintain the sectional strength and shape. However, simultaneously, the flanges of the CZ144 specimen still behaved elastically before the entire failure, and there is no load redistribution (Hartman R.J. and Neal J.A., 1992).

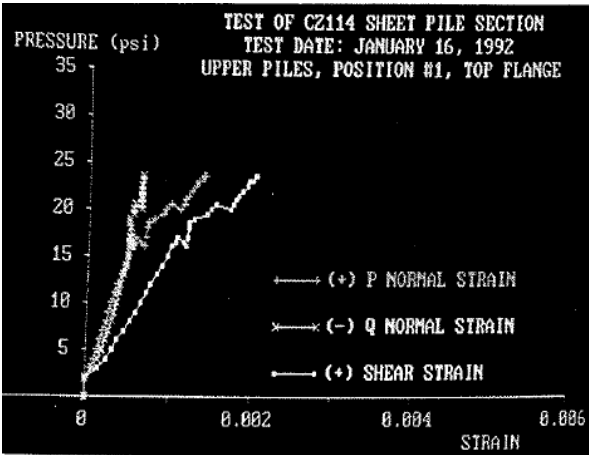


Figure 12a: Strain data at top flange

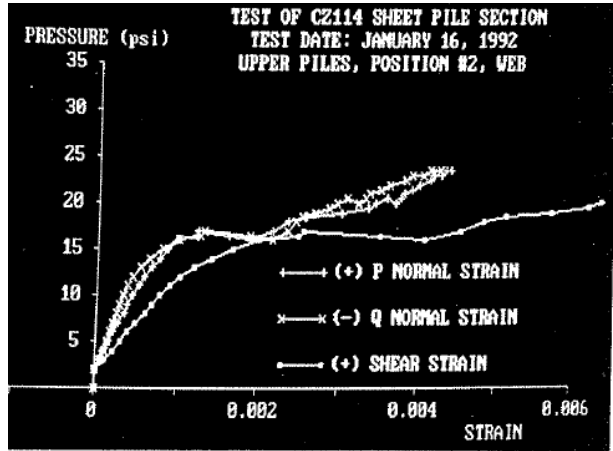


Figure 12b: Strain data at web

FIGURE 11: STRAIN DATA OF CZ114 (HARTMAN R.J. AND NEAL J.A., 1992)

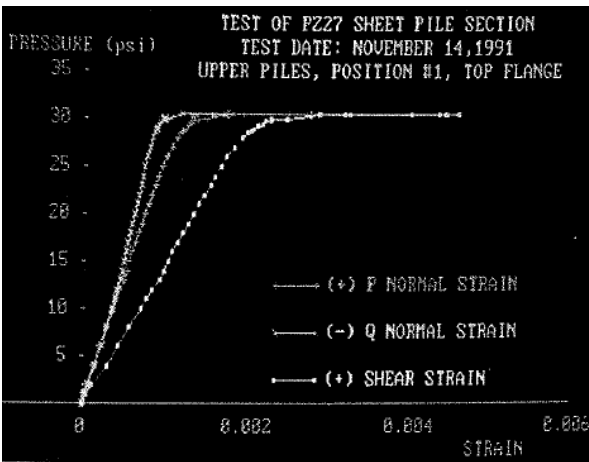


Figure 13a: Strain data at top flange

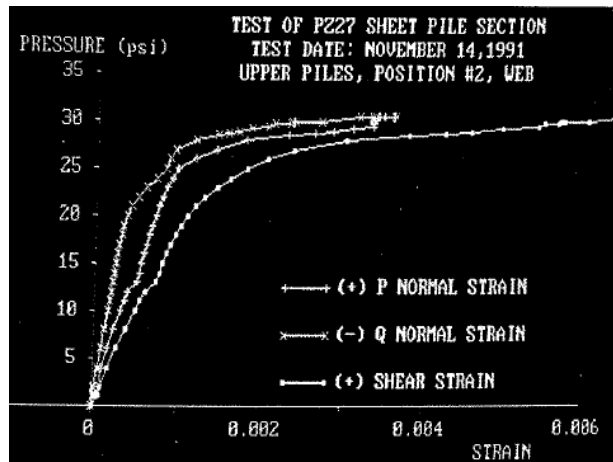


Figure 13b: Strain data at web

FIGURE 12: STRAIN DATA OF PZ27 (HARTMAN R.J. AND NEAL J.A., 1992)

Table 1 also shows the failure ratio of each test, which was calculated by the ratio of water pressure at the failure to first yield. The failure ratio indicates if the cross-section had used its full specified capacity. For the cross-section to use the full strength of steel, it must withstand the load up to the yield moment without premature failure. The section properties of the PZ27 specimen with prior flange yielding were changed, and this prevented the specimen from achieving the theoretical maximum load (Hartman R.J. and Neal J.A., 1992).

Conclusion

The cold-formed CZ114 section was not structurally equivalent to the hot-rolled PZ27 section; that is the capacity of the CZ114 section was approximately 65 percent of the PZ27 section. The difference in the geometry of CZ114 from PZ27 affects the flexural capacity. A better analysis technique to predict sheet piles' behavior was a combined longitudinal and transverse stress rather than a normal beam theory (Hartman R.J. and Neal J.A., 1992). According to Hartman's conclusion, the design practice using only section modulus was inadequate and must be improved. Bidirectional loading, slenderness ratio, and more factors should be considered.

2.4 Investigation of the Effect of Transverse Loads on the Behavior of Z-shape Steel Sheet Piling (Hartman R.J. and Neal J.A., 1997)

Introduction

This project was conducted to evaluate the effect of transverse loads on Z-shape steel sheet piles' capacity using stiffness approaches. The previous test result indicated that the hot-rolled and cold-formed sheet piling with the same sectional modulus were not structurally equivalent (Hartman R.J. and Neal J.A., 1992).. There was an effect of transverse stresses that accelerated the first yield of the specimens until they utilized their specified strength. This caused a problem for design engineers to evaluate sheet piling's actual capacity since they used only regular beam theories, which was not valid for sheet piling subjected to soil or water pressure (Hartman R.J. and Neal J.A., 1997).

The current phase intended to establish a technically reliable and appropriate design tool for engineers in practice. The tool resulted from this phase consists of two sets of equations and graphs for sheet piling adjacent to a wale or sheet piling in a span, which is more accurate but still convenient for the design process.

Formulation of Design Tool

General concepts involved the calculation of loads and stresses perpendicular to the longitudinal axis of the sheet pile. Then, the interaction between longitudinal and transverse stresses. Analyses were limited to the elastic behavior of steel, and traditional beam theories were used to calculate deflections and stress within the sheet pile.

1. Calculation of Transverse Loads and Stresses

Each sheet piling cross-section was modeled as a combination of finite segments, including a straight bar of uniform section, straight bars with uniform section with a hinge at left or right end, a circular bar of uniform section, and a straight with linearly varied thickness. The finite segments is shown in **Figure 14**

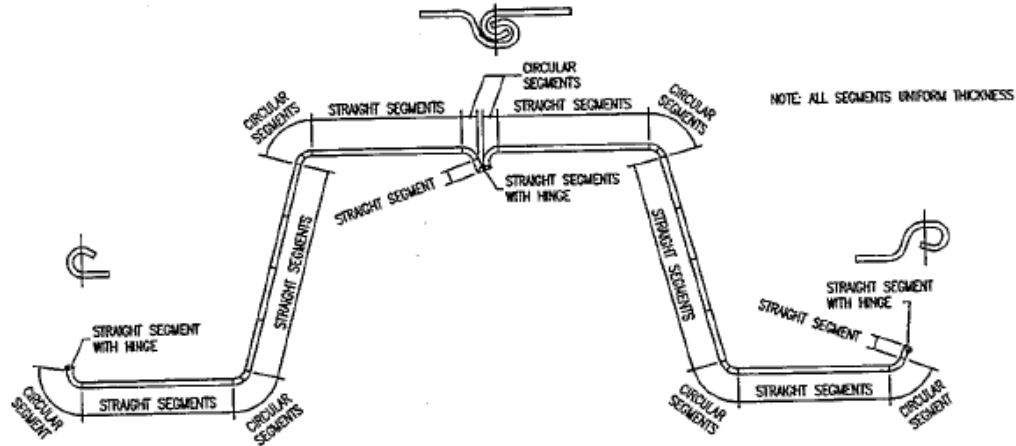


FIGURE 13: FINITE SEGMENT MODEL FOR SHEET PILING CROSS-SECTION (HARTMAN R.J. AND NEAL J.A., 1997)

The stiffness matrix of a sheet pile section was formed by a combination of various types of segments outlined in the text by Tuma, 1988. The degrees of freedom at each joint are two orthogonal displacements and one rotation to account for both axial and flexure deformations. After obtaining stiffness matrices of all individual segments, they were subjected to angular transformation, then were combined to achieve the stiffness matrix of the sheet piling cross-section (Hartman R.J. and Neal J.A., 1997). **Figure 14** shows a finite segment model for AZ13 sheet piling section and segment data.

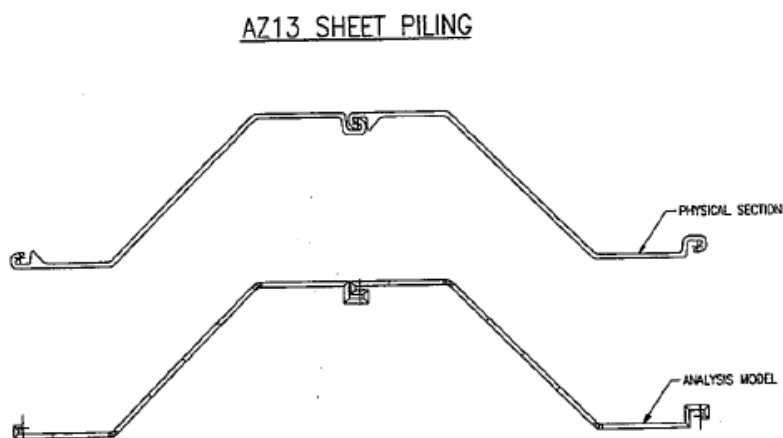


Figure 15a: Actual AZ13 Section versus Finite Segment Model

SEGMENT DATA								
SEGMENT NO.	TYPE	ROTATION (deg.)	STRAIGHT SECTION LENGTH (in.)	CIRCULAR SECTION		THICK (in.)	COORDINATES	
				RADIUS (in.)	ANGLE (deg.)		X (in.)	Y (in.)
1	1	+180.00	0.51			0.375	+0.00	+0.00
2	1	+270.00	0.68			0.375	-0.51	+0.00
3	1	+0.00	2.83			0.375	-0.51	-0.68
4	1	+0.00	4.29			0.375	+2.32	-0.68
5	5	+2.25	0.18			0.375	+6.61	-0.68
6	5	+12.95	0.18			0.375 : 0.396	+6.79	+0.67
7	5	+32.43	0.18			0.396 : 0.421	+6.97	-0.63
8	5	+43.14	0.18			0.421 : 0.396	+7.12	-0.53
9	1	+45.38	3.87			0.396 : 0.375	+7.25	-0.41
10	1	+45.38	3.87			0.375	+9.97	+2.34
11	1	+45.38	3.87			0.375	+12.69	+5.10
12	1	+45.38	3.87			0.375	+15.41	+7.86
13	5	+43.14	0.18			0.375	+18.13	+10.61
14	5	+32.43	0.18			0.375 : 0.396	+18.13	+10.61
15	5	+12.95	0.18			0.396 : 0.421	+18.26	+10.73
16	5	+2.25	0.18			0.421 : 0.396	+18.41	+10.83
17	1	+0.00	6.60			0.396 : 0.375	+18.59	+10.87
18	1	+270.00	1.36			0.375	+18.77	+10.88
19	1	+0.00	1.52			0.375	+25.37	+10.88
20	1	+90.00	0.68			0.375	+25.37	+9.52
21	3	+180.00	0.51			0.375	+26.89	+9.52
							+26.89	+10.20
							+26.38	+10.20

Figure 15b: Finite Segment Data

FIGURE 14: FINITE SEGMENT MODEL AND DATA FOR AZ13 SECTION (HARTMAN R.J. AND NEAL J.A., 1997)

Interlocks between sheet pile sections were modeled by a pin joint. However, transverse stresses in the interlocks are not considered due to a lack of bending moment transfer through an interlock.

Two support conditions are analyzed: support for sheet piling at a wale and support of sheet piling within a span between wales. A wale is a beam member that connects the sheet piling wall in the horizontal direction. The analysis considers a system of 10 interlocked sheet piles to simulate a wall system. Lateral restraint is provided at the edges of the sheet piling wall. Transverse stresses, axial stresses, and bending stresses were calculated based on a segment cross-section one inch wide and as thick as the actual sheet pile section at its location (Hartman R.J. and Neal J.A., 1997).

2. Failure Criterion

Evaluation of maximum shear stress at failure criterion with a safety factor for sheet piling is expressed as the following equation:

$$f_{BL} - f_{BT} = f_y / FS$$

where: f_{BL} is longitudinal principal stress,

f_{BT} is transverse principal stress,

f_y is yield stress of steel material,

FS used in this report is $1.0/0.65 = 1.54$

A safety factor was selected based on the typical allowable stress used in the industry during that time, which is 0.65 times the yield stress (Hartman R.J. and Neal J.A., 1997). An interaction graph for a sheet piling cross-section which relates applied pressure and available longitudinal bending moment can be established by applying the formula above. An example of interaction curves for AZ13 sections is demonstrated in **Figure 17**.

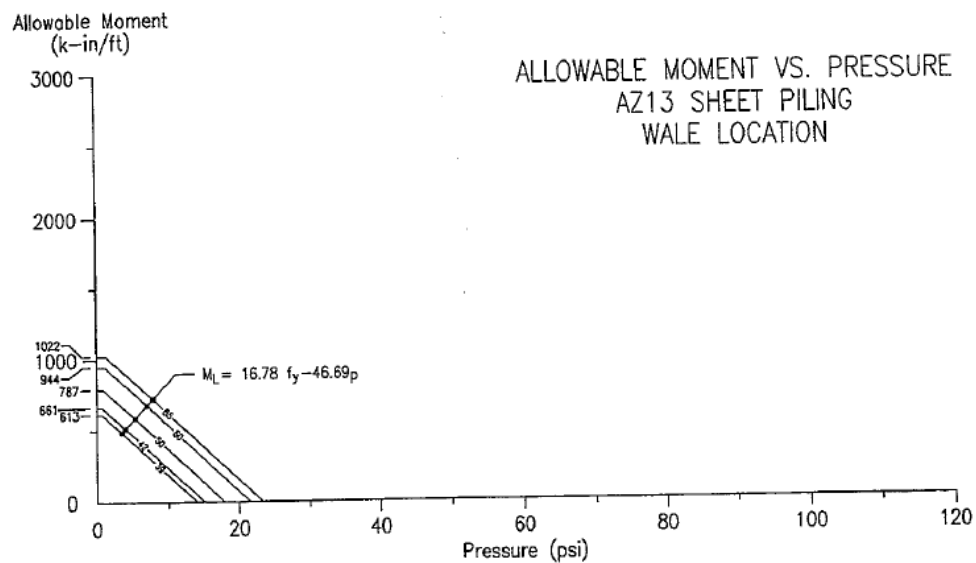


FIGURE 15: DESIGN INTERACTION CURVE FOR AZ13 SECTIONS (HARTMAN R.J. AND NEAL J.A., 1997)

Discussion

The study points that at zero pressure, the moment capacity of the cross-section is maximum, which can be computed by the yield stress times the section modulus. However, an increase in pressure reduces the capacity in applied pressure. The reduction in strength is plotted in the sloped lines, according to **Figure 15**. The line's slope on the graph is proportional to the maximum combined axial and bending transverse stresses (Hartman R.J. and Neal J.A., 1997). However, the moment capacity in the curves that tends to zero needed to be further investigated.

The flexure capacity is a function of the dimensions of the cross-section. Wider and deeper sections are more vulnerable to experience the transverse bending moment. Increasing bending strength can be achieved by increasing the thickness of flanges or an entire section using higher strength steel, fillets at high flexure strength locations, or reduced residual stresses from either cooling or cold forming. However, for this study, the most important factor that influences the moment capacity is the section properties of sheet piles (Hartman R.J. and Neal J.A., 1997).

Conclusions

Transverse stresses occur in sheet piling due to applied pressure and bracing condition from the adjacent sheet piles. They prevent the middle pile from spreading apart under flexure loading. The magnitude of transverse stresses is sufficient to affect the use of sheet piles, which reduces the capacity of the cross-section. It is essential for future design specifications and research to account for this existence.

An analysis method and the corresponding design tool is developed and published in this project. Engineers designing sheet piling structures should involve transverse loading into consideration. The tool derived in this project had been recommended until a better method was established. Hartman also suggested that research in this field should be continued. Effects of Residual stresses, local buckling, inelastic stress distribution, pile driving, and excavation and bracing consequences would be considered (Hartman R.J. and Neal J.A., 1997).

2.5 Flexural Behavior, Web Crippling, and Interaction of Transverse Stress and Bending Moment in Cold-formed Steel and Hot-rolled Steel Sheet piling (NBM Technologies, Inc., 2016)

Introduction

This research was a former project conducted by NBM in 2016. It provided structural comparisons of JZ -120/XZ-95 cold-formed sheet piling cross-sections and PZC 26/PZC 18 hot-rolled sheet piling cross-sections. These sections were selected for similar geometry and structural properties, but the difference in the manufacturing processes. Also, the study applied high computational simulations including nonlinear material properties, buckling instabilities, residual stresses, and variable wall thicknesses. These elements helped in evaluating flexural capacity, moment-rotation responses, web crippling and yielding, and transverse bending effects for the sheet piling sections outlined above (NBM Technologies, Inc., 2016). The cross-sectional views and properties are shown in **Figure 16** and **Table 2**.

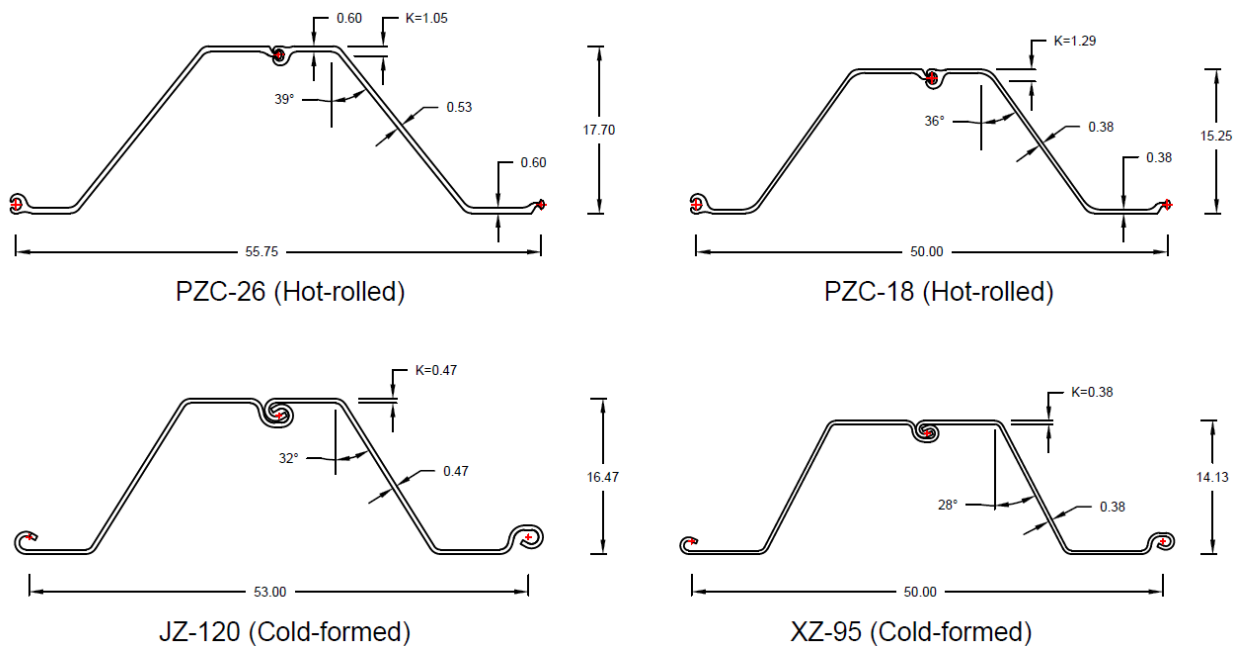


FIGURE 16: SECTIONAL DRAWING OF SHEET PILES (NBM TECHNOLOGIES, INC., 2016)

TABLE 2: SHEET PILE SECTIONAL PROPERTIES (NBM TECHNOLOGIES, INC., 2016)

Cross-sections	<i>H</i>	<i>W</i>	<i>I</i> /ft Calculated Moment of Inertia per unit width in ⁴ /ft	<i>S</i> /ft Calculated Section modulus per unit width in ³ /ft	<i>S</i> /ft Section modulus per unit width in design tables in ³ /ft	<i>Z</i> /ft Calculated Plastic modulus per unit width in ³ /ft
	Height	Width				
	in.	ft				
JZ-120 (Cold-formed)	16.47	4.417	395.2	48.0	48.5	58.1
XZ-95 (Cold-formed)	14.13	4.167	238.0	33.7	33.5	39.4
PZC-26 (Hot-rolled)	17.70	4.646	428.2	48.4	48.4	57.9
PZC-18 (Hot-rolled)	15.25	4.167	256.0	33.6	33.5	39.5

Flexural Response of Sheet Piling Cross-sections

Models are created using the commercial finite element program, ABAQUS. The effects of flexural boundary conditions, thickness variability in the hot-rolled sections, end rotation constraints, and numerical contacts and mesh in the interlocking regions are taken into account to induce the models' real flexure. Three-dimensional (3D) models and conditions are presented in **Figure 17**. The material properties used in the models are based on an elastic-perfect-plastic. The elastic modulus is assumed to be 29000 ksi with Poisson's ratio of 0.30, and the yield stress is 50 ksi (NBM Technologies, Inc., 2016).

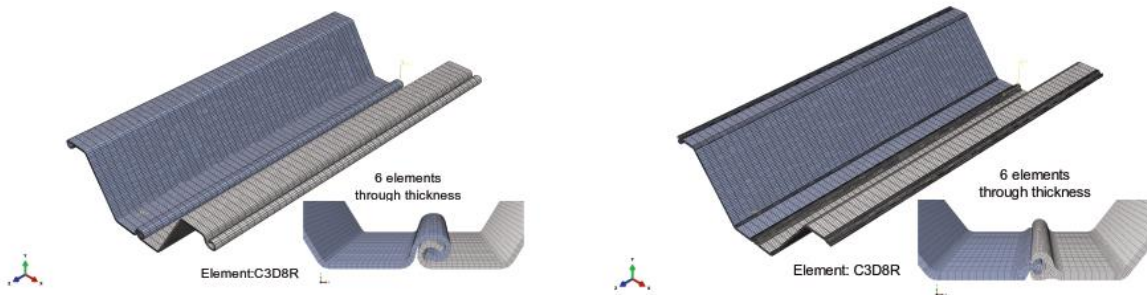


Figure 17a: Finite element model mesh for JZ-120 (left) and PZC-26 (right), other are similar

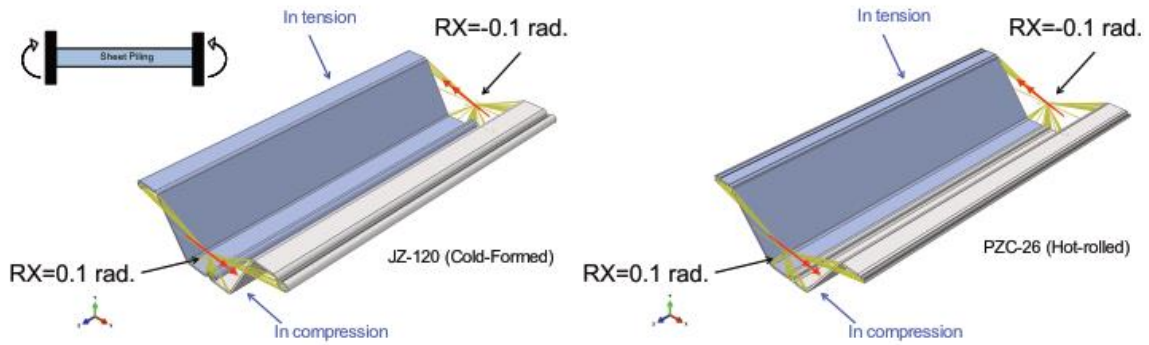


Figure 17b: End rotation constraints to induce flexure along the piling

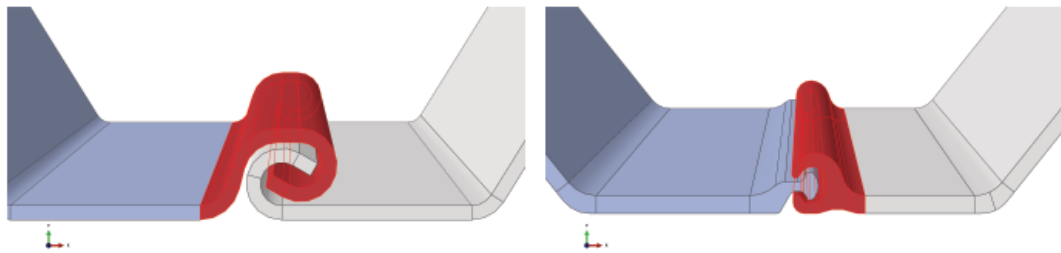


Figure 17c: Interlocking regions

FIGURE 17: FINITE ELEMENT MODELS OF SHEET PILING SPECIMENS (NBM TECHNOLOGIES, INC., 2016)

The results of the flexural simulation include stress distributions under a specific end rotation and moment-rotation responses. The von Mises stress distributions for the specimens under 0.02 radians are shown in **Figure 18**. The 0.02 radians correspond to the peak flexural strength of the piling cross-sections. The moment-rotation curves for both cold-formed and hot-rolled sheet pilings are presented in **Figure 19**. The responses show that both types of sheet piles maintain load-carrying abilities after their first yield, which allows them to reach their plastic moments. Besides, the difference in flexural capacity between comparable cold-formed and hot-rolled sheet piles is less than 5% (NBM Technologies, Inc., 2016).

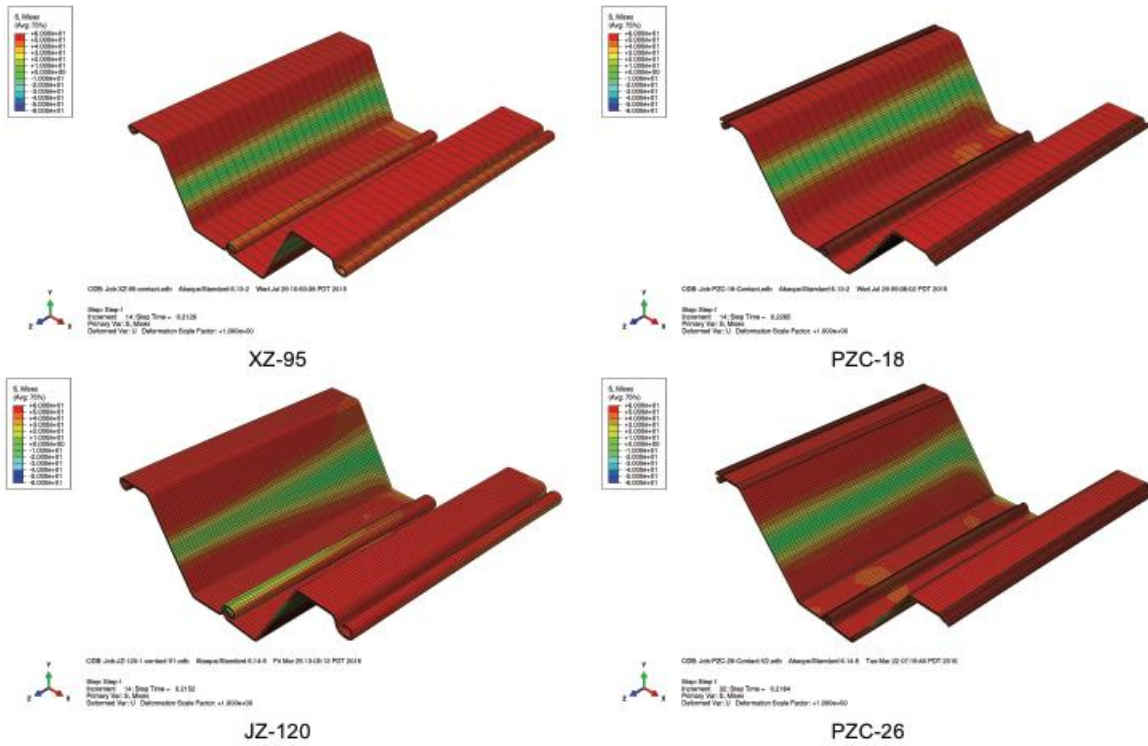


FIGURE 18: STRESS DISTRIBUTION AT 0.02 RADIAN OF BENDING (NBM TECHNOLOGIES, INC., 2016)

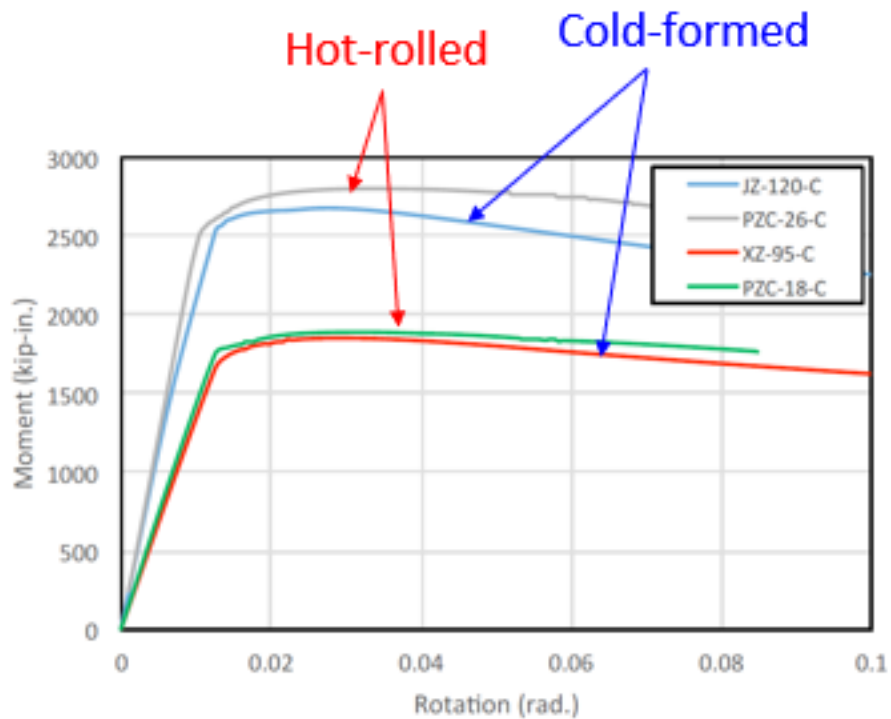


FIGURE 19: COMPARISON OF MOMENT-ROTATION RESPONSES (NBM TECHNOLOGIES, INC., 2016)

Web Crippling Capacity of Sheet Piling Cross-sections

Simulated capacities from this study are compared to available design predictions according to AISC 360-10 Chapter J, and the web crippling bearing load-displacement curves for different bearing lengths are presented in this section. The capacities calculated per AISC 360-10 with the bearing length of 16 inches are tabulated in **Table 3**. JZ120 and XZ95 are cold-formed, while PZC26 and PZC18 are hot-rolled. For the simulated study, the required span length of the member L_{max} to ensure the web crippling limit state for simple and fixed support conditions is shown in **Table 4**. A length of 100 inches is chosen for all pilings based on the data shown in **Table 4**. However, for the following future projects, a minimum span length of 16 ft will be used.

TABLE 3: WEB YIELDING AND CRIPPLING CAPACITIES PER AISC 360-10 (NBM TECHNOLOGIES, INC., 2016)

	Flange thickness		Web thickness	Outer face to end of fillet	Bearing length	Yielding	Crippling	
	F_{yw}	E	t_f	t_w	k	l_b	Middle	Middle
	ksi	ksi	in.	in.	in.	in.	R_n	R_n
JZ-120	50	29000	0.472	0.472	0.472	16	867	1680
XZ-95	50	29000	0.3875	0.3875	0.3875	16	695	1033
PZC-26	50	29000	0.6	0.525	1.04	16	1113	1828
PZC-18	50	29000	0.375	0.375	1.285	16	841	1061

TABLE 4: COMPUTED SPAN LENGTH TO ISOLATE WEB CRIPPLING LIMIT STATE (NBM TECHNOLOGIES, INC., 2016)

	Reduction Factors		R_n	M_p	Simple	Fix
	Angle	-			L_{max}	L_{max}
	deg.	-			in	in
JZ-120	32	0.85	735	12796	70	139
XZ-95	28	0.88	614	8217	54	107
PZC-26	39	0.78	865	13443	62	124
PZC-18	36	0.81	680	8229	48	97

The same models in the flexural study are used, except the boundary conditions and loading are modified, as demonstrated in **Figure 20**. A point load is applied by moving a frictionless rigid bearing surface, and the bearing width is varied. The mesh dimensions are decreased to ensure the accurate simulation of high local web curvature and plasticity during the failure (NBM Technologies, Inc.).

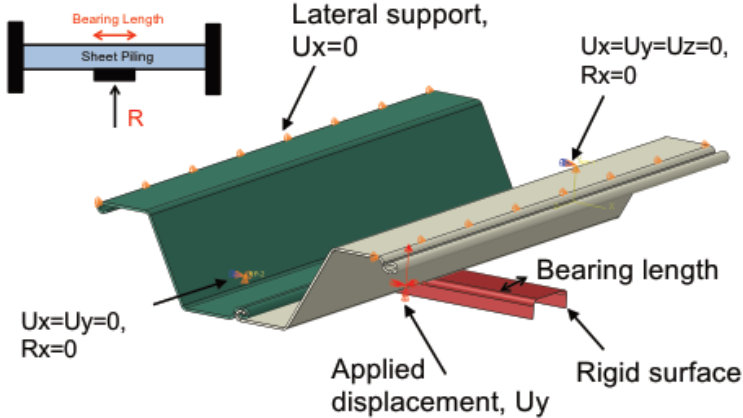


Figure 20a: Modified boundary conditions

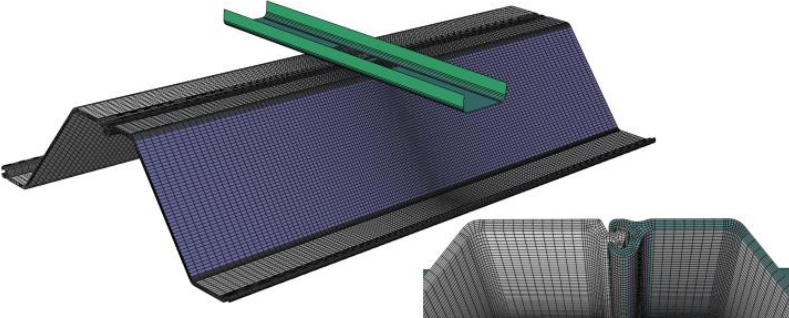


Figure 20b: Loading element and model meshing

FIGURE 20: MODEL FOR WEB CRIPPLING LIMIT STATE (NBM TECHNOLOGIES, INC., 2016)

The stress distribution results at 0.9 inches displacement of the rigid surface resulting in the collapse of all sheet pilings are presented in **Figure 21**. The webs adjacent to the bearing region yield spreads to the bottom flanges as local and longitudinal bending stresses. As far as the load-displacement response is concerned,

there is an increasing trend in capacity with bearing length. Most profiles have strength degradation after the peak load, according to **Figure 22** (NBM Technologies, Inc., 2016).

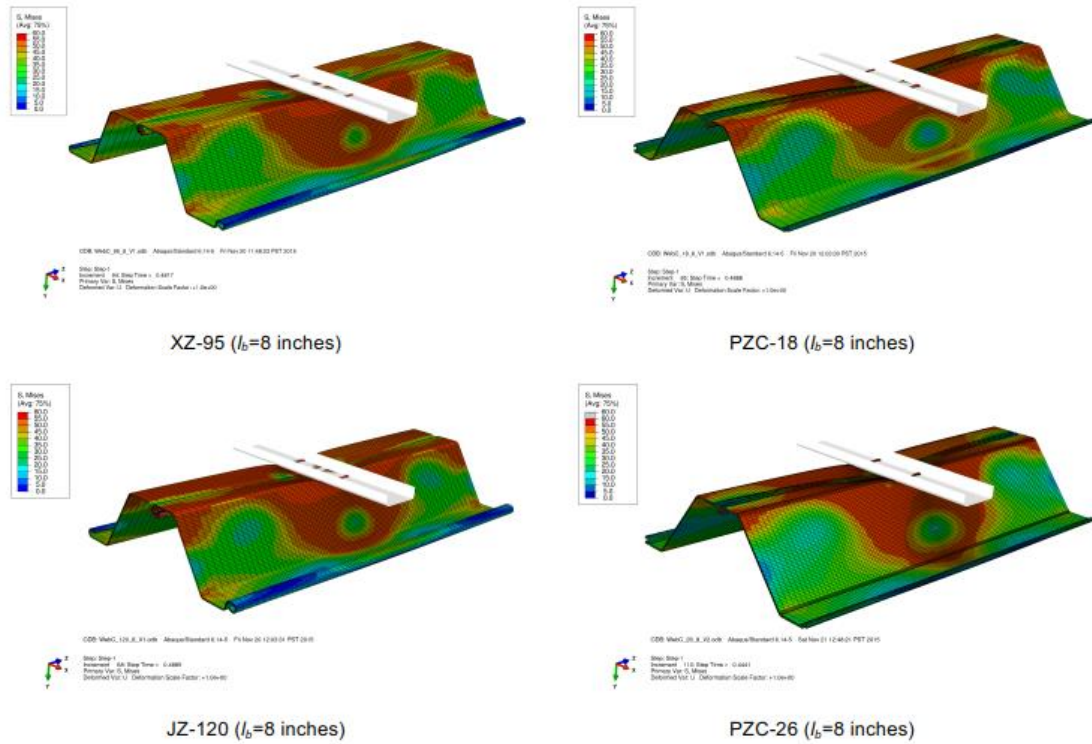


FIGURE 21: WEB CRIPPLING STRESS DISTRIBUTIONS NEAR PEAK LOAD (NBM TECHNOLOGIES, INC., 2016)

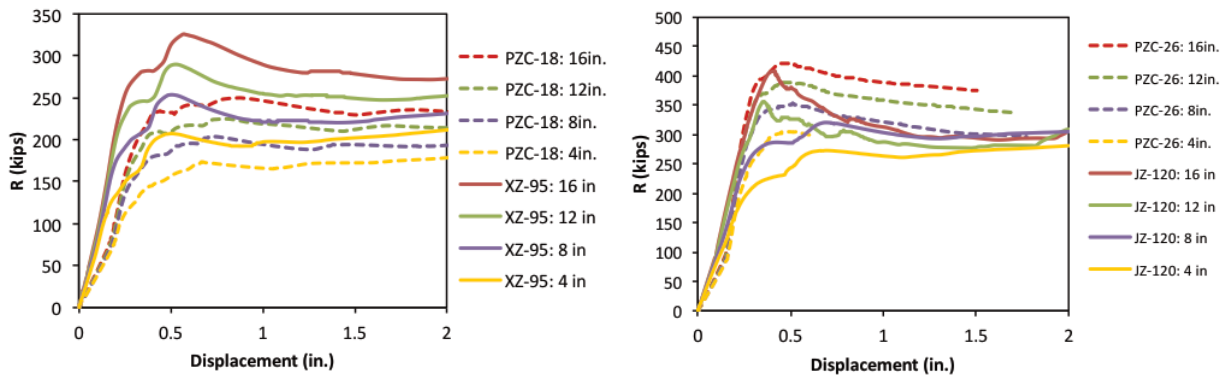


FIGURE 22: WEB CRIPPLING LOAD-DISPLACEMENT RESPONSES (NBM TECHNOLOGIES, INC., 2016)

Table 5 summarizes the comparison between the web-crippling capacities per AISC 360-10 and the simulation. A reduction factor calculated from the inclination of the webs is considered. **Table 5** shows that the design capacities per AISC estimate the web crippling and yielding well for short bearing lengths below four inches. However, the capacities are up to 1.5 times higher than the numbers achieved from the study.

Additionally, there are minimal differences in bearing strength between hot-rolled and cold-formed sheet piling profiles (NBM Technologies, Inc., 2016).

TABLE 5: COMPARISON OF THE CAPACITY PER AISC 360-10 AND FROM THE STUDY (NBM TECHNOLOGIES, INC., 2016)

Cross-sections	F_{yw} ksi	k in.	I_b in.	d in.	n_w -	R_n kips	Abaqus kips	Analysis-to-Predicted ratio
JZ-120	50	0.472	4	16.47	2	255	270	1.06
XZ-95	50	0.3875	4	18.67	2	203	200	0.98
PZC-26	50	0.6	4	17.7	2	286	297	1.04
PZC-18	50	0.375	4	16.47	2	178	166	0.93
JZ-120	50	0.472	8	16.47	2	415	320	0.77
XZ-95	50	0.3875	8	18.67	2	340	250	0.74
PZC-26	50	0.6	8	17.7	2	449	347	0.77
PZC-18	50	0.375	8	16.47	2	300	200	0.67
JZ-120	50	0.472	12	16.47	2	575	356	0.62
XZ-95	50	0.3875	12	18.67	2	477	284	0.60
PZC-26	50	0.6	12	17.7	2	612	387	0.63
PZC-18	50	0.375	12	16.47	2	421	228	0.54
JZ-120	50	0.472	16	16.47	2	735	408	0.56
XZ-95	50	0.3875	16	18.67	2	614	325	0.53
PZC-26	50	0.6	16	17.7	2	775	421	0.54
PZC-18	50	0.375	16	16.47	2	542	257	0.47

Interaction of Transverse Stresses and Bending Moment in Sheet Piling

In the reality, when sheet piles are used as a wall system to retain soil or water, there is pressure applying perpendicular to the piling profile. A combination of transverse and flexural stresses can decrease the capacity of the sheet pile. In this study, 3D nonlinear and finite element analyses are used to create interaction curves for the same cold-formed and hot-rolled cross-sections as introduced at the beginning of this research.

Effect of transverse stresses on sheet piling and full-scale testing of sheet piles under hydrostatic loading was very first reported by Hartman R.J. and Neal J.A. (1992 and 1997). In their study, there were five pairs of the piling cross-sections with lateral restraints at both the top and bottom of the webs. The profiles tested by Hartman R.J. and Neal J.A. were different from those in this study in 2016, but each sheet piling pair in

1997 also had the same structural characteristics for the same objective. The bending moment data from the test was used to determine the transverse stress using the following equation:

$$|f_L| + |f_T| = f_y/FS$$

where $|f_L|$ and $|f_T|$ are the absolute values of longitudinal and transverse stresses

f_y is the yield stress

FS is the factor of safety, assigned to be 1/0.65

Hartman R.J. and Neal J.A. stated that the selection of the factor of safety is based on the allowable stress of 0.65, which is typically used for steel sheet piling during that time (Hartman R.J. and Neal J.A., 1997). Then, by substituting with My/I , interaction curves for longitudinal bending capacity and pressure can be obtained as **Figure 23**.

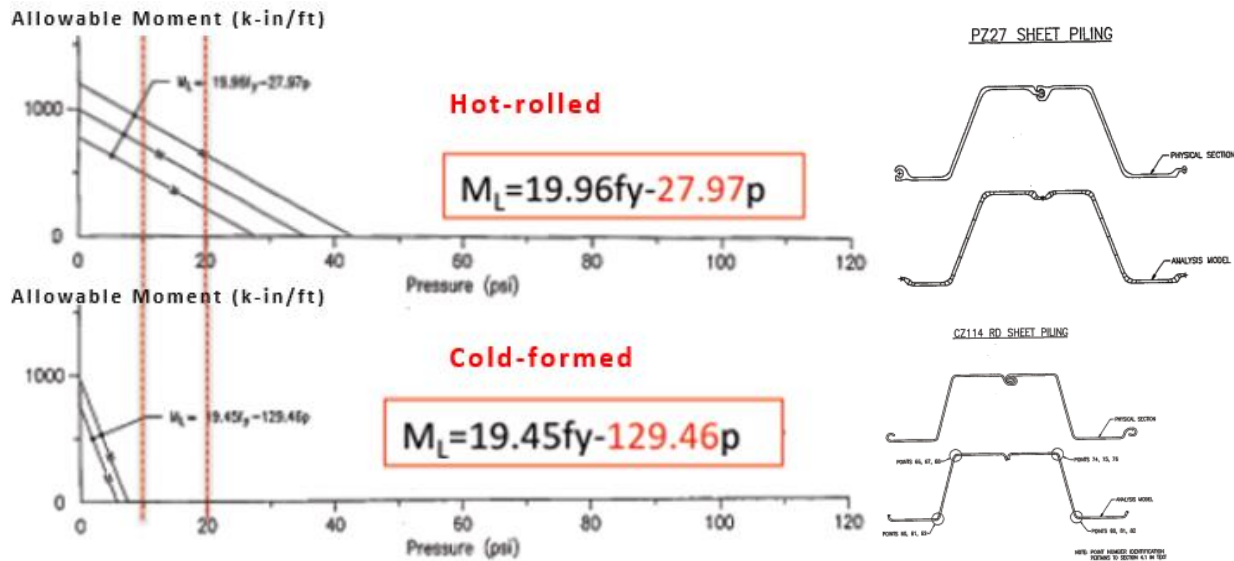


FIGURE 23: INTERACTION CURVES FOR HOT-ROLLED PZ27 AND COLD-FORMED CZ114RD PROFILES

(HARTMAN R.J. AND NEAL J.A., 1997)

In the study by NBM (2016), the two-dimensional (2D)-frame plastic hinge model is used to predict the results. Then, the same finite element models used in the previous sections are applied hydrostatic pressure perpendicular to the profiles. Lengths of the specimens are varied from 100 to 400 inches with 50 inches increase for each test. **Figure 24** demonstrates the von Mises stress distribution of one of the cross-sections at different piling lengths under pressure. The results show that when the length is short transverse stresses cause plastic hinges along with the folded corners, but this effect is minimal when the length is increased (NBM Technologies, Inc., 2016).

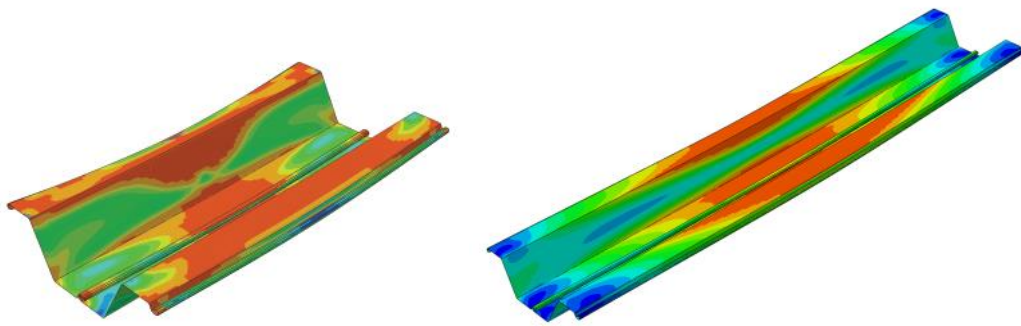


FIGURE 24: EXAMPLE OF VON MISES STRESS FROM HYDROSTATIC PRESSURE NEAR PEAK LOAD FOR DIFFERENT SPAN LENGTHS (NBM TECHNOLOGIES, INC., 2016)

The longitudinal moment relationship with the applied hydrostatic pressure for PZC-18 can be plotted in **Figure 25**. The interaction line is the backbone of all results, where the plastic moment and the yield moment are computed from the cross-sectional properties. All the profiles witness a degradation of the longitudinal moment capacity versus the pressure. The curves show that the effect of transverse stress can be neglected for low pressure (i.e., less than 20 psi). This effect, however, needs to be considered under higher pressures. The results also insist that the curve trends are consistent with Hartman's approach for the interaction diagram. Nevertheless, the 2D longitudinal and transverse stresses in design limits are very conservative compared to the full 3D plastic capacity. The interaction surface is not as sensitive to thickness variations of cold-formed and hot-rolled profiles as predicted by the 2D method (NBM Technologies, Inc., 2016).

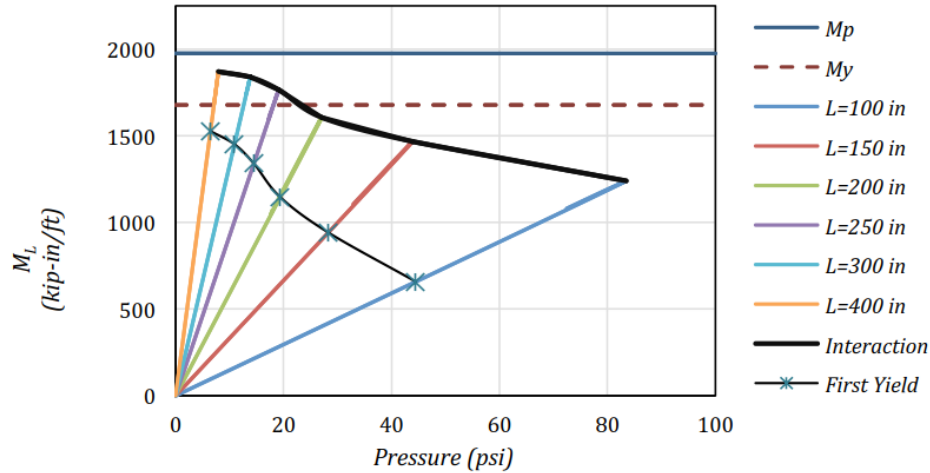


FIGURE 25: PRESSURE-MOMENT INTERACTION CURVE FOR PZC-18 (NBM TECHNOLOGIES, INC., 2016)

Effect of Residual Stresses on the Flexural Capacity of Cold-formed Sheet Piling

Residual stresses are formed during the cold roll-forming process resulting in initial stress states before loading starts. In this study, the stresses are calculated by dividing the sheet piling profiles into flat and corner parts. Then, initial residual stresses are applied depending on each part. The computed results, including longitudinal and transverse stresses, and effective plastic strains, for cold-formed XZ-95 and JZ-120 are presented in **Figure 26** and **Figure 27**.

The models of the cold-formed profiles are applied a hydrostatic pressure similar to the previous analyses, but residual stresses and strains are also included. These effects on the sheet piles' capacity are quantified using the interaction curves shown in **Figure 28**. The results demonstrate the maximum difference of 5% in value; the capacity of XZ-95 increases, but the capacity of JZ-120 decrease. As a result, the impact of residual stresses depends on the cross-sectional properties, but this effect is still small and negligible (NBM Technologies, Inc., 2016).

There are also residual stresses from the hot-rolling process. The sheet piling thickness is relatively thinner and more consistent than the typical W-shape, in which the connections between the web and flanges cause a different cooling rate from the outer and interior part. It is then assumed that the residual stresses have minimal effect on the flexural behavior.

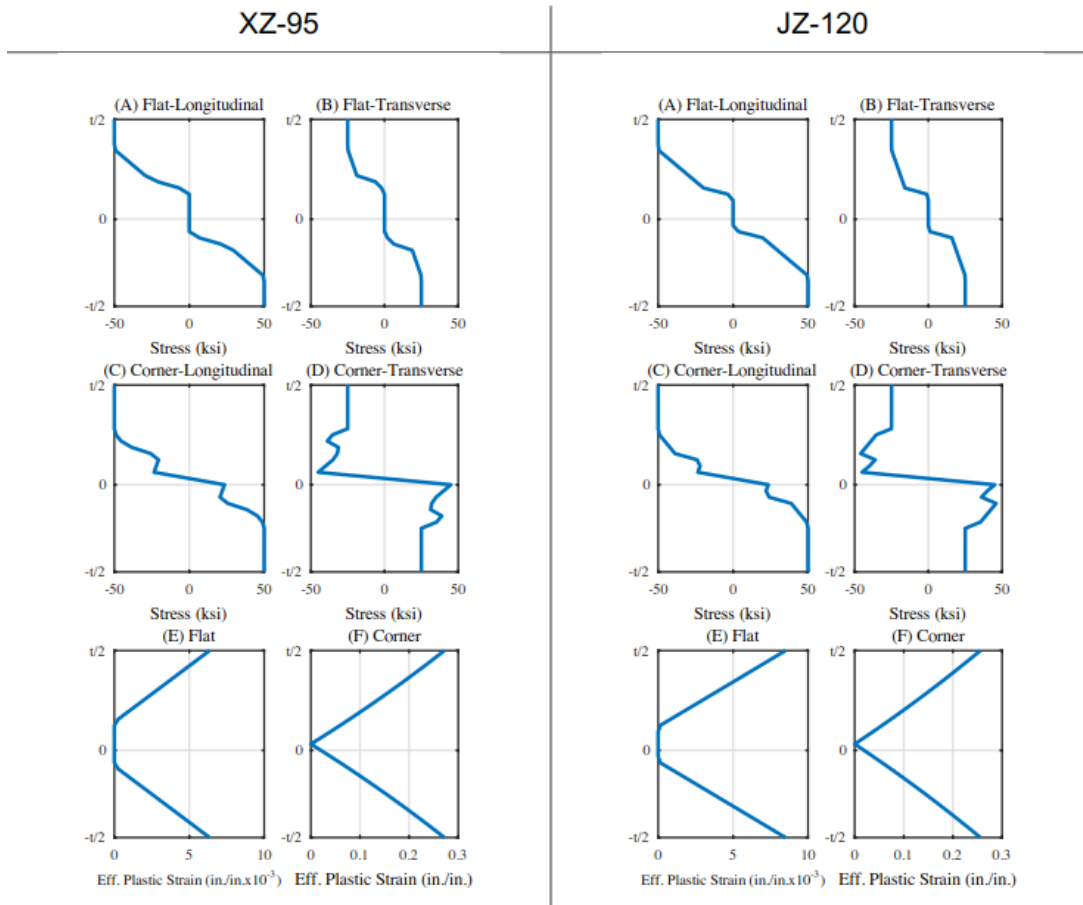


FIGURE 26: RESIDUAL STRESSES AND EFFECTIVE PLASTIC STRAINS FOR COLD-FORMED SHEET PILING PROFILES (NBM TECHNOLOGIES, INC., 2016)

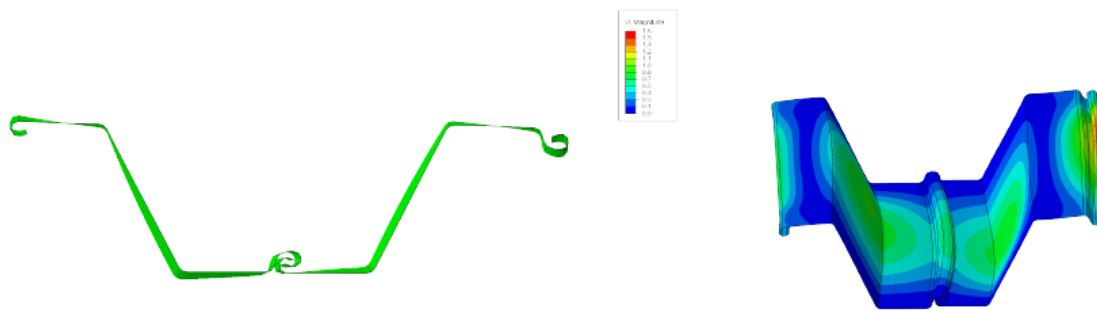


FIGURE 27: DEFORMED SHAPE DUE TO RESIDUAL STRESSES FOR XZ-95 PROFILE (NBM TECHNOLOGIES, INC., 2016)

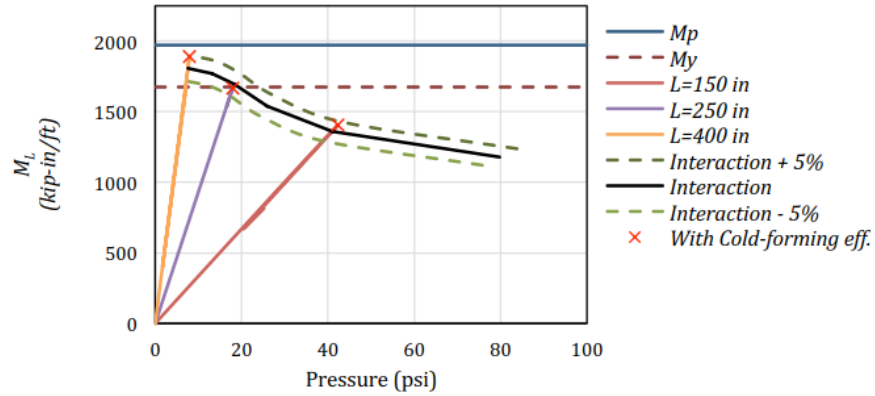


Figure 28a: Interaction curve for XZ-95

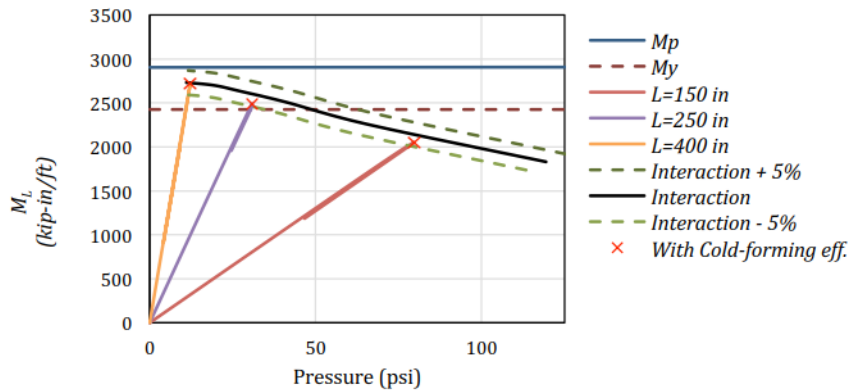


Figure 28b: Interaction curve for JZ-120

FIGURE 28: EFFECT OF RESIDUAL STRESSES ON COLD-FORMED XZ-95 AND JZ-120 (NBM TECHNOLOGIES, INC., 2016)

Conclusions

Three-dimensional finite element simulations were conducted to investigate the flexural and web crippling load-deformation responses of cold-formed and hot-rolled sheet pilings. There are four sheet piling cross-sections studied: JZ-120 and XZ-95 cold-formed cross-sections, and PZC-26 and PZC-18 hot-rolled cross-sections. The results indicate that both types of sheet piles with similar section properties have similar flexural and web crippling characteristics (NBM Technologies, Inc., 2016).

Some important points taken for developing the following research for the same sheet piling cross-sections are the equivalent strength of the similar hot-rolled and cold-formed cross-sections, the minimum clear span length to isolate the web crippling failure mode, and the interaction of transverse and bending stresses showing lower flexure strength of the sheet piles compared to the sheet piles with only flexural loading.

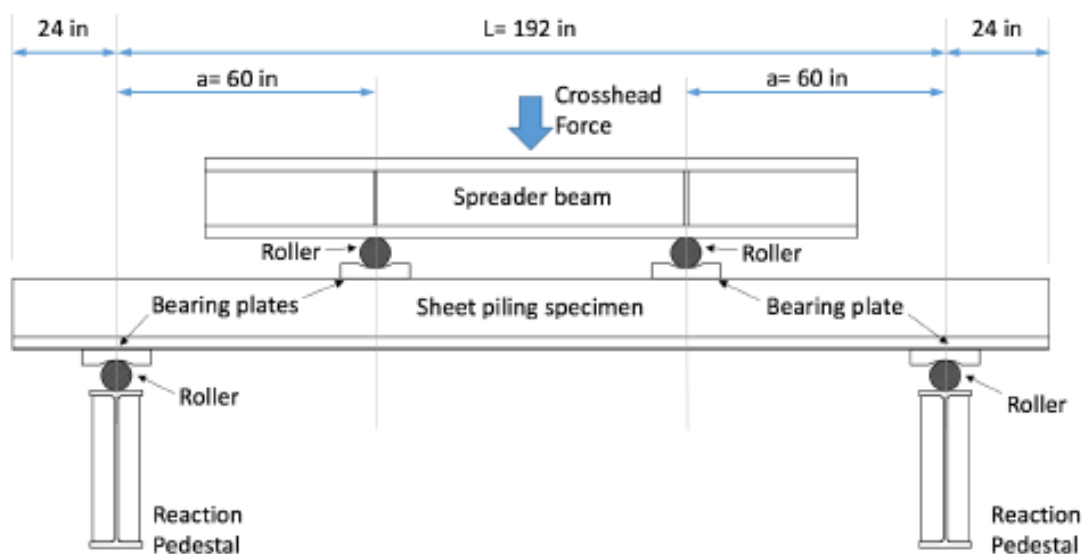
2.6 Experiments on Flexural Behavior of Cold-formed and Hot-rolled Steel Sheet Piling

Phase I: Four-point Bending Tests (NBM Technologies, Inc., 2017)

Introduction

This sheet-piling project was exactly before the Phase II project reported in this document. It was conducted by NBM and Lehigh University to evaluate four sheet-piling cross-sections demonstrated in **Figure 16**. Two of them were produced by the hot-rolled approach, while the others were from the cold-formed mill. Hot-rolled sections are produced from reheated steel drawn over a series of forming rolls to final shape. Cold-formed sections are produced from finished hot-rolled steel coil that is shaped on a cold-forming mill (NBM Technologies, Inc., 2016).

The project was designed to make a direct comparison between the flexural behavior of the cross-sections produced from the two approaches with the same modulus (NBM Technologies, Inc., 2017). Each of the hot-rolled cross-sections has its pair cold-formed profile from with the same modulus, as shown in **Table 2**. The experiment reported the failure mechanism, ultimate flexural capacity, moment rotation behavior, and longitudinal and transverse strain distributions (NBM Technologies, Inc., 2017). The four-point bending method was used to investigate the flexural behaviors (See **Figure 29**).



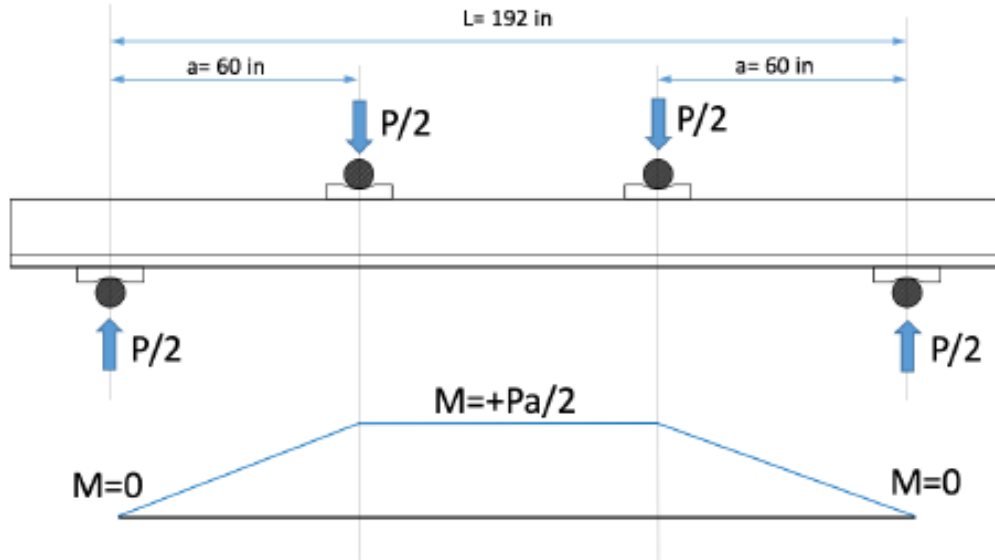


FIGURE 29: FOUR-POINT BENDING TEST SETUP (NBM TECHNOLOGIES, INC., 2017)

There are four sheet piling cross-sections studied: JZ-120 and XZ-95 cold-formed cross-sections, and PZC-26 and PZC-18 hot-rolled cross-sections. Three specimens of each cross-section (a total of 12 specimens) were tested (See **Table 6**). The span length from the centerline of the two supports is 16 ft, and the total length of each specimen is 20 ft. The maximum crosshead force was calculated based on the nominal plastic moment to be 500 kips, and this was used to design the test setup components (NBM Technologies, Inc., 2017).

TABLE 6: TEST MATRIX (NBM TECHNOLOGIES, INC., 2017)

Type	Cross-sections	Nominal Fy (ksi)	Mp (k-in/ft)	Width (ft)	a (in)	L* (in)	P Crosshead (kip)	R=P/2 Reaction	No. of Specimens
Cold-formed	JZ120	50	2907	4.417	60	192	428	214	3
	XZ95	50	1972	4.167	60	192	274	137	3
Hot-rolled	PZC26	50	2894	4.646	60	192	448	224	3
	PZC18	50	1975	4.167	60	192	274	137	3

Specimen Design

The reaction demands each cross-section are calculated based on the four-point bending test configuration shown in **Table 7**. The simulation by NBM in 2016 provided the nominal web crippling capacity. The estimated strength was multiplied by a strength reduction factor of 0.75 per AISC 360-10 using 60 ksi yield strength (NBM Technologies, Inc., 2017). The table suggests that the reaction demands are less than the web crippling capacity.

TABLE 7: SPECIMEN WEB CRIPPLING CAPACITY (NBM TECHNOLOGIES, INC., 2017)

Type	Cross-sections	Nominal Fy (ksi)	Mp (k-in/ft)	Width (ft)	a (in)	L* (in)	R=P/2 Reaction	Estimated Web-crippling capacity for braing length=16" (kip)
Cold-formed	JZ120	50	2907	4.417	60	192	214 <	306
	XZ95	50	1972	4.167	60	192	137 <	244
Hot-rolled	PZC26	50	2894	4.646	60	192	224 <	316
	PZC18	50	1975	4.167	60	192	137 <	193

Table 8 shows the shear capacity of the specimens calculated per AISC 360-10 compared to the shear demand at the plastic moments, which is adequate.

TABLE 8: SPECIMEN SHEAR CAPACITY (NBM TECHNOLOGIES, INC., 2017)

Type	Cross-sections	Nominal Fy (ksi)	Web Height, H (in)	Web Thinkness, t_w (in)	Web angle (deg)	R=P/2 Reaction	Estimated Shear Strength per AISC
Cold-formed	JZ120	50	16.47	0.47	32	214 <	295
	XZ95	50	14.13	0.38	28	137 <	213
Hot-rolled	PZC26	50	17.7	0.53	39	224 <	328
	PZC18	50	15.25	0.38	36	137 <	211

The specimens were bolted with four 1-inch diameter bolts to an end bearing plate at each support to prevent end rolling and the lateral spreading of the specimens, as shown in **Table 9**. However, the bolts were resized to 1-1/4" due to overstrength from the specified yield strength (NBM Technologies, Inc., 2017).

TABLE 9: SPECIMEN CONNECTING BOLT DESIGN (NBM TECHNOLOGIES, INC., 2017)

Type	Cross-sections	R=P/2 Reaction	Web angle (deg)	No. of Bolts	Bolt Diameter (in)	Bolt Type	F _{uv} (ksi)	Horiz. Demand (kip)	Shear Strength (kip)
Cold-formed	JZ120	214	32	2	1.0	A490	84	67 <	99
	XZ95	137	28	2	1.0	A490	84	36 <	99
Hot-rolled	PZC26	224	39	2	1.0	A490	84	91 <	99
	PZC18	137	36	2	1.0	A490	84	50 <	99

Test Setup Design

The overall view of the test setup is demonstrated in **Figure 30**. A spreader beam was used to transfer the crosshead force to the loading rollers at the third location to create the four-point bending condition. The lateral support geometry was designed to provide lateral bracing to the specimens while they were able to displace down. It consists of 3 parts: base plate, vertical posts, and slider, as shown in **Figure 31**. Teflon sheets were attached between the moving parts to reduce friction. Four of the lateral supports were used at two sides of the third location.

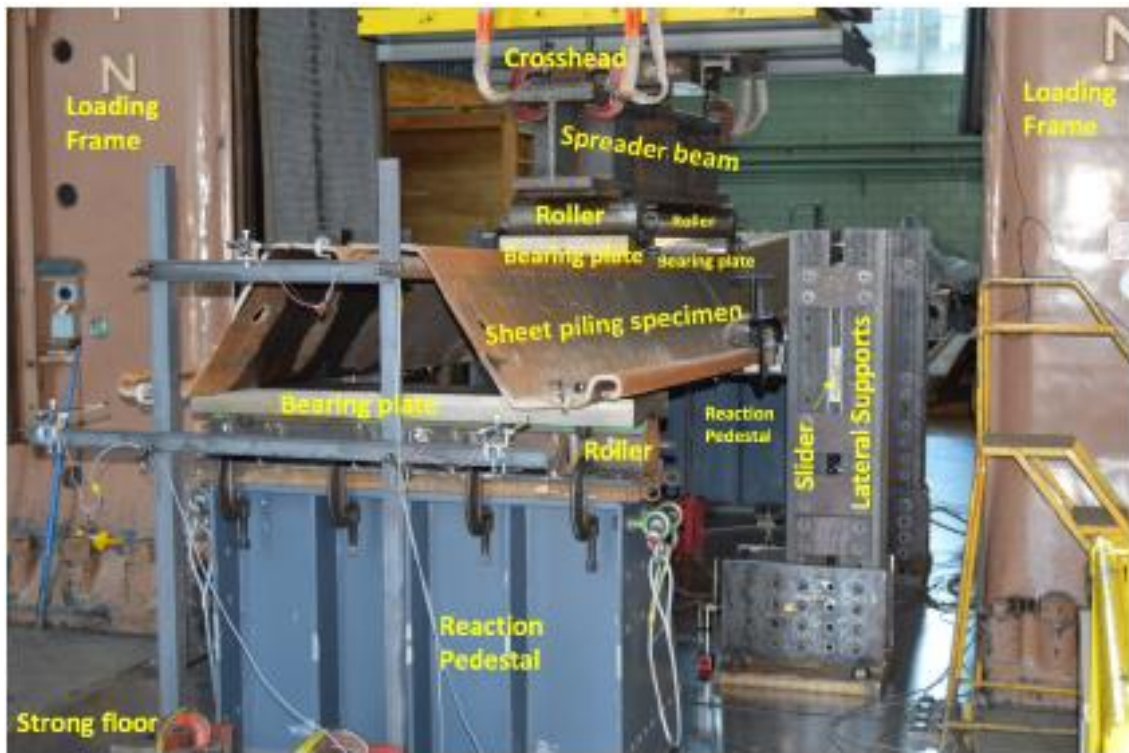


FIGURE 30: TEST SETUP FOR PHASE I PROJECT (NBM TECHNOLOGIES, INC., 2017)

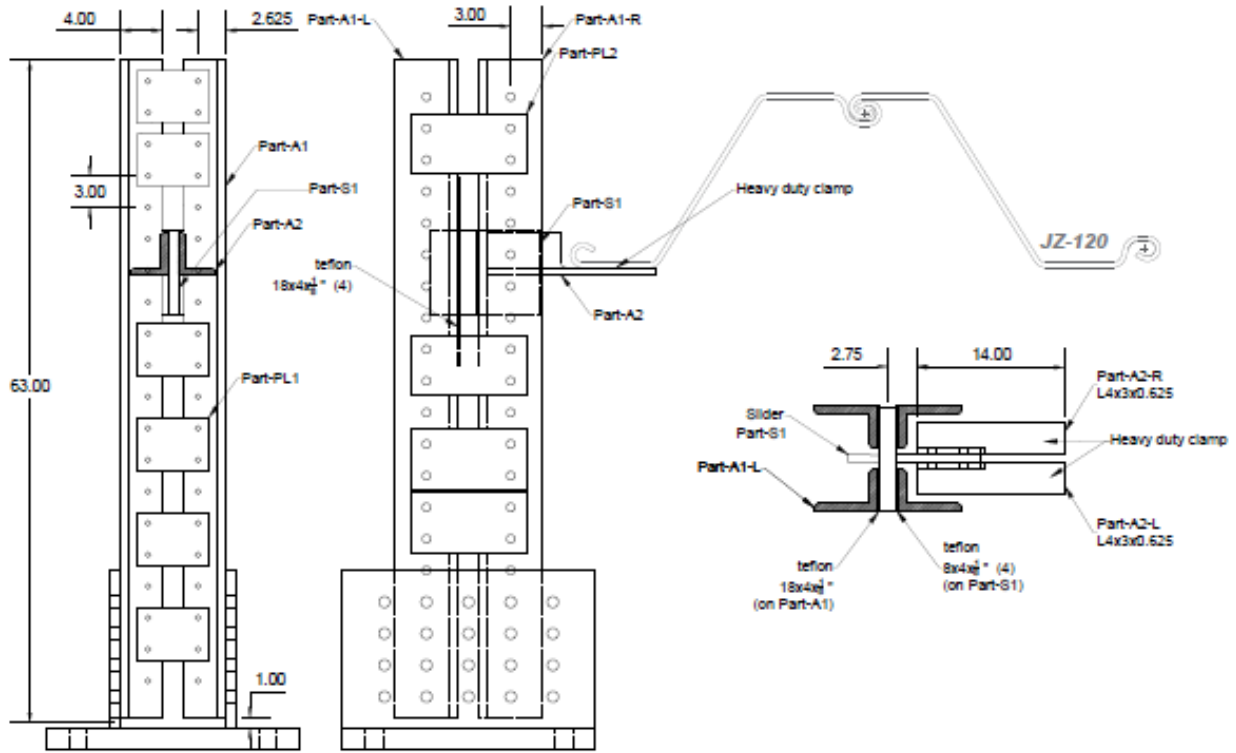


FIGURE 31: LATERAL SUPPORT ASSEMBLY (NBM TECHNOLOGIES, INC., 2017)

Instrumentation Plan

According to the report from NBM, 19 string potentiometers were installed to measure vertical and transverse displacements at the midspan, the loading points, and the end displacements in the longitudinal direction, according to **Figure 32**. Sixteen strain gauges were installed at the midspan at both sides of the specimens to measure local strains in both longitudinal and transverse directions as shown in **Figure 33**.

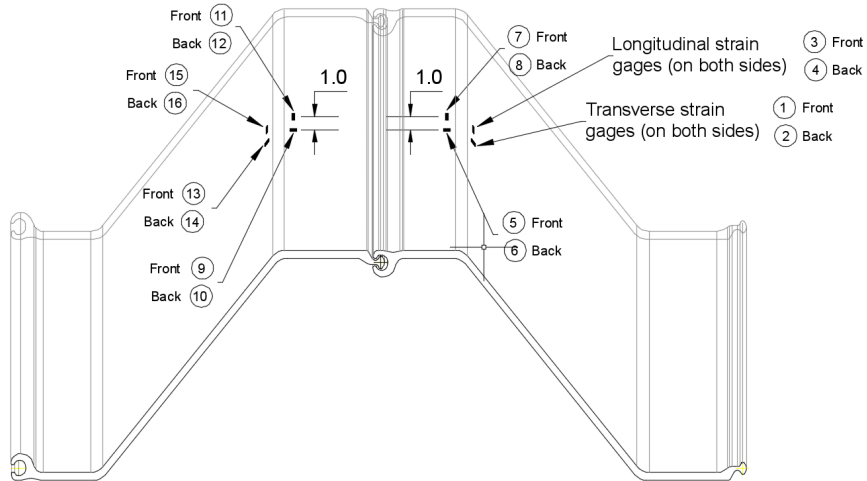
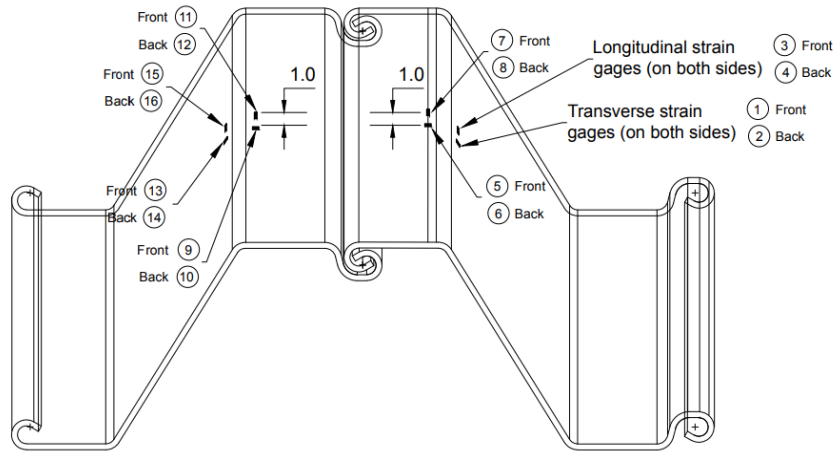


FIGURE 33: STRAIN GAGE LOCATION (NBM, 2017)

Experimental Results

1. Material Testing

Tensile coupon tests were conducted to obtain actual yield strength, ultimate strength, and elongation of each specimen. The average of the results from 3 tensile coupons of each cross-section is calculated in **Table 10**.

TABLE 10: TENSILE COUPON RESULT (NBM TECHNOLOGIES, INC., 2017)

Type	Cross-sections	0.2% Offset Yield Strength (ksi)	Ultimate Tensile Strength (ksi)	Elongation in 2 inch (%)
Cold-formed	JZ120	62.0	75.3	35.3
	XZ95	59.8	74.5	38.0
Hot-rolled	PZC26	52.5	65.7	42.3
	PZC18	51.3	64.3	44.7

2. Load-deformation Response

Figure 34 shows the load-deformation response at mid-span for each test. This figure indicates that results for each type of sheet piling cross-sections are consistent. In some curves, sudden drops resulted from the failure of a bolt at the end bearing plates from the first few tests, but this problem was solved by the pre-tension of the bolted connection for the later tests. Transverse deformation occurred at the specimens' interlock due to flange local buckling, but there was no interlock separation (NBM Technologies, Inc., 2017).

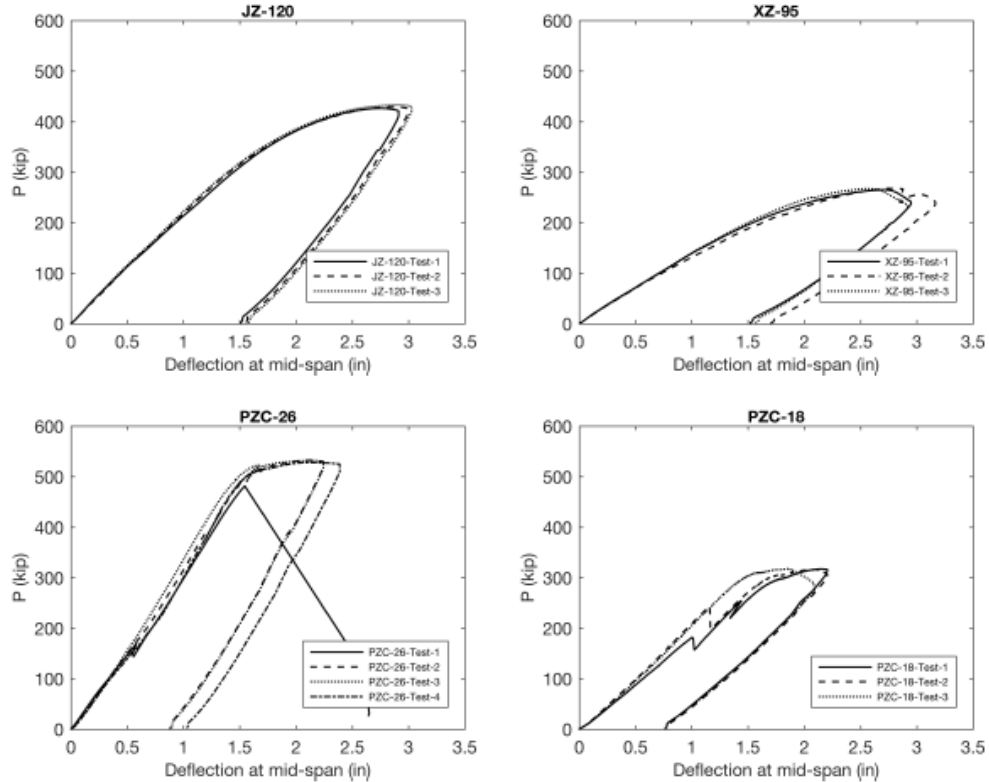


FIGURE 34: LOAD-DEFORMATION RESPONSE (NBM, 2017)

3. Moment-deformation and Moment-rotation Response

Moment-deflection responses are plotted in **Figure 35**. All cross-sections achieve the yield moment, whereas the cord-formed JZ-120 and the hot-rolled PZC-26 cross-sections reach their plastic moment (NBM Technologies, Inc., 2017).

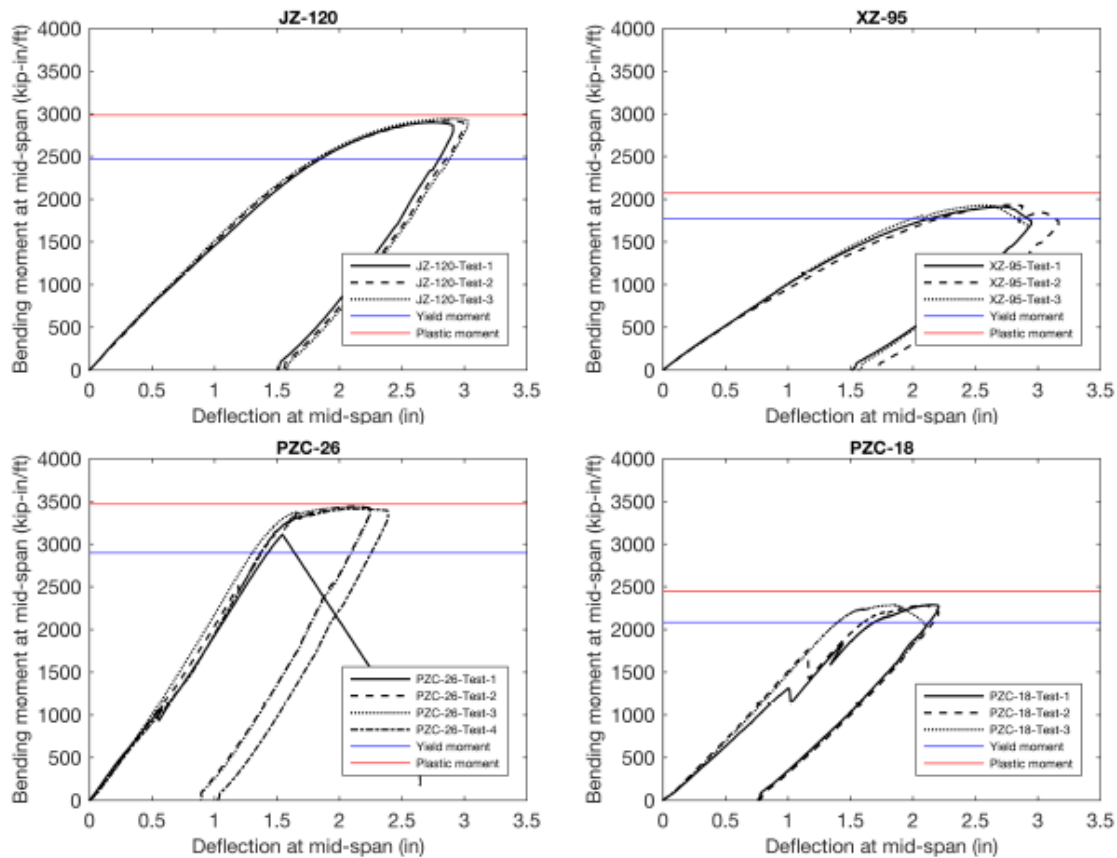


FIGURE 35: MOMENT VS DEFLECTION AT MIDSPAN (NBM TECHNOLOGIES, INC., 2017)

Moment-rotation responses are shown in **Figure 36**. The curves represent less local deformation effects and demonstrate general flexural behavior more clearly (NBM Technologies, Inc., 2017). Bending moments at midspan is normalized with each specimen's corresponding yield strength to make the comparison more meaningful (NBM Technologies, Inc., 2017). End rotations are calculated as the average of both ends of the specimens.

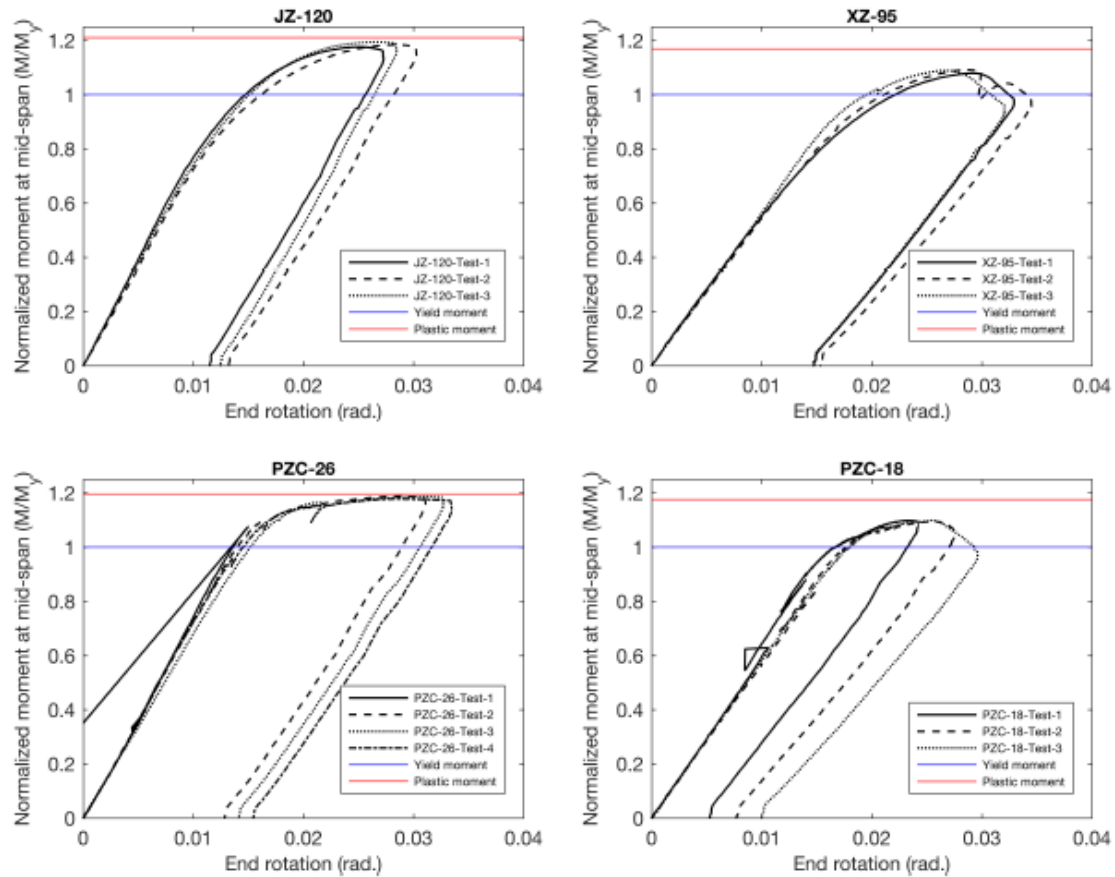


FIGURE 36: MOMENT AT MIDSPAN VS END ROTATION RESPONSE (NBM TECHNOLOGIES, INC., 2017)

Comparison of Cold-formed and Hot-rolled Sheet Piling

1. General Behavior and Flexural Performance

Figure 37 and Figure 38 show a direct comparison between the cold-formed and hot-rolled cross-sections. The plots are created to compare the cross-sections with the same modulus; however, the moments of inertia are different. Therefore, the deflections at midspan need to be scaled to the moment of inertia of the cross-sections to make the comparison more reasonable (NBM Technologies, Inc., 2017). The comparison of normalized moments and scaled end rotations in Figure 38 shows that all equivalent sheet-piling cross-sections match well because end rotation is free from cross-section distortion (NBM Technologies, Inc., 2017).

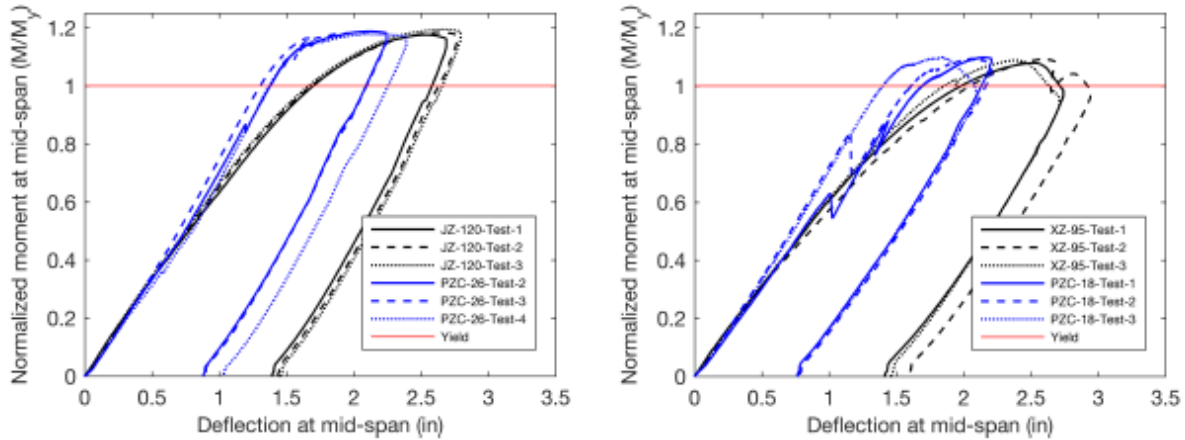


FIGURE 37: COMPARISON OF NORMALIZED MOMENT VS SCALED DEFLECTION AT MIDSPAN IN COLD-FORMED AND HOT-ROLLED CROSS-SECTIONS (NBM, 2017)

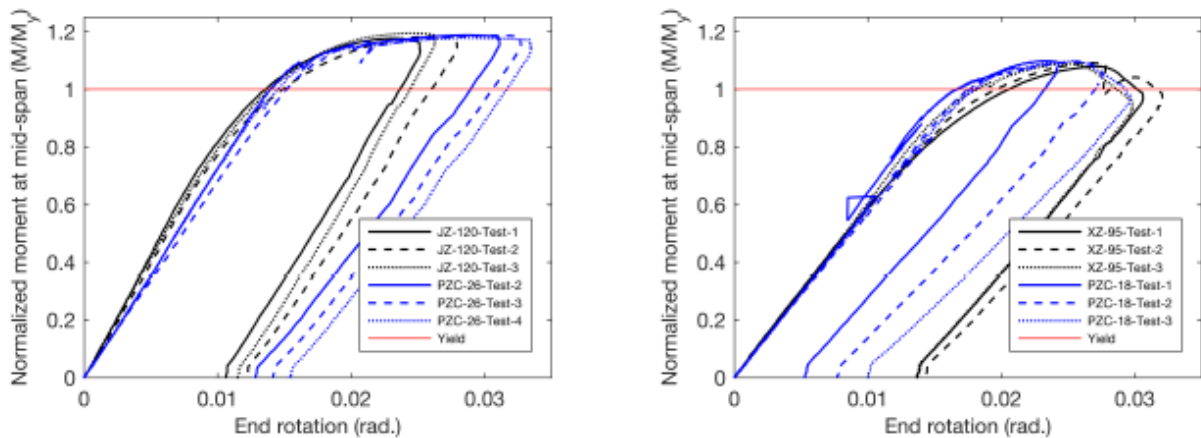


FIGURE 38: COMPARISON OF NORMALIZED MOMENT VS SCALED END ROTATION AT MIDSPAN IN COLD-FORMED AND HOT-ROLLED CROSS-SECTIONS (NBM, 2017)

2. Local Longitudinal and Transverse Strains

To investigate the relationship between local longitudinal and transverse strains, two groups of strain gauges were attached to the specimens. Recorded strains are normalized by the yield strains obtained from the tensile coupon tests. **Figure 39** demonstrates the relationship between the yield bending moments and the maximum longitudinal strain on the top flange. The results showed that the longitudinal strain demand is less than the material elongation limit shown in **Table 10**.

According to **Figure 40**, both types of sheet piling cross-sections experienced high strains about two times the yield strains at the midspan. The opposite signs of the front and back strain gages

indicate transverse bending stress on the specimens (NBM Technologies, Inc., 2017). The study by NBM (2016) showed that transverse stresses and plastic strains start to affect flexural capacity only when transverse demand is high enough to make the steel fully plastic through its thickness. Therefore, localized transverse stresses with magnitudes near the yield strength that occur from the tests do not affect flexural capacity in the combined stress state (NBM Technologies, Inc., 2017).

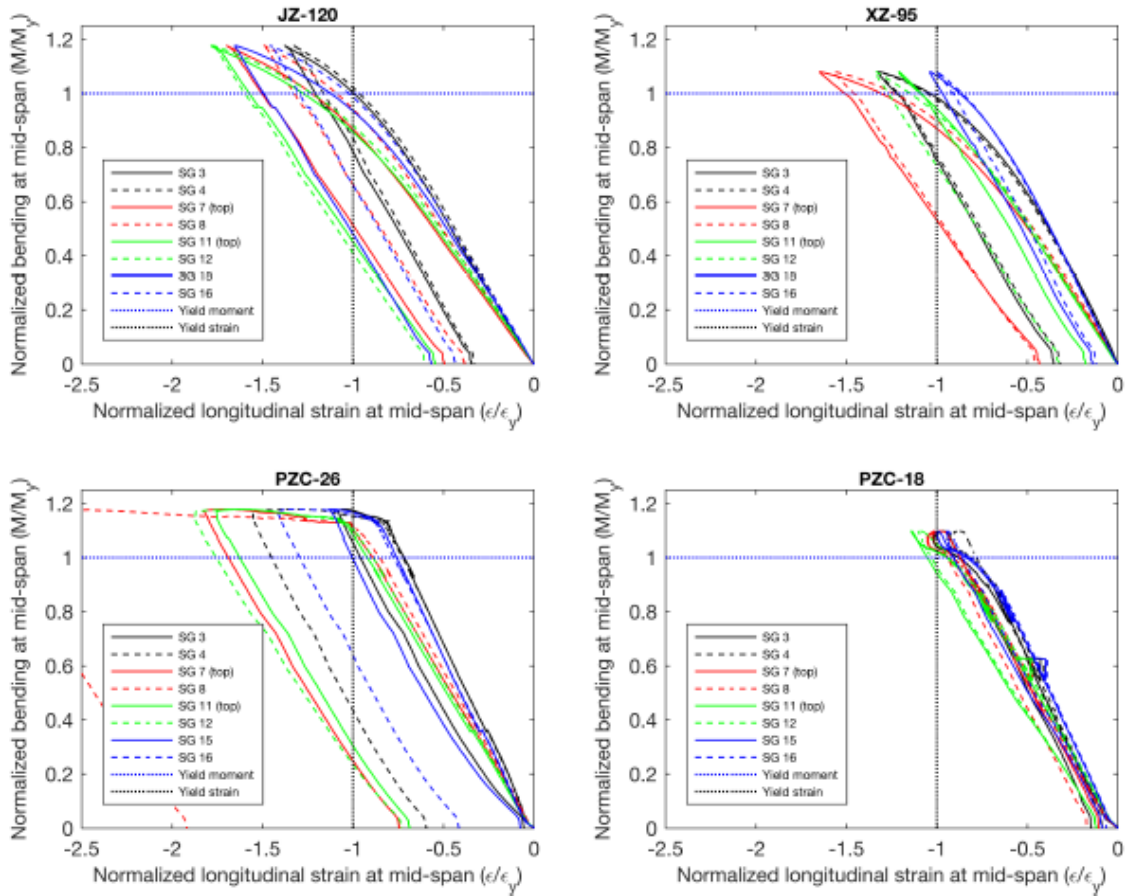


FIGURE 39: NORMALIZED LONGITUDINAL STRAIN VS NORMALIZED BENDING MOMENT AT MIDSPAN (NBM, 2017)

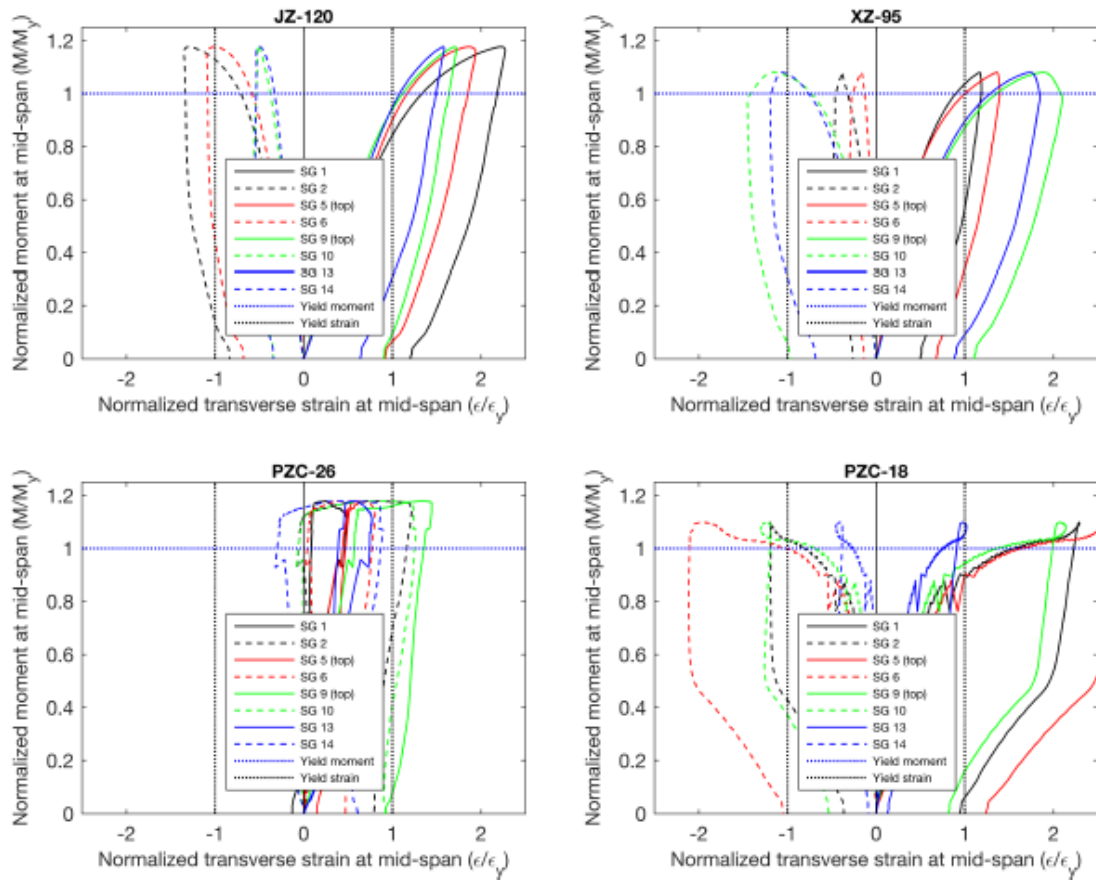


FIGURE 40: NORMALIZED TRANSVERSE STRAIN VS NORMALIZED BENDING MOMENT AT MIDSPAN (NBM, 2017)

Conclusions

Four-point bending tests were conducted to investigate the flexural performance of four sheet piling cross-sections produced from hot-rolled and cold-formed methods. According to the NBM's report (2017), flexural load-deformation response was consistent between cold-formed and hot-rolled cross-sections. Transverse stresses higher than the yield stress have a localized influence on the longitudinal flexural capacity. Interlock at the middle of the cross-sections was consistent between both types of the sheet piles, with minimal separation observed before yielding and failure. This experimental program indicates that hot-rolled and cold-formed sheet pilings have equivalent longitudinal flexural capacity when section and material properties are consistent (NBM Technologies, Inc., 2017).

CHAPTER 3: Experimental Testing Methods

The experiment explored the failure mechanism, flexural strength, moment-deflection response of the same sheet pilings tested by NBM Technologies, Inc. in 2016 and 2017. **Figure 16** and **Table 2** show four cross-sectional drawings and their structural properties. The strength is typically divided by the width of the cross-sections to obtain the sectional properties per unit foot of a sheet piling wall. As shown in **Table 2**, the JZ-120, and PZC-26, profiles have comparable modulus properties, as do the XZ-95 and PZC-18 profiles. However, the yield stresses of the specimens are different. Therefore, data from the tests needed to be normalized by their corresponding properties. The comparison will be used to investigate the influence of hot-rolled and cold-formed production methods on the cross-sections with equivalent sectional modulus.

The design of the specimen and the test setup aimed to simulate the actual behavior of a sheet piling wall. Previous other projects reviewed in Chapter 2 and the studies on the same sheet piling cross-sections were used as guidelines for designing the test components (NBM Technologies, Inc., 2016 and 2017). The test setup needed to control the specimen to behave under flexure without any other limit states, such as shear failure of the specimen and the bolts, before reaching the maximum moment capacity. Also, components of the test setup needed to provide a simple beam condition, a uniformly distributed load, and stability.

3.1 Test Parameters

In this project, the following parameters were investigated:

- Hydraulic ram load

The load data was obtained from the pressure sensor connected to the hydraulic ram. The applied load from hydraulic rams was transferred to be uniformly distributed pressure in the air bladder through the spreader frame.

- Air bladder pressure

Pressure in the air bladder had a direct relationship to the applied load on a specimen. The pressure generated uniform loading perpendicular to the surface of the sheet piling

specimens. For the purpose of the discussion in this thesis, “lateral load” is the horizontal pressure components on the webs of the sheet piling cross-section, which causes the cross-section to close or causes the webs to deform toward each other under the load.

- Deflection

Vertical and lateral deflections were caused by the load from the air bladder measured directly from string potentiometers

- Flexural strength:

Flexural strength is a function of material property and geometry. It is defined as the stress in the material just before it yields in a flexure test. This parameter can be calculated from bending moment obtained by structural analysis given the sectional properties of the specimen. The equation used for calculation of the flexural strength, as well as bending stress at a given moment is:

$$\sigma = \frac{M}{S}$$

Where: σ is flexural stress

M is the moment at the point of interest

S is the sectional modulus of the specimen

This equation can be used together with the structural analysis of the test setup to estimate the peak load of each specimen that will occur during the test.

- Maximum capacity

The maximum capacity of a specimen was calculated by the maximum ram load where a cross-section was fully yielded or where a load-deformation curve became horizontal.

- Longitudinal, transverse, and axial strains (or stresses):

In this thesis, there are three types of strains caused by the applied load from the air bladder and the restrained conditions as demonstrated in **Figure 41**. The three types of strains include longitudinal bending strains (or longitudinal strains), axial strains, and transverse bending strains. From the diagram, the longitudinal strains are mainly caused by bending of the entire cross-section under flexure as shown in **Figure 41a**. The axial strains in **Figure 41b** are created by the pressure components that applied axially on each of the flanges or webs of the specimen against the restrained conditions, which could be a bearing plate (or support), the middle interlock, or a lateral bracing that prevented the cross-section from spreading apart. Finally, in **Figure 41c** the transverse bending strains are mainly caused by the bending of the individual webs or flanges under the pressure perpendicular to their surfaces. Note that the direction of axial strains or transverse bending strains varies by the local axis of each of the flanges or webs, but it is always perpendicular to their local longitudinal axis.

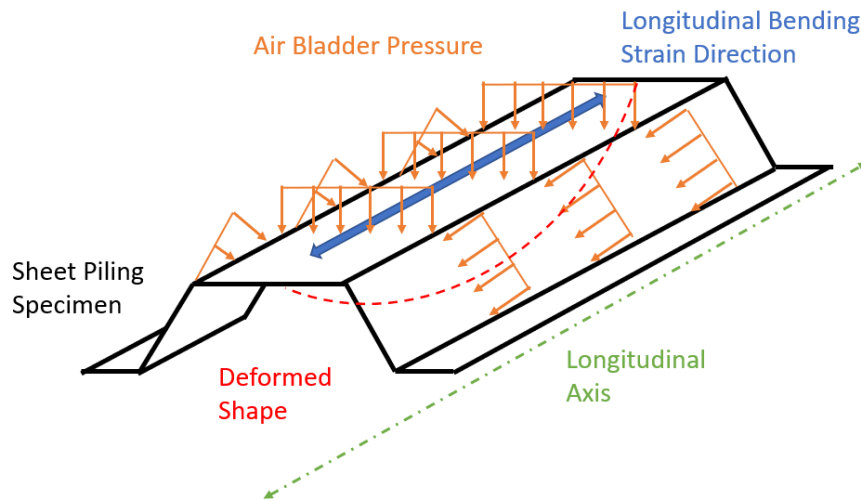


Figure 41a: Longitudinal Strain Direction

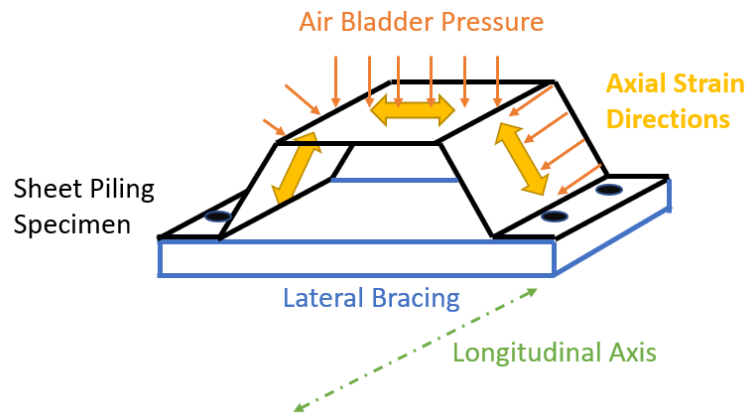


Figure 41b: Axial Strain Directions

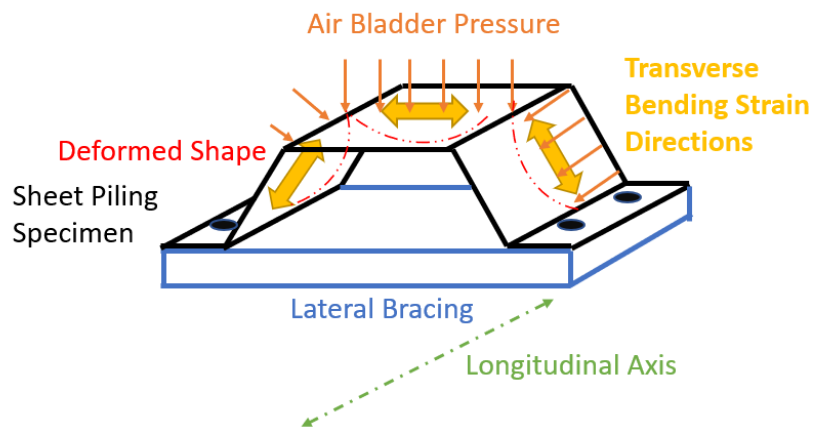


Figure 41c: Transverse Bending Strain Directions

FIGURE 41: THREE DIFFERENT TYPES OF STRAINS ON A SHEET PILING

The total strain in the direction perpendicular to the local longitudinal axis of each of the webs or flanges is a combination of the axial strains and the transverse bending strains. For the ease of the discussion in this thesis, this combination of strains will be called “transverse strains”. To directly measure the strains in the longitudinal and transverse directions during the test, two strain gauges were attached in both directions at each location. The instrumentation plans are presented in Chapter 3.4.

- **Span Length**

The span length is an important parameter that helps investigate the effect of lateral loading on the sheet piling specimens. According to the structural analysis of the simple beam, when the span length increases, the load required to obtain the same amount of moment of the shorter span decreases. However, since the sheet pilings were loaded with a uniform pressure from the air bladder, a decrease in the total amount of load also reduced the amount of the lateral loading component on the specimens. **Figure 42** shows the configurations from the variation of the span lengths.

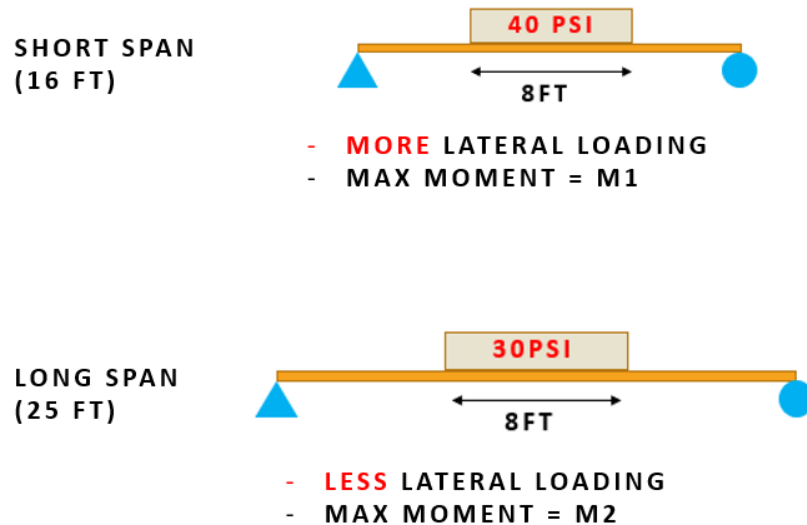


FIGURE 42: DIFFERENT SPAN LENGTH CONFIGURATION

For a typical beam, without lateral loading, the difference in the load on the span can lead to the same amount of moment ($M1=M2$). However, for the sheet piling specimens

loaded under pressure, the maximum moment obtained were not equal ($M1 \neq M2$) due to the different amount of lateral loading.

3.2 Specimen Design

To control the specimens to fail under the flexural mode, a few more mechanisms, including web-crippling, shear, lateral spreading of the specimens, were controlled. First, the clear span lengths of 16ft, 25ft, and 35ft will be used to prevent the web-crippling failure, which would occur under the span length of under 12 ft, according to the simulation study from NBM (2016). Second, NBM (2017) calculated the shear capacities of the specimens. The results confirmed that shear failure would not occur before flexure for the shortest span length of 16 ft. Third, the bolts' actual shear strength at the bearing plates from the test by NBM (2017) was higher than the calculated values due to the overstrength of steel material. This resulted in a bolt's failure and a sudden drop in load from the slippage of the bolted connection at a bearing plate in the first shakedown test of a PZC-26 specimen. Therefore, larger high strength A490 bolts were installed at the bearing plate of each. The size of the bolts was changed from 1 inch to 1-1/4 inch, and the bolts were pre-tensioned for the later tests to resolve the problem (NBM, 2017). This size of the bolts was used in this project at Virginia Tech. Finally, sheet piles are loaded with pressure from soil or water in the actual application. Therefore, the use of an air bladder to apply uniformly distributed pressure on the specimens was introduced. The study by NBM (2016) also provided the target load and pressure at the yield moment of a sheet piling cross-section. These numbers were used as a guideline and expected target in the experiment to confirm the results from the simulations.

As mentioned previously, there are four cross-sections tested in this project. JZ120 and XZ95 are cold-formed with a specified yield strength of 50 ksi. PZC26 and PZC26 are hot-rolled with a specified value of 60 ksi. The cross-sections are the same profiles used in the previous projects (NBM Technologies, Inc., 2016 and 2017). The sectional drawings and properties are shown in **Figure 16** and **Table 2**.

Table 11 shows the test matrix. The tests included three different span lengths and the four cross-sections. A different span length caused a varied total amount of load on the specimen. This helped investigate the effect of different transverse stress to the longitudinal stress ratios on the flexural capacity. The 16-ft JZ120 specimens on this project were used for comparing with the four-point bending test result in 2016. The 35-ft long specimens were used in the comparison between the hot-rolled and cold-formed sheet pilings. For each of the test configuration, there were a total of three specimens. All of them had displacement sensors installed, while one out of the three has strain gauges attached. The instrumentation plan will be discussed later in this chapter.

TABLE 11: TEST MATRIX

Type	Cross-section	Span Length	Specimen No.	Specimen Name	Remark
Cold-formed	JZ120	16	1	JZ120-16-1	-
			2	JZ120-16-2	-
			3	JZ120-16-3	Strain-Gauged
		35	1	JZ120-25-1	-
			2	JZ120-25-2	-
			3	JZ120-25-3	-
	XZ95	25	1	XZ95-25-1	-
			2	XZ95-25-2	Strain-Gauged
			3	XZ95-25-3	-
		35	1	XZ95-35-1	Strain-Gauged
			2	XZ95-35-2	-
			3	XZ95-35-3	-
Hot-rolled	PZC26	35	1	PZC26-35-1	-
			2	PZC26-35-2	Strain-Gauged
			3	PZC26-35-3	-
	PZC18	35	1	PZC18-35-1	-
			2	PZC18-35-2	-
			3	PZC18-35-3	Strain-Gauged

3.3 Test Setup

The sheet piling flexural test was designed as a simple beam. The specimens were loaded with a hydraulic ram through a spreader frame and an air bladder at midspan to apply vertical and lateral loading simultaneously according to **Figure 43a**. The side and front elevation views are shown in **Figure 43b** and **Figure 43c**. The span length varied from 16ft, 25ft, and 35 ft to investigate the longitudinal-transverse stress ratios' difference. Each specimen was laterally braced at four locations, which are 4-ft apart from the midspan on both sides and both supports to prevent the cross-section from spreading apart. 2D and 3D views of the setup are illustrated in **Figure 43**. The components of the setup consisted of a sheet piling specimen, two load frame beams at the bottom, two supporting beams, two roller supports, two bearing plates bolted to the specimen, two lateral bracings to the specimen at both ends of the loading region, an air

bladder, a built-up spreader frame, two vertical rollers, a hydraulic loading ram, crosshead beams, and columns.

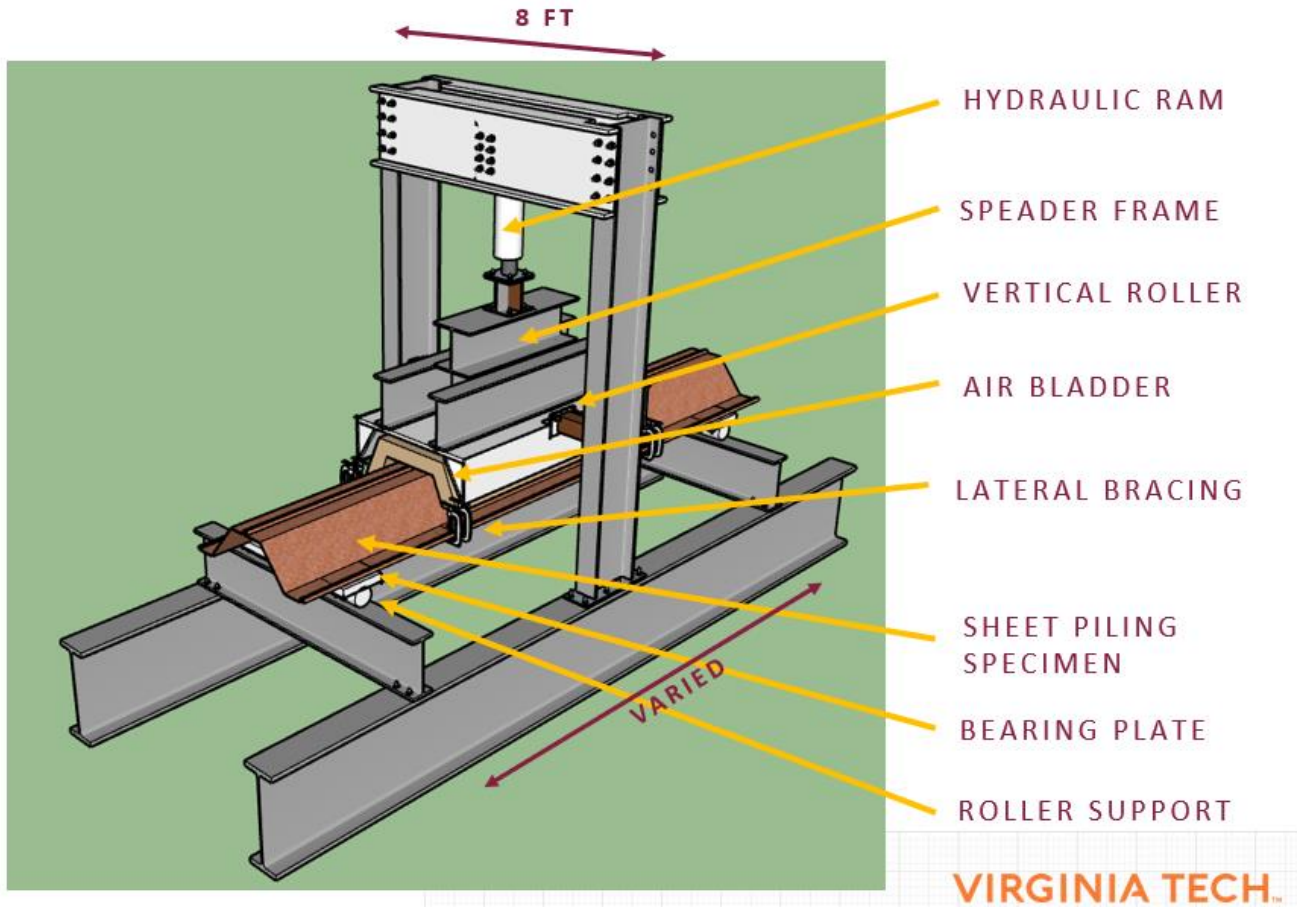


Figure 43a: 3D View of Test Setup

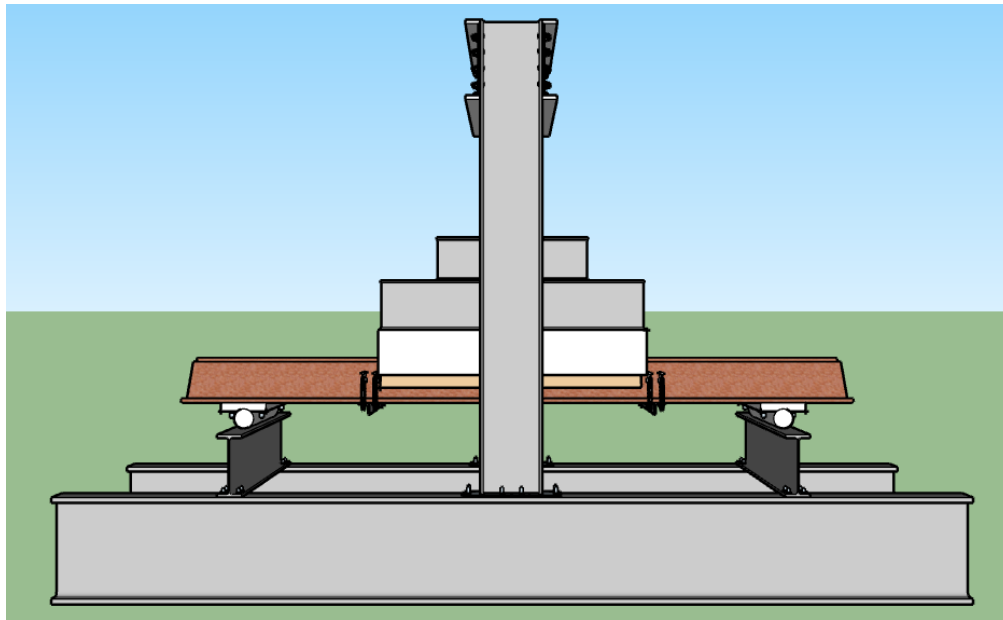


Figure 43b: Side Elevation View of Test Setup

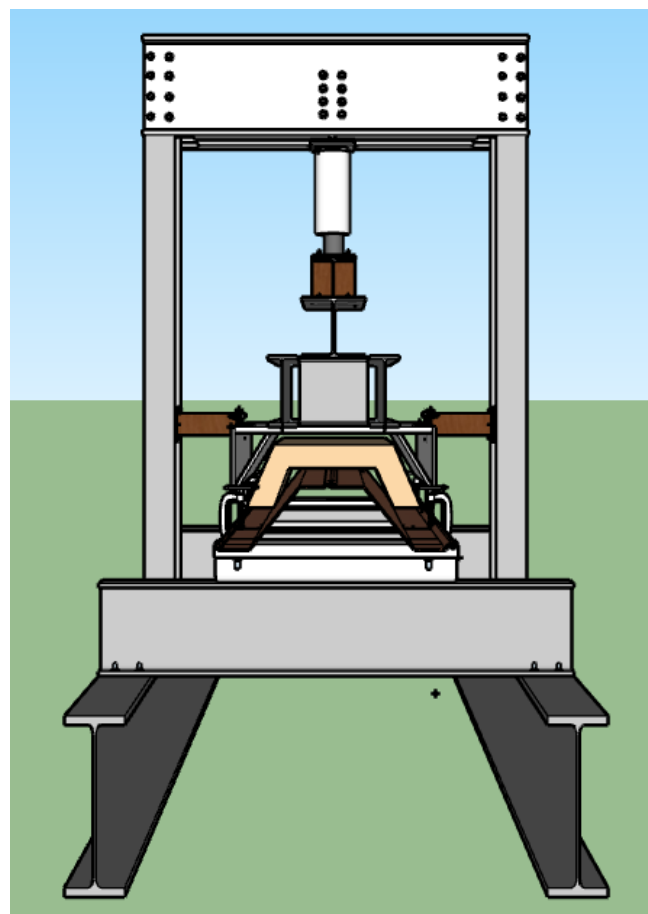


Figure 43c: Front Elevation View of Test Setup

FIGURE 43: TEST SETUP VIEWS

Figure 44 shows the actual boundary conditions of a sheet piling wall. The boundary conditions consist of restrained lateral (x-axis) and longitudinal (z-axis) displacements, and restrained rotations along the vertical (y-axis) at the edges of the cross-sections from the adjacent sheet pilings. However, there is a challenge to continuously brace the specimen to perform a laboratory test for these sheet-piling cross-sections. Therefore, four discrete locations, including two bearing plates and two lateral bracings are attached to the specimen in order to brace the specimens laterally. Displacement sensors were installed to at the bracing locations to measure the vertical and horizontal deflection to examine the difference between the real bracing condition and the one performed in the laboratory.

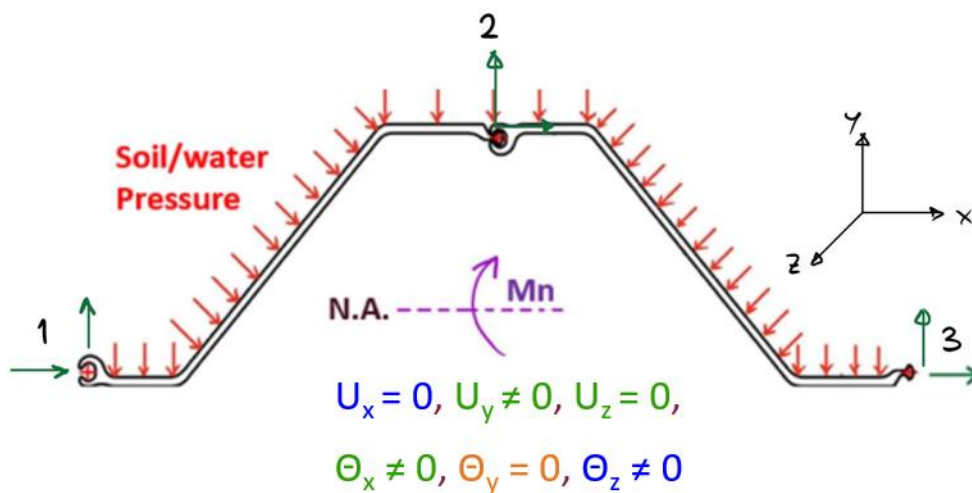


FIGURE 44: ACTUAL BOUNDARY CONDITION OF SHEET PILING

Lateral supports providing lateral stiffness were made of two double angles 2L4x4x3/8. The required axial strength of the angles was approximated from the force's lateral components from the air bladder. The lateral bracings' locations were at 4 ft from the midspan on both sides (or at two ends of the air bladder). The loading region was between the lateral bracings. Each bracing angle was attached to the bottom flanges of the specimen using four 12-inch heavy-duty clamps as shown in **Figure 45** to ensure that the specimen would develop transverse stresses. The clamp's dimension and specification is included in Appendix D. Each clamp has a slipping resistance of 20,000 lbs. The use of four big clamps at a bracing location provided

sufficient slipping resistance from the axial force and provides enough reach past the interlock at the cross-sections' edges. The location of the lateral support is shown in **Figure 46**.

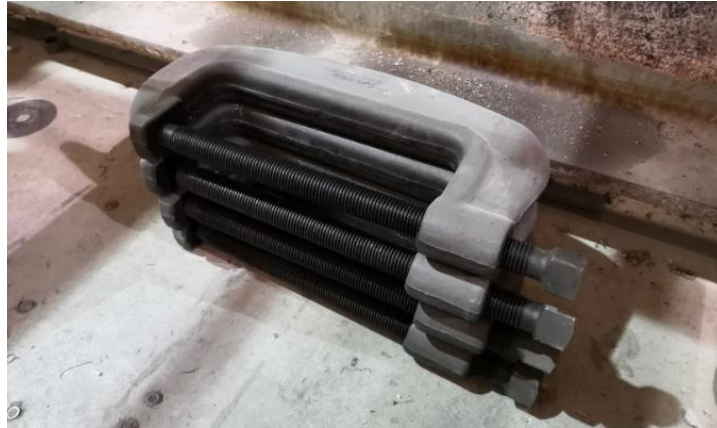


FIGURE 45: 12-INCH HEAVY DUTY CLAMPS

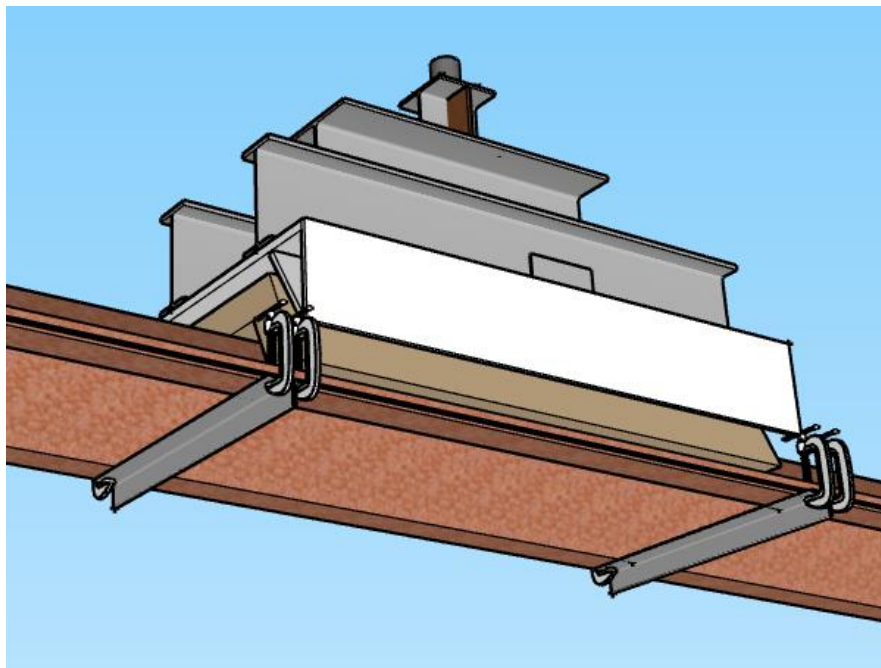


FIGURE 46: 3D VIEWS OF LATERAL SUPPORTS

However, after a few tests, the clamps started to bend and fatigue due to several loading and unloading sequences. As a result, the test data for 25-ft PZC18 were unusable and not included in the test matrix. Later for 35-ft span lengths, four 1-in bolted connections were used instead to connect the bracing angles with the specimen, and the problem was solved.

The spreader frame transferred the point load from the hydraulic loading ram to applied pressure on the specimen through the air bladder. The frame was permanently attached to the ram by a threaded rod tapped to a plate. The plate was bolted to the top of the spreader frame to hang the frame to the ram. This setup makes it easier to replace a new specimen after each test. Hilman-roller parts shown in **Figure 47** were bolted to both sides of the spreader frame to provide stability. The rollers were free to move vertically on the column webs, but they were restrained from moving laterally. All of these keep the spreader frame centered during the test. **Figure 48** shows the components of the spreader frame.

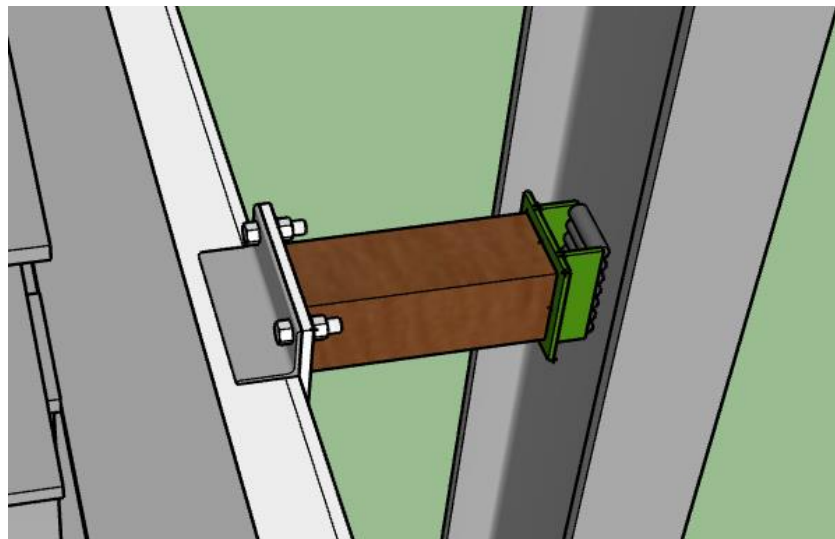


FIGURE 47: HILMAN ROLLER PARTS

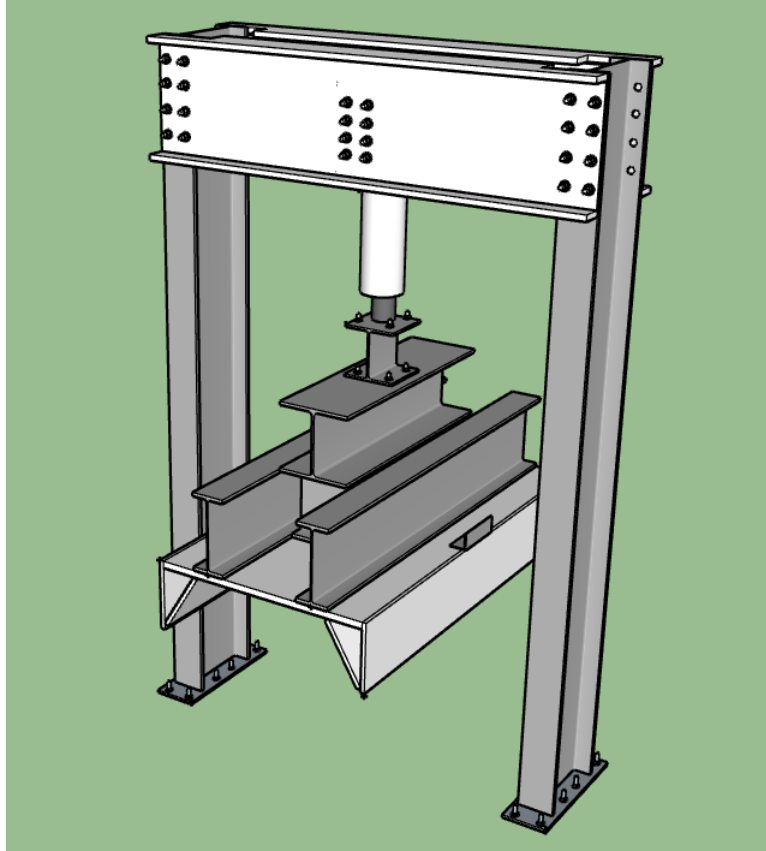


FIGURE 48: SPREADER FRAME COMPONENTS

An air bladder was a vital component used for applying uniformed pressure to the specimen. The cross-sectional drawing of the air bladder is demonstrated in **Figure 49**. The dimensions of the bladder was designed to fit the dimensions of the JZ120 profile. However, because of the bladder's flexibility, it was used for other cross-sections as well. The result from this use will be discussed more in Chapter 5. The bladder was fabricated from a nylon reinforced coated fabric, and it was designed to withstand pressure up to 100 psi. However, after the first couple of tests, the air bladder had some leakage at a joint. Thus, a new stringer air bladder was fabricated using Kevlar material, a heat-resistant and strong fiber with high tensile strength. The bladder had two sensor ports for a pressure transducer to measure the pressure inside and a pressure hose to input air pressure. The air bladder's shape was designed to fit the space between the spreader frame and a sheet piling specimen as demonstrated in **Figure 50**.

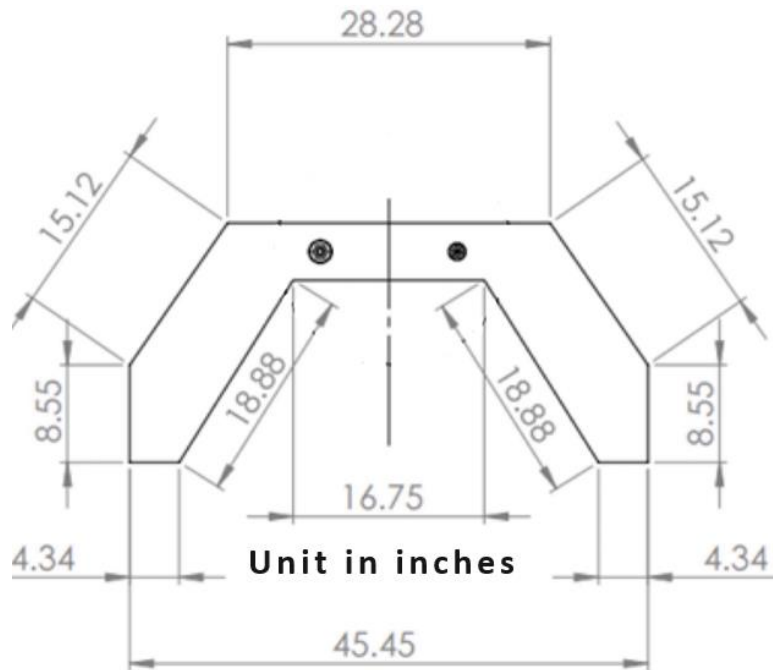


FIGURE 49: AIR BLADDER CROSS-SECTION



FIGURE 50: AIR BLADDER ASSEMBLY

There were two methods to increase the load on the specimen. The main approach was to increase air bladder pressure by adding more air into it using a pressure hose and a valve. This caused the bladder to expand, pushing the specimen to bend down and pushing the hydraulic ram up to increase the load. The air pressure was controlled by the recorded pressure from a pressure transducer. The other loading approach was to move the hydraulic ram down. The ram was controlled by an Enerpac pump with a controller. The

force added from moving the ram was monitored by another pressure transducer. More details on the Enerpac ram is shown in Appendix E.

3.4 Specimen Instrumentation

A total of 15 String potentiometers and 16 strain gauges were installed to measure specimen deformation, as shown in **Figure 51a** and **Figure 51c**. There were five string potentiometers to measure the lateral and vertical deflections in a cross-section: two for each of the bottom flanges, and the other for vertical deflection at the center of the cross-section as shown in **Figure 51a** and **Figure 51b**. Three locations of string potentiometers were at the midspan, and two ends of the air bladder. Strain gauges were attached at the midspan for one specimen out of three in each test configuration. From **Figure 51c**, The total of 16 strain gauges were attached to two sides of the webs and two flanges on the top and bottom of the specimen. There were eight transverse and eight longitudinal locations. These strain gauges on both sides of the specimen demonstrated the stress state at the attached locations during the test. They also indicated whether the specimen is yielding locally at the midspan. See Appendix E for sensors' model and specification.

To design the string potentiometers' stands, the maximum elastic deflection was calculated using the specified yield stresses, which were 50 and 60 ksi for the cold-formed and hot-rolled sheet-pilings, respectively. The calculation was done by NBM using a simple beam model subjected to uniformly distributed load at the middle. The largest elastic deflection computed for the 16-ft, 25-ft, and 35-ft specimens were approximately 0.75, 1.75, and 4.25 inches. Thus, the stands for the string potentiometers needed to be designed for more deflection as the specimen would be fully yielded. Since 10-inch potentiometers were used, their stands were designed to accommodate 9.5 inches of deflection to prevent damage to the sensors.

The data were recorded using Campbell Specific CR9000X, a large modular multiprocessor system that provides precision measurement capabilities in a rugged, battery-operated package (Campbell Scientific, 2020). The wiring diagram for all the sensors are shown in Appendix A. The sample rate was set to be 40 Hz considering it was reasonable for a static loading test.

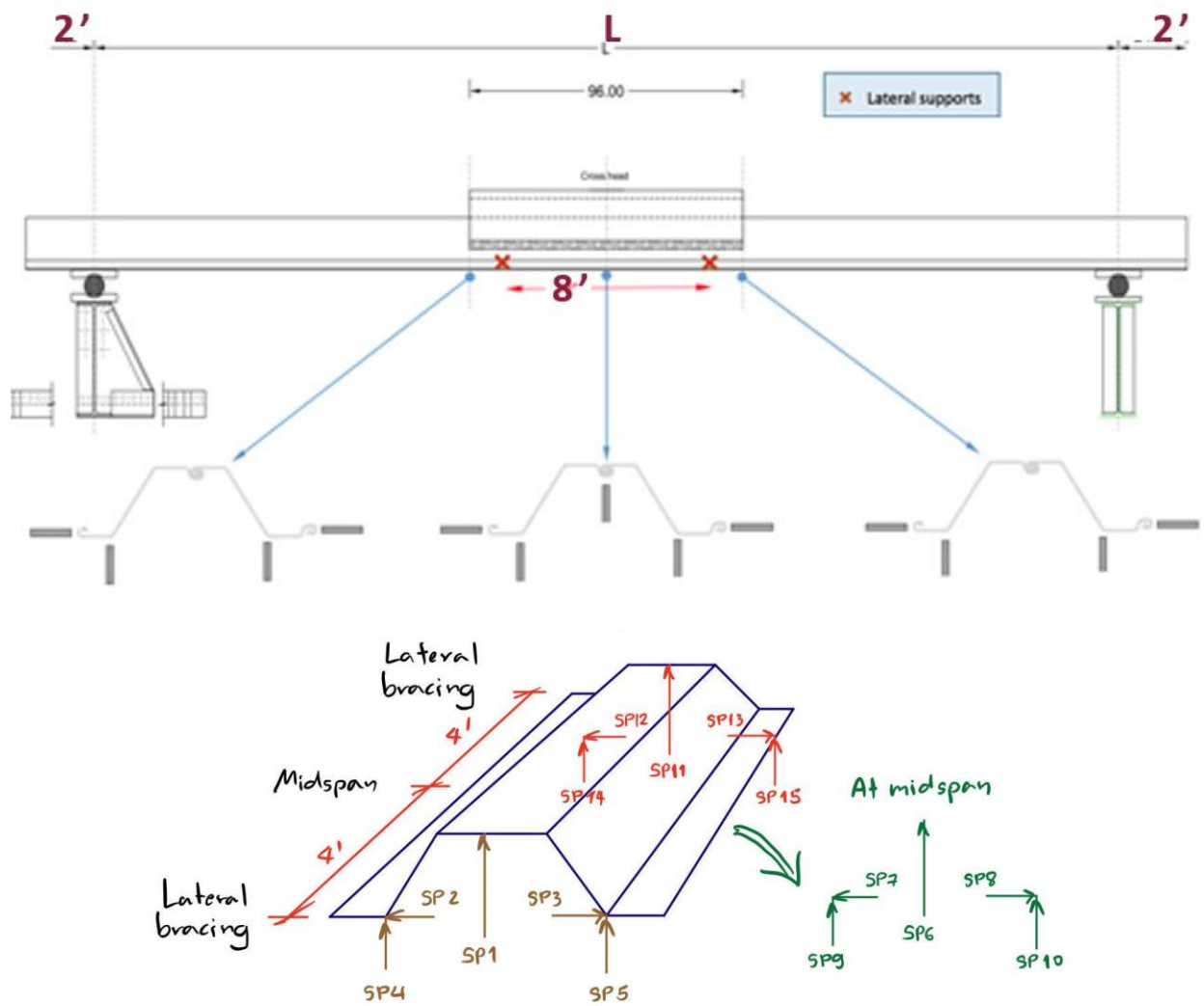


Figure 51a: 3D view of String Potentiometer Location

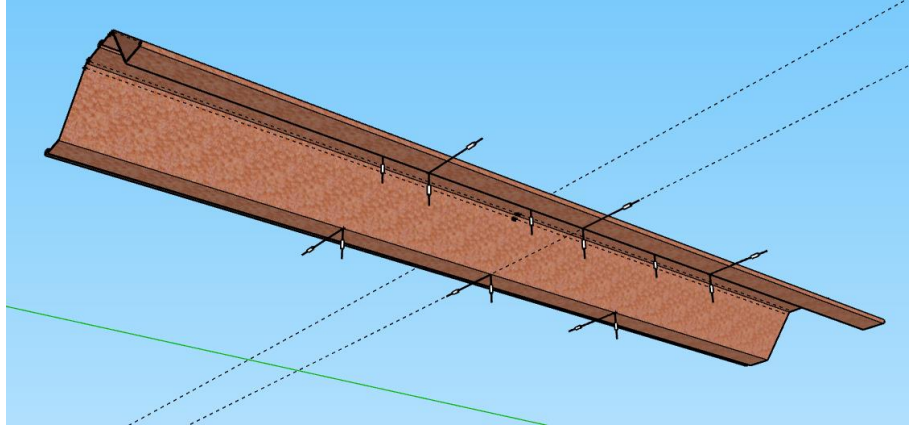


Figure 51b: 3D view of String Potentiometer Location

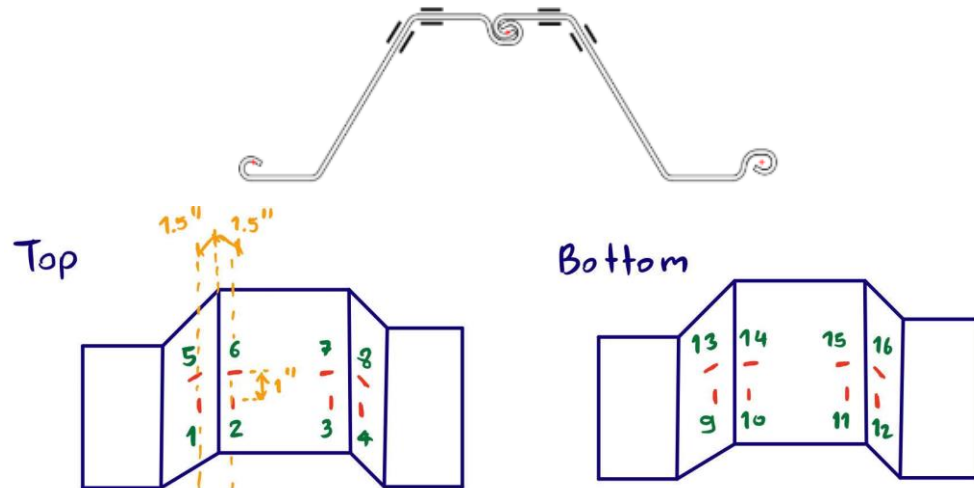


Figure 51c: Strain Gage Pattern at Mid-spans

FIGURE 51: INSTRUMENTATION LOCATIONS

There were also two pressure transducers to measure the load in the ram and the pressure in the air bladder. The ram's transducer was install to the hose ran into the ram. The sensor was calibrated to read the load value using a load cell. The bladder's transducer was connected to the smaller port shown in **Figure 49**.

3.5 Flexural Testing Procedure

There were two methods to increase a load on the specimen: adding the air bladder pressure and moving the ram down. A test began by moving the ram down by 4 inches to have some stroke for the air bladder to push it back up. Then, the air pressure was mainly added. However, after some points during the test, the ram needed to move more down to increase the available stroke since the expansion of the air bladder not only pushed the specimen down, but it also pushed the ram up. The specimen was first loaded to 10% of the expected capacity to check if all components and sensors were working well and reasonably. The test then continued to reach the target load and pressure obtained from the finite element analysis of each test configuration. The target load and pressure for each cross-section and span length is shown in **Table 12**. After that, the specimen was loaded more to achieve a clear yielding pattern of the load-deformation curve, where the curve became flat (See **Figure 52**). The monitoring process during the test will be discussed more in Chapter 4.2. Photos and videos were taken during the test. The videos were recorded from the side view to show the deflection clearly. The photos were taken from a wide angle from one side every 1 inch of deflection, after a loud noise, or at the maximum deflection, etc. Ambient air temperature, observed behavior, and loud noise were recorded. After a test was done, preliminary analyses were performed to ensure everything went well. The analyses included load-pressure, load-deflection, and load-strains plots from the test data obtained.

TABLE 12: TARGET LOAD AND PRESSURE GIVEN FROM FINITE ELEMENT ANALYSIS BY NBM

Type	Cross-section	Span Length (ft)	Target Load (kip)	Target Pressure (psi)
Cold-formed	JZ120	16	286.0	65.6
		35	120.0	27.0
	XZ95	25	110.0	26.0
		35	77.0	18.0
Hot-rolled	PZC18	35	91.2	22.8
	PZC26	35	171.6	37.2

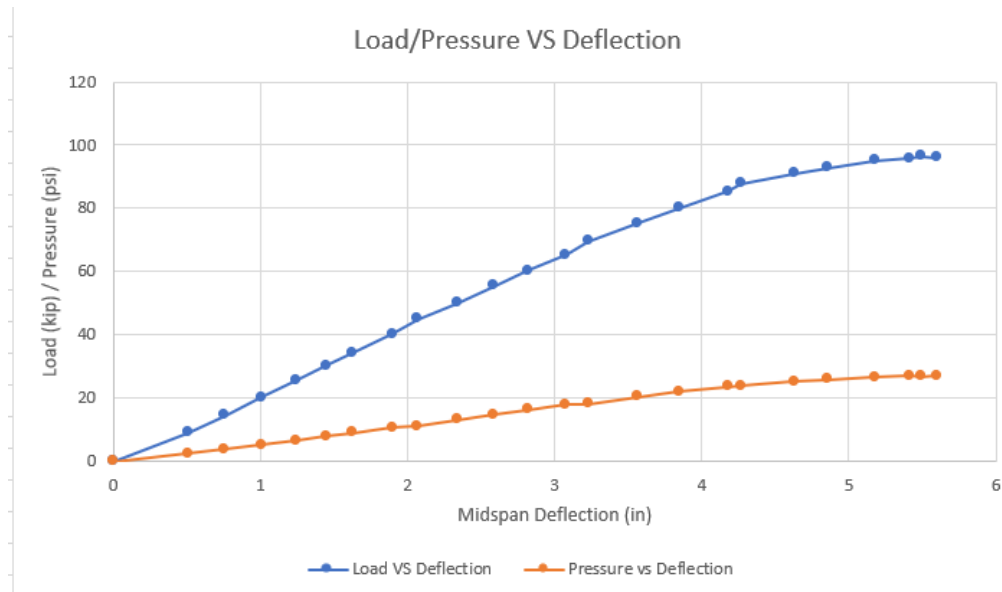


FIGURE 52: MANUAL LOAD AND PRESSURE VS MIDSPAN DEFLECTION PLOT FOR PZC18-35

3.6 Material Testing

Four representative tensile coupons were taken from the end of each specimen after the flexural testing had been completed. Two were from both of the top flanges, and two were from both of the webs in the longitudinal direction (See **Figure 53**). This test procedure complied with ASTM E8 using 18-inch long samples. The necessary parameters were the initial width and thickness of each sample, ultimate tensile strength, elongation in 2 inches, and 0.2% offset yield strength. **Figure 54** shows a drawing for the coupon cut of all sheet piling specimens.

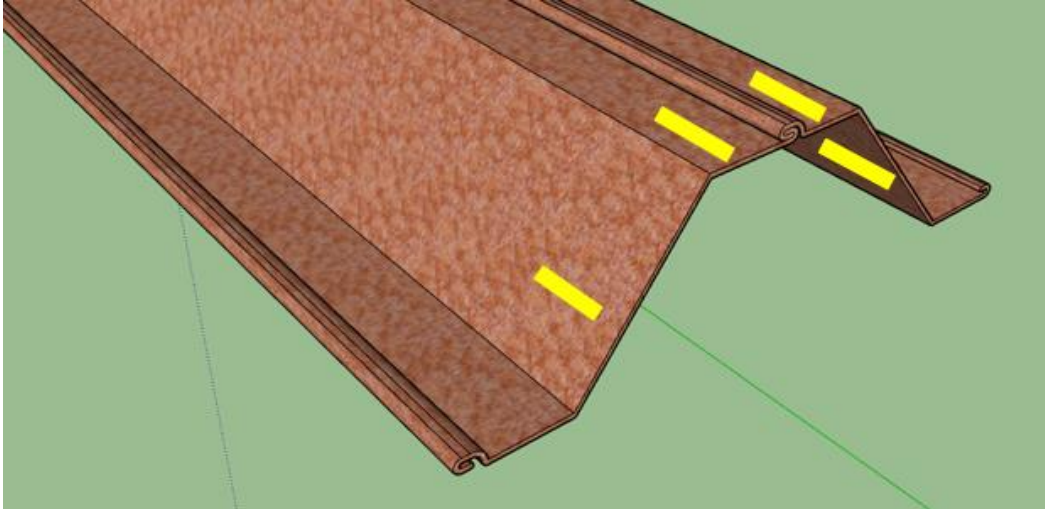


FIGURE 53: TENSILE COUPON CUT

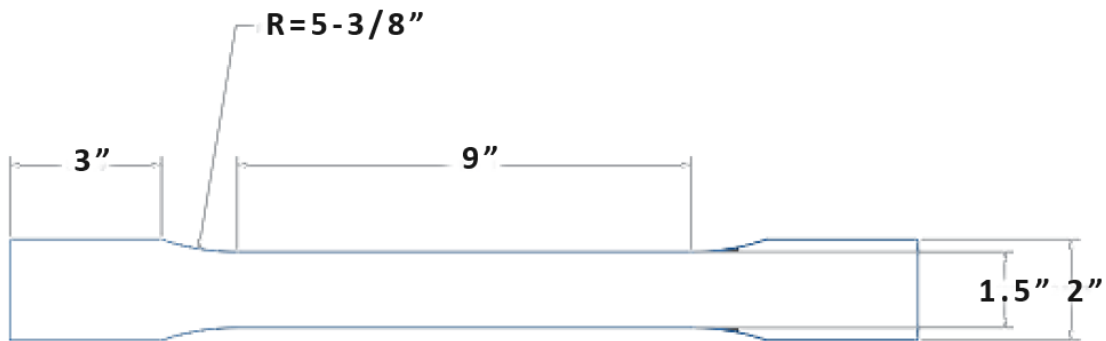


FIGURE 54: TENSILE COUPON DRAWING PER ASTM E6

3.7 Data Evaluation and Documentation

Material Properties

From the coupon test, ultimate tensile strength, elongation in 2 inches, and 0.2% offset yield strength were determined. The yield strength of each sheet piling specimen was used for normalizing the moment-deflection results. The normalize-moment deflection curves of the hot-rolled and cold-formed specimens and the same cross-sections with different span lengths were compared to investigate their performance and effect of transverse stresses.

General Behavior and Observations

The peak load occurred when the specimen was fully yielded in a longitudinal direction. Transverse stresses prevented some cross-sections from reaching its theoretical yield or plastic moments. Transverse deformations were caused by local buckling of the top flanges or webs. The interlock of the sheet piling should not be separated while the specimen is loaded to the maximum load. Global buckling or lateral-torsional buckling should not occur. There might be some slipping noise from the bolt components and some noise from the specimen itself.

Local Longitudinal and Transverse Strains

The normalized longitudinal and transverse strains were plotted to show that the amount of transverse stresses is significant. The sign of recorded strains, which is compression for the negative value and tension for the positive value, and should follow the sign of the moment at that location.

Moment-deformation and Moment-rotation Responses

The peak load in the moment-deformation response was influenced by the yield strength of the specimen.. The moment-deformation curves were normalized to the associated yield strength of each specimen in order to make the comparison between different cross-sections more reasonable and more meaningful. The normalized plots of the cold-formed and the hot-rolled sections with matching modulus were compared and investigated. The maximum capacity were compared with the yield and plastic moments to investigate the influence of lateral loading on the cross-section.

CHAPTER 4: Results

This chapter presents the summary of the test results. It also discusses some obvious trends and aspects of the results that can be seen without further analysis. The recorded data included load-deflection, load-strain, load-pressure, and tensile coupon data. As outlined previously, there were 18 sheet-piling specimens tested. This chapter will show examples of the test data from some specimens. The remaining test data are included in Appendix C.

4.1 Recorded Data

Data from the instrumentation outlined in Chapter 3 were recorded during a test. The data included lateral and vertical displacements from the string potentiometers, local transverse and longitudinal strains from the strain gauges, hydraulic ram load, and air bladder pressure. After a test was done, raw data from the displacement sensors and strain gauges could be plotted with the applied load. Consideration of the raw data was important because it informs whether the test went well, and it demonstrated the general behavior of the specimen. For instance, the string potentiometers' record values could indicate if the specimen was twisted during the test if the vertical displacements at each side of the cross-section were significantly different. Then, further analysis, such as moment calculation, moment normalization, and comparison, could be performed. Deformed specimens during the test at their maximum loads are shown in **Figure 55** and **Figure 56**. The photos show the maximum deformation at the maximum load of a 16-ft JZ120 and a 35-ft JZ120 specimens. JZ120 was one of the cold-formed cross-sections. The maximum loads of the specimens were 315 and 142 kips, respectively.



FIGURE 55: DEFORMED JZ120-16 SPECIMEN DURING TEST



FIGURE 56: DEFORMED JZ120-35 SPECIMEN DURING TEST

4.2 Test Results

Although moment-deflection responses will be used later to compare the performance between the hot-rolled and cold-formed cross-sections, the calculation of moments needs some further steps. Therefore, the most convenient way to monitor the data during the test is to manually plot the load vs. air pressure curve and the load and midspan deflection response. The information was shown from the data acquisition system during the test.

During each test, the response was plotted automatically using the datalogger system and manually using a spreadsheet. The manually created plot helped the research team know how the test was going and how close to the target load and pressure, given from the finite element analysis with the same cross-section provided by NBM at each loading state. This load-deflection curve can also be used as a guideline loading for later tests. **Table 12** summarizes the given target load and pressure at the first yield of the specimens

subjected to a uniformly distributed load. **Figure 57** demonstrates a load-pressure plot created by a spreadsheet for a PZC18 specimen with a 35-ft clear span length. The orange line represents the ideal path from the beginning of the test to the target point, and the gray line is the real testing state. The point where the orange line stops is the target load and pressure, which are 91.2 kip and 22.8 psi for the PZC26-35 test group. Each of the gray points represents each time that the specimen was loaded.

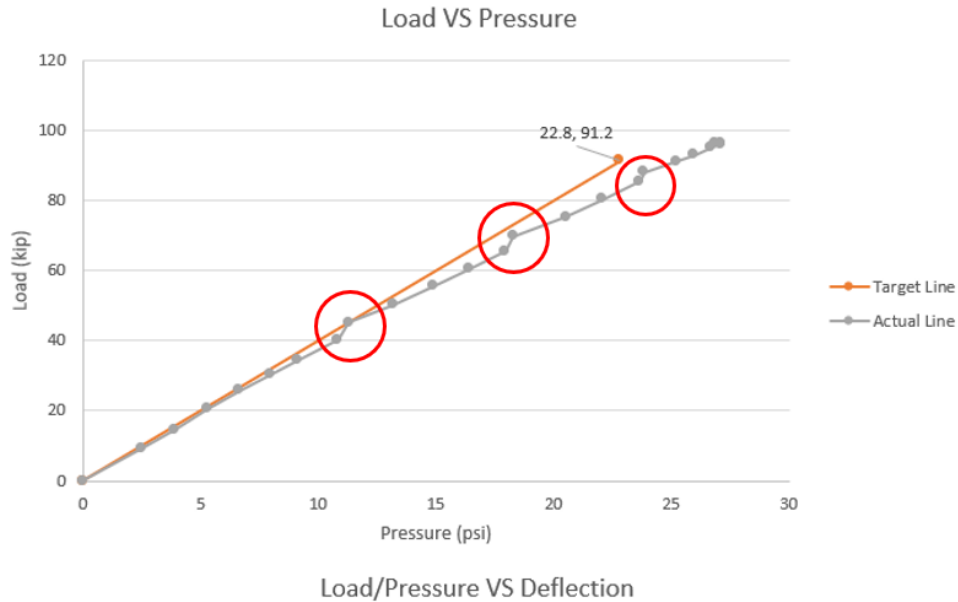


FIGURE 57: MANUALLY RAM LOAD VS AIR BLADDER PRESSURE PLOT FOR PZC26-35

As outlined previously, there were two methods to increase the load on the specimen. The primary approach was to increase air bladder pressure by adding more air into it. The pressure was added via a pressure hose connected to the bladder. There was a valve used for controlling the air flow. Increase in pressure caused the bladder to expand, pushing the specimen to bend down and pushing the hydraulic ram up to increase the load. This method resulted in a desirable parallel slope to the ideal path between loading points. The second loading way was to move the ram down, pressing both the specimen and the air bladder. This loading method established a more dramatic change in slope, meaning that the ratio of the load to the pressure increased is less than the first method. The red circles in **Figure 57** indicates where the ram was moved for this specimen, which were at 40, 65 and 85 kips.

Furthermore, according to the very first shakedown tests, the first approach was more convenient and controllable. However, moving the ram down was still necessary during the test since when the bladder expands and pushes the ram up, the stroke of the ram reduced. Thus, the ram needed to be moved down a few times to maintain the stroke during the test.

Another plot conducted manually during the test was load-deflection and pressure-deflection curve as shown in **Figure 52**. This plot helped the research team know when to stop the test. Also in **Figure 52**, the flatter slope informs that the specimen deformed linearly at the beginning and started to yield after a higher load. The test stopped when the specimen was fully yielded and reached the highest load, which was 98 kips, where the slope is nearly zero.

Load and Pressure Responses

The load and pressure data were important for monitoring the tests by comparing the responses with the target line. Also, they were used to compare the loading progress for all specimens in a test group. However, the relationship between these two parameters did not help indicate the capacity or the flexural behavior of the cross-sections. After completed test configurations, the load-pressure curve for each specimen using the recorded data were compared in the same plot. **Figure 58** shows the comparison of the load-pressure relationship for 35-ft PZC18 specimens and 16-ft JZ120 specimens respectively. According to **Figure 58a**, The solid black line in the figure is the target load-pressure path, in which the target point is at 91.2 kips and 22.8 psi for 35-ft PZC18 specimens. It is evident that the loading curves for all three specimens in this configuration are consistent. All the three tests finished after around 10 kips beyond the target load, where their load-deformation responses became flat. The same trend occurred for all the test groups (See Appendix C.1 for the plots for all other test groups). However, only the load-pressure curves for 16-ft JZ120 specimen were close to the target line when reaching higher load. This observation will be discussed later in Chapter 5.

Comparison of Load-Pressure Plots for 35ft PZC18 Specimens

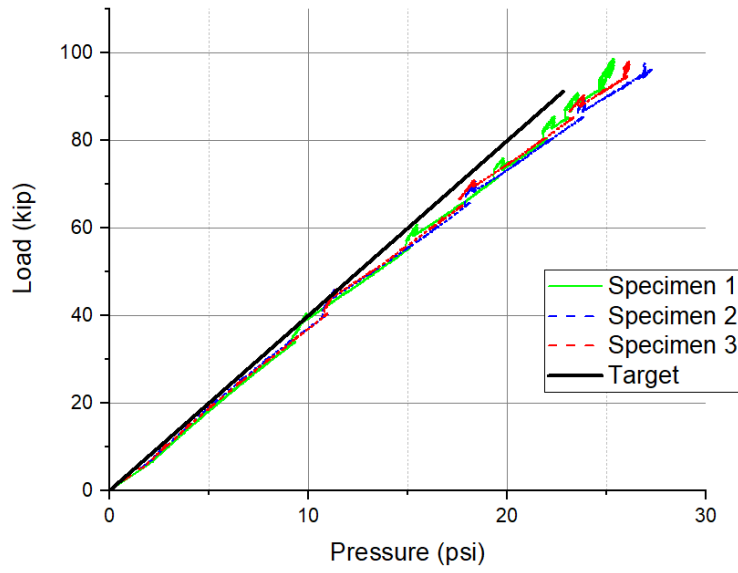


Figure 58a: 35-ft PZC18 Specimens

Comparison of Load-Pressure Plots for 16ft JZ120 Specimens

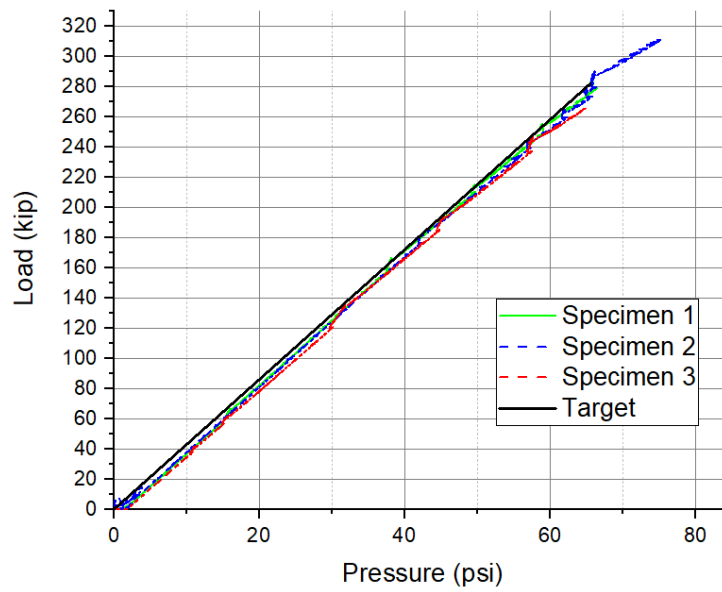


Figure 58b: 16-ft JZ120 Specimens

FIGURE 58: COMPARISON OF LOAD-PRESSURE PLOTS FOR PZC26-35 AND JZ120-16 TEST GROUPS

Specimen Load-Deflection Responses

The load-deflection relationship is a basic tool to evaluate how a specimen behaves under the applied load and pressure. The load and deflection data were readily obtained from the pressure transducer and the string potentiometers via the data acquisition system. This load-deflection information were used to calculate moment-deflection responses in Chapter 5 for further evaluation and comparisons between hot-rolled and cold-formed sheet piling cross-sections. However, without additional effort, the load and deflection data could be plotted from the data collected from the data acquisition system.

As outlined in Chapter 3, 16 string potentiometers were installed in both vertical and horizontal directions in the different locations within the span length. **Figure 59** shows the load and deflection data obtained from the test of JZ120-16-3 specimen. The positive sign for the vertical deflection means that the specimens moved down. The negative sign for both horizontal deflections indicates that the cross-sections were closed due to the lateral component of the air bladder pressure, which is reasonable. After the specimen was unloaded, it deformed back to some permanent deflections, indicating that the cross-section was yielded. See Appendix C.2 for all other plots for the other specimens.

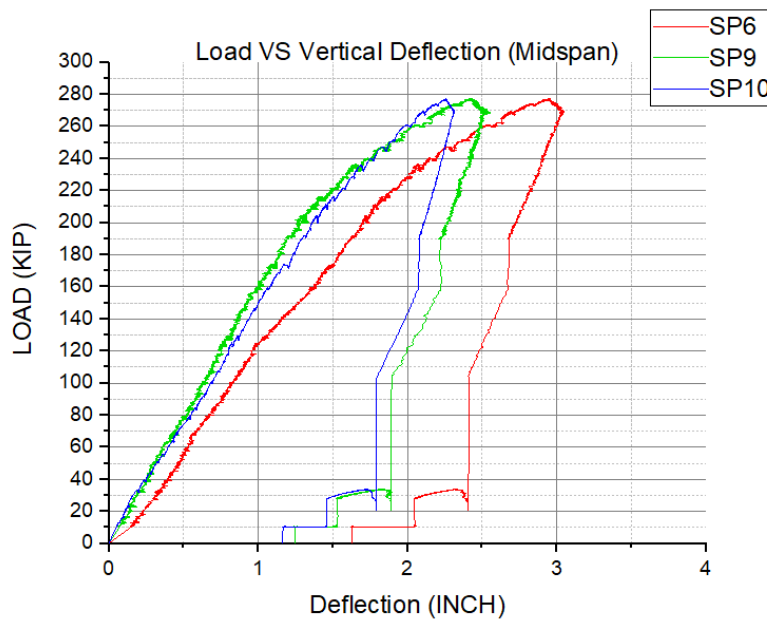


Figure 59a: Load VS Vertical Deflection at midspan

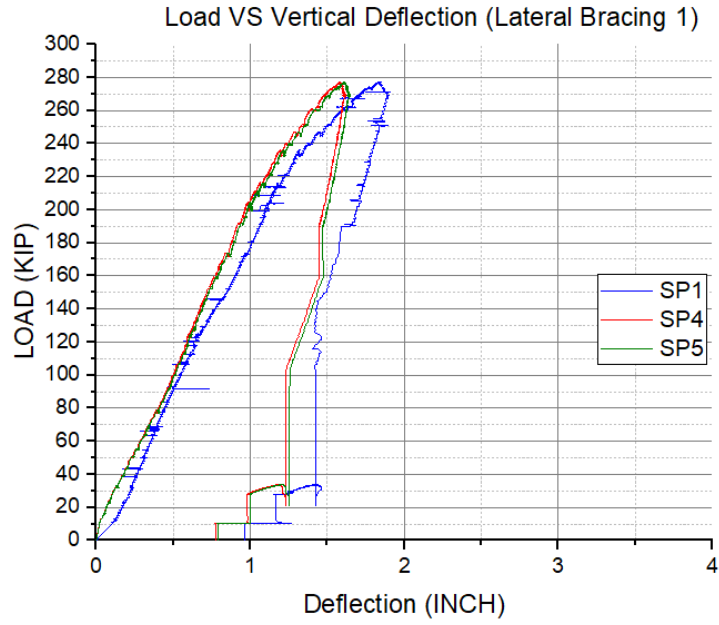


Figure 59b: Load VS Vertical Deflection at Lateral Bracing 1

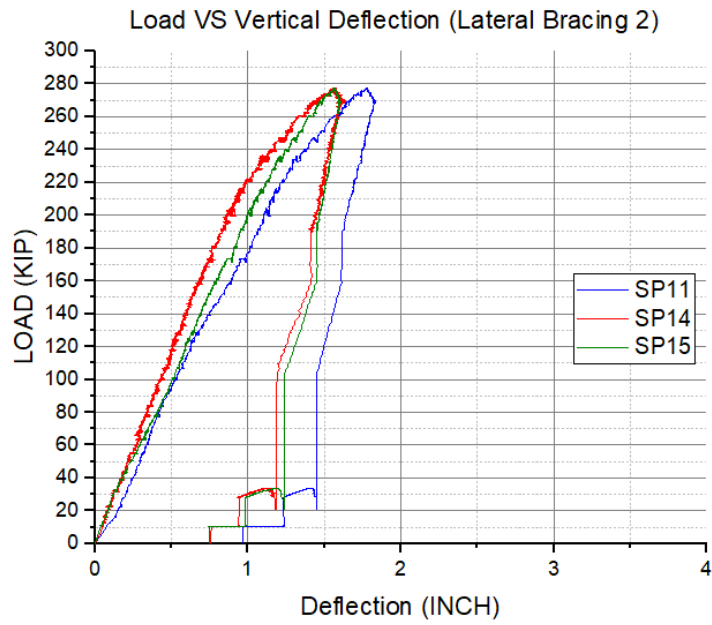


Figure 59c: Load VS Vertical Deflection at Lateral Bracing 1

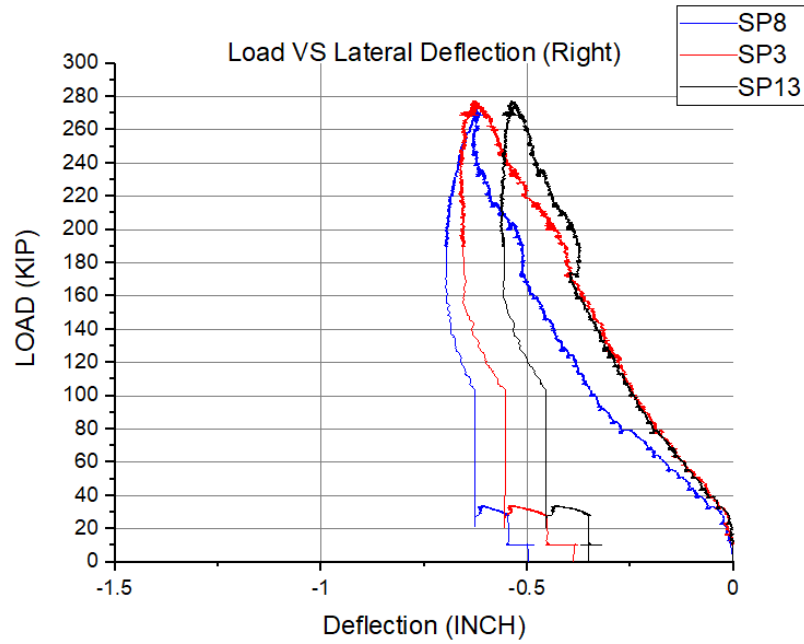


Figure 59d: Load VS Right-horizontal Deflection

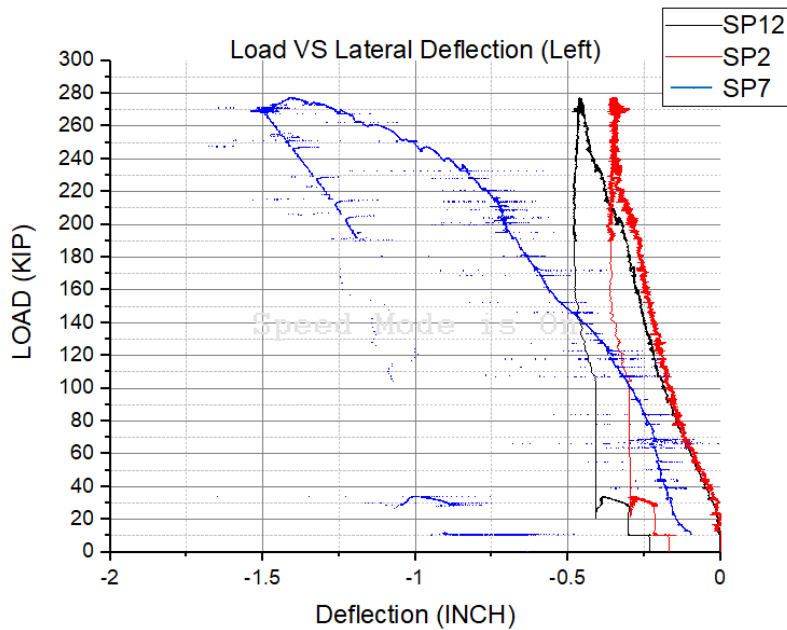


Figure 59e: Load VS Left-horizontal Deflection

FIGURE 59: LOAD-DEFORMATION PLOTS FOR JZ120-16-3

The names of the string potentiometers and their locations are shown in **Figure 51a** in Chapter 3. According to **Figure 59a**, **Figure 59b**, and **Figure 59c**, the vertical deflections at the middle of the top flange, for example, SP6, are more than the deflections of the bottom flanges (SP9 and SP10). This indicates that there

was some local deformation of the webs or the flanges, and the specimen developed transverse stresses since the specimen was braced laterally. The difference between the deflections of the bottom flanges (SP9 and SP10) was due to the fact the the cross-section was not perfectly symmetric because of the interlocks at the ends as presented in **Figure 16**. This non-symmetry caused the cross-section to twist a little during the test. The difference in the horizontal displacements on each side of the cross-section, SP7 and and SP8 in **Figure 59d** and **Figure 59e**, confirms that the cross-section moved laterally due to the non-symmetry. The vertical and horizontal deflections at the midspan are more than those of the lateral bracing locations, which is in accordance with the structural analysis of a simple beam.

Figure 60 shows a permanently deformed specimen after the test. It is obvious that the cross-section was deformed and closed more in the middle region, where the specimen was directly loaded by the air bladder. There is also some clear pattern of local buckling at the midspan on the right side of the cross-section shown.



FIGURE 60: DEFORMED JZ120-16-3 SPECIMEN AFTER TEST

Specimen Load VS Local Stress Data

As outlined in Chapter 3, one of the three specimens in a test configuration had 16 strain gauges installed according to the instrumentation plan shown in **Figure 51c**. The load vs. local stresses for JZ120-16-3 are plotted in **Figure 61** (all other data for other test groups are shown in Appendix C.3). The negative sign for the longitudinal stresses indicates that they were in compression, which is reasonable since the strain gauges were installed on the top flanges. The difference in the signs of transverse stresses shows the local direction for the state of stresses between the top and the bottom of the cross-section as shown in **Figure 61b**. As mentioned previously, the transverse stresses were caused by the combination of transverse bending stresses and axial stresses on each of the flanges or webs. All the longitudinal strain gauges show values exceeding the yield strain, which is 2000 micro-strains, meaning that the cross-section was fully yielded during the test.

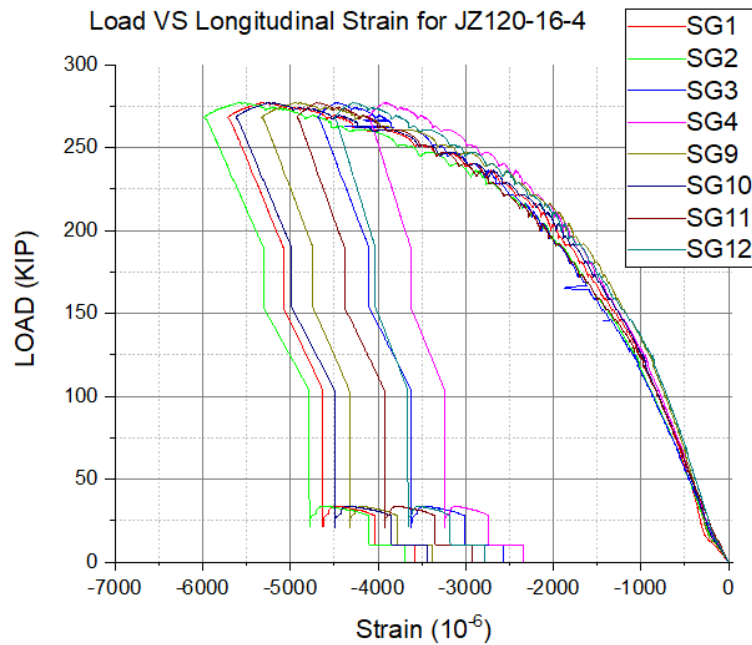


Figure 61a: Load VS Longitudinal Stress

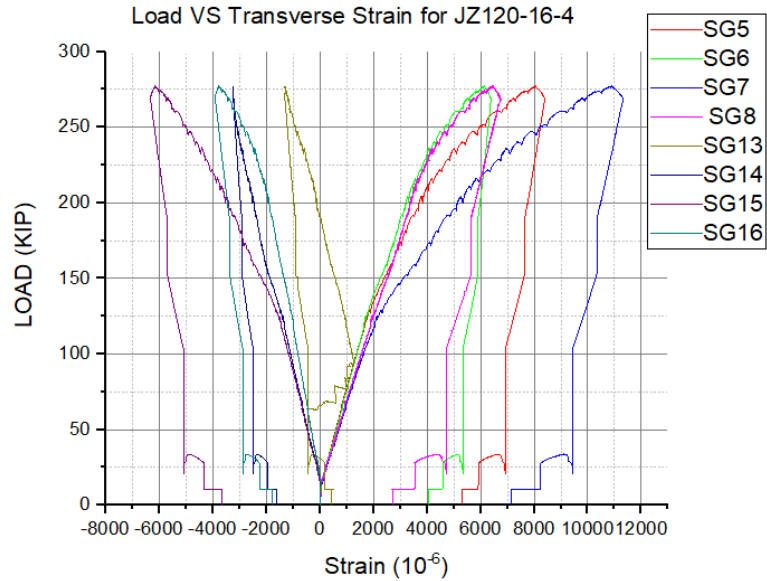


Figure 61b: Load VS Transverse Stress

FIGURE 61: LOAD VS LOCAL STRESSES FOR JZ120-16-3 SPECIMEN

Load and Vertical Midspan Deflection Responses in a Test Group

From the individual test data, the midspan deflections (SP6) of all the three specimens in a test group can be compared in the same plot. **Figure 62** shows the load and vertical deflection in the same plot for each test group. The difference in the plots is caused by the actual material properties of each specimen, which will be investigated and normalized by the result from the tensile coupon tests in Chapter 5. Most test groups could reach their highest load; however, 35-ft XZ95 specimens experienced a new limit state, which is the buckling of the middle interlock of the cross-section. This incident prevented the sheet piling configuration from achieving their maximum capacity, which will be discussed further in Chapter 5.

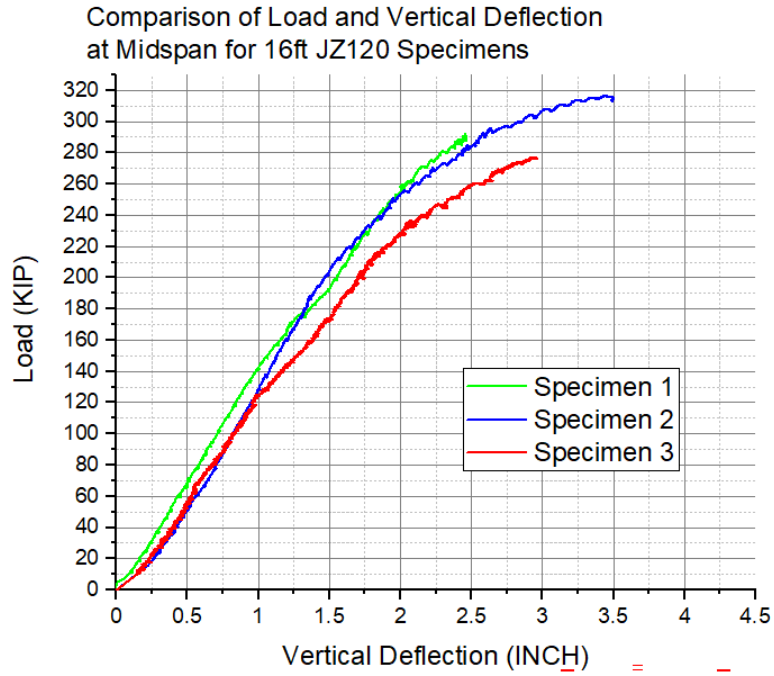


Figure 62a: JZ120-16

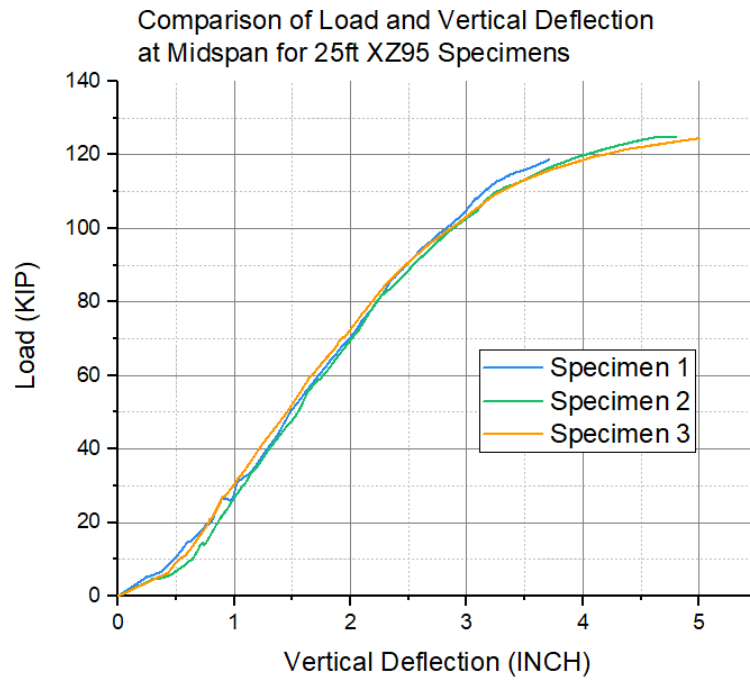


Figure 62b: XZ95-25

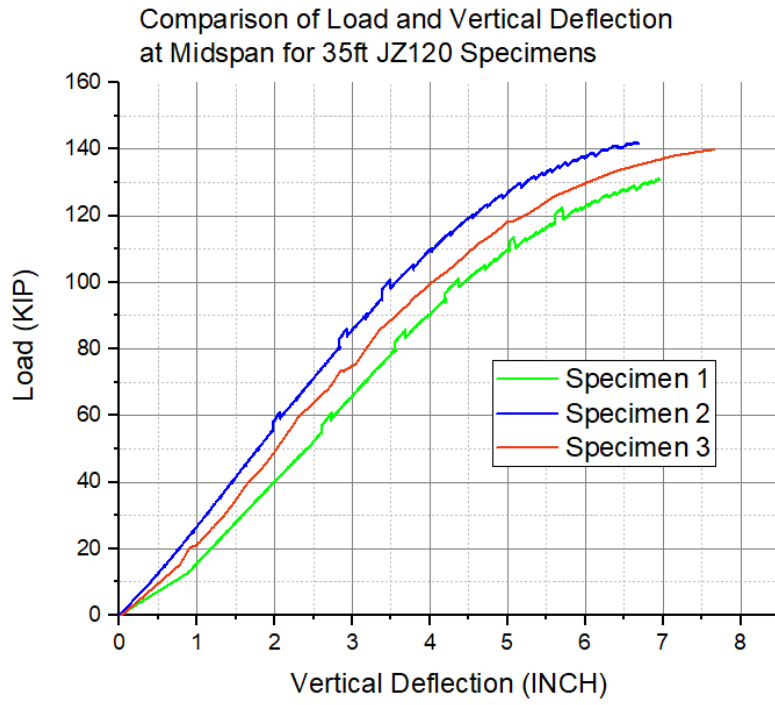


Figure 62c: JZ120-35

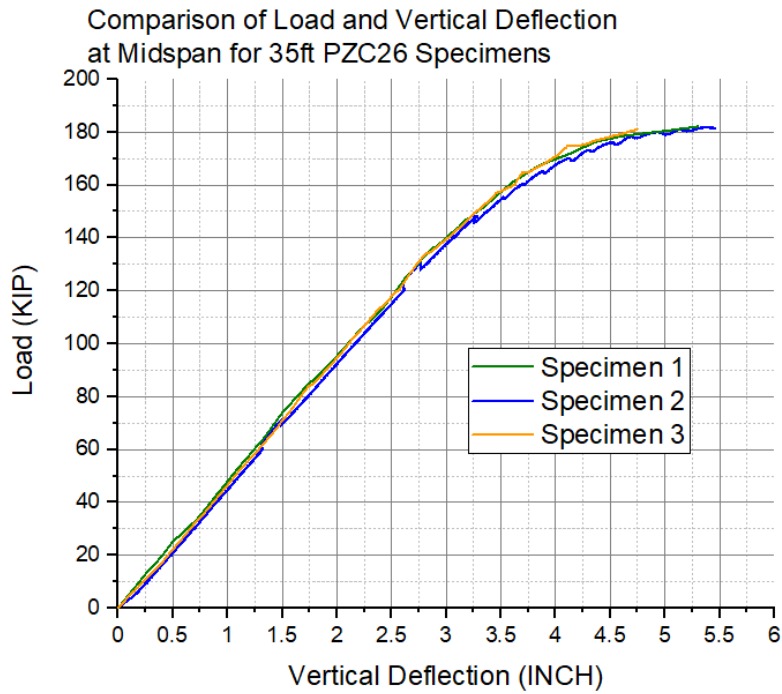


Figure 62d: PZC26-35

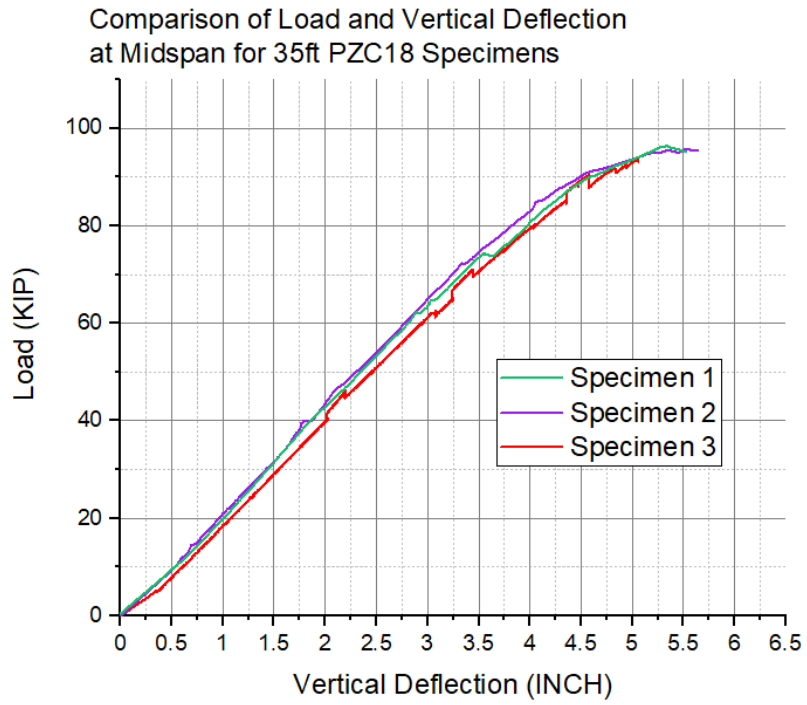


Figure 62e: PZC18-35

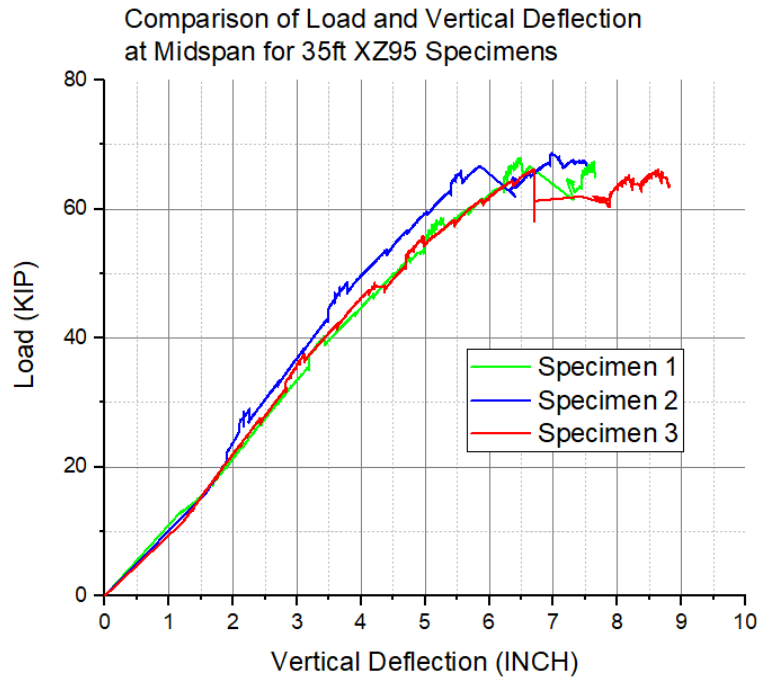


Figure 62f: XZ95-35

FIGURE 62: LOAD VS MIDSPAN DEFLECTION FOR ALL SPECIMENS IN A TEST GROUP

Tensile Coupon Results

After a test was done, four tensile coupons were cut from the specimen to investigate the actual material properties. Then, the corresponding yield stress obtained from the tensile test were used for normalizing the moment responses of each specimen in order to make the comparison more meaningful on the same scale. In this part, an example of load-displacement curves for a tensile coupon and the final average result for all sheet piling specimens will be presented. The tensile tests were conducted using a universal testing machine. The displacement was recorded by an electronic extensometer attached to the coupons with the gauge length of eight inches, and the sensor was removed prior to the failure of the coupons to prevent damage. The test setup before and after the test is illustrated in **Figure 63**.

From the recorded load and elongation data, the stress and strain can be computed using the undeformed area at the reduced section and the undeformed gauge length, respectively. The next step is to plot a stress-strain curve. According to the American Society for Testing and Materials standard E6 (ASTM, 2016), yield stress can be determined by finding the intersection between the stress-strain response and the linear line from 0.2% offset strain parallel to the linear portion of the response. The ultimate strength can also be found directly from the maximum stress in the response. **Figure 64** demonstrates the stress-strain curve (shown in blue) for the tensile coupon cut from the right top flange of JZ120-16-2. The orange line is the 0.2% offset strain, where the intersection to the blue line is the yield stress. In the figure, the yield stress and the ultimate stress of the tensile coupon are 56.2 and 67.1 ksi.



FIGURE 63: TENSILE COUPON TEST SETUP

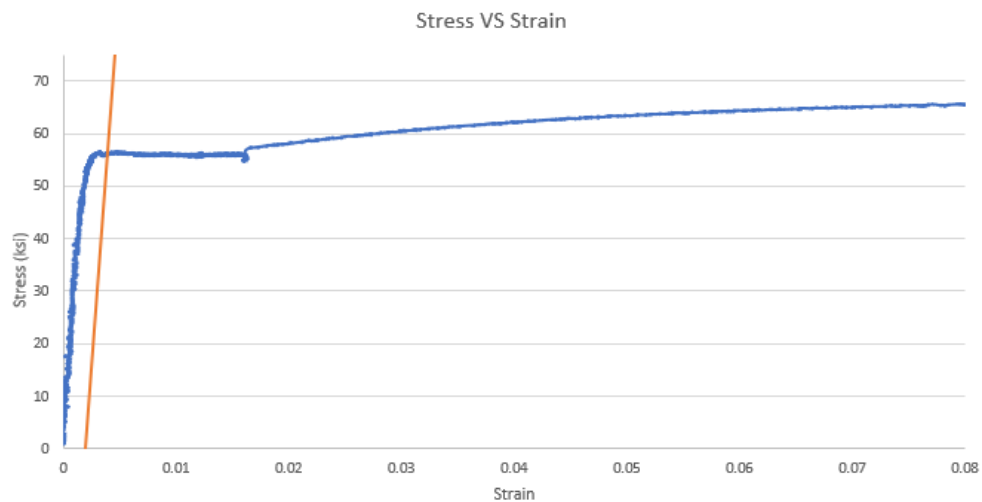


FIGURE 64: EXAMPLE OF STRESS-STRAIN RELATIONSHIP FOR TENSILE COUPON TEST

The stress results for all the coupons were determined with the same procedure discussed above. Once all the tensile coupon tests completed, all the tensile results from a sheet piling specimen were averaged to determine the representative values of the specimen, which will be used for normalizing the moments later.

Table 13 summarizes the tensile coupon results of all sheet piling specimens. The individual coupon results are included in Appendix C.4.

TABLE 13: TENSILE COUPON RESULTS

Type	Test Group	Specimen No.	Yield Stress (ksi)	Ultimate Stress (ksi)
Cold-formed Sheet-piling	JZ120-16	1	57.2	68.2
		2	55.5	67.1
		3	51.7	63.9
	XZ95-25	1	58.1	69.7
		2	56.3	68.9
		3	55.0	69
	JZ120-35	1	56.5	67.4
		2	58.2	69.4
		3	57.7	68.9
	XZ95-35	1	57.8	69.5
		2	58.4	70.2
		3	58.1	69.8
Hot-rolled Sheet-piling	PZC18-35	1	57.2	69.7
		2	57.1	70.1
		3	58.1	71.0
	PZC26-35	1	62.7	74.2
		2	62.5	77.6
		3	61.8	77

CHAPTER 5: Discussion

5.1 General Behavior

General Behavior

Overall, the tests went well with some minor issues that were resolved after the very first tests. The pre-tensioned bolts that connected the specimens to the bearing plates performed as expected without failure. The vertical rollers, which braced the spreader frame, had experienced some movement at the very first specimens. Still, the problem was solved due to the improvement in their connections and locations. The air bladder could resist the pressure during the test and expand fully to fill the space between the specimen and the loading frame. Nevertheless, after the air bladder was used a few times, there was some air leaking sound. The leakage started from the joint of the fabricated bladder. The first air bladder, which made of nylon-reinforced coated fabric, blasted. Then, the new material, Kevlar, which is much stronger, was used to fabricate a new bladder. However, the leakage issue had not solved. As a result, the bladder was reinforced especially at its joints, and the longer 25-ft and 35-ft spans were tested to reduce the amount of pressure. There were some loud noises during some of the tests, which originated from the bolts' slippage or some local buckling of the interlock of the specimens.

The elastic deflection calculated for JZ120 specimens with a 16-ft span length was approximately one inch. This means, theoretically, at first yield, the vertical deflection would be around that number. Before the first test started, this was expected behavior. However, according to the longitudinal strain data for JZ120-16-3 shown in **Figure 61a**, the sheet piling specimen reaches the yield strain (2000 micro-strains) at around 200 kips, which is lower than the target load of 282 kips. The load-deflection response in **Figure 62a** shows the displacement of 1.75 inches, which is also higher than the calculated value of 0.75 inches. At the maximum load, the specimen reached more than three inches of deflection. This indicates that the specimens were yielded earlier before the theoretical yield load and were loaded far beyond the yield point.

It also reinforces the assumption that transverse stresses have an impact on the behavior of the sheet-pilings under flexure. The influence of these stresses will be discussed further in Chapter 5.2.

The maximum load shown in **Figure 62** occurs when a cross-section was fully yielded, where the vertical load-deflection curves become flat. The transverse stresses were established from the local buckling of the flanges or webs since the cross-sections were braced laterally from spreading. This point can be confirmed from the displacement data shown in **Figure 59d** and **Figure 59e**, in which the horizontal deformations occur. **Figure 61b** indicates that most of the transverse strain gauges were yield as well. Despite these deformations, the interlocks between the cross-sections were not separated.

Applied Load and Air Bladder Pressure Relationship

The applied load and pressure plots demonstrate the relationship between the hydraulic ram load and air bladder pressure. Examples of the plots are shown in **Figure 58** (the rest are included in Appendix C.1). It is obvious that most of the load-pressure plots are off from the target load and pressure lines, which were given from the analysis(NBM, 2016). However, the plot for JZ120-16 is precisely on the target line. There are a couple of reasons for this behavior. First, the actual dimensions of the air bladder were designed to fit with the shape of the JZ120 profile. Since the bladder was considered flexible, it was used for the other cross-section and some differences from the target curves. Second, how close the actual relationship to the target line depended on how well the air bladder fully contacted the whole sheet-piling cross-section. From the analysis that provided the target load and pressure by NBM, the cross-sections were fully loaded along the top surface. However, in the actual tests, the air bladder did not fully contact the webs, and the bottom flanges all the time. In the beginning, when the bladder pressure was low, and the bladder was not much-expanded, it fully contacted the top surface of the cross-section. As a result, the initial part of the load-pressure responses is identical to the target lines. On the other hand, when the pressure increased, the air bladder expanded more and floated up from the bottom flanges. **Figure 65** illustrates the behavior of the air bladder when the test reached a higher load. It is clear that the bladder does not contact the bottom flanges and does not contact some bottom part of the webs. This results in the load-pressure curves that are

slightly off from the target lines. In other words, when the contact area is less, more pressure is required to get the same load.



FIGURE 65: AIR BLADDER BEHAVIOR UNDER HIGH LOAD

Another reason that affects how close the actual load-pressure curve to the target line is the sheet pile's stiffness. Specimens with shorter span length had more flexural stiffness, which resulted in the less vertical deflection. This made the air bladder contacts the top surface better since it was pressed against a stiffer surface. For all the reasons discussed above, that why the load-pressure relationships for 16-ft JZ120 specimens are identical to the target line. In contrast, others are similar to the targets at the beginning and are slightly off at a higher load.

All specimens needed to reach higher loads more than the target load to achieve their maximum capacity. For instance, PZC18-35 specimens reached a maximum load of 115 kips, which was 26% higher than the target load of 91.2 kips. Similarly, JZ120-16 specimens achieved 315 kips, which was 12% more load than

its target load calculated. As mentioned previously, the target load was calculated at the yield moment (or first yield) of the cross-section. Therefore, in order to obtain the capacity of the cross-sections, where the specimens were fully yielded, more loads were applied. The load added depended on the cross-section and the span length. The capacity of the cross-sections occurred when the load-deflection curves became flat.

For these reasons, using the pressure data was not an accurate way to calculate the moments on the sheet piles and to study their maximum capacities. Instead using the load data measured at the ram were more appropriate. However, having a reduction in the contact area did not change the fact that the shorter span length need more amount of load to achieve the moment strength. The research team studied the influence of the different amount of lateral loading on the maximum moment capacities. The amounts of the lateral loading on different span lengths were not similar whether there was the reduction in the contact area or not.

Interlock Buckling Limit State

Sheet-piling is made of two pieces of steel plate hot-rolled or cold-formed into a shape. Both sides of the cross-section are connected at the middle interlock. The research team called the event when the interlock at the middle buckles or rotates immediately along the longitudinal axis of the sheet pile “Interlock Buckling”. This limit state is uncommon. The event made the top flanges bent along the axis and causing a loud noise. This limit state resulted in some drop in load, as shown in the load-deflection curves of XZ95-35 specimen plotted in **Figure 62f**. The same behavior occurred during all three tests for XZ95-ft specimens at very similar load and vertical deflections of around 60 to 65 kips and six to seven inches. **Figure 66** shows the shape of the top flanges for an XZ95-35 specimen after the event. It is obvious that both top flanges bent toward each other along the interlock, and they were no longer horizontal.



FIGURE 66: INTERLOCK BUCKLING OF XZ95-35

After the interlock buckled, the specimens were loaded more, and they obtained a similar amount of load before the buckling event, where the specimens reached their highest load and the test finished. The loads dropped from this incident were approximately 5 kips. In other words, the interlock buckling limit state prevented the sheet piles from achieving at least 5 kips higher capacity for 35-ft XZ95 specimens. **Figure 67** shows strain gauge data for XZ95-35-3. The interlock buckling results in 0.2-0.3% increase in local strains in both longitudinal and transverse directions. The amounts of strain increased due to the buckling are significant compared to the specimen deforms' total strains. This event prevented the XZ95-35 specimens from achieving their target load.

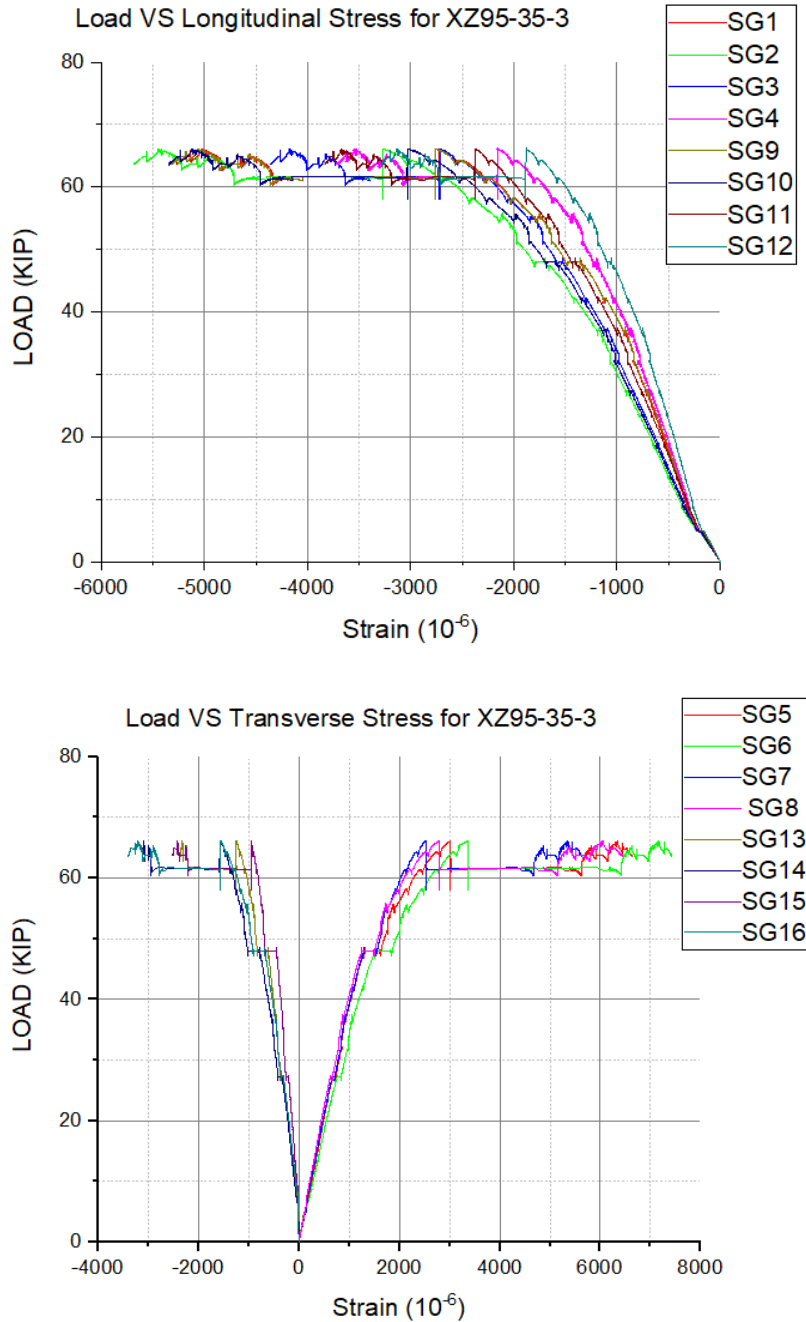


FIGURE 67: STRAIN GAUGE DATA FOR XZ95-35-3

However, the test of the same cross-section with 25-ft span length experienced no interlock buckling. The specimens were tested to around 120 kips of load and five inches of vertical deflection. Even though the tests ran to a higher load, their maximum deflections were still less than the point where the interlock buckling happened, which was around six to seven inches. Therefore, this limit state could be considered

deflection-controlled. However, since the event was uncommon and beyond the scope of the project, further research on the interlock buckling is still required to confirm this point.

Interlock buckling occurred only for 35-ft XZ95 specimens. The tests for JZ120-35, which was also cold-formed and had the same shape of the middle interlock as shown in **Figure 16**, exceeded both load and deflection at XZ95-35's buckling, but the event did not happen. The reason is that JZ120 is a larger cross-section with 1.4 times more sectional modulus and 1.7 more moment of inertia according to the properties presented in **Table 2**. A JZ120 specimen with a span length longer than 35-ft may experience this limit state if the sheet pile is subjected to larger deflection. However, the maximum deflection of 7.5 inches for JZ120-35 was still capable for cross-section to reach its capacity. The tests for the hot-rolled cross-sections, PZC18-35, and PZC26-35, which has a different shape of interlock, finished at the maximum deflection of 5.5 inches without interlock buckling according to the load-deflection data from **Figure 62d** and **Figure 62e**. Therefore, these two cross-sections work well within this 35-ft configuration but interlock buckling could also occur if the span length is longer.

The interlock buckling of XZ95 would be a factor that prevents the cross-section from reaching the same capacity of PZC18 although they have similar sectional modulus. A comparison between both cross-sections will be made later in this chapter to investigate the effect of the interlock buckling on the performance of the cold-formed and hot-rolled sheet pilings.

However, the four-point bending tests on the same XZ95 cross-section did not experience the interlock buckling (NBM Technologies, 2017). There were a couple of reasons that would prevent the specimens from having this limit state. First, according to **Figure 35**, the maximum deflection for XZ95 specimens is 3.2 inches, which is less than 5.8 inches of the buckling deflection in the uniform pressure test. Second, the loading method was also different. The four-point bending was conducted by applying the load on the steel rollers placed on the top flanges of the specimen (See **Figure 30**). Unlike the rollers, the air bladder was flexible. The vertical components of the pressure applied to the specimens could bend the top flanges to

rotate toward each other around the middle interlock. For these reasons, the interlock buckling occurred in the uniform pressure test but not in the four-point bending test.

In the application, the interlock buckling is uncommon. The difference between the actual configuration and the test setup in the laboratory would be a factor isolating the limit state. In the reality, a sheet piling member is continuously braced from spreading not only by the adjacent members connected at the interlocks but also by other sheet piling wall components. For example, a beam member, also known as a wale, is connected to the sheet piling members horizontally along the wall length. However, in the laboratory, there were some discrete locations of the lateral bracings. Thus, the sheet piles in the wall system have more lateral stiffness, making them harder to experience the interlock buckling.

5.2 Moment-deflection Responses

Moments can be computed from the load data obtained from the tests since they were more accurate than the pressure data as discussed in Chapter 5.1. Structural analysis of the sheet piling beam subjected to a uniform load partially distributed on the span was used. A calculation aid is presented in AISC – Steel Construction Manual (AISC, 2017) shown in **Figure 68**. In this case, the maximum moment occurs at the midspan, which corresponds to the maximum vertical deflection at the same location.

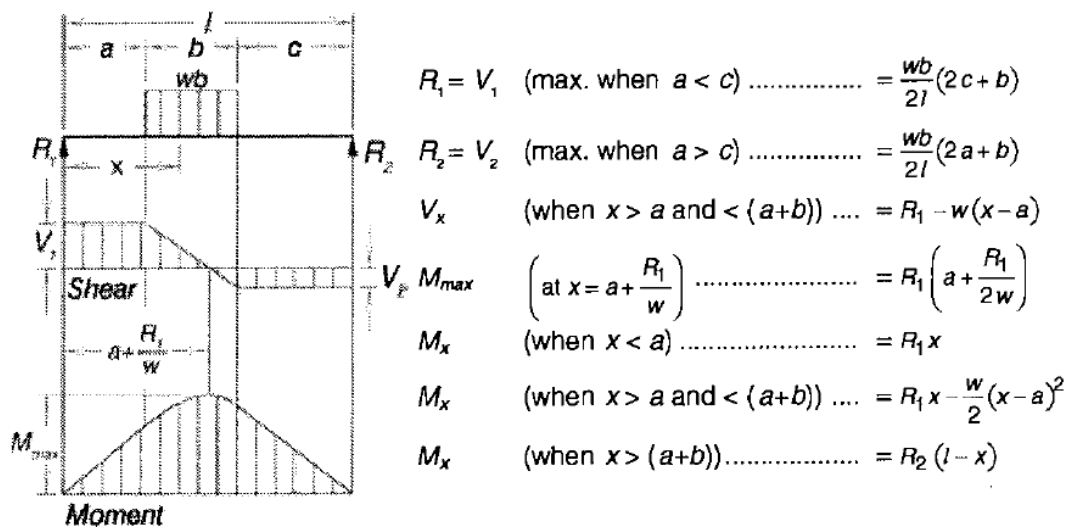


FIGURE 68: CALCULATION AID FOR STRUCTURAL ANALYSIS OF TEST SETUP (AISC, 2017)

The yield moment and plastic moment can be determined from the sectional properties in **Table 2** with the specified yield stress, which are 50 ksi and 60 ksi for cold-formed and hot-rolled cross-section, respectively. Note that these moments were calculated based only on the vertical components of load projected on the width of the air bladder. **Figure 69** shows the moment-deflection curves for all the test groups. The curves were plotted from the actual test data, in which each specimen typically have higher material properties according to the tensile coupon results presented in **Table 13**. In contrast, the yield and plastic moments correspond to the constant specified yield stress.

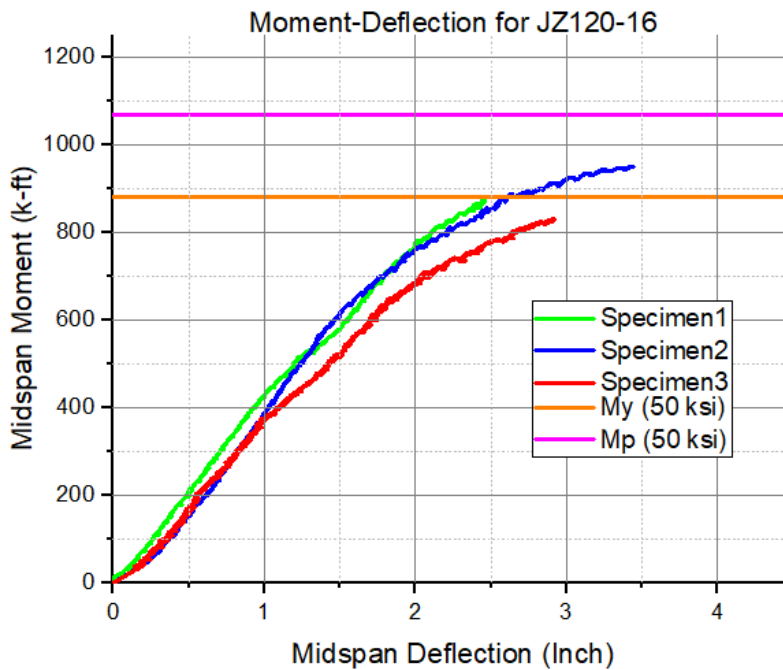


Figure 69a: JZ120-16

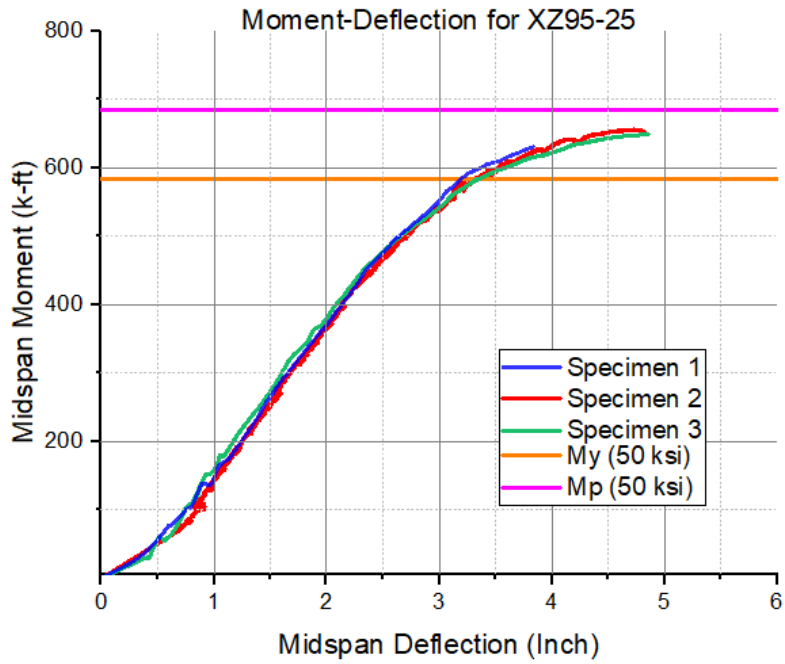


Figure 69b: XZ95-25

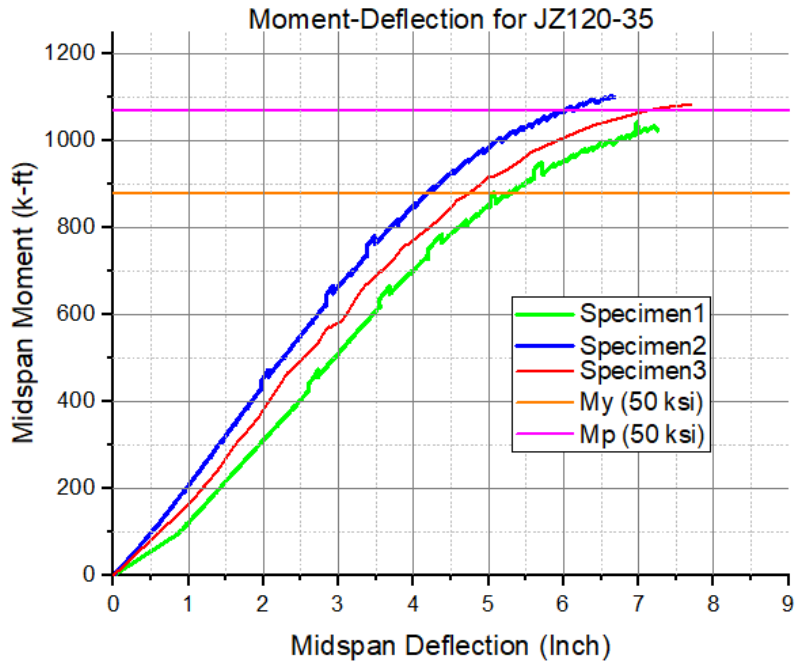


Figure 69c: JZ120-35

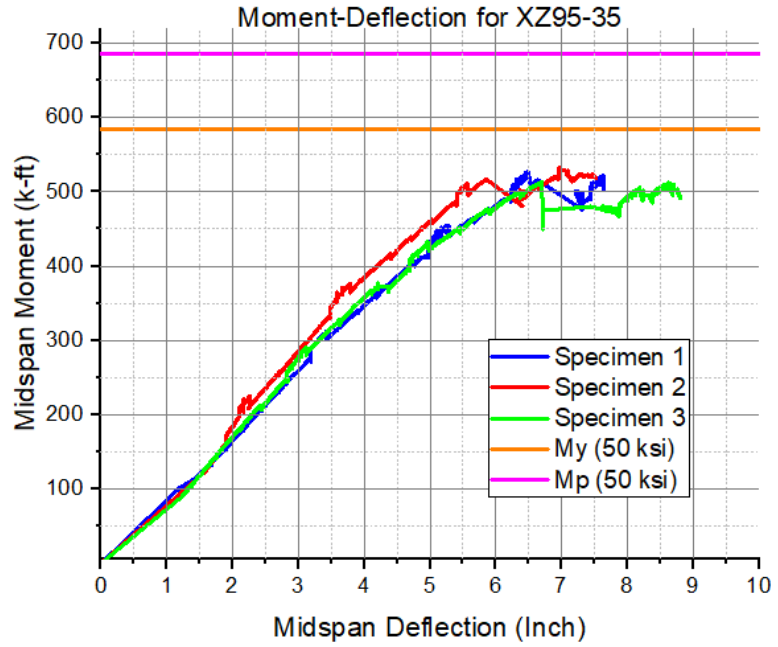


Figure 69d: XZ95-35

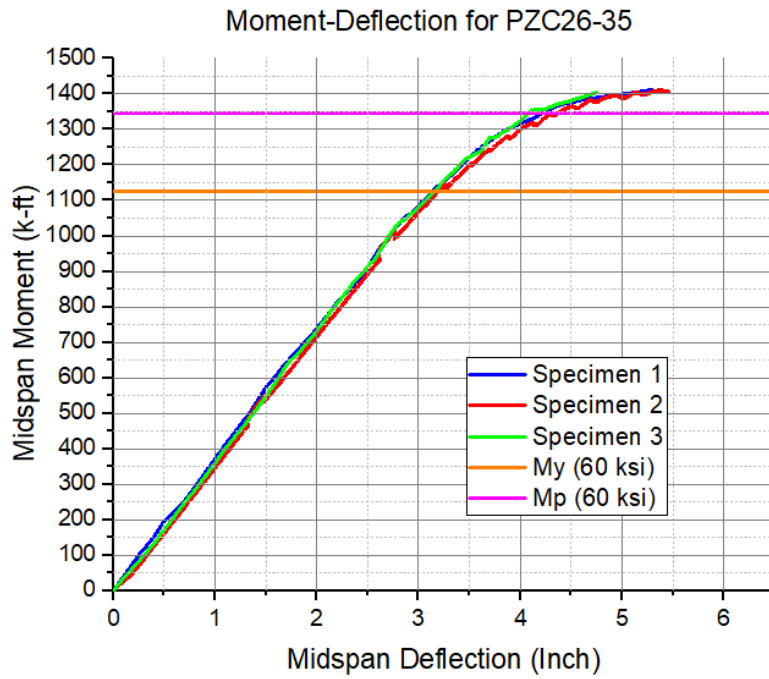


Figure 69e: PZC26-35

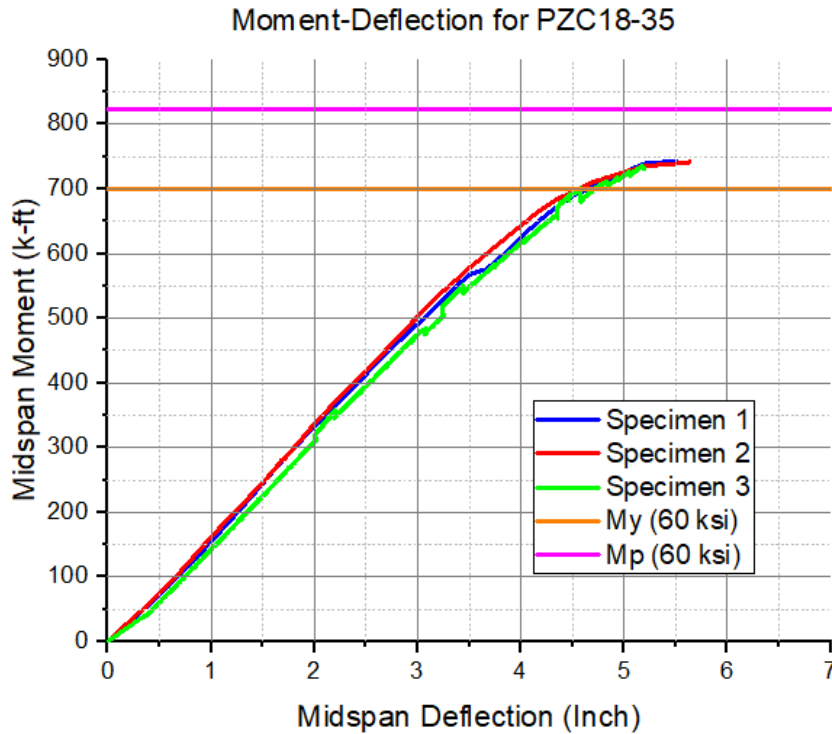


Figure 69e: PZC18-35

FIGURE 69: MOMENT-DEFLECTION RESPONSES FOR ALL SPECIMENS IN A TEST GROUP

Moment-deflection responses have similar shapes to the load-deflection curves. However, they better illustrate the cross-section behaviors because the curves are plotted in terms of moment related to the sectional properties. For the same cross-section, the load data could be different due to the span length, but the moment data are in the same order. In this project, there were some variations in the moment values of the same cross-section with different span length. For example, JZ120-16 has a maximum moment of 950 kip-ft, but JZ120-35 can reach 1100 kip-ft, according to **Figure 69**. This is the influence of transverse stresses, which are not equal for each span length. This point will be discussed further in Chapter 5.3.

It is evident that all the specimens started to yield earlier before reaching the specified yield moments since the curves were no longer linear. Beyond the linear parts, the responses became flatter, indicating that more of the cross-section experiences yield. Eventually, when the curves became horizontal, the entire cross-section was yielded. The lateral pressure from the air bladder or the transverse stresses made the cross-

section yield earlier and prevented the cross-sections from achieving their theoretical yield or plastic moments.

Moment-deflection responses are useful for preliminary analysis. They illustrate how much the capacity of the cross-sections are close to the specified yield moment and plastic moment. However, the actual yield stresses of material are typically more than the specified values. This means some cross-sections shown reaching either yield or plastic moments in **Figure 69** may not be accurate. Therefore, the curves need to be normalized by the corresponding tensile coupon results, which will be done later in this chapter.

5.3 Existence of Transverse Stresses and Their Effects on Flexural Behavior

Transverse stresses on sheet-piling originate from the lateral deformation of the cross-section. Not only can the uniformly distributed load cause the stresses, but point loads from the four-point bending test can create them as well. The study by NBM in 2017 on the same sheet-piling profiles with four-point bending showed that the transverse stresses exist according to the strain data shown in **Figure 40**. The stresses prevented some cross-sections from achieving their plastic moment. However, the loading method in 2017 did not represent the actual loading configuration in the sheet-piling application. This issue was the motivation for this new project.

The amount of transverse stresses that occurred during the tests was very significant. To illustrate, the local strain data presented in **Figure 61** for JZ120-16-3 shows that the maximum longitudinal strain in compression is 6000 micro-strain, while the minimum transverse strain is even more than four times of that value. Other strain data included in Appendix C.3 are also significant. Therefore, the effects of transverse stresses on the flexure behavior of the sheet-piling need to be considered.

Transverse stresses accelerated the first yield of the cross-section. According to the longitudinal strain data of JZ120-16 specimens in **Figure 61a**, the specimen reaches the yield strain at 200 kips and 48 psi, which are significantly lower than the given target load and pressure of 282 kips and 63 psi. Another example is the XZ95-35 data plotted in **Figure 67**, the specimens start yielding at around 60 kips, but the calculated

target load is 77 kips. This indicates that the existence of transverse stresses makes the cross-section yield earlier. Transverse stresses also prevented some cross-sections from obtaining its theoretical plastic capacity. This point shown in the normalized moment-deflection responses, which will be analyzed in Chapter 5.4.

5.4 Normalized Moment vs. Deflection Responses

Normalized moment-deflection responses were essential for all the comparisons made in this project. The tensile coupon results presented in Chapter 4 showed that the material's actual yield stress was typically more than the specified yield stress. Normalization of moments helped compare all specimens in a test group, specimens with different span lengths, and hot-rolled and cold-formed cross-sections more meaningful. The normalized curves for all the test groups indicate whether the cross-section can develop their yield moment or plastic moment. A direct comparison between the same cross-section with different span lengths can be made. The performance between hot-rolled and cold-formed specimens can be examined. The moment-deflection curves were normalized by the corresponding yield stress of each specimen. The yield moment and plastic moment were also normalized to the specified yield moment calculated from the sectional properties and the specified yield strength to be 1.0 and around 1.2 respectively. **Figure 70** presents the normalized moment-deflection responses with their yield and plastic moments for all specimens in a test group.

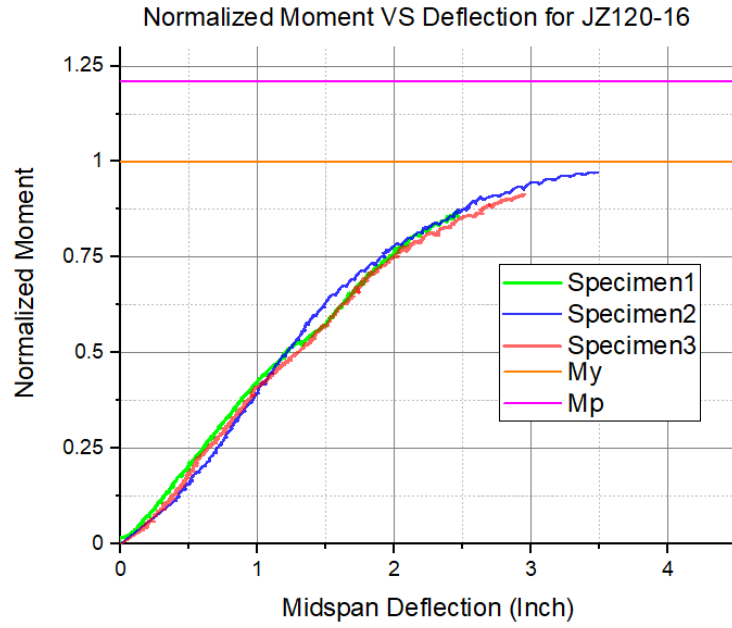


Figure 70a: JZ120-16

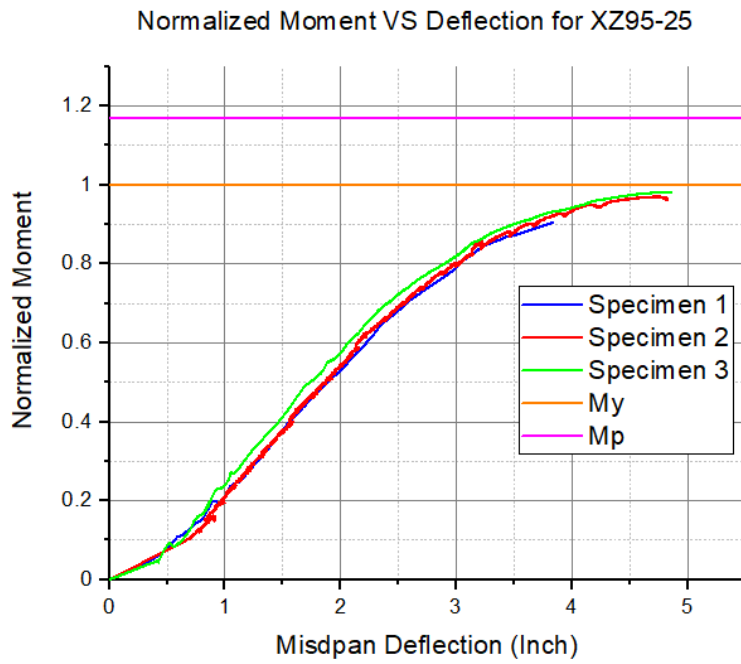


Figure 70b: XZ95-25

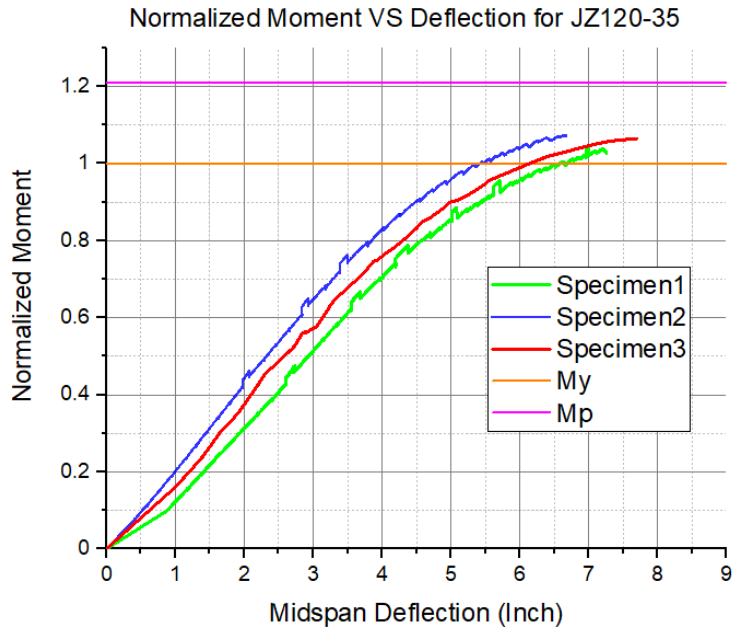


Figure 70c: JZ120-35

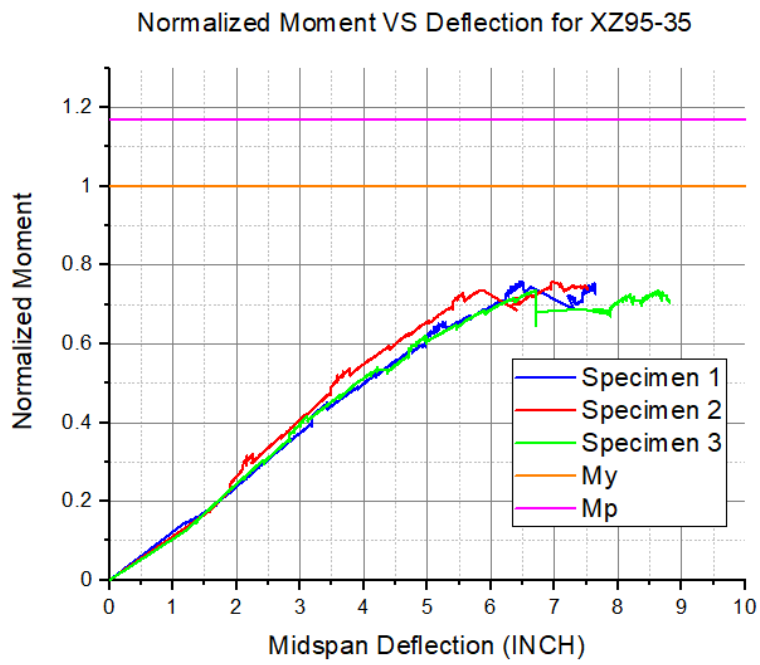


Figure 70d: XZ95-35

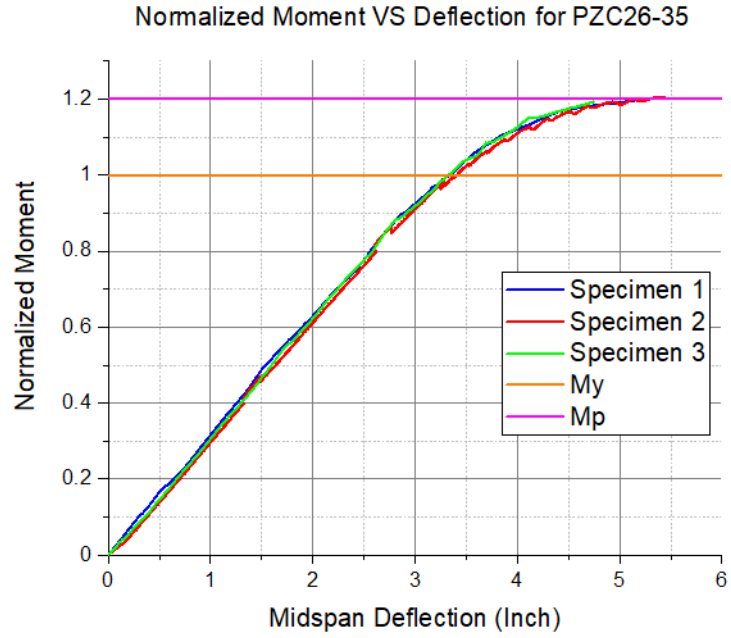


Figure 70e: PZC26-35

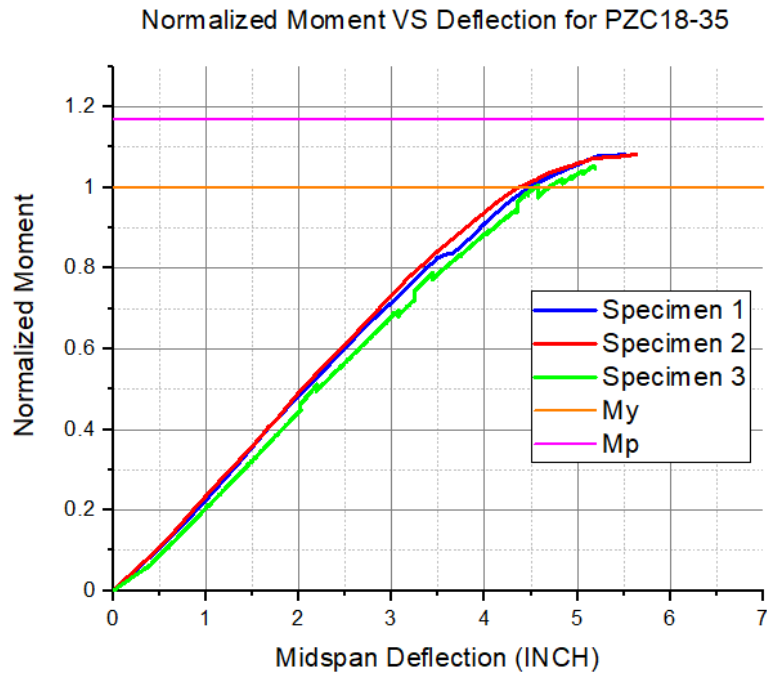


Figure 70f: PZC18-35

FIGURE 70: NORMALIZED MOMENT-DEFLECTION RESPONSES OF ALL SPECIMENS

According to the normalized moment-deflection responses shown in **Figure 70**, all specimens' curves in a test group become more identical (closer to each other than the original moment-deflection plots). The plots still confirm that the cross-sections started to yield earlier due to the existence of transverse stresses, making JZ120-16, and XZ95-25 no longer reach their yield moments. JZ120-35 and PZC18-35 specimens can develop the yield moments, but they cannot achieve the full capacity, which is the plastic moments. This reinforces the influence of transverse stresses mentioned in Chapter 5.3 on the flexural behavior. The stresses accelerate the first yield to occur, resulting in lower actual moment capacities compared to the theoretical values. The XZ95-35 specimens experienced interlock buckling, which the event prevented them from obtaining higher moment capacity.

However, from **Figure 70**, only PZC26-35 specimens achieve the plastic moment. This cross-section has the largest and tallest dimensions of all with the highest thicknesses as presented in **Figure 16**. As discussed previously, the air bladder did not fully contact the top surface when it expanded more. For the tallest cross-section, this behavior makes the contact surface even less, resulting in less amount of lateral loading. Furthermore, PZC26 has the highest thicknesses of the webs and flanges which help resist transverse bending better. These reasons help the cross-section to obtain its full capacity. **Table 14** summarizes the ratio of the maximum moment capacity to the yield moment and the plastic moment for all test groups.

TABLE 14: RATIO OF MAXIMUM MOMENT TO YIELD AND PLASTIC MOMENTS

Test Group	Maximum Moment	My	Mp	M/My	M/Mp
JZ120-16	0.97	1.00	1.20	0.97	0.81
XZ95-25	0.98	1.00	1.17	0.98	0.84
JZ120-35	1.07	1.00	1.20	1.07	0.89
XZ95-35	0.76	1.00	1.17	0.76	0.65
PZC18-35	1.08	1.00	1.17	1.08	0.92
PZC26-35	1.20	1.00	1.20	1.20	1.00

From the table, JZ120-35 and PZC18-35 exceed the yield moment at 7% and 8% higher, while only the PZC26-35 test group achieves the plastic moment. JZ120-16 and XZ95-25 achieve 97% and 98% of the yield moment. The longer JZ120 specimens can reach the yield moment. This trend should happen with

XZ95-35 specimens as well; however, the interlock buckling limit state prevented them from doing so. The effect of span length will be further evaluated in Chapter 5.5.

Four-point bending tests on the same sheet-pilings were conducted by NBM in 2017. This loading method established point loads on the specimens, which did not simulate the actual application's true loading configuration. In reality, sheet-piling members are used as a retaining wall subjected to soil or water pressure. The new experiment in 2020 was designed to account for this issue. **Figure 71** compares the normalized moment-deflection curves obtained from four-point bending tests (**Figure 70a**) and uniformly distributed loading tests (**Figure 70b**). The cross-section tested is JZ120 with the same 16-ft span length. **Figure 70a** shows that the cross-section can develop the yield moment and almost reach the plastic moment with the maximum capacity of 1.18 times M_y .

On the other hand, the same JZ120-16 sheet pile with lateral loading could not even achieve the yield moment at $0.97M_y$. The reduction in the flexural strength is due to the increase in transverse strains obtained from the new test setup as shown in **Figure 72**. The numbers in orange are the maximum strain data in micro-strains. It is obvious that the amounts of transverse strains for both tension and compression in the new study are more than four times the strains obtained from the previous project. This causes the maximum moment to decrease by $0.21M_y$, which is very significant. Therefore, this reduction in the flexural capacity needs to be accounted for in designing a sheet piling wall.

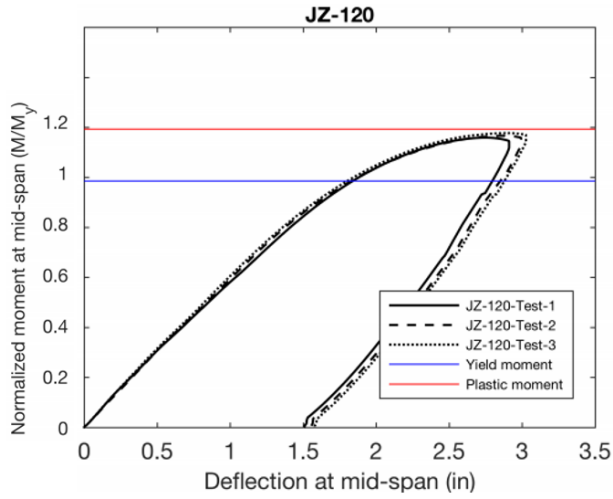


Figure69 a: Four-point Bending Result

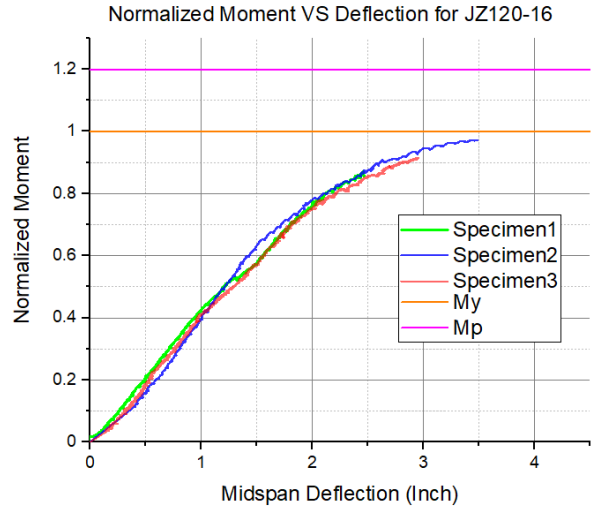


Figure69b: Uniform Pressure Result

FIGURE 71: COMPARISON ON CAPACITIES OF JZ120-16 TESTS FROM NBM (2016) AND VT (2020)

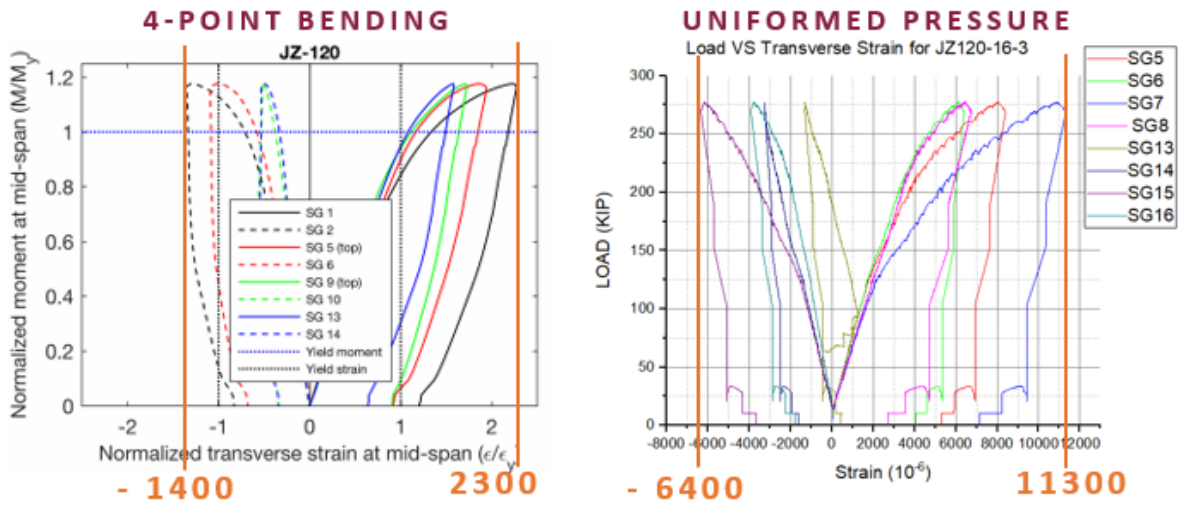


FIGURE 72: COMPARISON ON TRANSVERSE STRAINS OF JZ120-16 FROM NBM (2016) AND VT (2020)

5.5 Effect of Span Length to Moment Capacity

Span lengths affected the amount of load required to reach the same moment and affect the number of transverse stresses established on the sheet-piling specimens. According to the simulation (NBM Technologies, Inc., 2016), specimens with varied span lengths have a different amount of transverse stress to longitudinal stress ratio (see **Figure 24**), which leads to variation in flexural performance. This experiment's results also confirm the influence of the span length on the number of transverse stresses and its effect on the moment capacity. **Figure 73** compares the normalized moment vs. normalized strain curves of JZ120 with 16-ft and 35-ft span lengths.

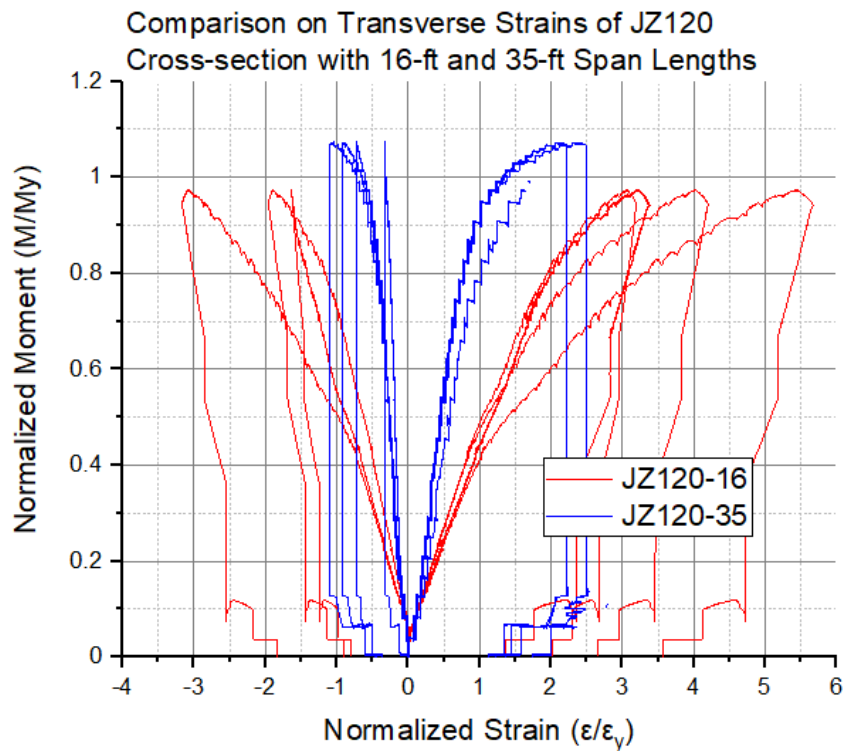


Figure73a: Transverse Strains

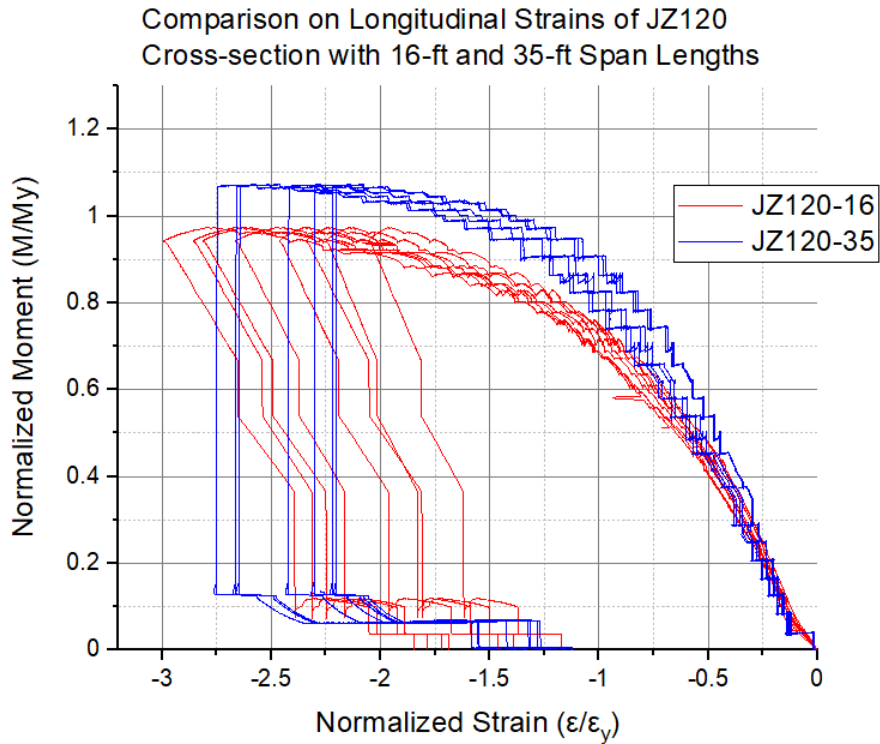


FIGURE 73: COMPARISON ON TRANSVERSE STRESSES OF JZ120-16 AND JZ120-35

Figure 73a clearly shows that when the span length increases, the amount of transverse strains decreases significantly. For instance, the maximum tensile stress for 16-ft span length is reduced from 5.6 times the yield strain to 2.5 times the yield strains for 35-ft span length, which is more than two times lower. In fact, the different span length required different amounts of load to reach the same amount of the longitudinal moment. Without lateral loading, the moment on the cross-section would be the same. However, this difference in the total load on the span varied the amount of lateral loading, and then the transverse strains on the specimens. As a result, the moment capacities for different span lengths were no longer equal even though the maximum longitudinal strains for both span length are very close between -2.75 and 3 times the yield strains as shown in **Figure 73b**. The moment capacity is higher for the longer span. This well concludes the effect of lateral loading on the flexural capacity of the sheet piling.

From the discussion in Chapter 5.4, it is evident that the difference in the span lengths affects the maximum capacity of the cross-section. The normalized moment-deflection curves with different span lengths for JZ120 and XZ95 are compared on the same plot shown in **Figure 74**.

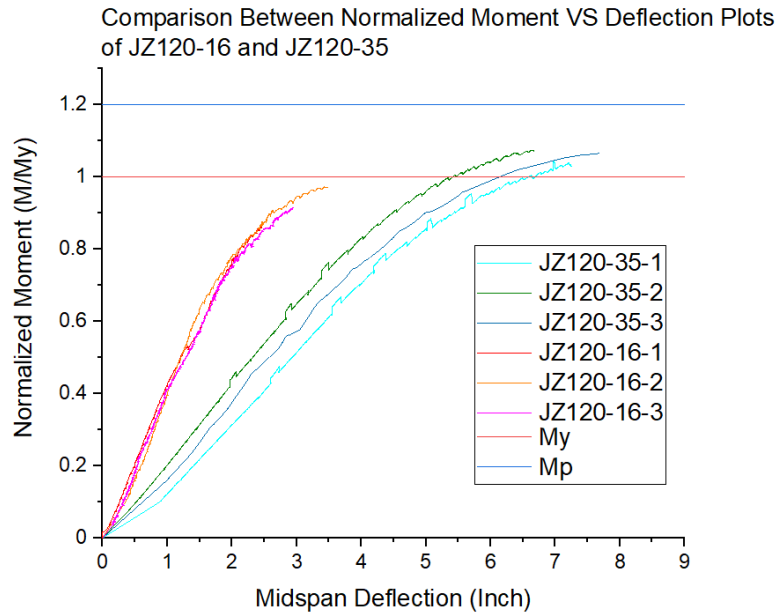


Figure 74a: JZ120-16 vs. JZ120-35

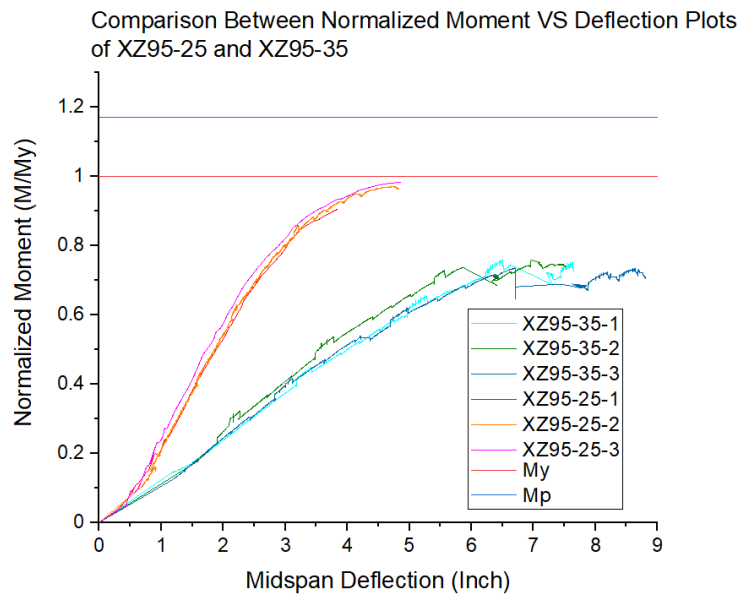


Figure 74b: XZ95-25 vs. XZ95-35

FIGURE 74: COMPARISON ON NORMALIZED MOMENT VS. DEFLECTION CURVES FOR DIFFERENT SPAN LENGTHS

The comparison of JZ120 tests in **Figure 73** and **Figure 74a** indicates that the shorter span length has more effect on transverse stress, resulting in less moment capacity. This finding reinforces the results from the finite element model by NBM (2016). However, for the XZ95's comparison, the interlock buckling limit state occurred during XZ95-35 tests, preventing the 35-ft span from having a higher capacity. The maximum capacity for the XZ95 profile is not only controlled by the span length, but also the interlock buckling. Thus, a longer span length may not always be better for a sheet pile considering there is another limit state that may apply.

5.6 Comparison between Hot-rolled and Cold-formed Sheet Piling

From the previous sections of Chapter 5, the performance of individual sheet-piling cross-sections, and the effects of their span lengths have been investigated. The normalized moment-deflection curves can now be used for the comparison between hot-rolled and cold-forms sheet pilings. JZ120 and XZ95 are hot-rolled, and PZC18 and PZC 26 are cold-formed. As outlined in Chapter 3, there are two pairs of cross-sections that have similar sectional modulus: JZ120 with PZC26, and XZ95 with PZC18. Theoretically, a flexural member with the same sectional modulus should have the same moment capacity when the yield strength is the same. Therefore, normalization of the moments to their corresponding material properties will make the comparison more meaningful and reasonable. The pairs of the equivalent cross-sections with the same span length, 35 ft, are compared on the same plot in **Figure 75**.

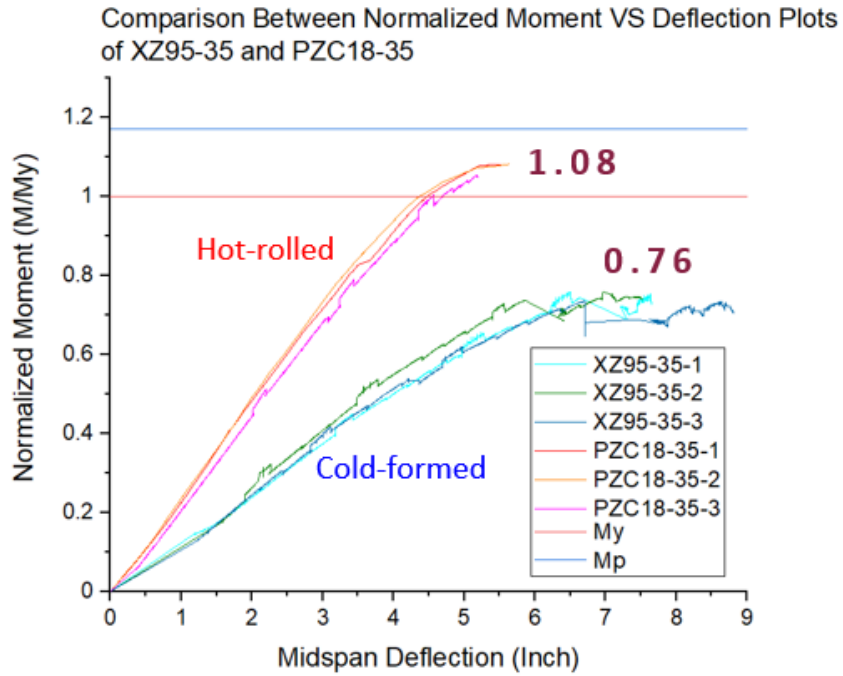


Figure 75a: XZ95-35 vs PZC18-35

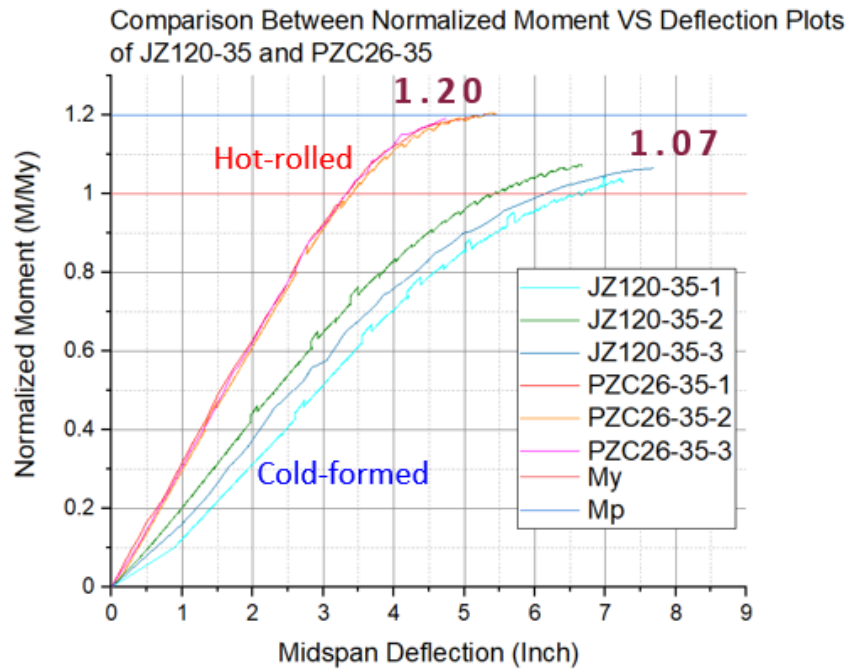


Figure 75b: XZ95-35 vs PZC18-35

FIGURE 75: COMPARISON ON NORMALIZED MOMENT VS. DEFLECTION CURVES FOR HOT-ROLLED AND COLD-FORMED SHEET PILING

The comparisons clearly show that, for this span length, the hot-rolled cross-sections have the higher flexural capacity. **Figure 75a** compares XZ95-35 and PZC18-35 and demonstrates that the interlock buckling plays an important role in the reduction of XZ95-35's maximum capacity. **Figure 75b** shows closer capacities of JZ120 and PZC26 cross-sections without the limit state, but the hot-rolled one has 13% of M_y more capacity. The deflections are different due to the moment of inertia values. According to **Table 2**, JZ120 and XZ95 cross-sections have 395.2 and 238.0 in⁴/ft, while PZC26 and PZC18 profiles have 428.2 and 256 in⁴/ft. The shape of the middle interlocks may affect the deflections as well since the midspan deflections were measured at the bottom of the interlock. The interlock buckling occurred in the cold-formed XZ95 tests, whereas the cold-formed PZC18 did not experience this limit state. Thus, the cold-formed's interlock might have more local deformation. All hot-rolled cross-sections also have more stiffness than the cold-formed ones due to the moment of inertia values and thicknesses. Higher stiffness values make the hot-rolled specimens have more resistance to both global and local deformation and rotation.

The simulation model results, shown in **Figure 19**, suggest that JZ120 had a little less capacity than PZC26, while the other two cross-sections were equivalent. The four-point bending results in 2017 suggested the equivalent results between all hot-rolled and cold-formed sheet piles as shown in **Figure 37**. However, in the uniform pressure tests, the existence of transverse stresses affects the flexural performance of the specimens. The interlock buckling limit state occurred during the tests in 2020 for the XZ95-35 cross-section, but it did not occur in the tests in 2017. Furthermore, even though the hot-rolled and cold-formed sheet piles have similar sectional modulus, the dimensions and thicknesses are not the same. Thus, the influence of transverse stresses on flexural behavior could be different. To investigate this point, the transverse strain data vs. moment of each pair of the equivalent cross-sections need to be compared. The moment values are normalized by the corresponding yield moment of the specimens, while the strains are normalized by the yield strain, which is 2000 micro-strains. The comparisons on both pair of the cross-sections are demonstrated in **Figure 76**.

The comparisons show that the amount of transverse strains for both types of sheet piles are not the same. The amount for the hot-rolled cross-sections plotted in blue is less than the cold-formed specimens shown in red, although the span length is equal. Thus, the maximum capacity of PZC26-35 is higher than JZ120-35. This reinforces that the transverse stresses influence the flexural capacity. The effect of span lengths on the capacity of the sheet piling cross-section was due to the amount of transverse strains and the profile of the cross-section itself.

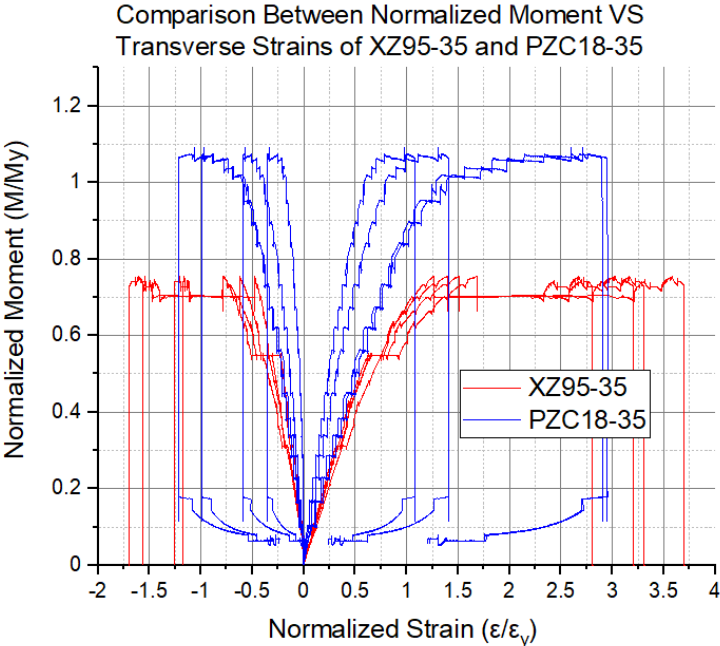


Figure 76a: XZ95-35 vs. PZC18-35

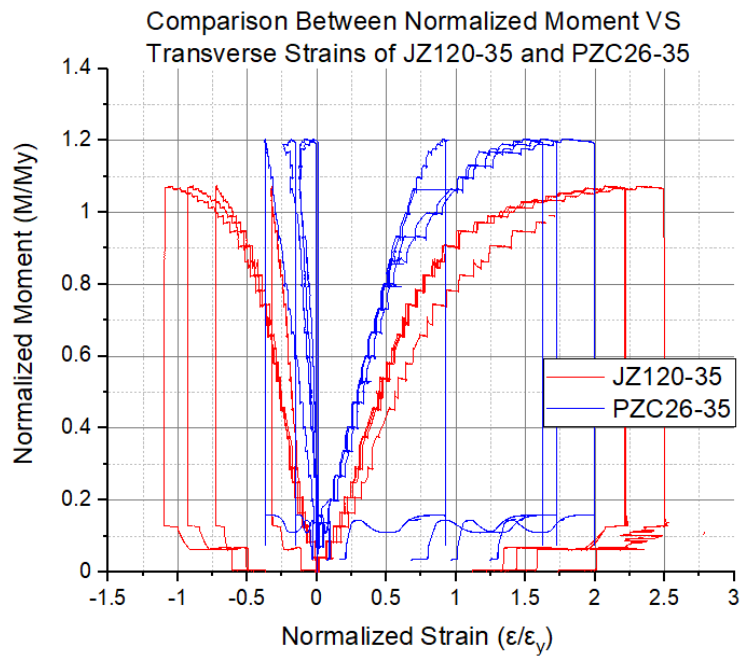


Figure 76a: JZ120-35 vs. PZC26-35

FIGURE 76: COMPARISON ON TRANSVERSE STRAIN DATA OF HOT-ROLLED AND COLD-FORMED CROSS-SECTIONS

CHAPTER 6: Conclusions

6.1 Conclusions

General behavior and Structural Capacity of Steel Sheet Piling

The experimental program on the cold-formed and hot-rolled sheet-pilings' flexural behavior was designed to capture the actual behavior. In reality, these types of members are subjected to uniformly distributed load from soil or water pressure along the cross-sections' surface. The members are connected along their interlocks to form a retaining wall system. These connections help brace the cross-sections from spreading and opening, making them behave like a beam under flexure. In the test setup, the air bladder was fabricated to fit the sheet piles' shape to generate pressure along the surface. Lateral bracings were provided at both ends of the loading region and roller supports. The hydraulic ram's point load was transferred to the uniformly distributed load on the specimens by the air bladder. All the components were designed to simulate actual configuration in the sheet-piling application.

All sheet-pilings suggested similar flexure behavior. The load-deflection responses started from linear at the beginning while the sheet piles had not yielded. After the first yield, the curves became flatter and eventually horizontal when the cross-sections reached their maximum capacity where they were fully yielded. The load-pressure plots obtained from the tests also showed that the target load was higher than the actual first yield load. The specimens yielded earlier under the existence of transverse stresses.

The middle interlocks of the sheet piles did not separate during the test. This helped the cross-sections remain in shape and develop their flexural strength. Most of the cross-sections could reach the maximum loads; however, only XZ95 cross-section with 35 ft span length experienced the interlock buckling limit state. The event prevented those specimens from reaching higher loads. Cross-sectional geometry plays an important role in isolating the interlock buckling limit state. JZ120 and PZC26 profiles have significantly more thickness than XZ95, making them have more resistant to the local cross-sectional deformation that

caused the limit state. PZC 26 cross-section has the same thickness as XZ95, but the shape of the middle interlock is different. Thus, the event did not occur. After more evaluation, the results suggested that this limit state could be deflection-controlled. Therefore, other cross-sections may experience the same event if subjected to more vertical deflections.

However, the interlock buckling is not a common limit state. There was no interlock buckling in the previous four-point bending tests on the same cross-sections. The main reason was that the way to load a specimen did not generate the lateral loading on the cross-section. Two steel rollers were placed at the top of the specimens, and they only loaded the cross-section vertically. On the other hand, the use of the air bladder created a uniform load perpendicular to the surfaces of the webs and flanges. This type of load amplified the local deformation of the cross-section, which caused the interlock buckling. In the sheet piling wall, the event is also more difficult to occur. The sheet piling members have more lateral stiffness since they are connected and braced together along the full length, and there are also more sheet piling components connected to the members that make them harder to buckle.

Effects of Transverse Stresses

Transverse stresses are a combination of transverse bending stresses due to the load perpendicular to the sheet piling surface and axial stresses due to the load against the boundary conditions. The test results indicated that transverse stresses significantly influenced the flexural strength of both hot-rolled and cold-formed sheet piles. The normalized moment-deflection curves showed that all the cross-sections subjected to uniformly distributed loading yielded earlier before reaching the target load calculated. Some cross-sections could not develop their yield moments, while only one could reach its plastic moment. This reduction in flexural strength was due to transverse stresses, which caused local deformation of the flanges or web components of the cross-sections. An increase in transverse stresses amplified the combination of longitudinal and transverse stresses on the material, which influenced the moment capacity. This answered

the research questions about how the transverse stresses interact with the longitudinal stresses and affect the maximum moment capacity of the sheet piling cross-section.

The result confirms what Hartman mentioned in 1994 that transverse stresses on the flexural capacity needed to be considered in the design. As a result, the full plastic and yield moment capacities should not be used directly for designing sheet piling members. However, the reduction of the moment capacity from the yield moment depends on the cross-section and span length presented in the test results.

Effect of Different Span Lengths

The difference in the span length resulted in the difference in the amount of load required to obtain the maximum moment of the sheet piling cross-sections. The use of the air bladder generated more lateral loading when the total air pressure increased. The difference in lateral loading resulted in a different amount of transverse strains which influenced the maximum moment capacity. As discussed previously, the less transverse stresses reduced the cross-section deformation and also reduced the combination with the longitudinal stresses. The strain gauge data clearly showed that the amount of transverse stresses reduced significantly when the span length increased due to less amount of load required to achieve the maximum moment. This reduction in stresses reduced their effects and made the maximum moment of the cross-section increased. The experiment confirmed the results from the finite element model performed by NBM in 2016, which suggested the same trend, and answered the question of how and why how the different amounts of loading on the different span lengths affect the cross-sectional capacity. Most importantly, the reduction in the moment strength for different span lengths needs to be considered during the sheet piling wall's design.

Performance between of Cold-formed and Hot-rolled Cross-section

In general, cold-formed and hot-rolled steel sections have different material properties, especially yield stress, due to the heat during the production and the cold-rolling process. To make the comparison reasonable and meaningful, the moment-deflection responses need to be normalized by the corresponding yield strength of the material. On the same plot, the comparison on the normalized moment-deflection curves suggested a lower flexural capacity of JZ120 than PZC26. The flexural performance of XZ95 and PZC18 was also not equivalent because XZ95 specimens experienced the interlock buckling limit state, preventing them from achieving higher moment capacity. The strain data showed that both cold-formed cross-sections experienced more transverse strains due to the geometry of the cross-sections. This also reinforces that transverse stresses affect the flexural capacity. As a result, it cannot be concluded that both types of sheet piles are structurally equivalent if the transverse stresses are different and the other limit state occurs.

The finding shows some different aspects of the model and the experiment done by NBM in 2016 and 2017. It reinforces the result for JZ120 and PZC26 in 2016 but suggested an inequivalent result from 2017's tests, in which there was no lateral loading. The research by Hartman, R. J., & Neal, J. A. in 1994 indicated that hot-rolled sheet piling was better than the cold-formed one considering their flexural performance. The effects of transverse stresses to the maximum moment capacity were introduced. Some design aids were established, in which the cross-sections had the full moment capacity when the pressure is zero. The capacity was reduced linearly to zero when the pressure is higher, which was inaccurate because the sheet pile still has non-zero capacity. The report also mentioned that further study needed to be conducted since there were a couple of specimens tested. However, this conclusion between both types of sheet piling had been used for a couple of decades, and it affected the use of cold-formed sheet piles. From now on, this 2020's project could ignite the use of both types of sheet piling in the industry together with considerations on the transverse stresses and the interlock buckling limit state to design a retaining wall system.

In conclusion, many factors make the hot-rolled and cold-formed sheet pilings flexurally equivalent or inequivalent. The loading method and the boundary conditions provided in the tests or in the finite element model play an important role in doing so. The existence of lateral loading in the uniform pressure test amplified the total amount of transverse stresses which reduced the moment strength of the sheet piles compared with the four-point bending test. The difference in the geometry of the sheet piles affects the resistance to the cross-sectional deformation, resulting in different transverse stresses. The uniform loading method could trigger the interlock buckling to occur, while the four-point bending did not experience the event. The finite element model of the interlocks assumed that they were frictionless and hard-contact. All of these could be the reasons why the hot-rolled and cold-formed sheet pilings are equivalent or inequivalent in terms of flexural behavior.

Engineering Applications

The results obtained from the project can be very useful for designing a safer sheet piling wall system. It is obvious that lateral loading which occurs in the application reduces the sheet-piling capacity. From the test results, it is obvious that when the span length increased, the amount of transverse strains increases, while the moment capacity decreases. This trend reinforces the work from NBM in 2016 reviewed in Chapter 2, in which there were some interaction curves between the span length and the moment capacity of sheet pilings. The curves also show increases in moment capacity when the specimens' lengths increase. By plotting the interaction curve of JZ120 specimens obtained from NBM with the uniform loading results, a design aid can be created. The JZ120 profile was selected for introducing an example of the design aid shown in **Figure 77** since there was no interlock buckling in the tests.

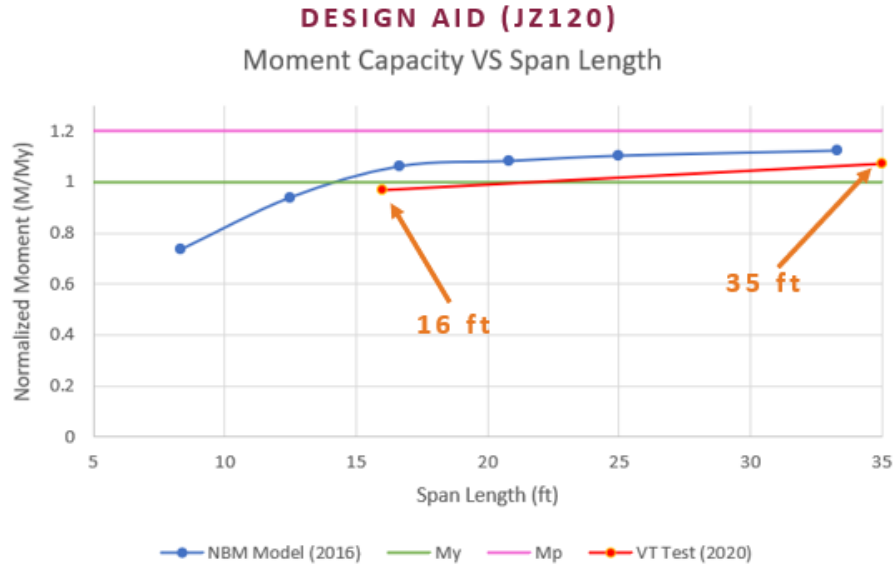


FIGURE 77: DESIGN AID EXAMPLE FOR JZ120 PROFILE

The curve for the uniform pressure tests shown in red is below the expected curve obtained from the model (blue line). This indicates some reduction in the capacity due to the actual configuration. However, considering the reduction, a full design aid can be plotted for all span lengths typically used in the sheet-piling wall application. This curve helps an engineer to choose the appropriate span length to obtain the capacity desired. For example, if the deflection is not the case, an engineer can choose 35-ft span to use 1.07 times the yield moment for designing the sheet piling wall. Using a longer span also reduces the number of components, such as a support, in the wall system.

However, for the XZ95 profile, there should be a limitation on the longest span length used. Using too long span for this cross-section may trigger the interlock buckling limit state, which reduces the capacity significantly.

6.2 Future Improvement and Research

The sheet piling project series with the same cross-sections had been conducted from 2016 to 2020. All the projects aimed to compare the flexural performance of cold-formed and hot-rolled sheet piles in many aspects and configurations. First, NBM (2016) performed the finite element analyses to investigate cross-sectional properties and behavior under different kinds of loading and boundary conditions. The analysis

results were then set as a baseline for the following experimental programs to compare the performance from the model and the real test configuration. The second project in 2017 was the first flexural experiment on the same sheet piling profiles using a four-point bending test. Finally, the specimens were subjected to uniformly distributed loading and reported in this document. As shown, many structural properties of the sheet pilings had been evaluated. However, there are still more interesting aspects of the sheet piling structure.

In the application, sheet piling members are usually installed as a cantilever wall, but most of the tests were conducted with a simple beam setup. There is curiosity about different performance between both structural configurations. Higher local stress concentration in a cantilever beam's cross-section is easier to achieve with the lower applied load. This might affect the flexural behavior and capacity. Several more failure mechanisms of the sheet piling itself could be tested. The test setup could be designed to be more realistic with as many as the same field configuration to represent the equivalent behavior. Furthermore, as the sheet piles do not behave alone in a wall system, other retaining wall components could also be investigated.

Interlock buckling is also an interesting topic since this limit state significantly reduces the moment capacity of sheet piling. A test setup in which it can uniformly load the sheet pilings to more vertical deflection would be useful. Not only can the use of longer span length reduce the effect of transverse stresses, but it introduces the interlock buckling limit state, which does not occur in shorter spans. The influence of this limit state to the flexural capacity will be useful for designing a long-span sheet-piling wall.

REFERENCES

- American Institute of Steel Construction. (2017). *Steel construction manual*.
- ASTM International. (2016). *Standard test methods for tension testing of metallic materials*.
- Campbell Scientific. (2020). *CR9000X - Measurement and Control Datalogger*. Retrieved November 20, 2020, from <https://www.campbellsci.com/cr9000x>
- Celesco Transducer Products, Inc. (2005). *Cable-Extension Position Transducer: PT101*. Retrieved November 20, 2020 from celesco.de/Pdf/pt101.pdf.
- Designingbuildings. (2018, March). *Sheet Piling*. Retrieved June 28, 2019, from All you need to know about sheet piling. Retrieved June 28, 2019, from https://www.designingbuildings.co.uk/wiki/All_you_need_to_know_about_sheet_piling
- Enerpac. *RR20013, 221 ton Capacity, 13.00 in Stroke, Double-Acting, General Purpose*. Retrieved November 20, 2020, from <https://www.enerpac.com/en-us/cylinders/general-purpose-cylinder/RR20013>.
- Eurocode. (1993). EN 1993: Design of steel structures. Retrieved November 20, 2020, from <http://eurocodes.jrc.ec.europa.eu/showpage.php?id=133>
- Harata, N. et al. (2008). *Development of Hat-Type Sheet Pile 900*.
- Hartman, R. J., & Neal, J. A. (1997). *Investigation of the effect of transverse loads on the behavior of Z-shape steel piling*. Hartman Engineering. Clarence, NY: Hartman Engineering.
- Hartman, R. J., & Neal, J. A. (1992). *Summary Excerpted from Report of Investigation and Test Program Related to Behavior of Steel Sheet Piling Subjected to Hydrostatic Test Loading*. Clarence, NY: Hartman Engineering.
- Jdfields. (2015, March 07). *History of Sheet Piling*. Retrieved June 28, 2020, from <https://jdfieldsusa.wordpress.com/2015/03/07/history-of-sheet-piling/>
- NBM Technologies, Inc. (2016). *Flexural Behavior, Web Crippling, and Interaction of Transverse Stress and Bending Moment in ColdFormed Steel and Hot-Rolled Steel Sheet Piling*.
- NBM Technologies, Inc. (2016). *Experiments on Flexural Behavior of Cold-Formed and Hot-Standard specification for steel sheet piling*.

Omega Engineering. (2019, April 4). *General Purpose, Stainless Steel Pressure Transducers*.
<https://www.omega.com/en-us/pressure-measurement/pressure-transducers/p/PX309>.

Tokyo Measuring Instruments Lab. (2017). *Strain Gauges*. Retrieved November 20, 2020 from
https://tml.jp/eng/documents/Catalog/StrainGauges_E1007E.pdf.

APPENDIX A

Wiring Diagram and Programming of Test Sensors

A.1 RTDAQ Program - CR9000X

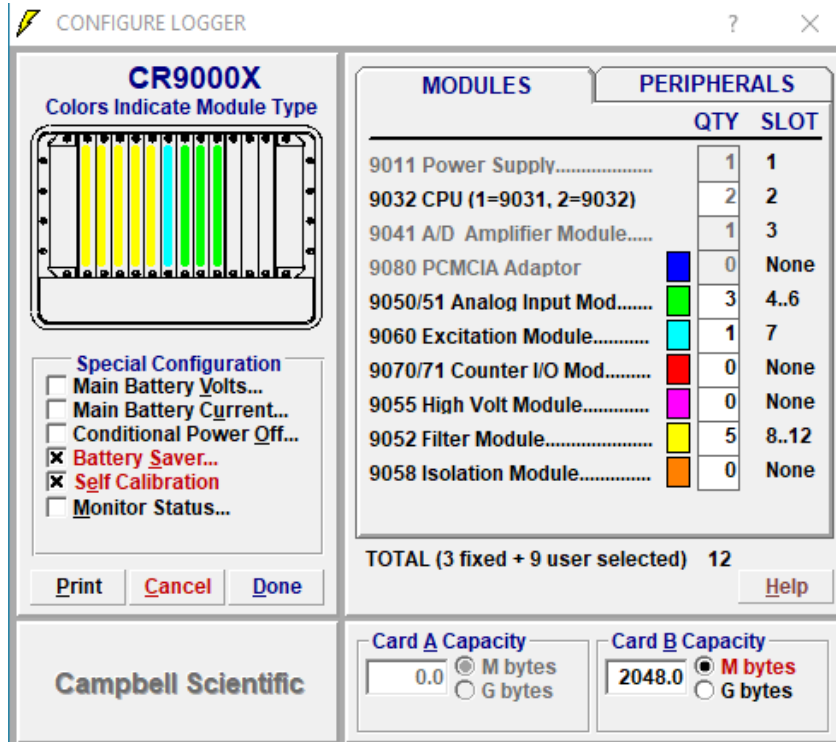


FIGURE 78: DAQ CONFIGURATION

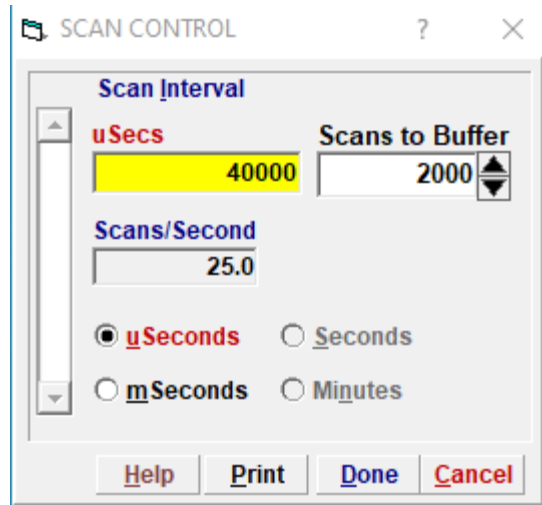


FIGURE 79: DAQ SCAN INTERVAL

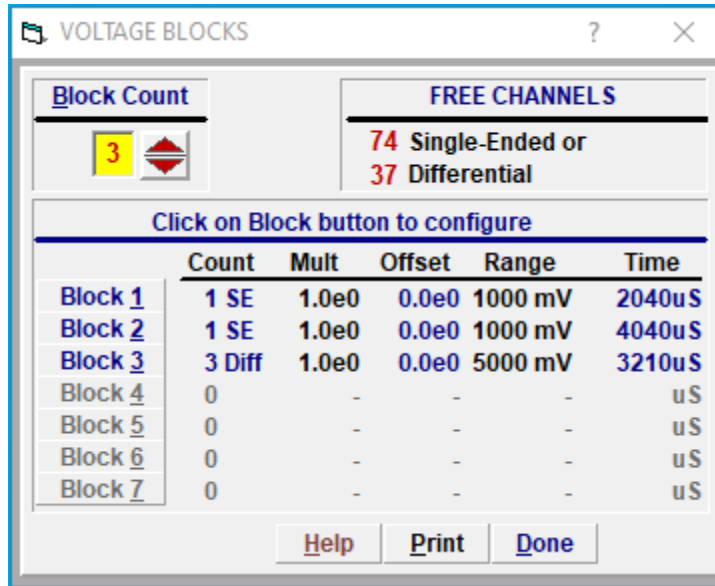


FIGURE 80: DAQ VOLTAGE BLOCK

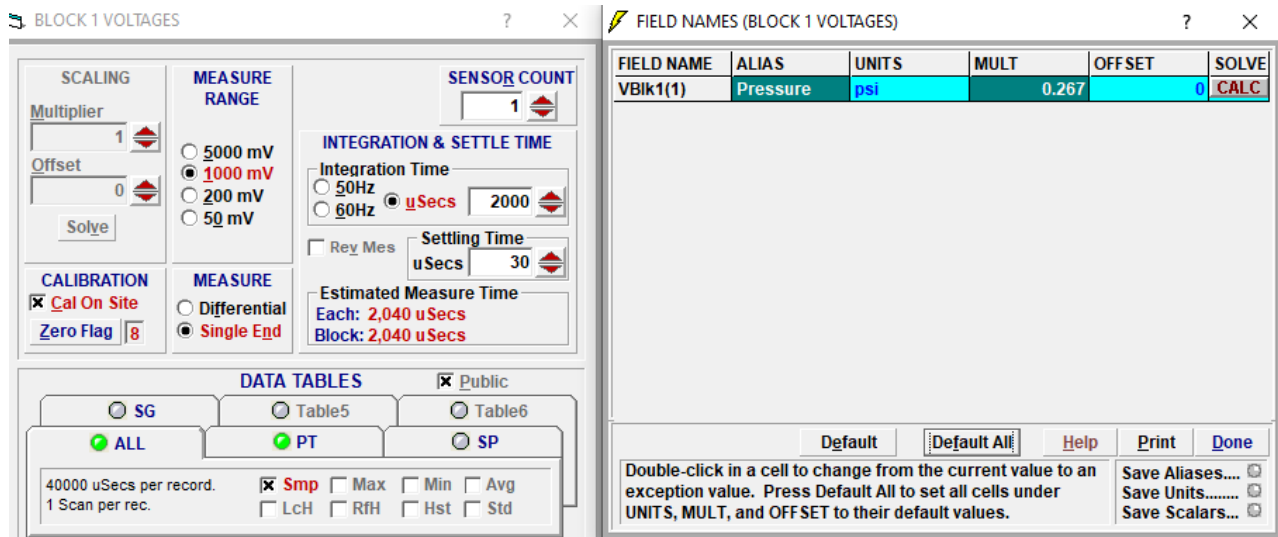


FIGURE 81: DAQ VOLTAGE BLOCK 1 (AIR BLADDER PRESSURE)

BLOCK 2 VOLTAGES ? X FIELD NAMES (BLOCK 2 VOLTAGES) ? X

SCALING

Multiplier: 1

Offset: 0

Solve

MEASURE RANGE

5000 mV

1000 mV

200 mV

50 mV

INTEGRATION & SETTLE TIME

Integration Time

50Hz

60Hz

μ Secs: 4000

Rey Mes Settling Time: 30 uSecs

Estimated Measure Time

Each: 4,040 uSecs

Block: 4,040 uSecs

CALIBRATION

Cal On Site

Zero Flag: 7

MEASURE

Differential

Single Egd

SENSOR COUNT

1

DATA TABLES Public

SG Table5 Table6

ALL PT SP

40000 uSecs per record. Smp Max Min Avg

1 Scan per rec. LcH RfH Hst Std

FIELD NAME	ALIAS	UNITS	MULT	OFFSET	SOLVE
VBIk2(1)	LOAD	KIP	0.8872	4.86	CALC

Default Default All Help Print Done

Double-click in a cell to change from the current value to an exception value. Press Default All to set all cells under UNITS, MULT, and OFFSET to their default values.

Save Aliases...
Save Units.....
Save Scalars...

FIGURE 82: DAQ VOLTAGE BLOCK 2 (HYDRAULIC RAM LOAD)

BLOCK 3 VOLTAGES ? X FIELD NAMES (BLOCK 3 VOLTAGES) ? X

SCALING

Multiplier: 1

Offset: 0

Solve

MEASURE RANGE

5000 mV

1000 mV

200 mV

50 mV

INTEGRATION & SETTLE TIME

Integration Time

50Hz

60Hz

μ Secs: 500

Rey Mes Settling Time: 30 uSecs

Estimated Measure Time

Each: 1,070 uSecs

Block: 3,210 uSecs

CALIBRATION

Cal On Site

Zero Flag: 6

MEASURE

Differential

Single Egd

SENSOR COUNT

3

DATA TABLES Public

SG Table5 Table6

ALL PT SP

40000 uSecs per record. Smp Max Min Avg

1 Scan per rec. LcH RfH Hst Std

FIELD NAME	ALIAS	UNITS	MULT	OFFSET	SOLVE
VBIk3(1)	SP1	INCH	0.01387	0	CALC
VBIk3(2)	SP7	mVolts	0.0117	0	CALC
VBIk3(3)	ExSP	mVolts	0.0111	0	CALC

Default Default All Help Print Done

Double-click in a cell to change from the current value to an exception value. Press Default All to set all cells under UNITS, MULT, and OFFSET to their default values.

Save Aliases...
Save Units.....
Save Scalars...

FIGURE 83: DAQ VOLTAGE BLOCK 3 (STRING POTENTIOMETERS)

SLOT 8, BLOCK 1 FILTERED VOLTAGES FIELD NAMES (SLOT 8, BLOCK 1 FILTERED VOLTAGES) ? X

SENSOR COUNT 6

SCALING
Multiplier 1
Offset 0
Solve

MEASURE RANGE
 5000 mV
 1000 mV
 200 mV
 50 mV
 20 mV

CALIBRATION
 Cal On Site
 Zero Flag 6

EXCITATION
 10 Volts
 5 Volts
 10 mA
 Off

FIELD NAME	ALIAS	UNITS	MULT	OFFSET	SOLVE
FVBik18(1)	SP2	INCH	0.5146	0	CALC
FVBik18(2)	SP3	INCH	0.3189	0	CALC
FVBik18(3)	SP4	INCH	0.2103	0	CALC
FVBik18(4)	SP5	INCH	0.2131	0	CALC
FVBik18(5)	SP6	INCH	0.211	0	CALC
FVBik18(6)	SP8	INCH	0.2056	0	CALC

Default Default All Help Print Done

FIGURE 84: DAQ FILTERED VOLTAGE SLOT 8 (STRING POTENTIOMETERS)

SLOT 9, BLOCK 1 FILTERED VOLTAGES FIELD NAMES (SLOT 9, BLOCK 1 FILTERED VOLTAGES) ? X

SENSOR COUNT 6

SCALING
Multiplier 1
Offset 0
Solve

MEASURE RANGE
 5000 mV
 1000 mV
 200 mV
 50 mV
 20 mV

CALIBRATION
 Cal On Site
 Zero Flag 6

EXCITATION
 10 Volts
 5 Volts
 10 mA
 Off

FIELD NAME	ALIAS	UNITS	MULT	OFFSET	SOLVE
FVBik19(1)	SP9	INCH	0.7778	0	CALC
FVBik19(2)	SP10	INCH	0.2142	0	CALC
FVBik19(3)	SP11	INCH	0.2215	0	CALC
FVBik19(4)	SP12	INCH	0.2129	0	CALC
FVBik19(5)	SP13	INCH	0.2078	0	CALC
FVBik19(6)	SP14	INCH	0.7869	0	CALC

Default Default All Help Print Done

FIGURE 85: DAQ FILTERED VOLTAGE SLOT 9 (STRING POTENTIOMETERS)

SLOT 10, BLOCK 1 FILTERED VOLTAGES FIELD NAMES (SLOT 10, BLOCK 1 FILTERED VOLTAGES) ? X

SENSOR COUNT 1

SCALING
Multiplier: 1
Offset: 0
Solve

MEASURE RANGE
 5000 mV
 1000 mV
 200 mV
 50 mV
 20 mV

CALIBRATION
 Cal On Site
 Zero Flag: 6

EXCITATION
 10 Volts
 5 Volts
 10 mA
 Off

FIELD NAME	ALIAS	UNITS	MULT	OFFSET	SOLVE
FVBik110(1)	SP15	INCH	0.2106	0	CALC

Default Default All Help Print Done

FIGURE 86: DAQ FILTERED VOLTAGE SLOT 10 BLOCK 1 (STRING POTENTIOMETERS)

SLOT 10, BLOCK 2 FILTERED VOLTAGES FIELD NAMES (SLOT 10, BLOCK 2 FILTERED VOLTAGES) ? X

SENSOR COUNT 5

SCALING
Multiplier: 1
Offset: 0
Solve

MEASURE RANGE
 5000 mV
 1000 mV
 200 mV
 50 mV
 20 mV

CALIBRATION
 Cal On Site
 Zero Flag: 5

EXCITATION
 10 Volts
 5 Volts
 10 mA
 Off

FIELD NAME	ALIAS	UNITS	MULT	OFFSET	SOLVE
FVBik210(1)	SKIP SG	ksi	0	0	CALC
FVBik210(2)	SG1	ksi	10.95	0	CALC
FVBik210(3)	SG2	ksi	10.95	0	CALC
FVBik210(4)	SG3	ksi	10.95	0	CALC
FVBik210(5)	SG4	ksi	10.95	0	CALC

Default Default All Help Print Done

FIGURE 87: DAQ FILTERED VOLTAGE SLOT 10 BLOCK 2 (STRAIN GAUGES)

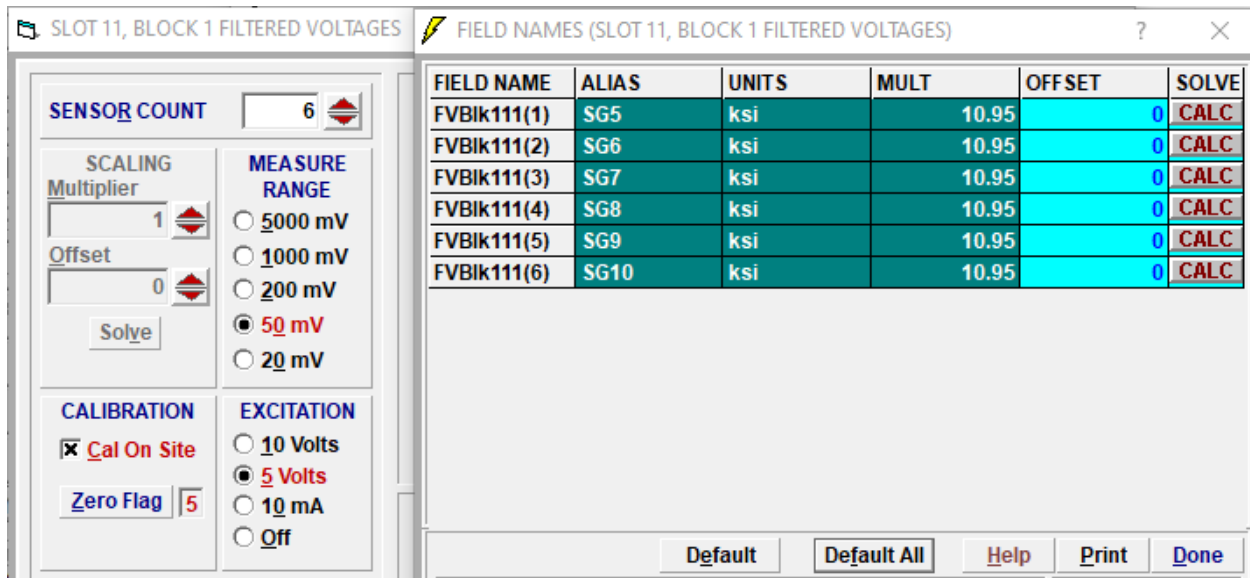


FIGURE 88: DAQ FILTERED VOLTAGE SLOT 11 (STRAIN GAUGES)

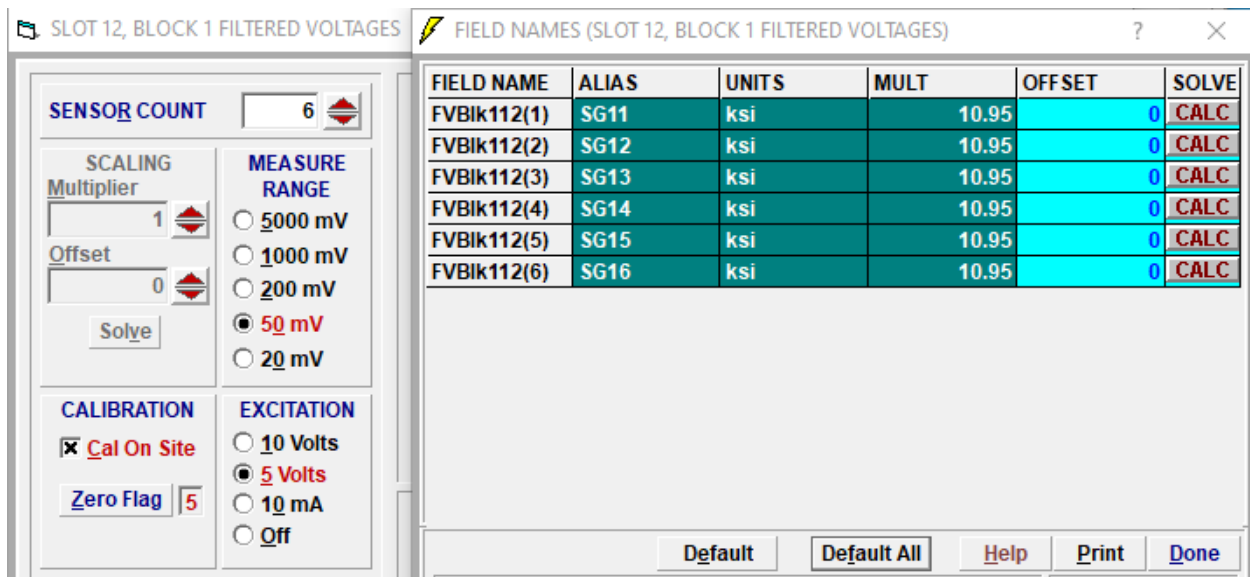


FIGURE 89: DAQ FILTERED VOLTAGE SLOT 12 (STRAIN GAUGES)

A.2 Wiring Diagram on CR9000X

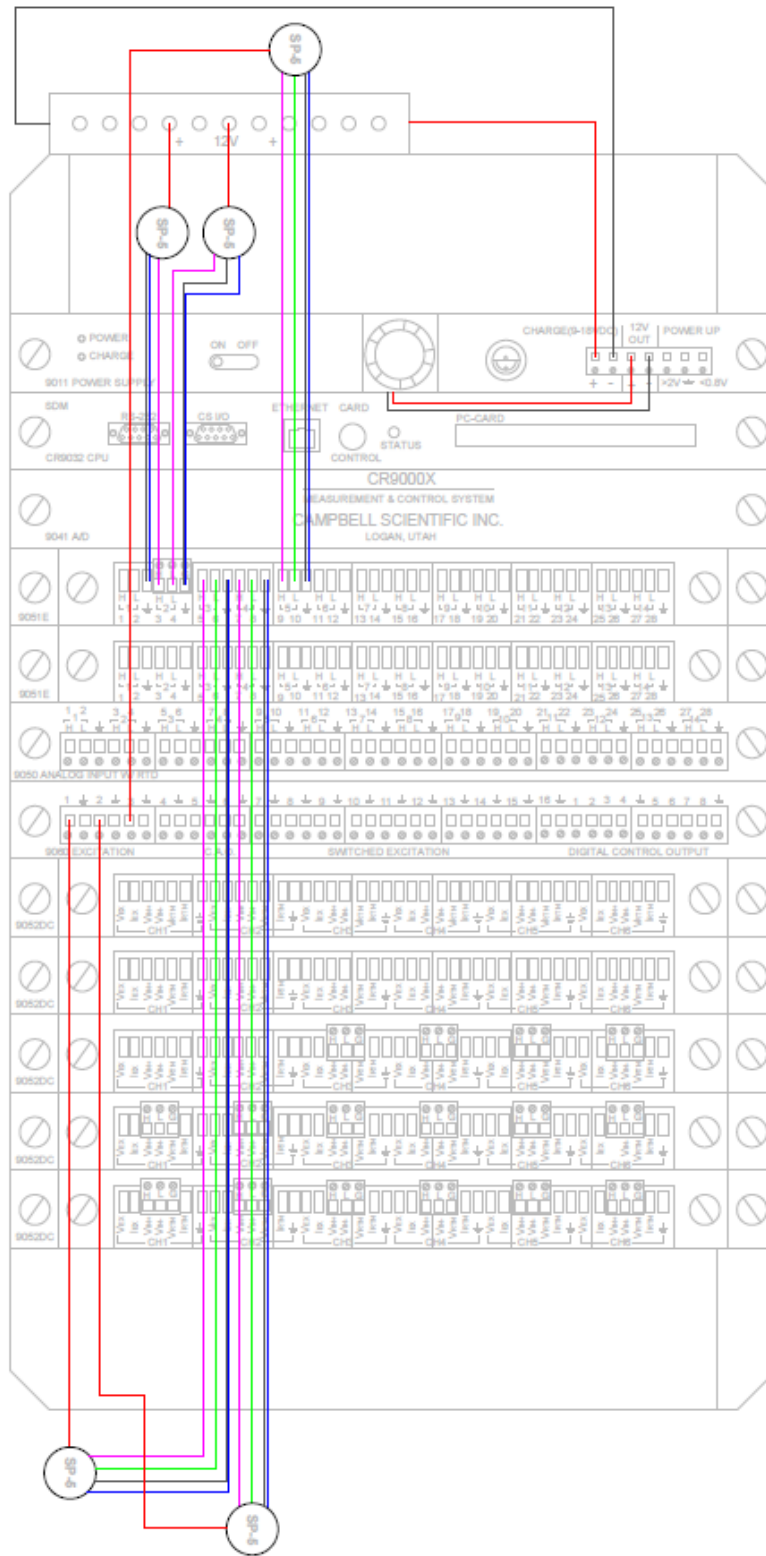


FIGURE 90: DAQ WIRING DIAGRAM FOR SLOT 1 TO 7

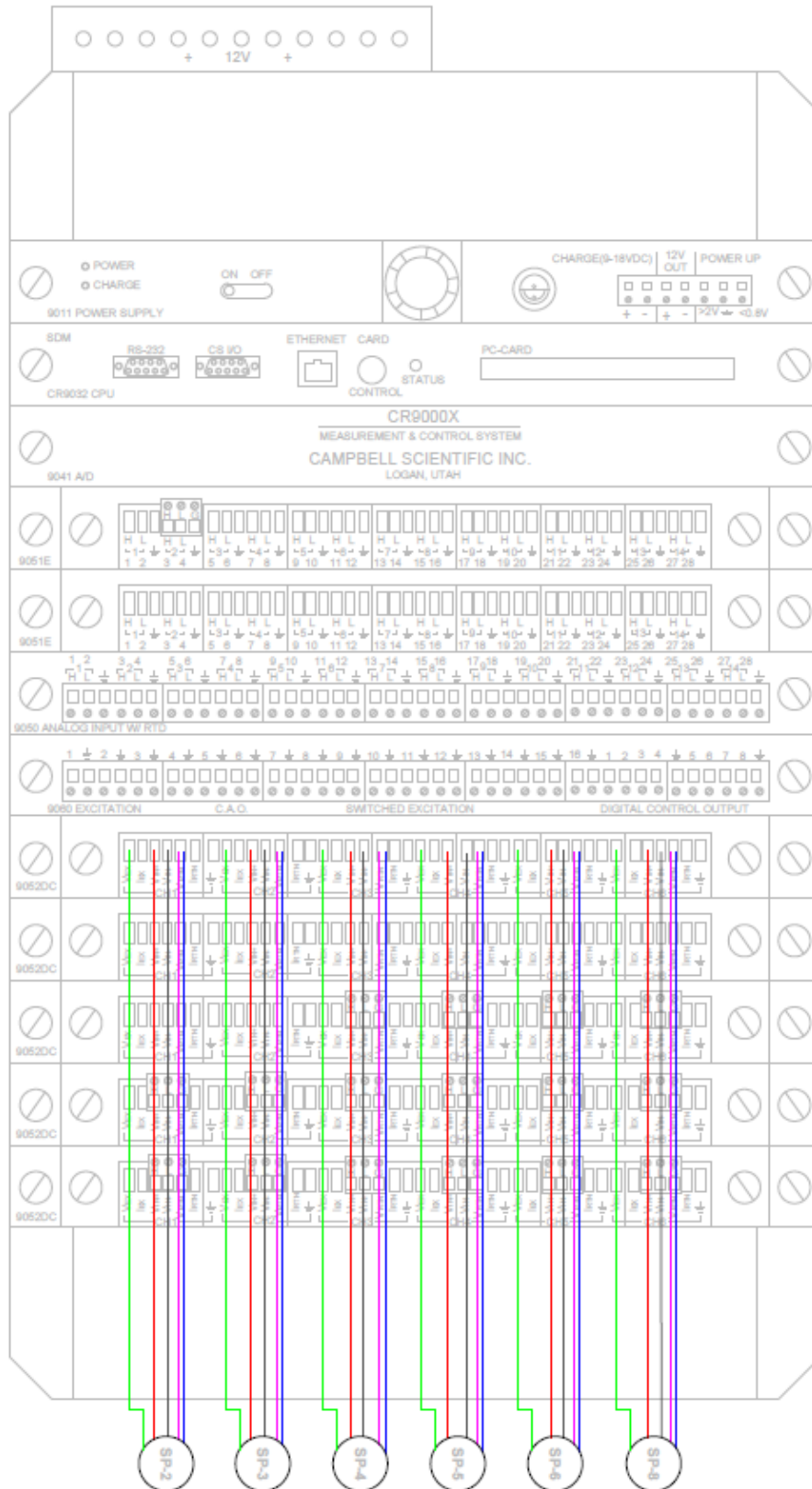


FIGURE 91: DAQ WIRING DIAGRAM FOR SLOT 8

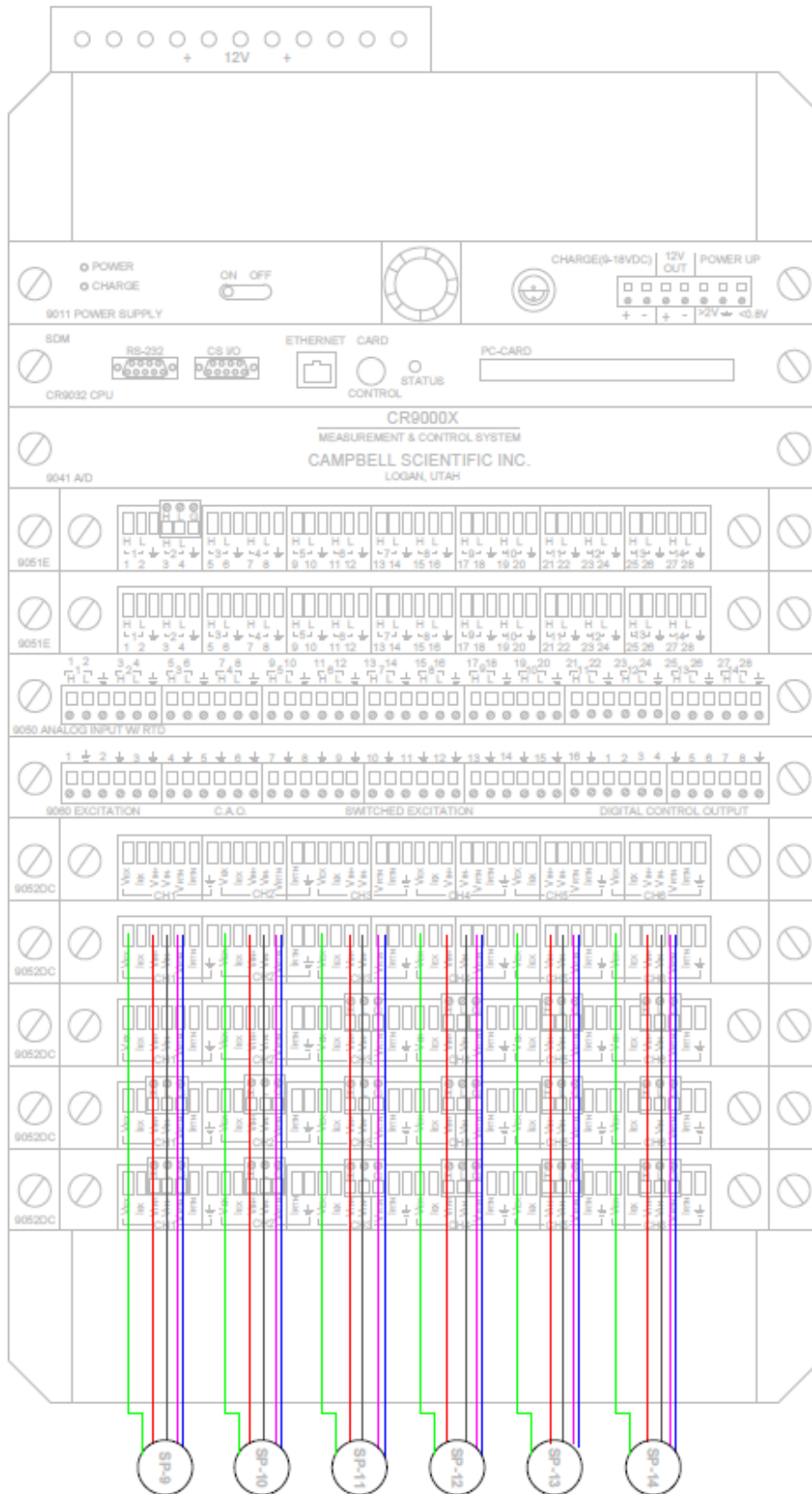


FIGURE 92: DAQ WIRING DIAGRAM FOR SLOT 9



FIGURE 93: DAQ WIRING DIAGRAM FOR SLOT 10

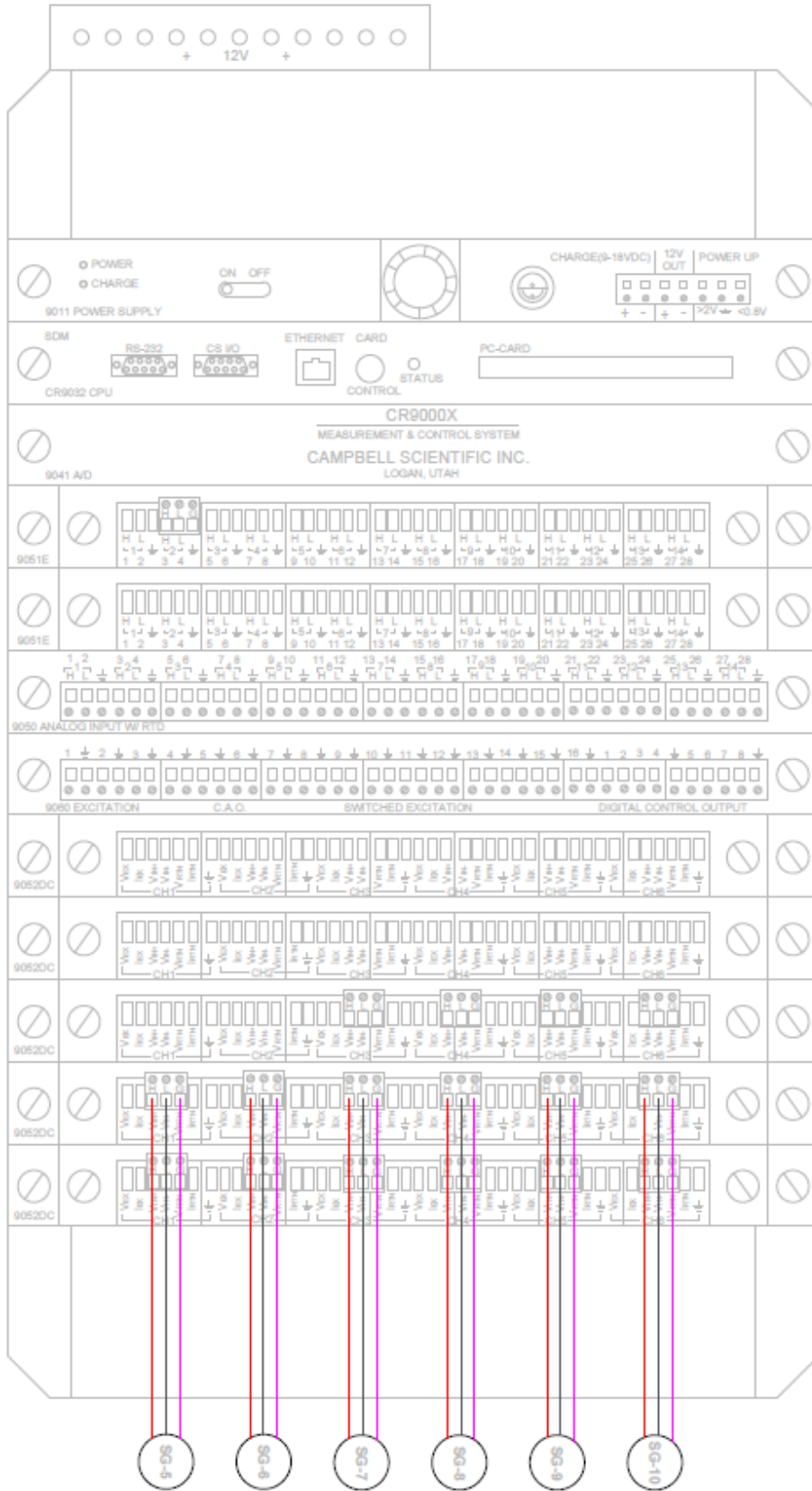


FIGURE 94: DAQ WIRING DIAGRAM FOR SLOT 11

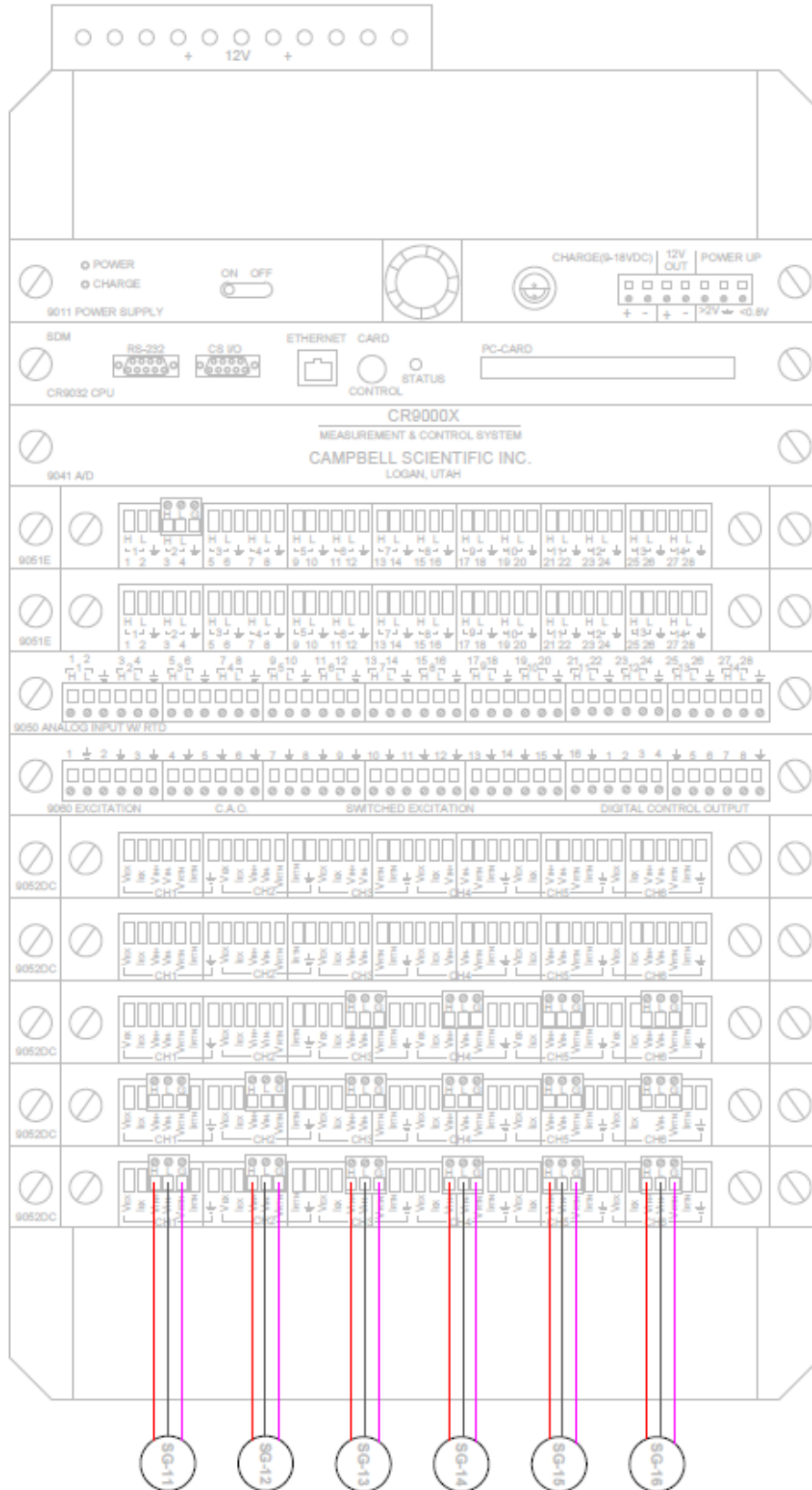


FIGURE 95: DAQ WIRING DIAGRAM FOR SLOT 12

APPENDIX B

Calculation of Sectional Modulus and Plastic Modulus

The sectional modulus and plastic modulus are necessary to calculate the yield and plastic moment of the sheet piling cross-sections. The actual yield moments of all sections were used to normalize the moment-deflection and moment-rotation curves in order to make the comparison between hot-rolled and cold-formed cross-sections more meaningful. These sectional properties were calculated using “MASSPROP” command in AutoCAD to the drawings of the cross-sections.

B.1 Sectional Modulus

JZ120

```
Area: 43.06
Perimeter: 184.33
Bounding box: X: -1220.08 -- -1164.05
               Y: 495.08 -- 511.55
Centroid: X: -1192.03
           Y: 503.32
Moments of inertia: X: 10908887.56
                   Y: 61189929.30
Product of inertia: XY: 25832286.37
Radii of gyration: X: 503.36
                  Y: 1192.13
Principal moments and X-Y directions about centroid:
I: 1741.12 along [1.00 -0.04]
J: 10934.94 along [0.04 1.00]
```

FIGURE 96: MASSPROP FOR JZ120

$$I=1741.12/53*12=394.2 \text{ in}^4/\text{ft}$$

$$S=I/C=394.2/(503.32-495.08)=47.84 \text{ in}^3/\text{ft}$$

PZC26

```
Area: 43.43
Perimeter: 159.85
Bounding box: X: -1217.55 -- -1160.90
               Y: 460.86 -- 478.56
Centroid: X: -1189.88
           Y: 469.71
Moments of inertia: X: 9584044.44
                   Y: 61502465.32
Product of inertia: XY: 24273680.67
Radii of gyration: X: 469.76
                  Y: 1189.99
Principal moments and X-Y directions about centroid:
I: 1989.16 along [1.00 0.00]
J: 11317.86 along [0.00 1.00]
```

FIGURE 97: MASSPROP FOR PZC26

$$I=1989.16/55.75*12=428.16 \text{ in}^4/\text{ft}$$

$$S=428.16/(469.71-460.86)=48.38 \text{ in}^3/\text{ft}$$

XZ95

```
Area: 30.79
Perimeter: 165.72
Bounding box: X: -1141.58 -- -1089.17
               Y: 495.05 -- 509.18
Centroid: X: -1115.35
           Y: 502.12
Moments of inertia: X: 7764009.30
                   Y: 38310782.39
Product of inertia: XY: 17244152.66
Radii of gyration: X: 502.15
                  Y: 1115.45
Principal moments and X-Y directions about centroid:
I: 991.67 along [1.00 -0.03]
J: 6794.48 along [0.03 1.00]
```

FIGURE 98: MASSPROP FOR XZ95

$$I=991.67/50*12=238.00 \text{ in}^4/\text{ft}$$

$$S=238.00/(502.12-495.05)=33.66 \text{ in}^3/\text{ft}$$

PZC18

Area:	29.65
Perimeter:	146.16
Bounding box:	X: -1142.40 -- -1091.50 Y: 460.84 -- 476.09
Centroid:	X: -1117.88 Y: 468.46
Moments of inertia:	X: 6507305.94 Y: 37054356.00
Product of inertia:	XY: 15525567.99
Radii of gyration:	X: 468.50 Y: 1117.97
Principal moments and X-Y directions about centroid:	I: 1066.63 along [1.00 0.00] J: 6338.80 along [0.00 1.00]

FIGURE 99: MASSPROP FOR PZC18

$$I=1066.63/50*12=225.92 \text{ in}^4/\text{ft}$$

$$S=225.92/(502.12-495.05)=33.58 \text{ in}^3/\text{ft}$$

B.2 Plastic Modulus

TABLE 15: PLASTIC MODULUS CALCULATION

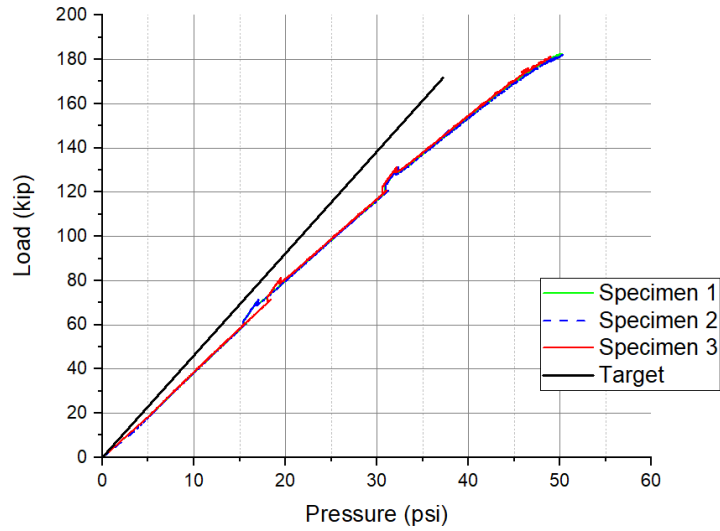
Section	A sq.in	y bar - y NA	Fy ksi	Mp k-in	Zx in^3	Width (in)	Zx in^3/ft
JZ120			50	12818.1	256.363	53	58.0444
Above NA	21.52	5.95					
Below NA	21.53	5.96					
PZC26			60	16133.6	268.894	55.75	57.8784
Above NA	21.72	6.19					
Below NA	21.72	6.19					
XZ95			50	8220.93	164.419	50	39.4605
Above NA	15.39	5.34					
Below NA	15.4	5.34					
PZC18			60	9873.45	164.558	50	39.4938
Above NA	14.83	5.55					
Below NA	14.82	5.55					

APPENDIX C

Test Results of All Specimens

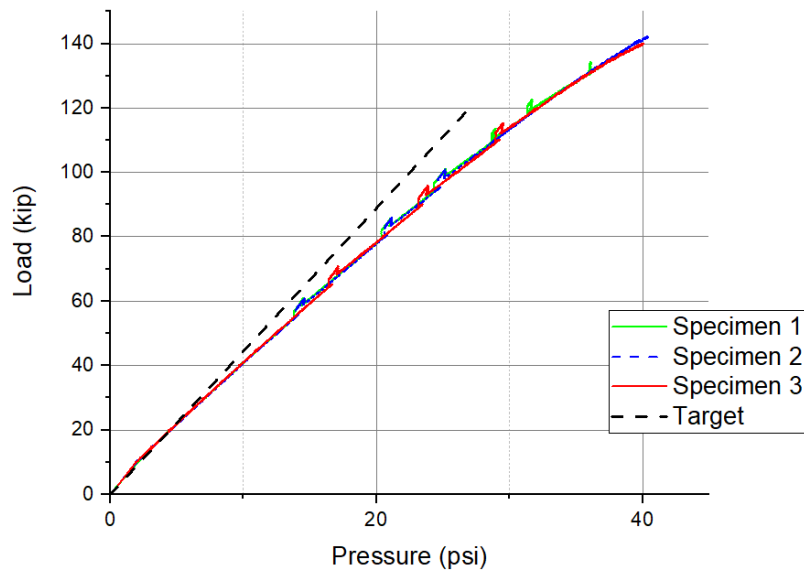
C.1 Load-Pressure Responses

Comparison of Load-Pressure Plots for 35ft PZC26 Specimens



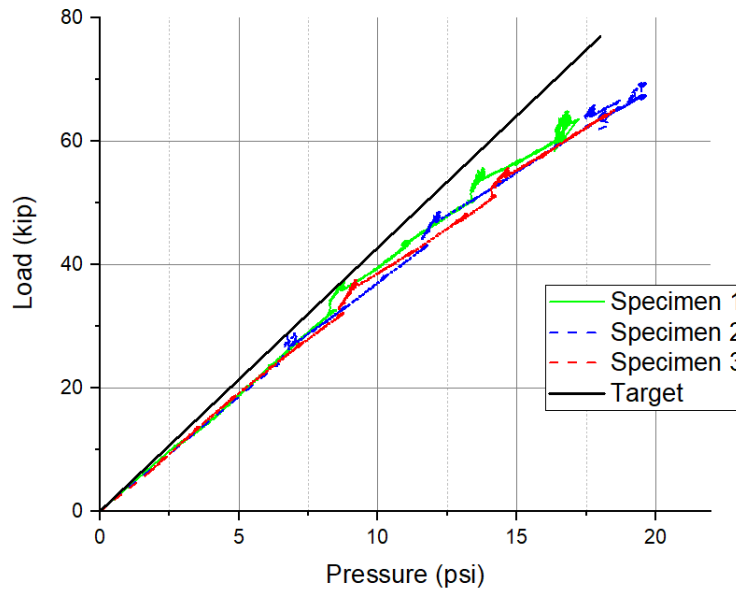
a) 35-ft PZC26 Specimens

Comparison of Load-Pressure Plots for 35ft JZ120 Specimens



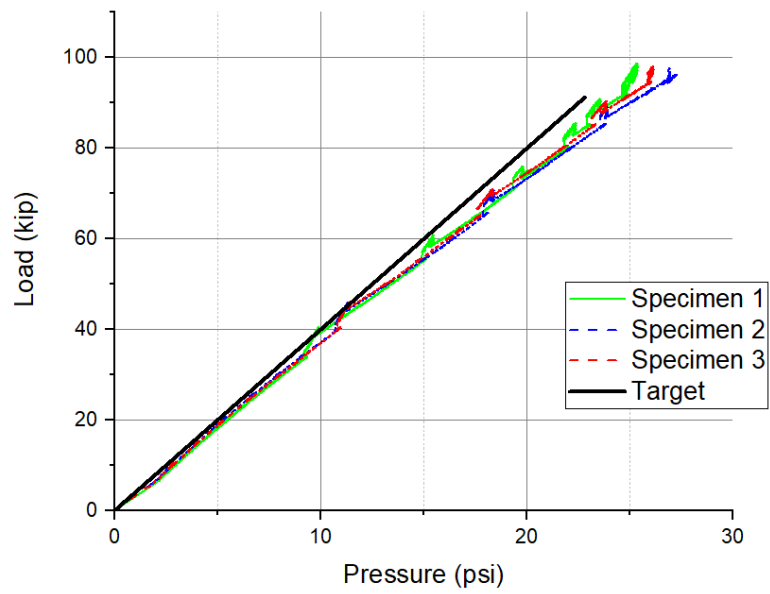
b) 35-ft JZ120 Specimens

Comparison of Load-Pressure Plots for 35ft XZ95 Specimens



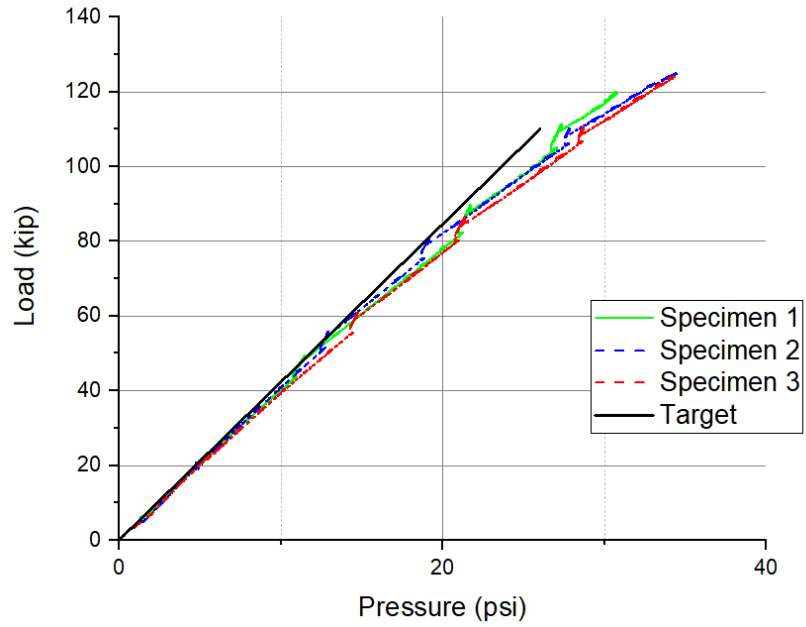
a) 35-ft XZ95 Specimens

Comparison of Load-Pressure Plots for 35ft PZC18 Specimens



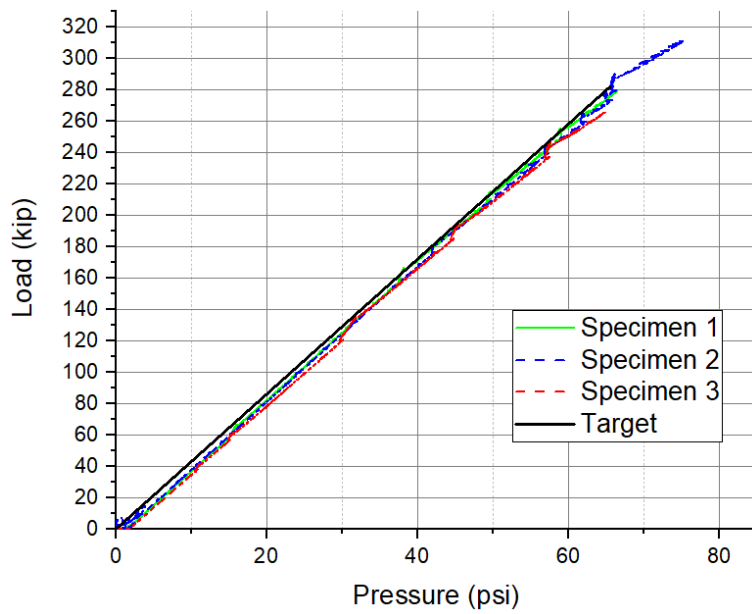
b) 35-ft PZC18 Specimens

Comparison of Load-Pressure Plots for 25ft XZ95 Specimens



c) 25-ft XZ95 Specimens

Comparison of Load-Pressure Plots for 16ft JZ120 Specimens



d) 16-ft JZ120 Specimens

FIGURE 100: LOAD-PRESSURE RELATIONSHIP FOR ALL SPECIMENS IN A TEST GROUP

C.2 Load-Deflection Responses

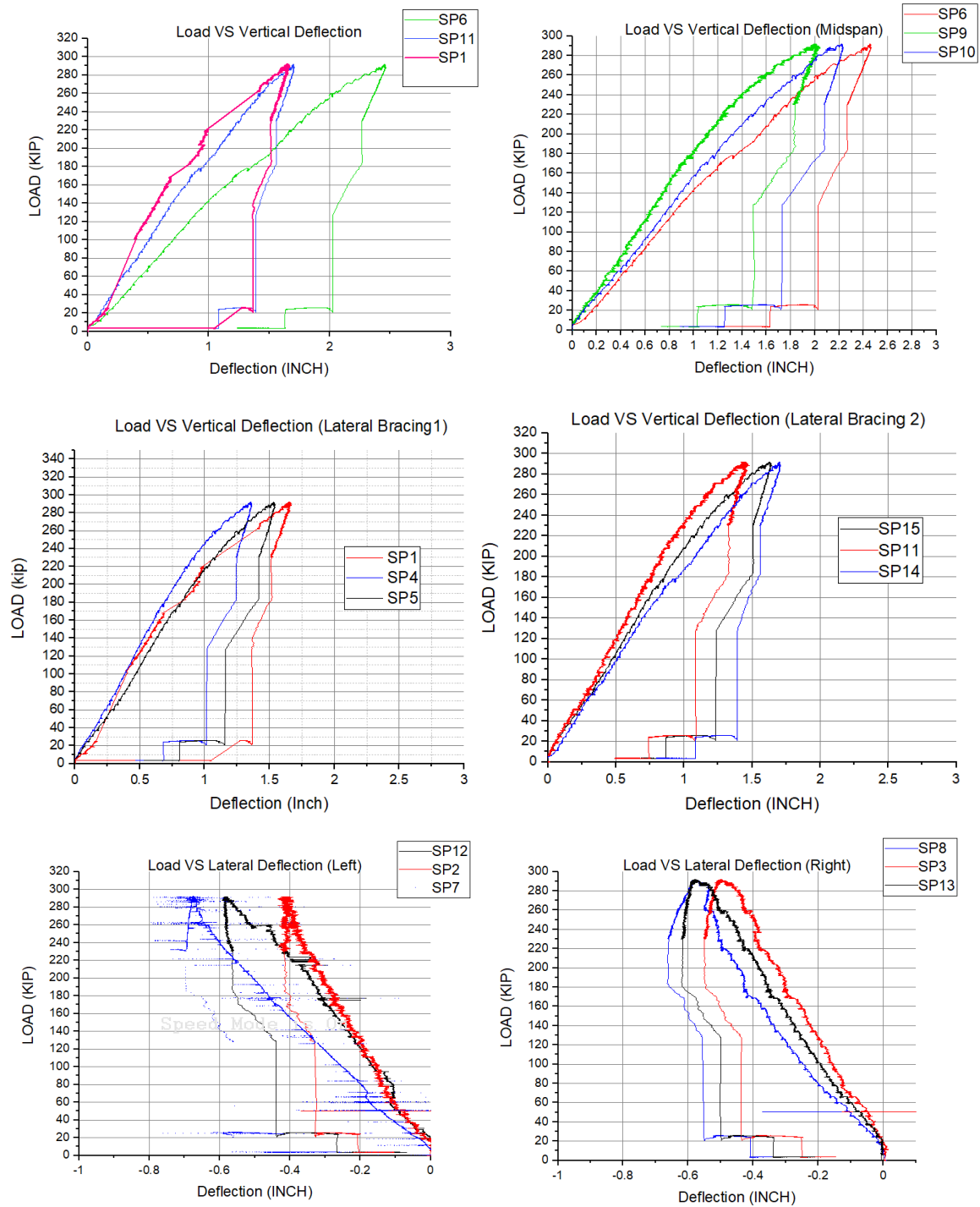


FIGURE 101: LOAD-DEFLECTION DATA FOR JZ120-16-1

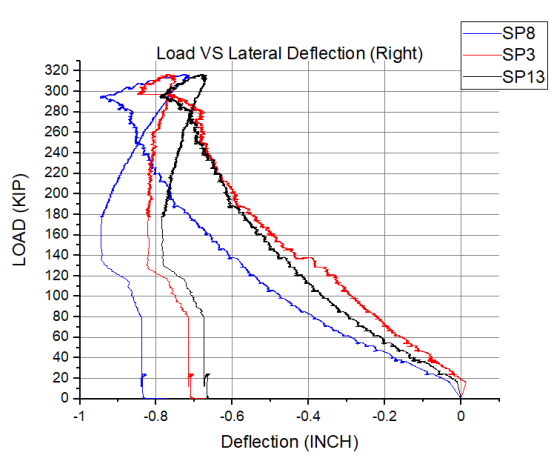
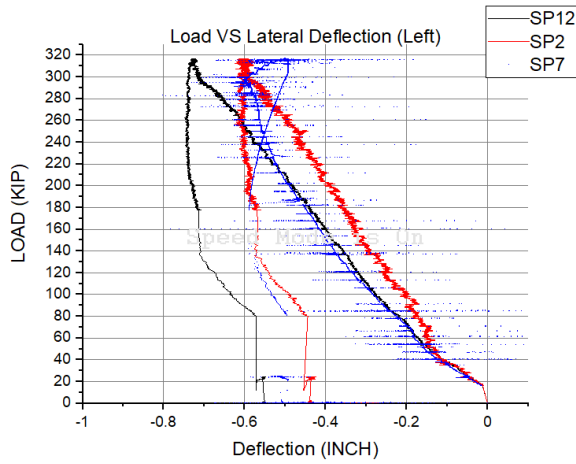
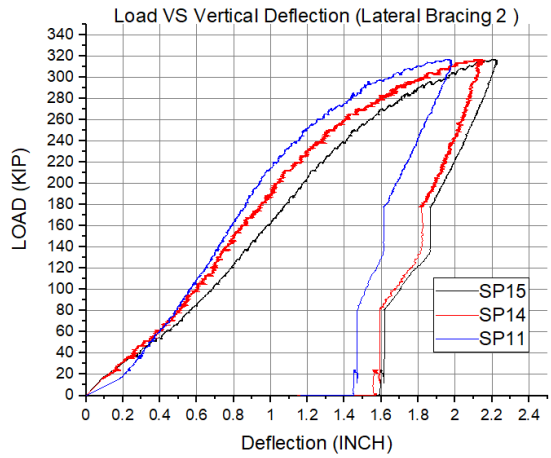
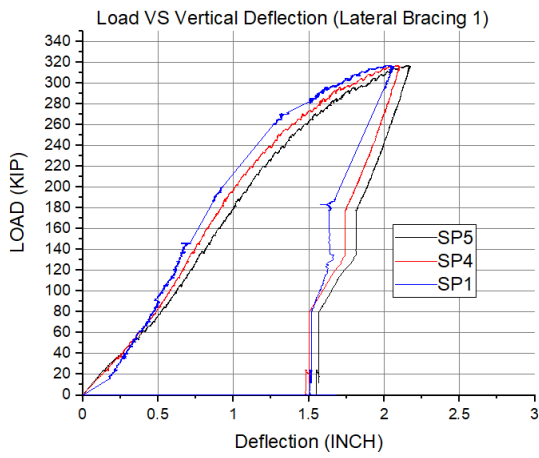
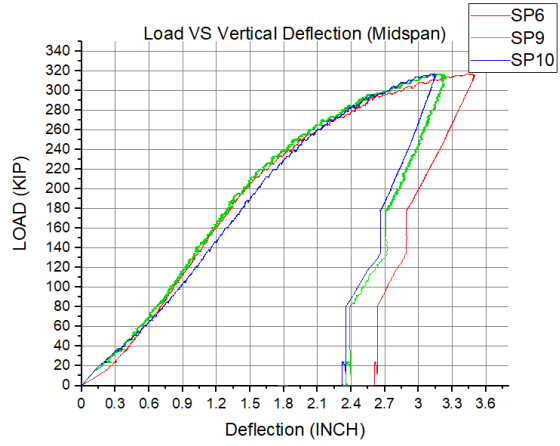
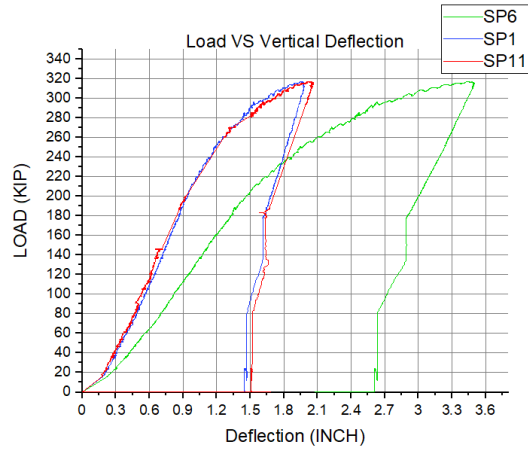


FIGURE 102: LOAD-DEFLECTION DATA FOR JZ120-16-2

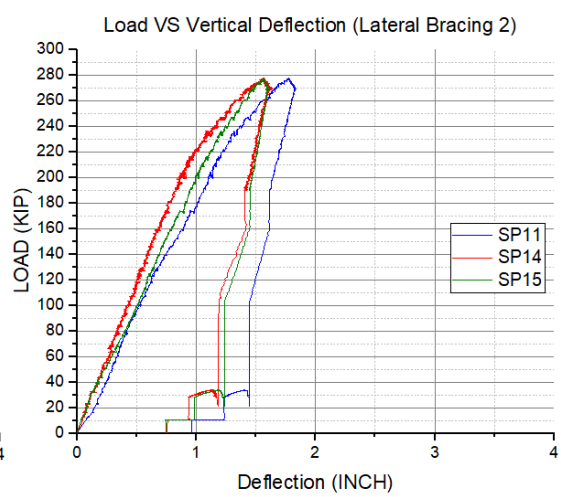
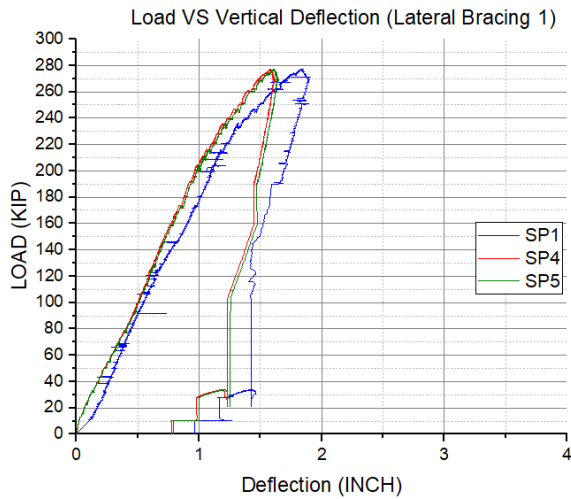
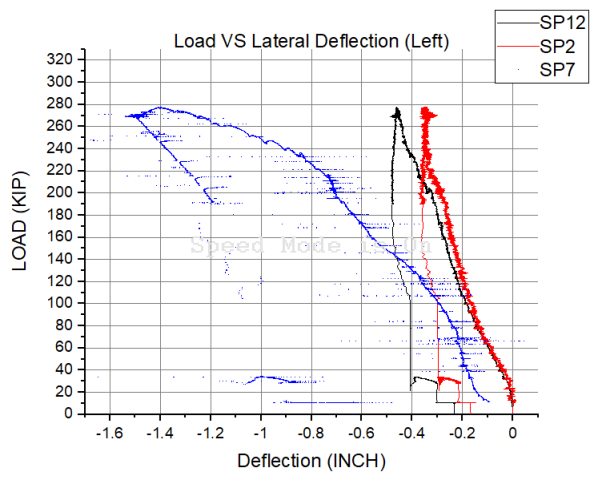
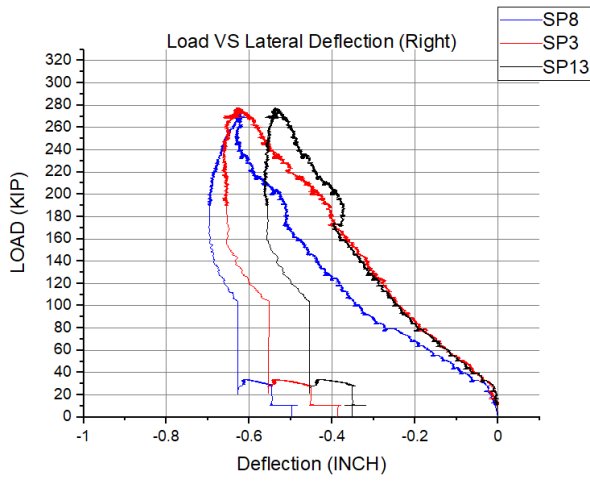
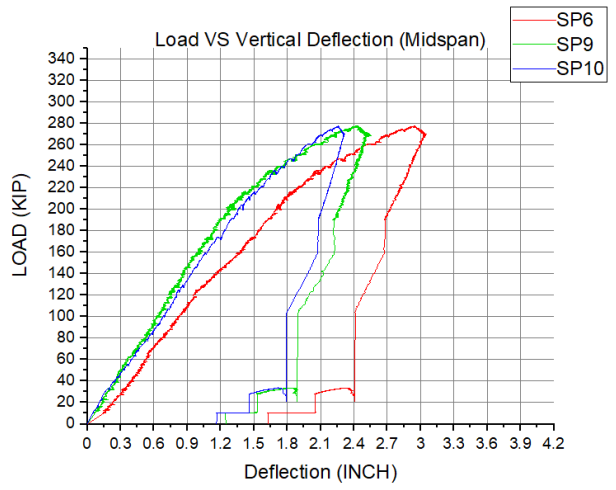
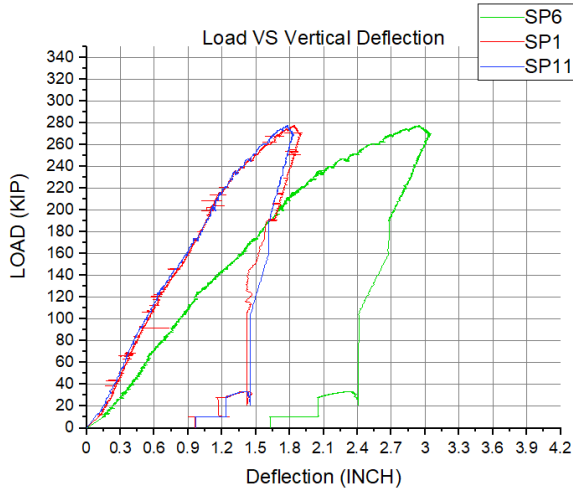


FIGURE 103: LOAD-DEFLECTION DATA FOR JZ120-16-3

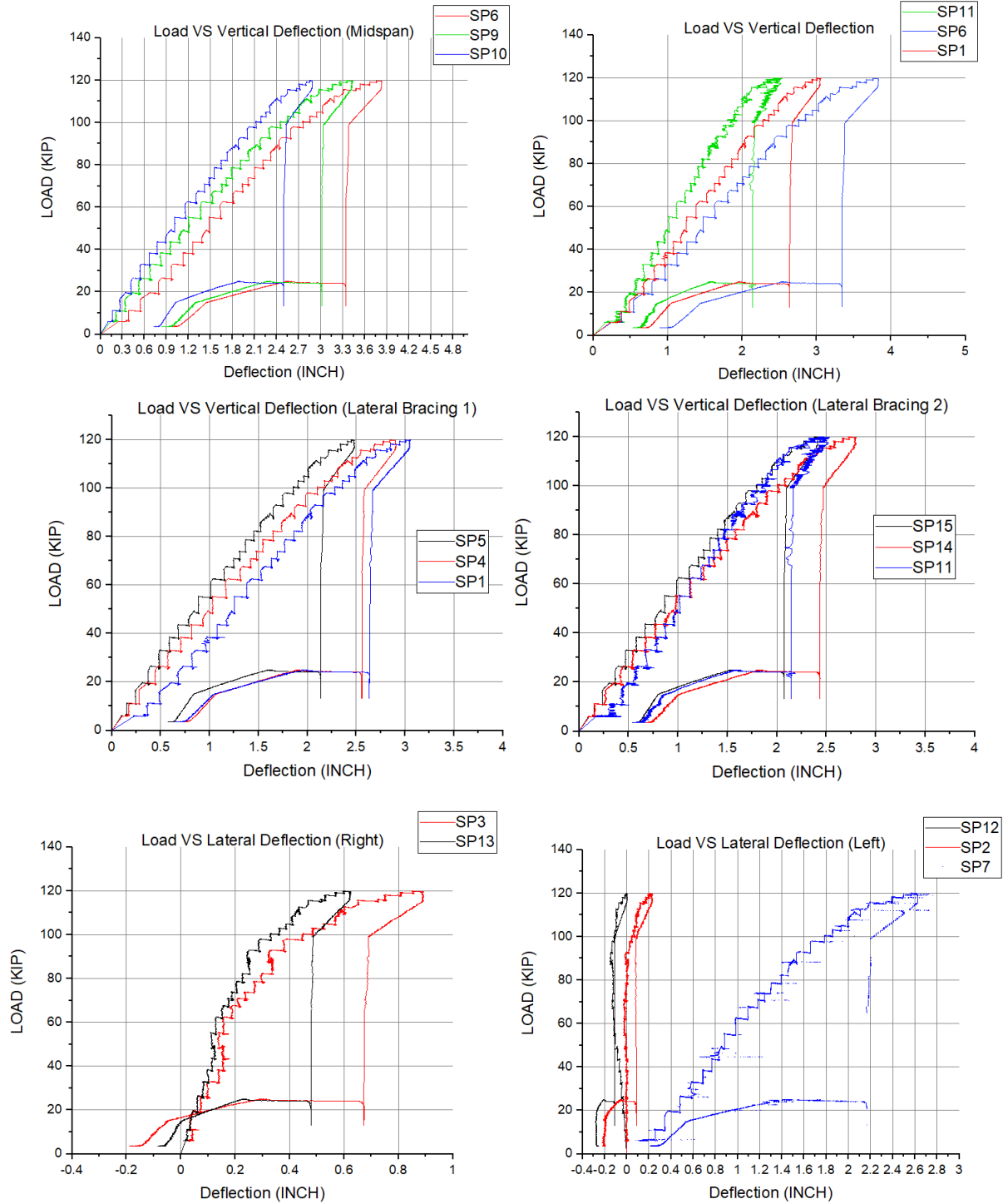


FIGURE 104: LOAD-DEFLECTION DATA FOR XZ95-25-1

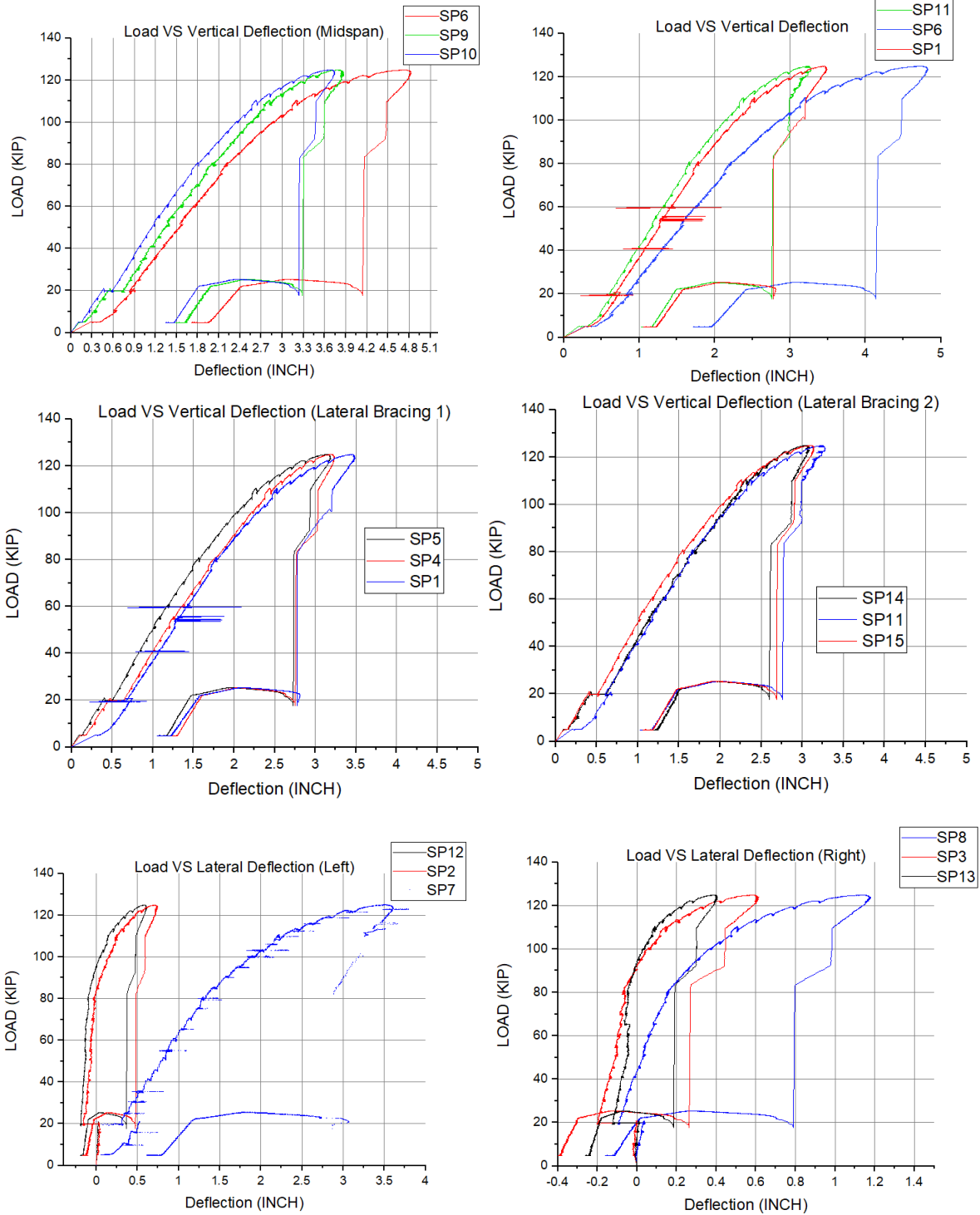


FIGURE 105: LOAD-DEFLECTION FOR XZ95-25-2

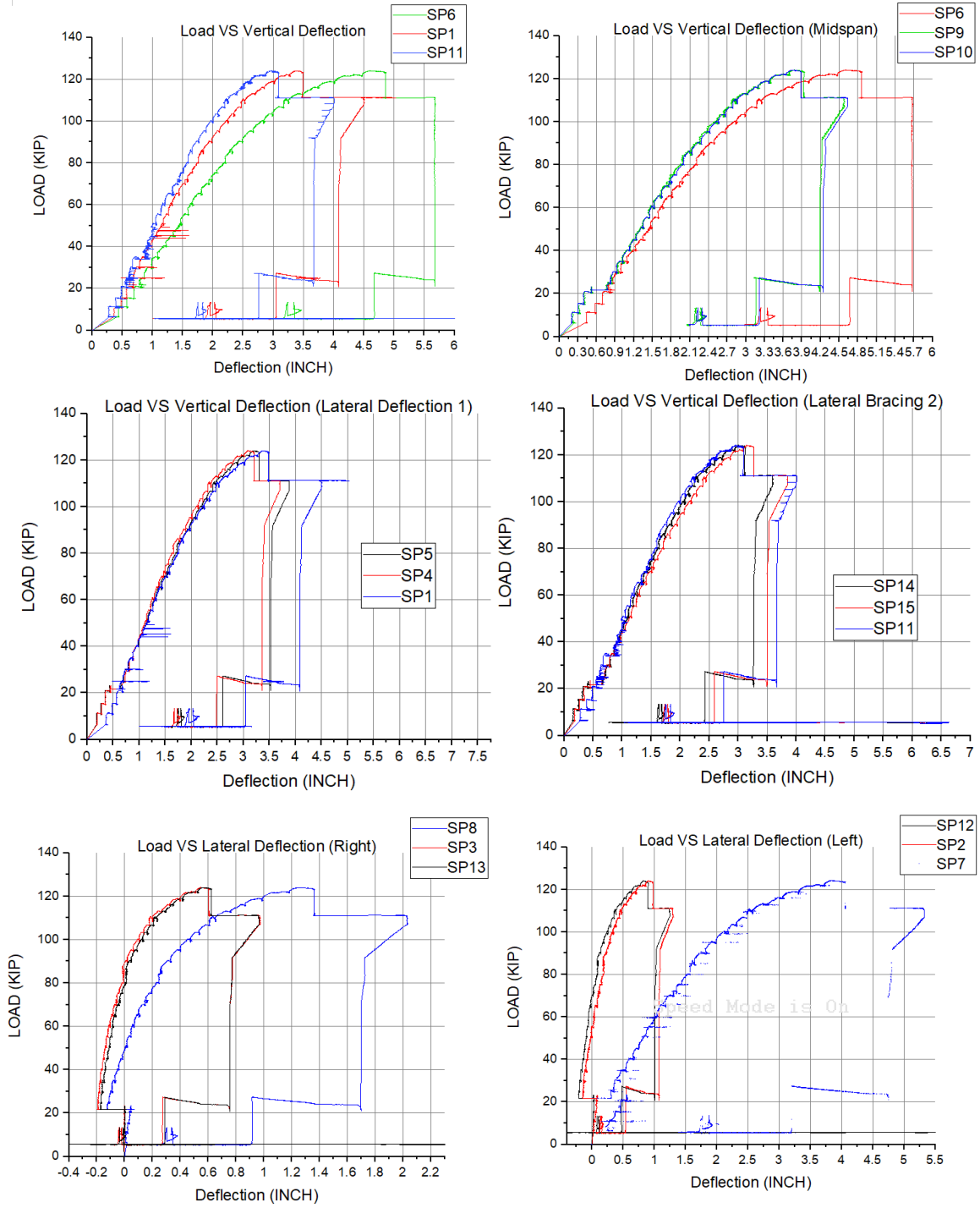


FIGURE 106: LOAD-DEFLECTION DATA FOR XZ95-25-3

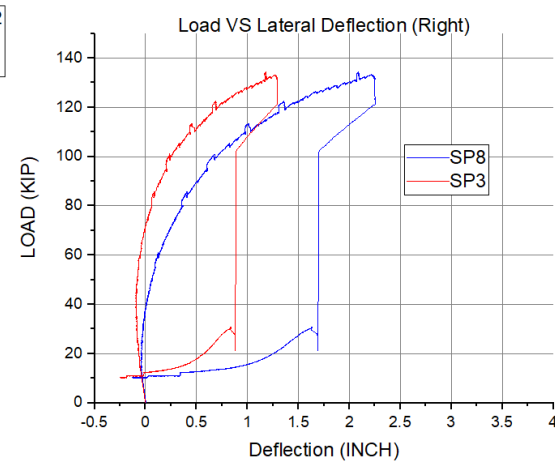
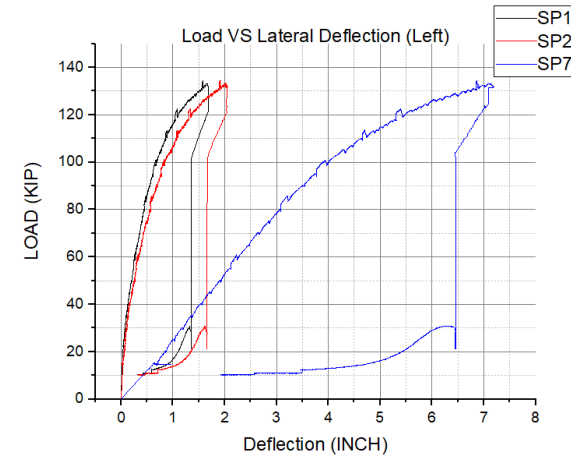
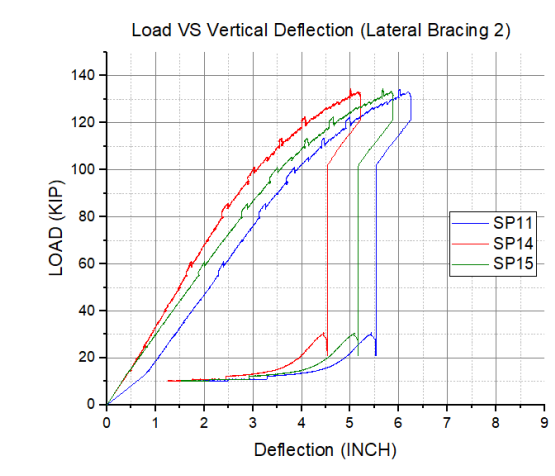
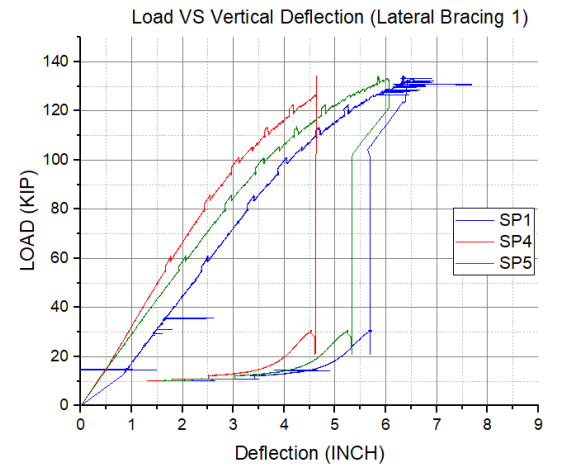
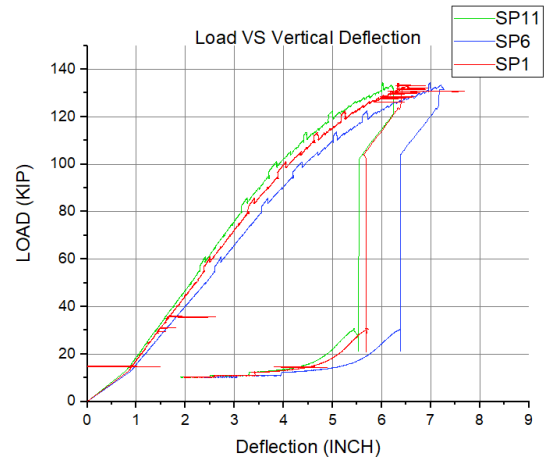
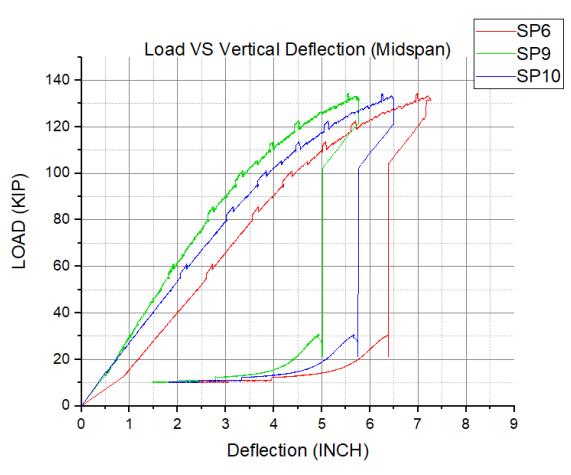


FIGURE 107: LOAD-DEFLECTION DATA FOR JZ120-35-1

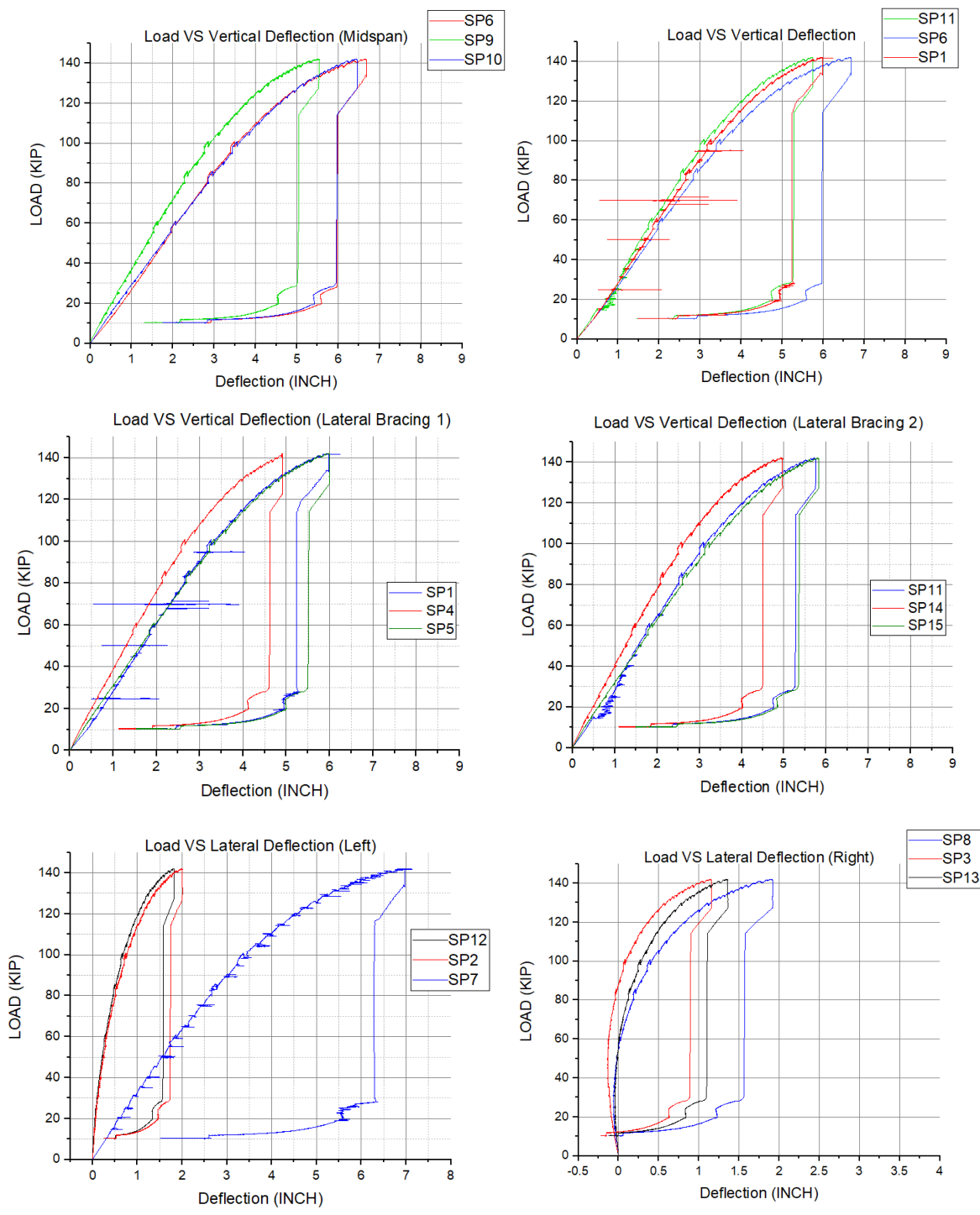


FIGURE 108: LOAD-DEFLECTION DATA FOR JZ120-35-2

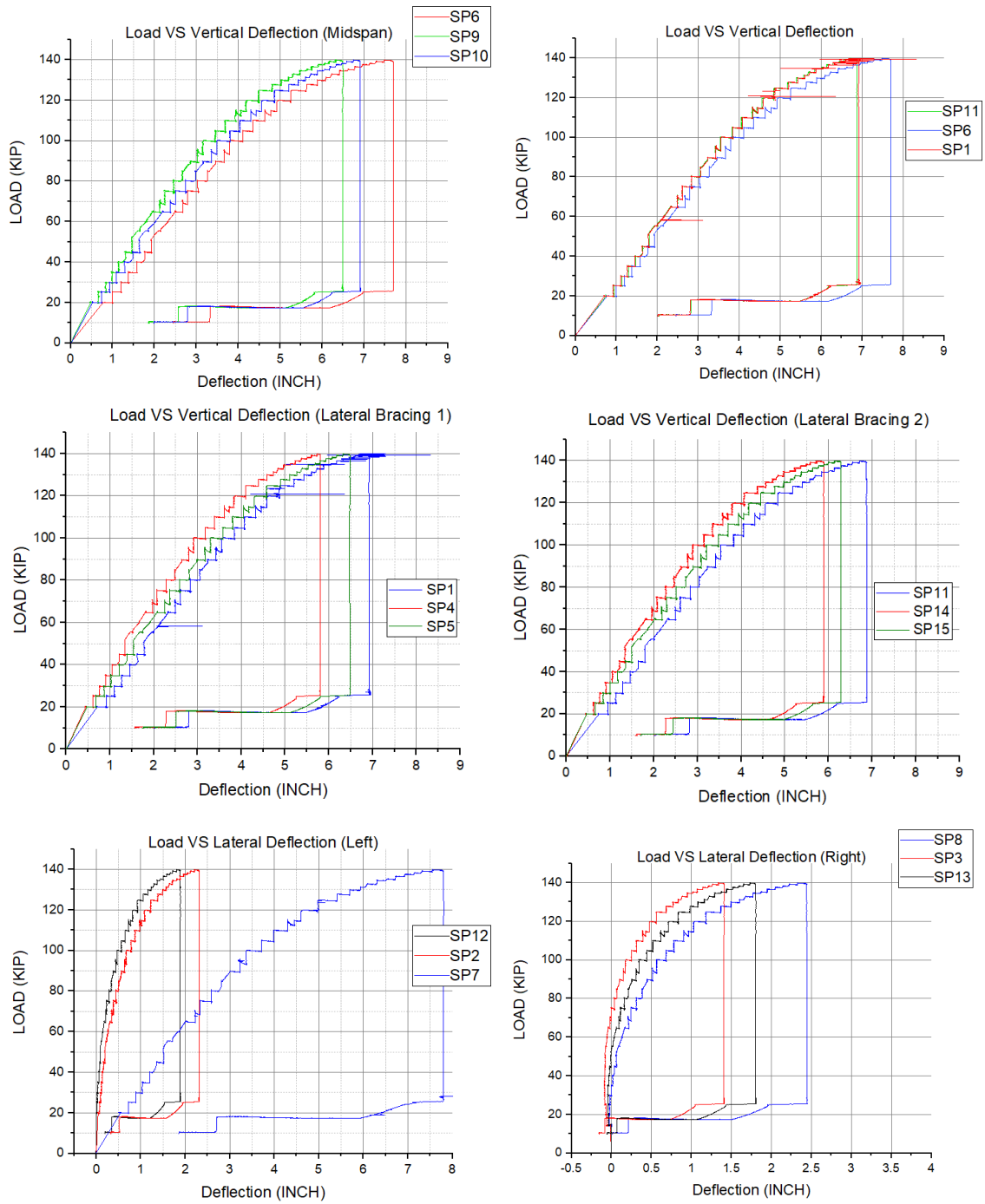


FIGURE 109: LOAD-DEFLECTION DATA FOR JZ120-35-3

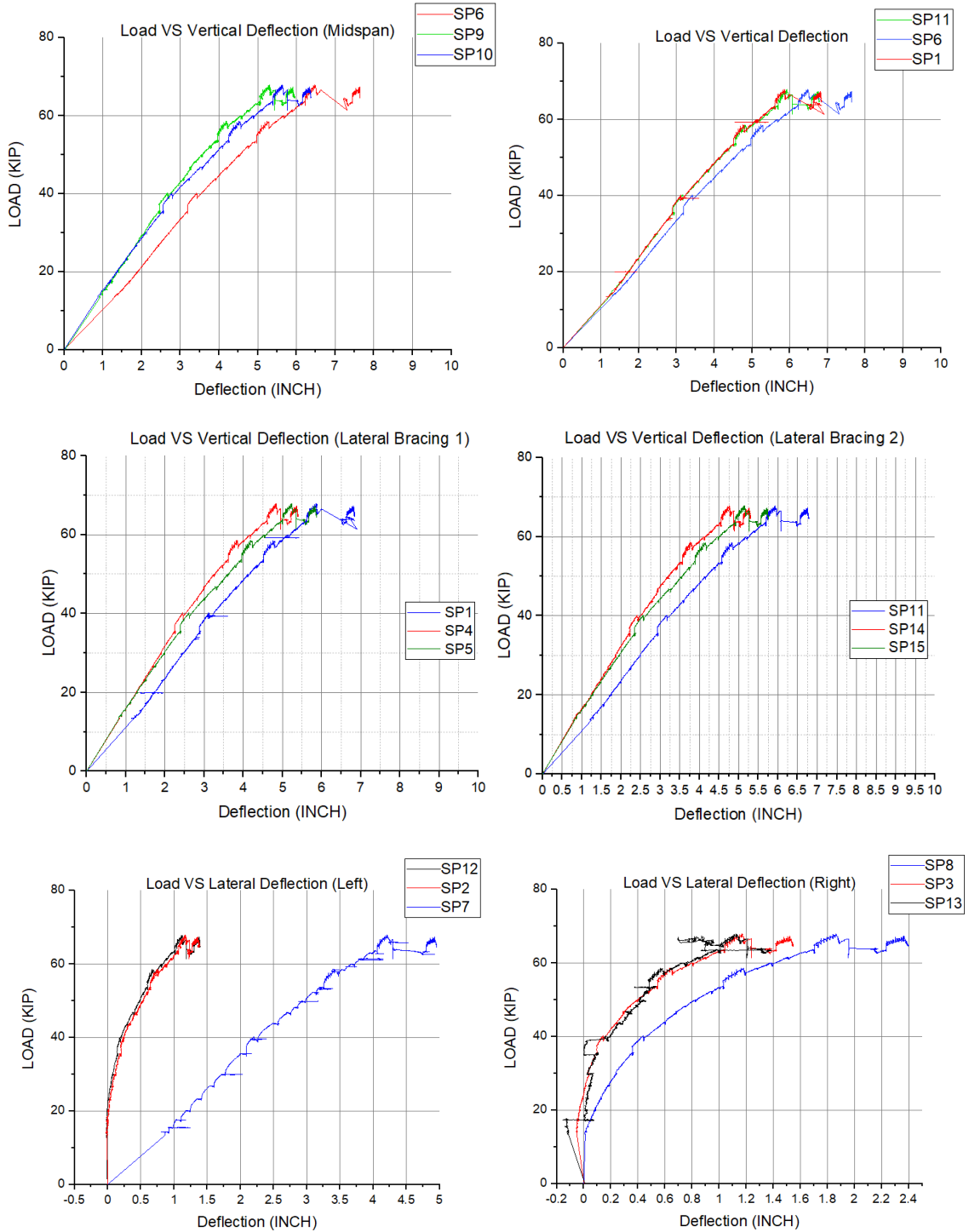


FIGURE 110: LOAD-DEFLECTION DATA FOR XZ95-35-1

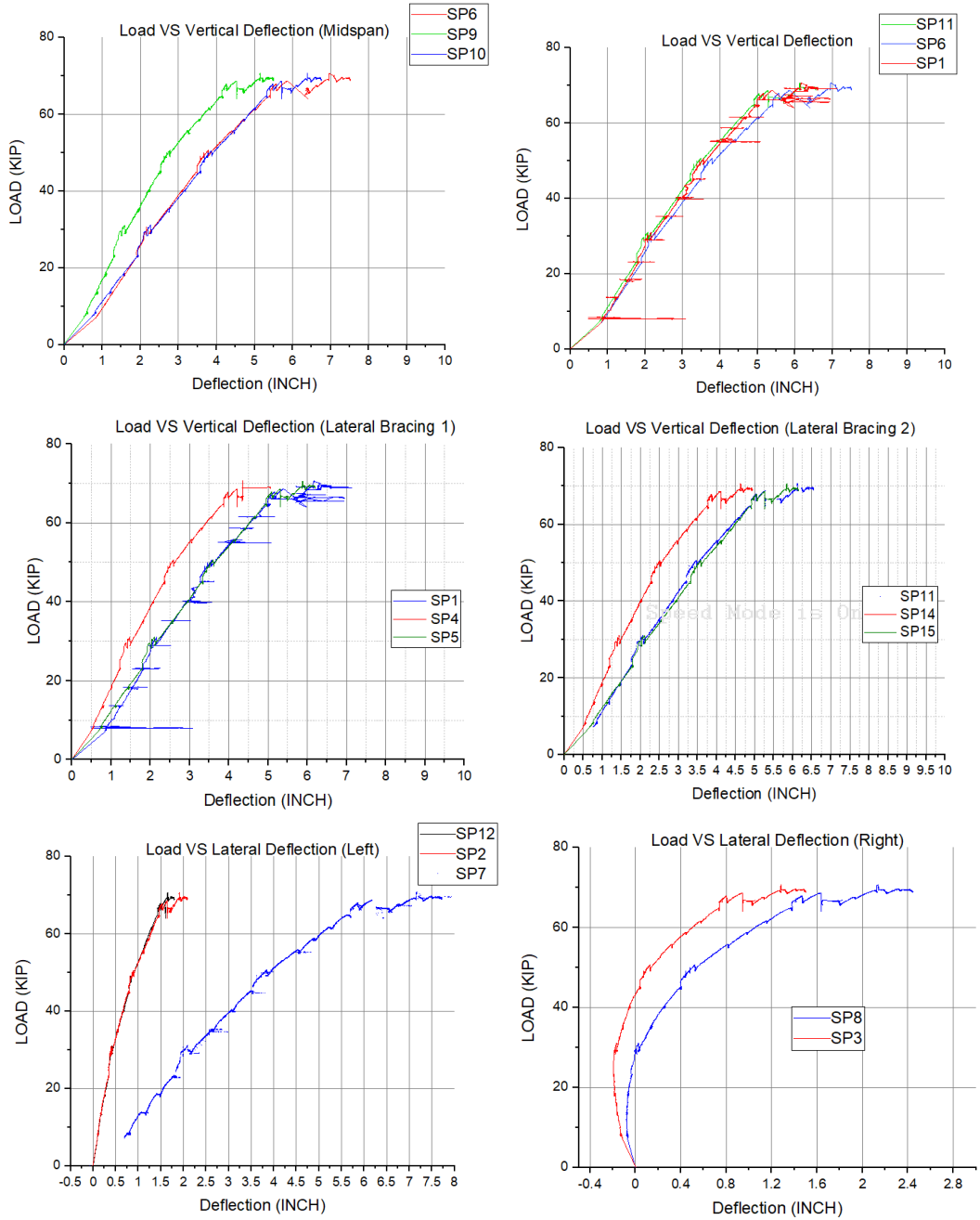


FIGURE 111: LOAD-DEFLECTION DATA FOR XZ95-35-2

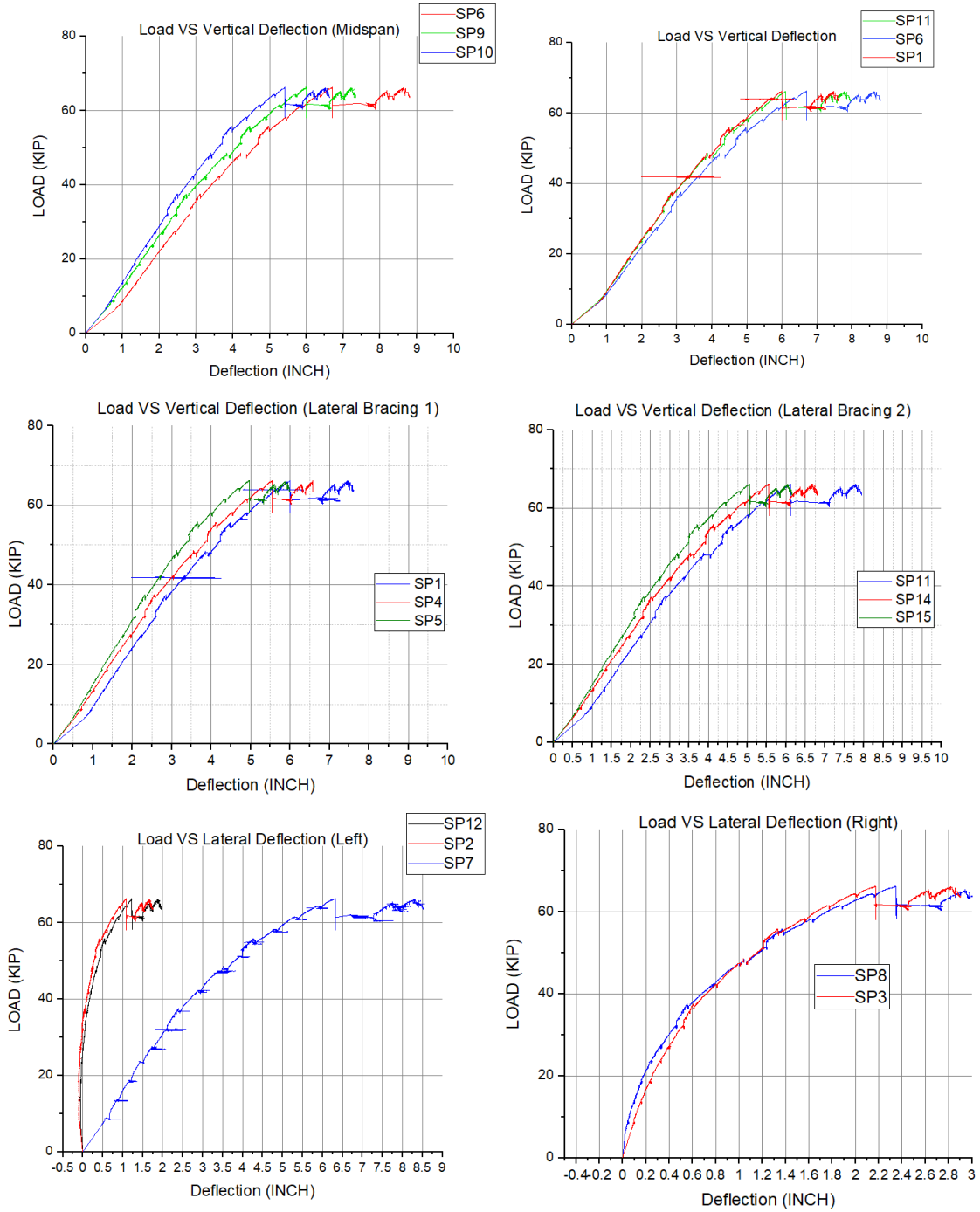


FIGURE 112: LOAD-DEFLECTION DATA FOR XZ95-35-3

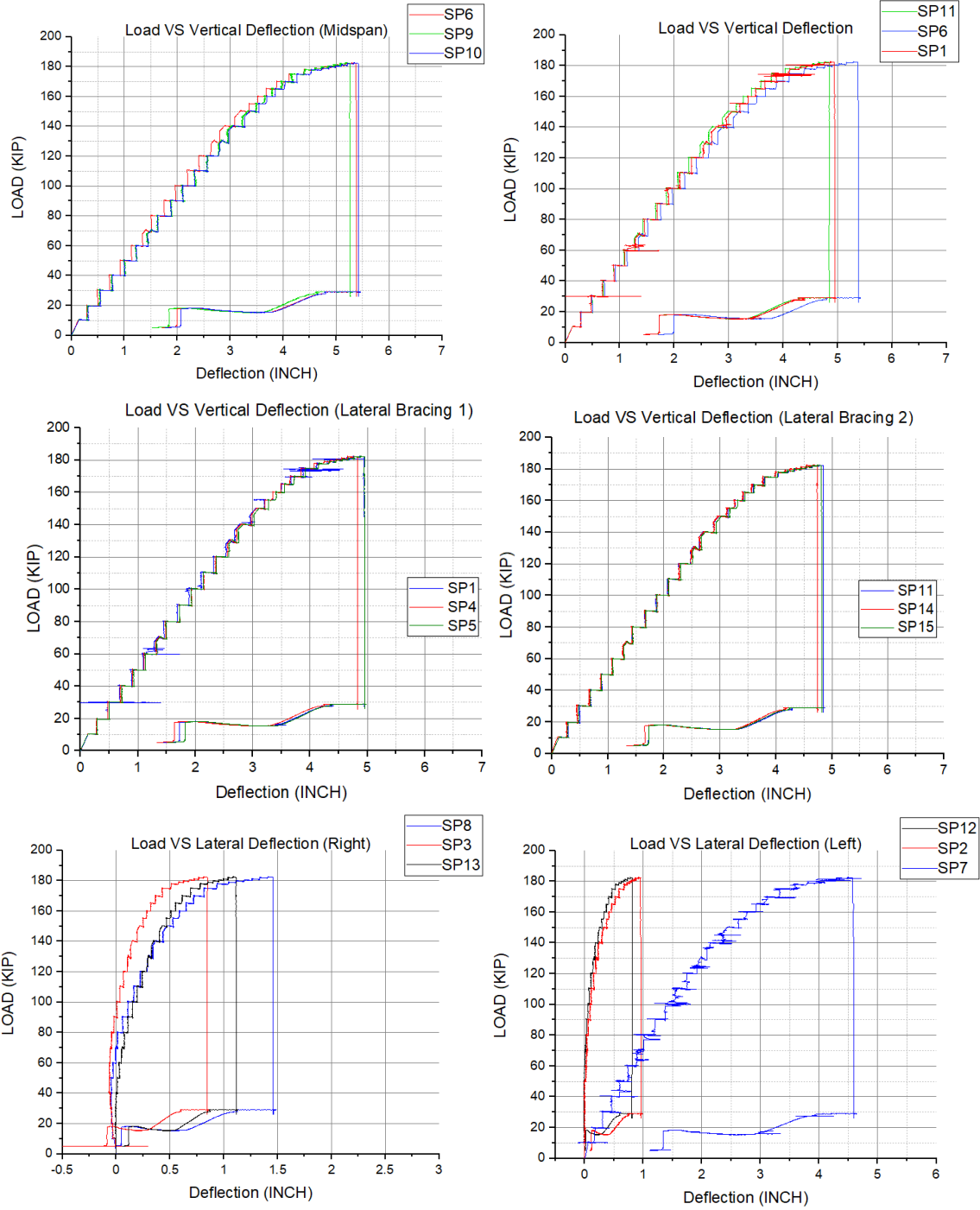


FIGURE 113: LOAD-DEFLECTION DATA FOR PZC26-35-1

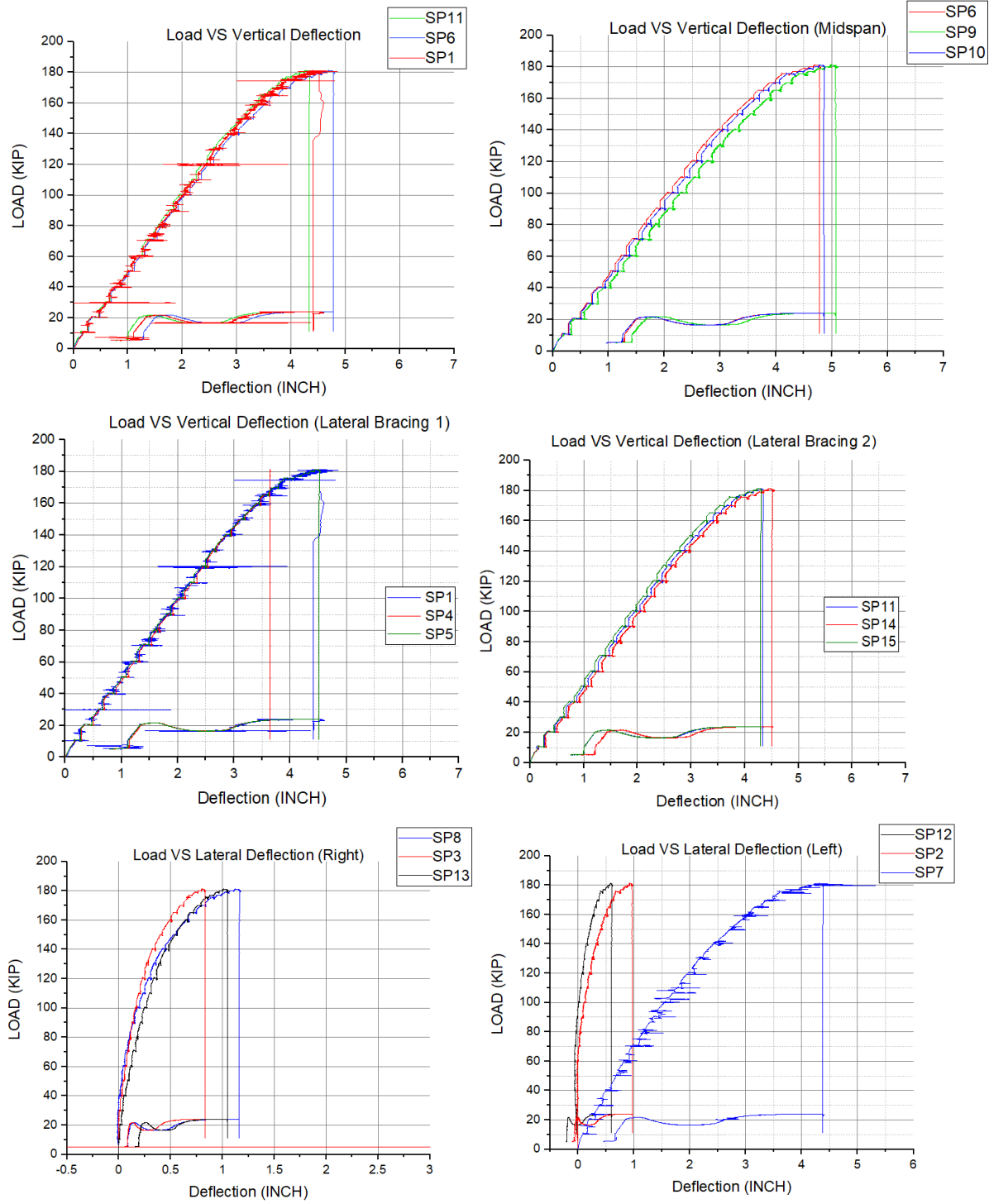


FIGURE 114: LOAD-DEFLECTION DATA FOR PZC26-35-2

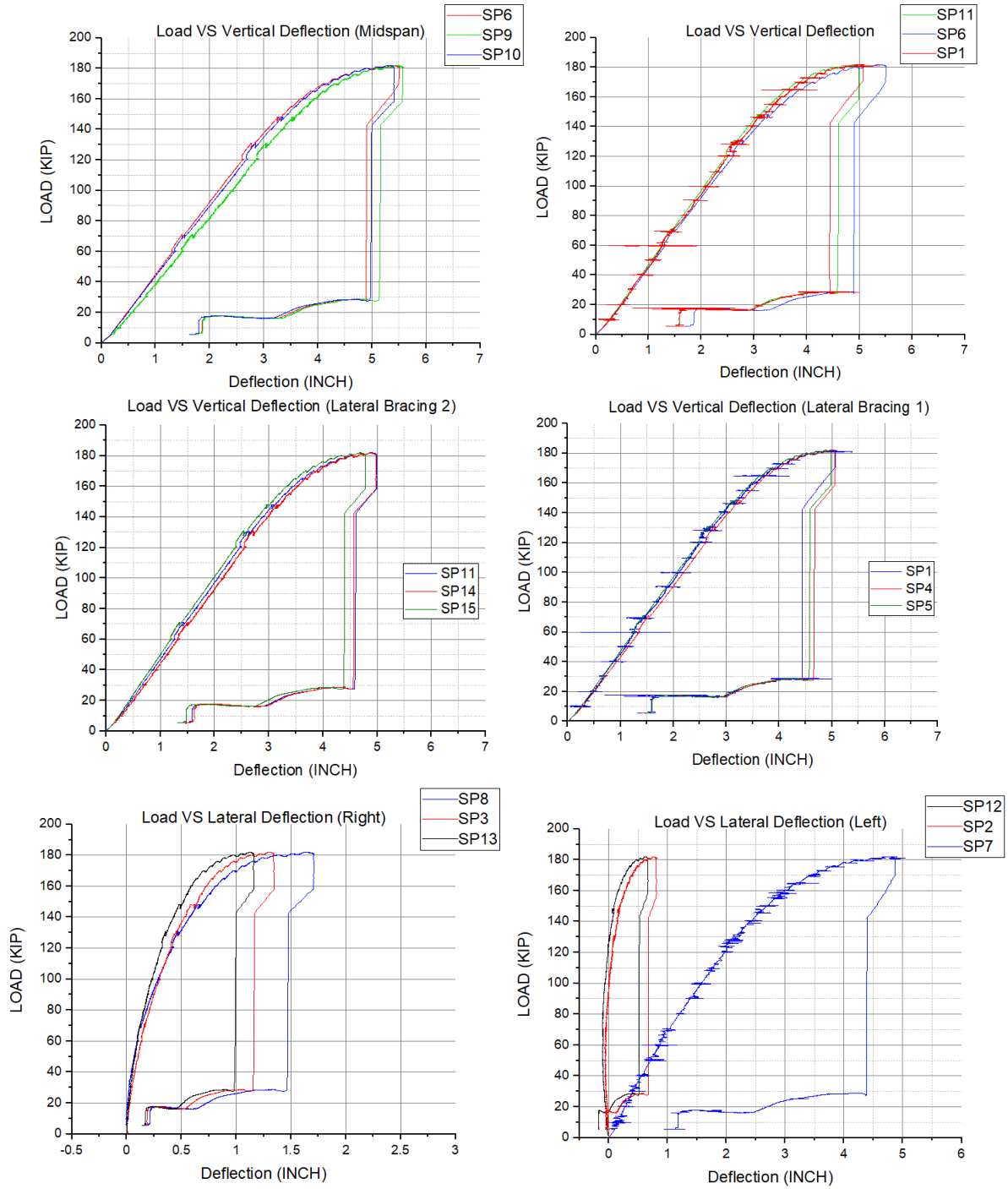


FIGURE 115: LOAD-DEFLECTION DATA FOR PZC26-35-3

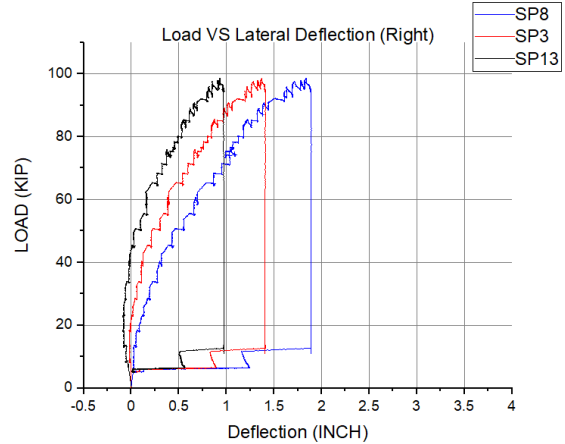
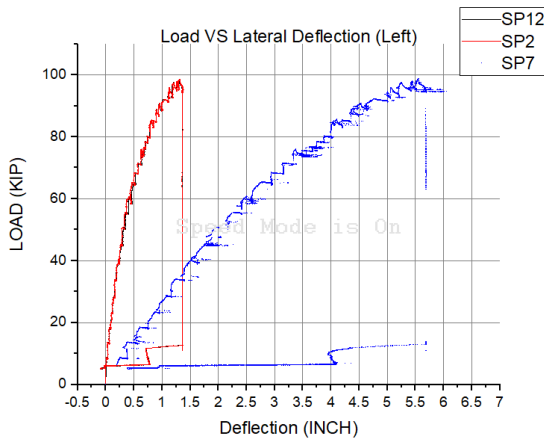
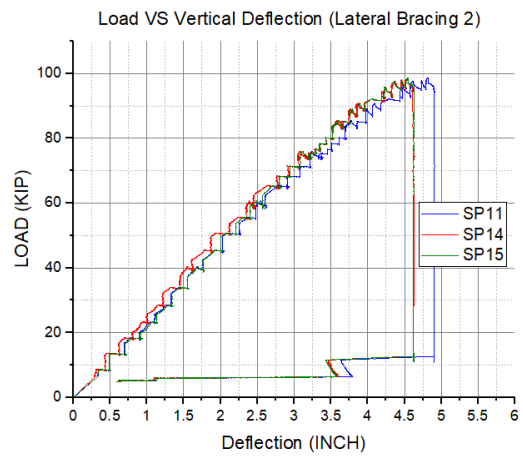
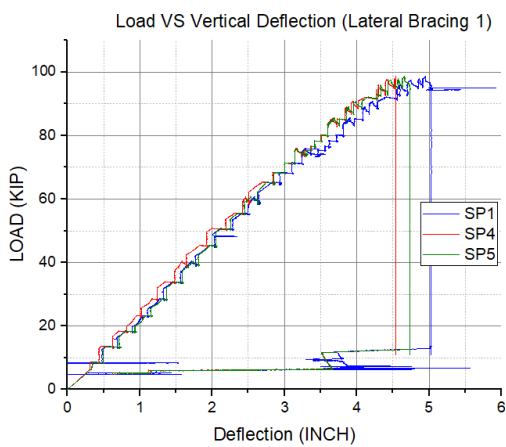
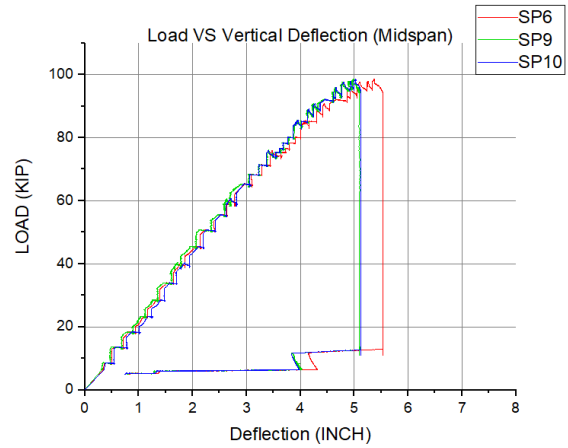
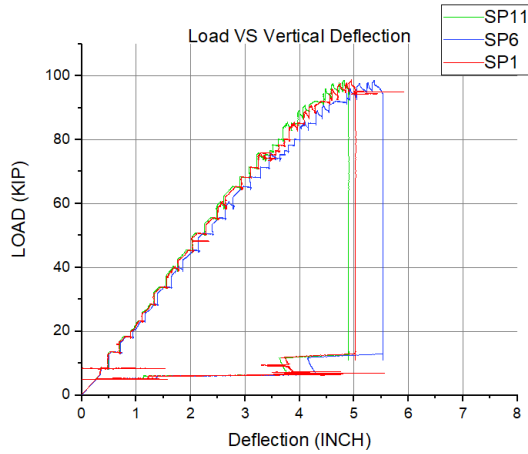


FIGURE 116: LOAD-DEFLECTION DATA FOR PZC18-35-1

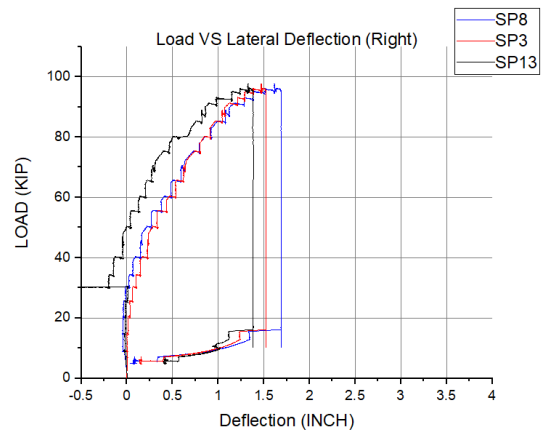
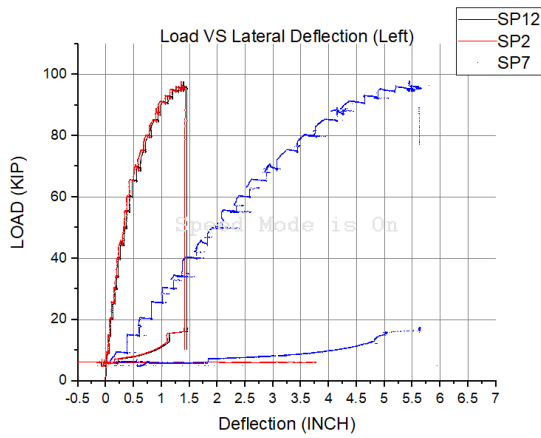
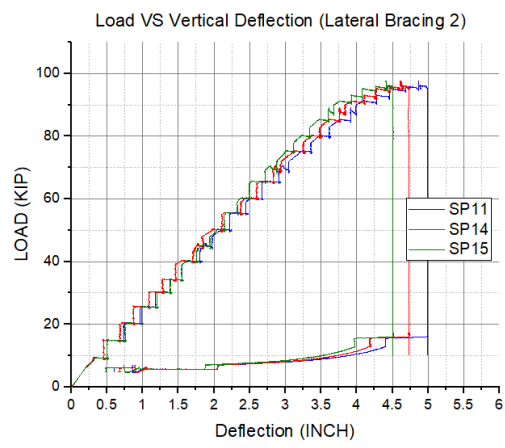
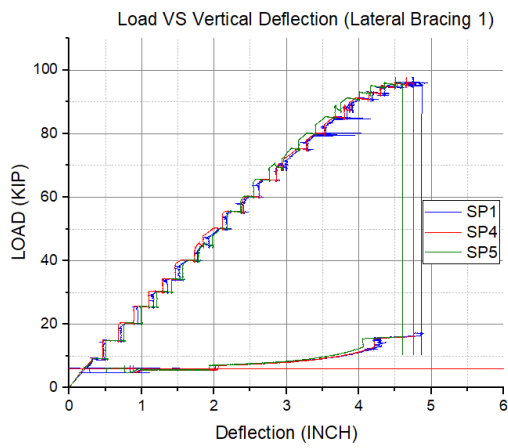
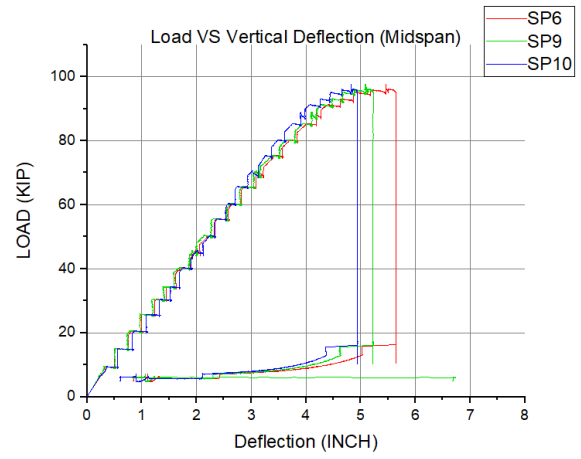
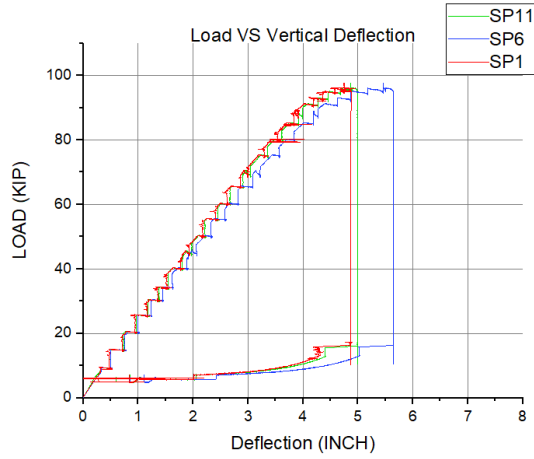


FIGURE 117: LOAD-DEFLECTION DATA FOR PZC18-35-2

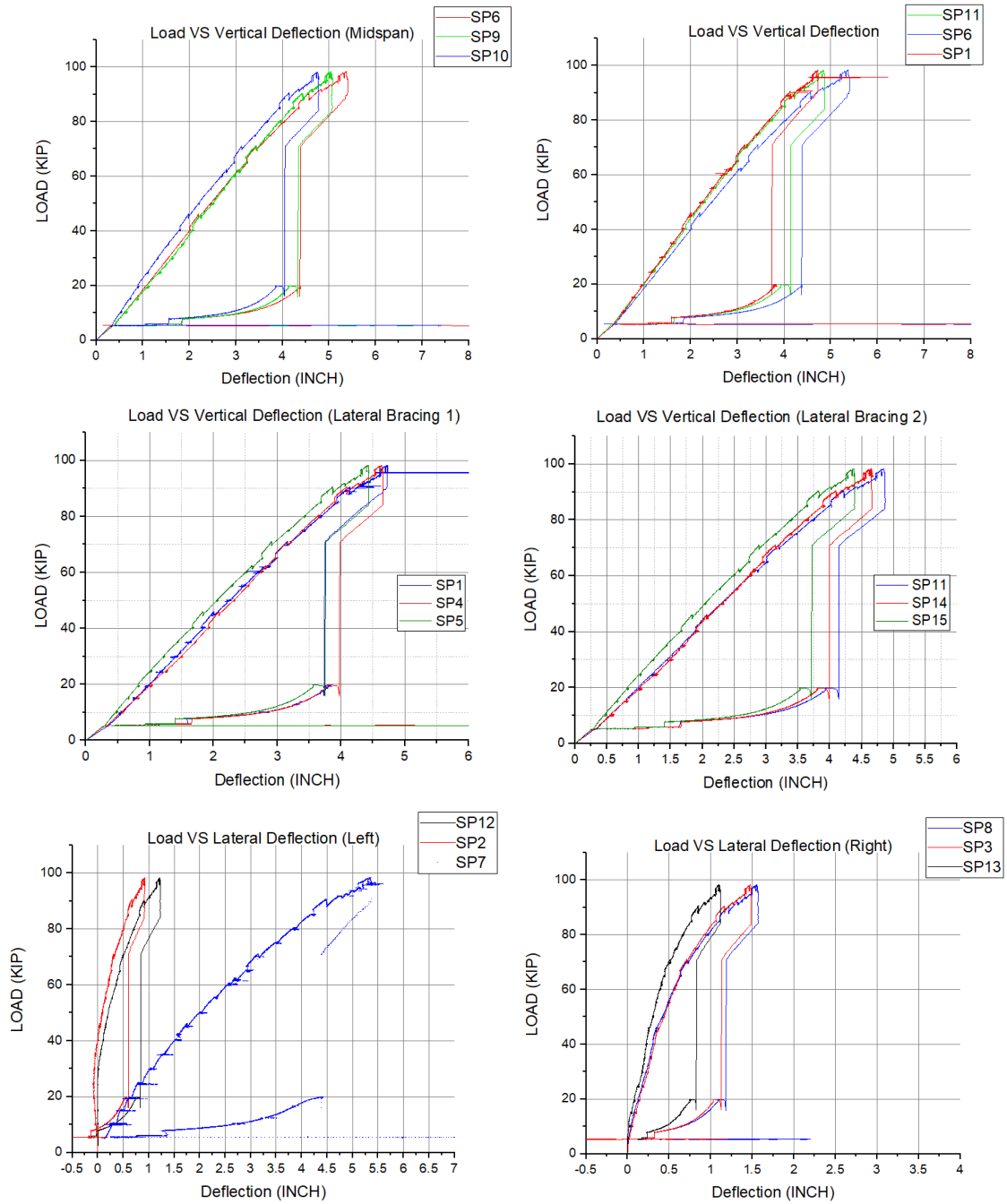
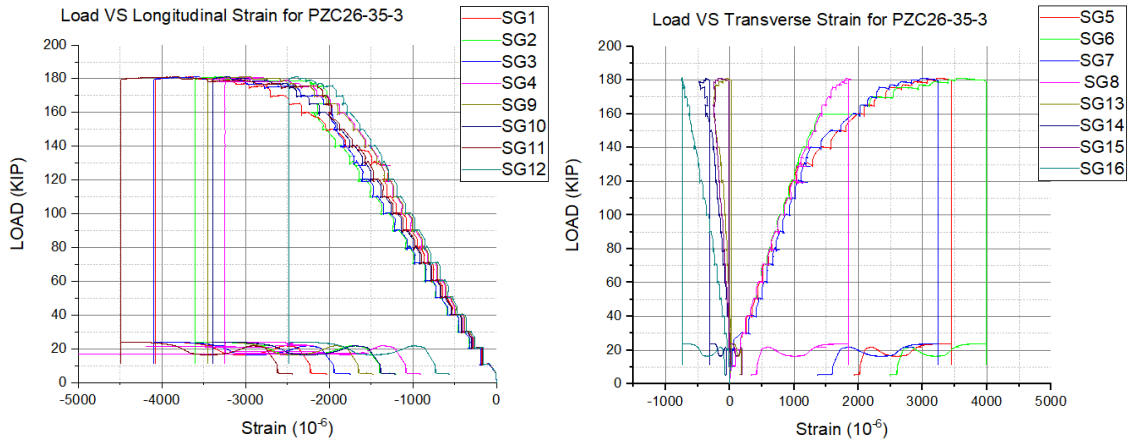
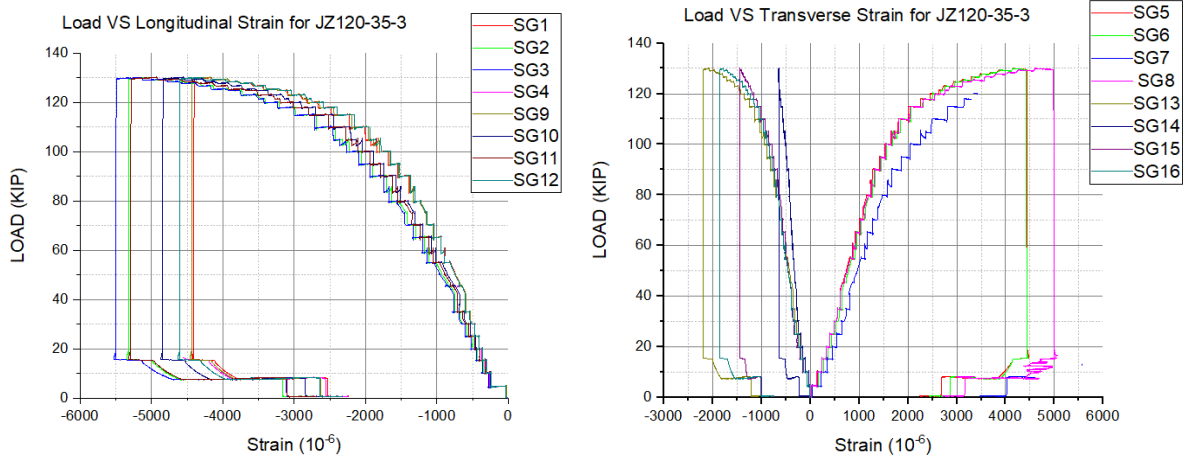


FIGURE 118: LOAD-DEFLECTION DATA FOR PZC18-35-3

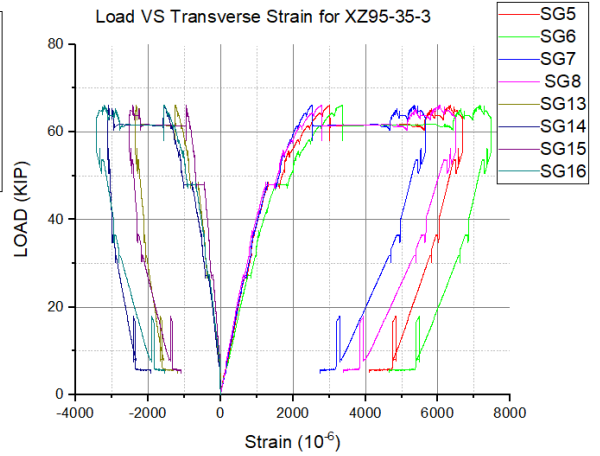
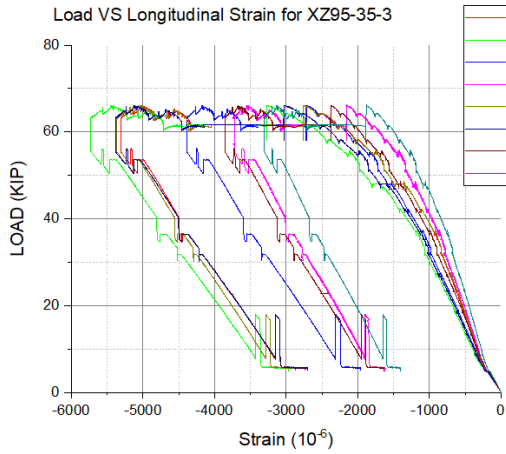
C.3 Strain Gauge data



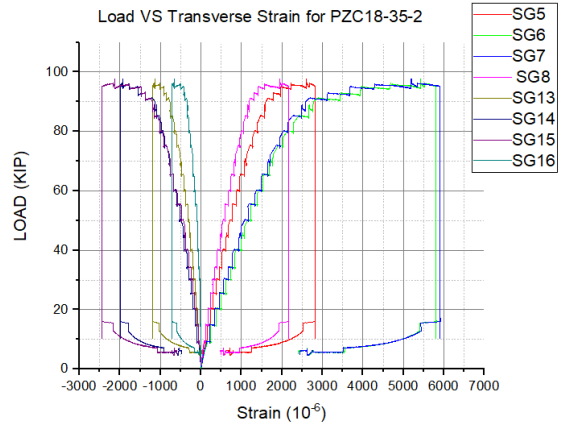
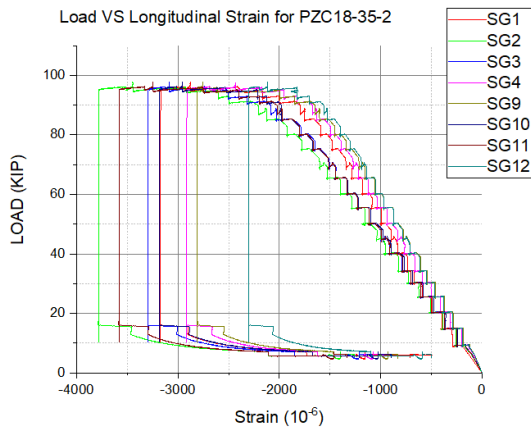
a) 35-ft PZC26 Specimens



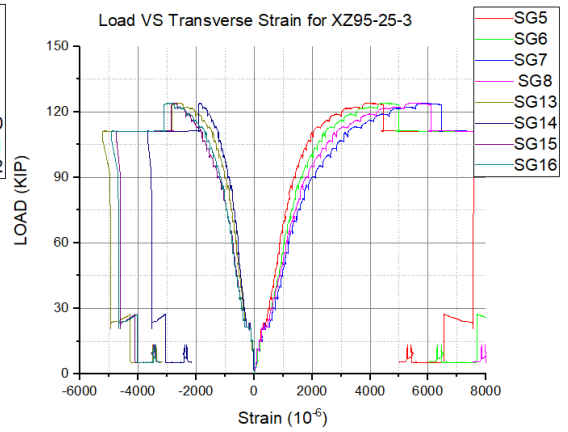
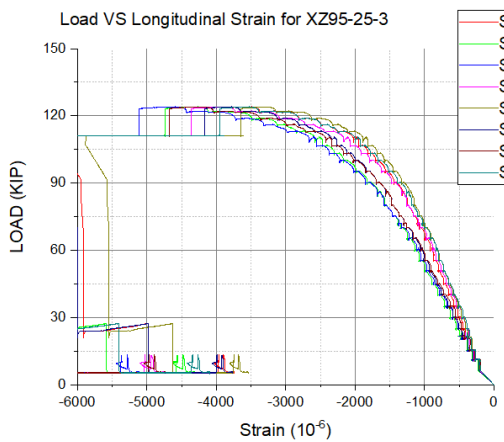
b) 35-ft JZ120 Specimens



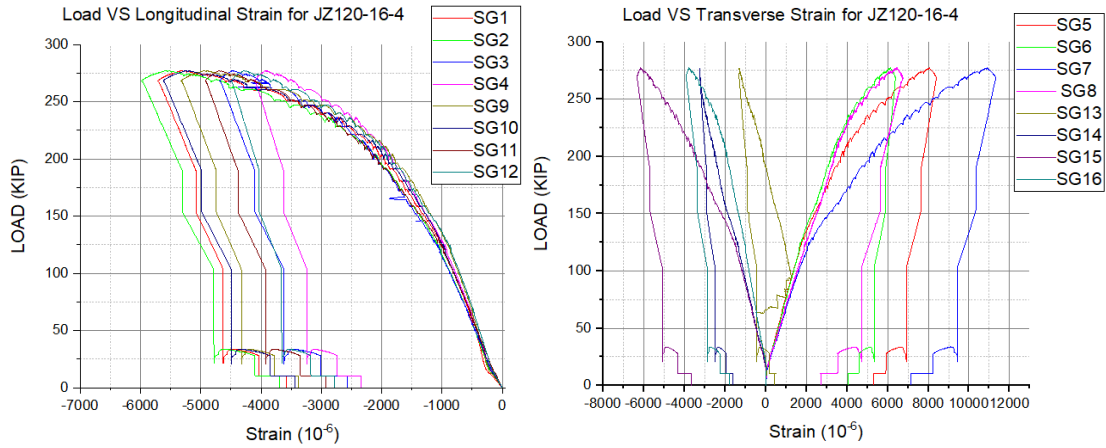
c)35-ft XZ95 Specimens



d)35-ft PZC18 Specimens



e)25-ft XZ95 Specimens



f) 16-ft JZ120 Specimens

FIGURE 119: STRAIN GAUGE DATA

C.4 Tensile Coupon Results

Profile	Specimen	Location	Fy	Fu	Fy	Fu	Fy	Fu
JZ120_16	1	FW	60.0	68.3	58.8	69.2	57.2	68.2
		WW	57.6	70.1				
		FE	56.0	67.1	55.6	67.2		
		WE	55.2	67.2				
	2	FW	55.0	67.7	55.3	66.9	55.5	67.1
		WW	55.6	66.0				
		FE	56.2	67.1	55.7	67.4		
		WE	55.1	67.7				
	3	FW	52.5	64.2	52.4	64.2	51.7	63.9
		WW	52.3	64.2				
		FE	51.2	63.1	51.1	63.7		
		WE	50.9	64.2				

a) JZ120-16

Profile	Specimen	Location	Fy	Fu	Fy	Fu	Fy	Fu
XZ95_25	1	FW	59.5	70.1	58.1	69.8	58.1	69.7
		WW	56.7	69.5				
		FE	58.4	69.5	58.1	69.5		
		WE	57.7	69.5				
	2	FW	57.7	68.6	56.9	68.6	56.3	68.9
		WW	56.1	68.6				
		FE	56.3	68.8	55.8	69.3		
		WE	55.3	69.7				
	3	FW	55.3	68.7	54.6	68.9	55.0	69.0
		WW	53.9	69.0				
		FE	56.4	68.9	55.4	69.1		
		WE	54.3	69.3				

b) XZ95-25

Profile	Specimen	Location	Fy	Fu	Fy	Fu
JZ120_35	1	FW	55.7	67.0	56.5	67.4
		FE	57.3	67.8		
	2	FW	57.9	67.5	58.2	69.4
		FE	58.4	71.2		
	3	FW	57.3	69.0	57.7	68.9
		FE	58.1	68.8		

c) JZ120-35

Profile	Specimen	Location	Fy	Fu	Fy	Fu
XZ95_35	1	FW	57.2	68.9	57.8	69.5
		FE	58.3	70.0		
	2	FW	58.3	70.6	58.4	70.2
		FE	58.5	69.8		
	3	FW	58.4	70.4	58.1	69.8
		FE	57.9	69.5		
	WE	57.9	69.6			

d) XZ95-35

Profile	Specimen	Location	Fy	Fu	Fy	Fu
PZC26_35	1	FW	58.6	73.1	62.7	74.2
		FE	66.7	75.3		
	2	FW	63.1	78.2	62.5	77.6
		FE	61.8	77.0		
	3	FW	60.7	76.4	61.8	77.0
		FE	62.8	77.6		

e) PZC26-35

Profile	Specimen	Location	Fy	Fu	Fy	Fu
PZC18_35	1	FW	56.9	70.0	57.2	69.7
		FE	57.5	69.3		
	2	FW	56.9	69.6	57.1	70.1
		FE	57.3	70.6		
	3	FW	57.6	70.7	58.1	71.0
		FE	58.5	71.3		

f) PZC18-35

FIGURE 120: TENSILE COUPON RESULTS

APPENDIX D

Frictional Resistance of Clamps

The total of four 12-inch heavy-duty clamps (2 clamps on each side of the cross-section) were attached to each lateral bracing to the specimens. The properties of the clamp according to McMaster Catalog are shown in the figure below.

Extra Heavy Duty C-Clamp

Square Handle, 0" to 4-1/2" Opening



Each In stock
\$123.62 Each
5029A33

ADD TO ORDER

Clamp Type	C
Opening	
Maximum	4 1/2"
Min.	0"
Reach	2 7/8"
Holding Capacity	20,000 lbs.
Body Material	Steel
Fixed Clamping Surface	
Location	Body
Material	Steel
Texture	Smooth
Fixed Tip Clamping Surface	
Location	Screw
Material	Steel
Texture	Smooth
Body Height	9 5/8"
Screw Material	Steel

FIGURE 121: 12-INCH HEAVY-DUTY CLAMP CATALOG (MCMASTER, 2020)

Holding force of a 12-inch heavy-duty clamp tighten with a wrench is 20 kips. Assuming the coefficient of friction between 2 steel surfaces is 0.6, the frictional resistance for each clamp is $0.6 \times 20 \text{ kips} = 12 \text{ kips}$. The friction force required can be computed using the lateral pressure components from the air bladder. The maximum target pressure occurs at JZ120 with 16 clear span length. Given the maximum pressure of 65 psi from NBM (2016), air bladder length of 96 inches, and the vertical web height of 16.47 in, the total lateral force on each side of the cross-section is $65/1000\text{ksi} \times 16.7 \times 96\text{in} = 104.21 \text{ kips}$. The lateral force on

each lateral bracing is $104.21\text{kips}/2 = 52.1\text{kips}$. Assumed more than half of the lateral force on each is of the cross-section is balanced via the top flange, the remaining force required for each clamp is approximately $0.45*52.1\text{kip}/2 = 11.7$ kips. Therefore, the frictional capacity is sufficient to resist the required lateral force.

APPENDIX E

Sensor Models and Specifications

E.1 Enerpac Hydraulic Ram

Model: RR20013, 221 ton Capacity, 13.00 in Stroke, Double-Acting, General Purpose Hydraulic Cylinder

Specifications	Single Cylinder
Return Type	Double-Acting, Hydraulic Return
Maximum Cylinder Capacity (tons)	
Advance	221
Retract	112.5
Stroke (in)	13
Cylinder Weight (lbs)	440
Cylinder Effective Area (in ²)	
Advance	44.21
Retract	22.5
Oil Capacity (in ³)	
Advance	574.78
Retract	293
Collapsed Height (in)	23.94
Cylinder Rod Diameter (in)	
Plunger Internal Thread (in)	2½" - 12
Center Hole Diameter (in)	
Plunger External Thread (in)	
Collar Thread (in)	9 3/4" - 12



FIGURE 122: ENERPAC RAM PROPERTY (ENERPAC, 2020)

Dimensions

Units: **Imperial** Metric

Collapsed Height A (in)	23.94
Extended Height B (in)	36.94
Outside Diameter D (in)	9.75
Cylinder Bore Diameter E (in)	7.5
Plunger Diameter F (in)	5.25
Base to Advance Port H (in)	2.25
Top to Retract Port (in)	3.81
Saddle Diameter J1 (in)	5.25
Saddle Protrusion from Plunger K (in)	0.88
Plunger Internal Thread O (in)	2½" - 12
Plunger Thread Length P (in)	2.5
Base Mounting Holes Bolt Circle U (in)	5
Base Mounting Holes Thread V	1" - 8
Collar Thread Size W	9¾" - 12
Collar Thread W (in)	9 3/4" - 12
Collar Thread Length X (in)	2.13
Base Mounting Holes Thread Depth Z (in)	1

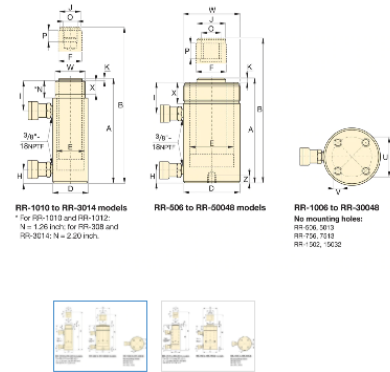


FIGURE 123: ENERPAC RAM DIMENSIONS (ENERPAC, 2020)

E.2 String Potentiometers

Model Number: PT101-0010-111-5110

Specification Summary:

GENERAL

Full Stroke Range Options.....0-2 to 0-100 inches
 Output Signal Options..... voltage divider (potentiometer)
 Accuracy ± 0.25% to ± 0.10% full stroke *see ordering information*
 Repeatability ± 0.02% full stroke
 Resolution essentially infinite
 Measuring Cable Options019-in. dia. nylon-coated stainless steel
 Enclosure Material powder-painted and anodized aluminum
 Sensor plastic-hybrid precision potentiometer
 Potentiometer Cycle Life *see ordering information*
 Maximum Retraction Acceleration *see ordering information*
 Weight 2 lbs. max.

ELECTRICAL

Input Resistance Options..... 500, 1K, 5K, 10K or bridge, *see ordering information*
 Power Rating, Watt 2.0 at 70°F derated to 0 at 250°
 Recommended Maximum Input Voltage 30 V (AC/DC)
 Output Signal Change Over Full Stroke Range..... 94% ± 4% of input voltage

ENVIRONMENTAL

Enclosure NEMA 1
 Temperature Coefficient of Sensing Element..... 88 PPM/°F
 Humidity 100% RH @ 90°F (32 C)
 Operating Temperature..... -40° to 200°F (-40° to 90°C)
 Vibration up to 10 G's to 2000 Hz maximum



FIGURE 124: STRING POTENTIOMETER SPECIFICATION (CELESCO, 2005)

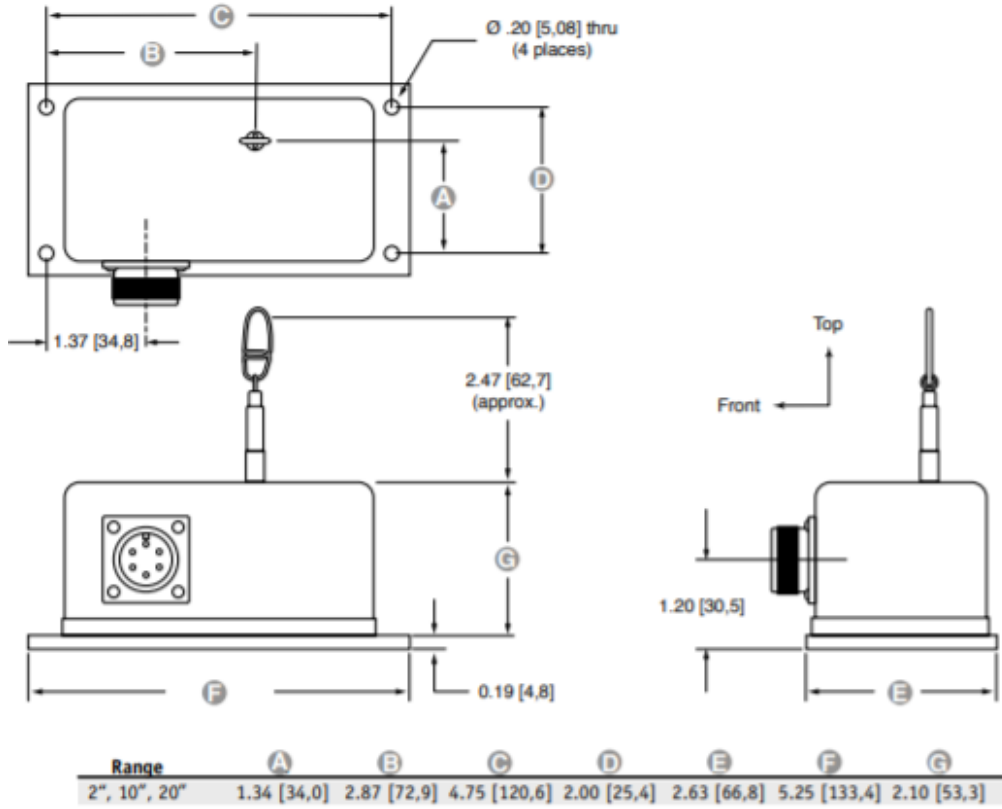


FIGURE 125: STRING POTENTIOMETER DRAWING (CELESCO, 2005)

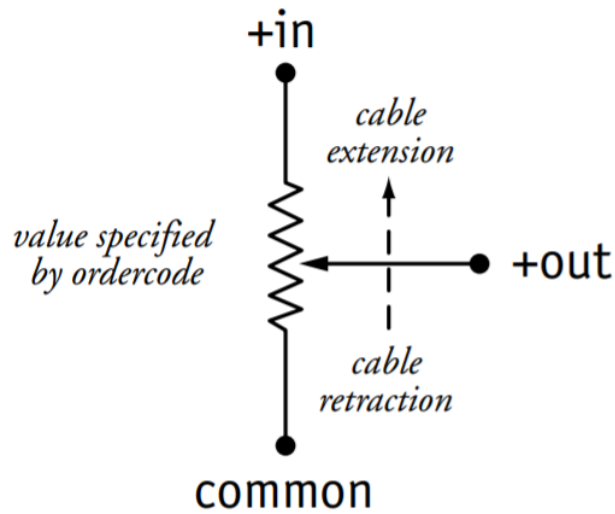


FIGURE 126: STRING POTENTIOMETER CIRCUIT (CELESCO, 2005)

E.3 Strain Gauges



FIGURE 127: STRAIN GAUGE PACKAGE

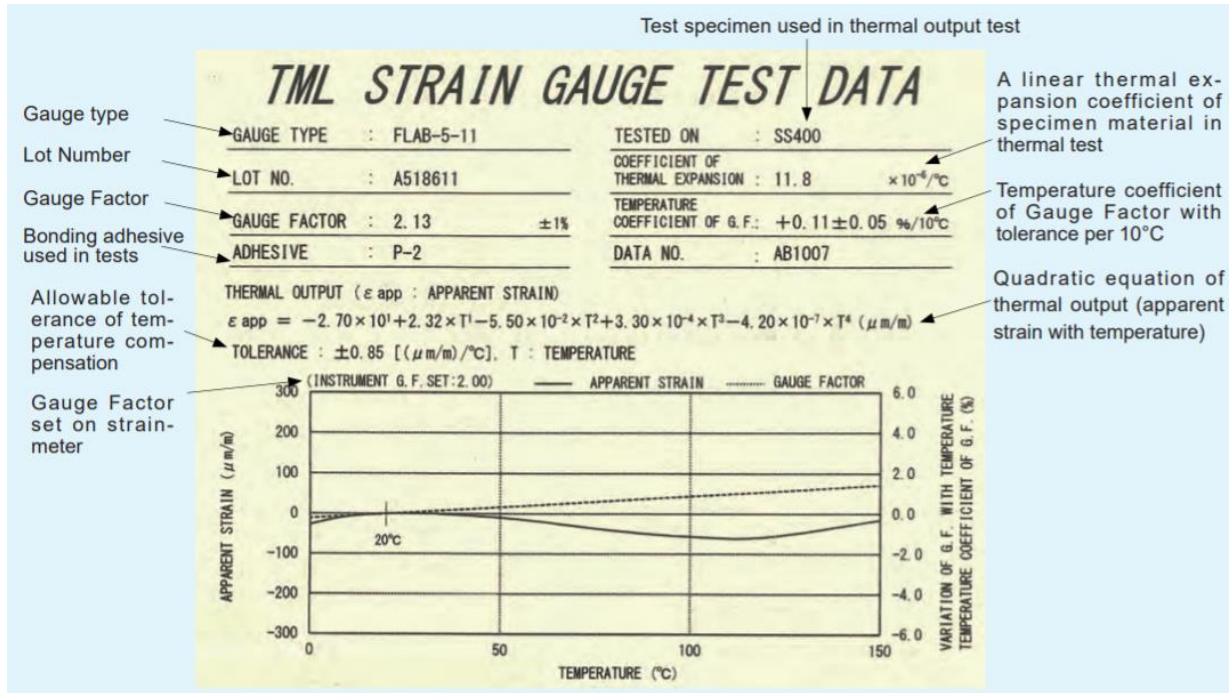


FIGURE 128: STRAIN GAUGE DATA SHEET (TOKYO MEASURING INSTRUMENTS LAB., 2017)

E.3 Pressure Transducer



FIGURE 129: PRESSURE TRANSDUCER (OMEGA ENGINEERING, 2019)

Rugged, General Purpose Transducer

Common Specifications for 100 mV, 0 to 5 Vdc, and 0 to 10 Vdc, 4 to 20 mA Outputs



- ✓ 1, 2 & 5 psi Low Pressure Ranges!
- ✓ All Stainless Steel Construction
- ✓ Gage or Absolute Pressure
- ✓ Rugged Solid State Design
- ✓ High Stability, Low Drift
- ✓ 0.25% Static Accuracy
- ✓ IP 65 Protection Class

Omega's PX309 Series models below 100 psi use a high-accuracy silicon sensor protected by an oil-filled stainless steel diaphragm. Units 100 psi and above use silicon strain gages molecularly bonded to the stainless steel diaphragm.

Common

Specifications

Ranges: -15 to 50 psig, 0 to 1000 psia, 100 to 10,000 psig

Accuracy (Combined Linearity, Hysteresis and Repeatability): ±0.25% BSL, max

Minimum Resistance Between Transducer Body and Any Wire: 1M Ω @ 25 Vdc

Calibration: In vertical direction with fitting down, compound ranges are calibrated for positive pressure output only

Pressure Cycles: 10 million, minimum

Pressure Overload: -15 to 50 psig and 0 to 1000 psia: 3 times rated pressure or 20 psi whichever is greater, 100 to 10,000 psig: 2 times rated pressure

Burst Pressure: -15 to 50 psig and 0 to 1000 psia: 4 times rated pressure or 25 psi whichever is greater, 100 to 10,000 psig: 5 times rated pressure

Long Term Stability (1 Year): ±0.25% of FS, typical

Operating Temperature: -40 to 85°C (-40 to 185°F)

Pressure Port: ¼-18 MNPT

Pressure Port Material: -15 to 50 psig and 0 to 1000 psia: 316 SS, 100 to 10,000 psig: 17-4 PH SS

Bandwidth: DC to 1 kHz (typical)

CE: Compliant

Shock: 50 g, 11 ms half-sine

Vibration: ±20 g

Response Time: <1 millisecond

Weight:

PX309: 154 g (5.4 oz),

PX319/329/359: 100 g (3.5 oz)

IP Rating: IP65

RoHS: Compliant

Order a snubber to protect your pressure transducer!



PS-4G, shown actual size.

Snubbers protect sensors from fluid hammers/spikes.

FIGURE 130: PRESSURE TRANSDUCER SPECIFICATION (OMEGA ENGINEERING, 2019)

mV Output Wiring			
Wiring	Cable	M12 and mini DIN	Twist-Lock
Excitation (+)	Red	Pin 1	Pin A
Output (+)	White	Pin 3	Pin C
Output (-)	Green	Pin 4	Pin D
Excitation (-)	Black	Pin 2	Pin B
Spare	—	—	Pin E
Vent	—	—	Pin F

5 and 10 Vdc Output Wiring			
Wiring	Cable	M12 and mini DIN	Twist-Lock
Excitation (+)	Red	Pin 1	Pin A
Excitation (-)	Black	Pin 2	Pin B
Output (+)	White	Pin 3	Pin C
N/C†	—	Pin 4	Pin D
Spare	—	—	Pin E
Vent	—	—	Pin F

mA Output Wiring			
Wiring	Cable	M12 and mini DIN	Twist-Lock
Supply (+)	Red	Pin 1	Pin A
Supply (-)	Black	Pin 2	Pin B
N/C†	—	Pin 3	Pin C
N/C†	—	Pin 4	Pin D
Spare	—	—	Pin E
Vent	—	—	Pin F

† N/C: Do not connect any wires to this pin.

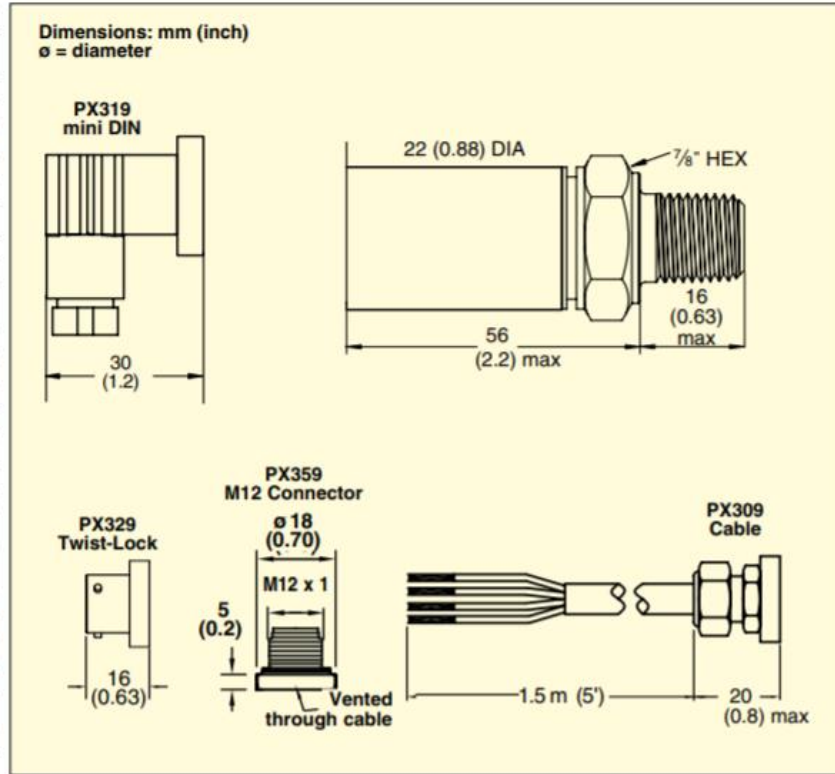


FIGURE 131: PRESSURE TRANSDUCER WIRING DIAGRAM (OMEGA ENGINEERING, 2019)